Instabilities in Nonequilibrium Solid Solutions with Respect to Amorphization and Melting

Thesis by

Carl Emil Krill III

In Partial Fulfillment of the Requirements
for the Degree of
Doctor of Philosophy

California Institute of Technology
Pasadena, California

1992

(Submitted 20 May 1992)

To my parents

Acknowledgments

Despite the common conception of scientists as mentally imbalanced misanthropes slaving away in search of the one great discovery that will make them either rich enough to buy their own spaceship or powerful enough to subdue the world, most of us are (somewhat) normal people just trying to have a good time. If anyone doubts these words, let him or her meet Bill Johnson. No one I have ever met gets a bigger kick out of solving scientific problems, interpreting puzzling data or figuring out how Mother Nature operates, despite her best efforts to cover her tracks. And no one goes to greater lengths than Bill does to convey this enthusiasm to his students. If only there were a way he could pass on some of his scientific intuition, which no doubt contributes to his great enjoyment of science and to his success at it. Time will tell if any of it rubbed off on me during the past six years!

Not only did Bill hustle the funds to keep the research of the group going strong through some lean years, but his considerable reputation attracted a number of first-rate visitors and post-docs to our group, almost all of whom have contributed to this thesis work in some manner. Most significant and timely was the advice given by Rainer Birringer, who looked at some DSC data that had puzzled me for months and made a clever suggestion that solved every remaining open question in the $ErFe_2$ deuteride experiment! What a privilege it was to bounce ideas off such an insightful scientist.

I was once told by a Caltech faculty member that the usual pattern for graduate students doing experimental work is to slave away for four or five years with limited success and then to do all of the research that eventually winds up in the thesis in the last six months. My graduate work fit this prediction to a tee. In fact, most of the significant results described in this thesis were obtained during a one-month marathon of neutron diffraction data collection at the Missouri University Research Reactor (MURR) under the supervision of Bill Yelon. Without his cooperation and guidance, I would still be toiling away at this project. It was Dr. Yelon's suggestion to look at atomic mean-square displacements in the Nb–Pd solutions, an idea whose development constitutes the bulk of Chapter 4.

The term *marathon* hardly does justice to those thirty hectic days of neutron measurements. It is impossible, of course, for one person to stay awake for such a long period of time, but not for *two* people, as my fellow graduate student and assistant, Jianzhong Li, helped to prove! Jianzhong's past experience with neutron diffraction proved invaluable during our stay in Missouri. (Even more impressive than his success at fitting diffraction scans was his ability to tolerate living with me during those stressful days.) And his knack for finding cheap places to eat kept the trip reasonably affordable, even though most of his favorite places served only Chinese food!

All of the electron microscopy performed as part of this thesis bears the mark of Carol Garland's patience in teaching me how to handle the basics (Chapter 2) and her enormous skill in tackling more difficult situations (Chapter 4). Working with Carol on various microscopy projects was one of the real pleasures of my graduate school years.

The attentive reader of Chapter 4 will notice that my splat-quenched Nb–Pd samples made two trips across the Atlantic Ocean to destinations in Germany. (That's two more trips to Europe than I've made in my lifetime.) In Saarbrücken, Manfred Klingel measured the thermal expansion coefficient of a large number of samples on very short notice. His work disproved a promising and exciting hypothesis with which we had become enamored, but we've decided not to hold that against him! At first, it seemed as if the Debye-temperature measurements made by Christoph Ettl at Augsburg were destined to be equally disappointing, but when considered from the proper perspective (i.e., from Bill Johnson's perspective after he's had a chance to put his aforementioned intuition to work), they were the key to understanding the compositional dependence of the Nb–Pd mean-square displacements! Special thanks to both of these graduate students for their assistance.

Now, some words of appreciation for my officemate, Zezhong Fu. Not only did she make a useful sounding board for my latest crazy ideas about highly nonequilibrium solutions, most of which will never be made public (unless she squeals on me!), but she was always eager to share her data on hydrogenated $ErFe_2$, despite the fact that I was attempting to duplicate an experiment she had already performed (Chapter 3). That cooperation was absolutely necessary to the success of the hydrogen experiments.

It is a pleasure to acknowledge many of the others who have played a large role in my scientific and social life over the past several years: Hans Fecht (who never ceases to amaze me), Channing Ahn (whose sunny disposition never wavered in the face of my many last-minute pleas for help), Jürgen Eckert (who got me into ball milling), Joe Holzer (who got me into beer), Dave Lee, Jorge Kittl, Mo Li, Yoshi Abé, Phil Askenazy, Atakan Peker and many others I have forgotten to list. Special mention must be made of two Applied Physics classmates: Mike "Newk of Earl" Newkirk, who kept me sane during the homework-intensive first year (to this day I can't do a quantum mechanics problem without asking, "I wonder what answer Newk got?"), and Ed Yu, who got me through "superadvanced" quantum mechanics and taught me not to be impressed by Ivy League degrees.

My first real exposure to experimental science came as an undergraduate working in the laboratory of Gregory I. Gellene, Associate Professor of Chemistry at the University of Notre Dame. It was an experience that completely changed my outlook on science. Prior to working for Greg, I felt completely incapable of getting even the simplest experiment to work (a failed attempt at making soap in tenth-grade chemistry lab still comes to mind). By both instruction and example, he taught me how to perform reliable experiments and, in so doing, conveyed a feeling for the satisfaction that comes from experimental discovery.

I am most grateful to the National Science Foundation and to the Clark fund at Caltech for fellowship support. The United States Department of Energy supported virtually all of the research described in this thesis through its ongoing funding of Bill Johnson's research program.

Finally, it is with great joy that I dedicate this thesis to my parents! A deep commitment to well-rounded, liberal education has always informed their guidance and support, complemented by a constant exhortation to give one's best effort. On so many occasions and in so many ways I have seen how these values have served them well in their own lives—it is a great challenge and reward to make them a part of my own. What a privilege it has been to rely on their advice in times of difficulty and to share with them the exciting moments of new understanding that motivate scientific investigation.

Abstract

Recent years have witnessed the discovery of crystal-to-amorphous phase transformations induced by a variety of experimental processes. The kinetic and thermodynamic parallels between such amorphization transitions and ordinary melting are rather extensive, suggesting that the underlying physics are similar. In particular, the idea that melting occurs as the response of the crystalline phase to development of an intrinsic instability is quite controversial, but its analogue with respect to amorphization is gaining acceptance. This thesis investigates the validity of the instability concept for amorphization by searching for precursors to topological collapse in highly nonequilibrium solid solutions. In Chapter 2 the advantages and disadvantages of various means of synthesizing solid solutions beyond equilibrium solubility ranges are discussed, with particular attention being devoted to prediction of an alloy's potential for supersaturation from the characteristics of its equilibrium phase diagram. Hydrogenation and rapid quenching from the melt are found to achieve the best compromise between the kinetic requirements for sample preparation and the desired sample geometry for property measurements. Hydrogenation is applied in Chapter 3 to the progressive destabilization and amorphization of the intermetallic compound $ErFe_2$. Through a combination of high-temperature neutron diffraction and differential scanning calorimetry, the enthalpy release and structural change associated with the amorphization transition are studied. The transition is found to be strongly exothermic and driven by short-range clustering of the metal atoms. Rapid quenching from the melt is used in Chapter 4 to prepare highly supersaturated alloys of Nb–Pd. Low-temperature neutron diffraction measurements made at several compositions of the bcc α-Nb solution find an anomalously large increase in the atomic root-mean-square displacement to about half of the value at which the Lindemann criterion predicts the lattice should melt. Low-temperature heat capacity measurements find a concomitant decrease in the Debye temperature, suggesting that supersaturation causes an elastic modulus to soften. Single crystals of the α-Nb solution at the highest supersaturation have a highly anisotropic structure visible in transmission electron microscopy images; it is consistent with the development of a local instability with respect to the bcc-to-ω phase transformation. The ramifications of these experimental findings are considered in the final chapter. Violation of the polymorphous constraint with increasing supersaturation complicates quantification of the stability of a solid solution, but the results of this thesis definitely favor some proposed stability parameters over others. In particular, the anomalously high atomic mean-square-displacements found in supersaturated α-Nb solutions are most consistent with a mechanism of highly local topological fluctuations leading to shear softening as a precursor to—and probable cause of—amorphization.

Contents

List of Figures

List of Tables

Chapter 1

Introduction

In less than ten years the study of crystal-to-amorphous phase transitions has progressed from the simple development of new methods for inducing amorphization to the brink of a single conceptual framework unifying the various processing techniques. While no consensus yet exists regarding a proper order parameter for characterizing crystal-to-amorphous phase transitions, there is growing suspicion that such transitions occur in response to one or more underlying instabilities of the crystalline phase (combined with kinetic constraints preventing the crystal from transforming to an energetically more favorable final state than the amorphous phase). It is the goal of this thesis to search for the presence of underlying instabilities in crystals driven to the highly nonequilibrium states in which amorphization can occur.

In this chapter I will describe the fundamentals of instability theories for crystal-to-amorphous phase transitions and the ways in which they can be tested experimentally. This explanation will serve as an elucidation of the historical motivation for our studies and, to a certain extent, as an introduction to the concepts with which we will interpret the results of the following chapters. I shall endeavor in the final chapter to assess as objectively as possible the validity of the conceptual framework erected in the first.

Rather than diving immediately into details, let us first consider an outline of the main parts of this chapter. I shall begin by briefly describing the variety of processing methods known to induce crystal-to-amorphous phase transitions. The similarity of the symmetry change, nucleation behavior and structural change of crystal-to-amorphous and crystal-to-liquid (i.e., melting) transformations will suggest a similarity in the underlying physics of amorphization and melting. A comparison of evidence for instability theories of melting with that for instability theories of amorphization will strengthen the proposed connection between the two phenomena. Fecht and Johnson [1] have developed a unified thermodynamic picture of (nonequilibrium) melting and amorphization based on the idea that both occur as the response of the crystal to the *same* underlying instability. I shall describe their framework and its experimental implications regarding the melting and amorphization of supersaturated solid solutions at various temperatures and pressures. In particular, their approach entails the existence of a critical point at which the crystalline, amorphous and liquid states may become indistinguishable, raising the possibility of *continuous* melting and amorphization. I shall conclude the chapter with an overview of the chapters of this thesis describing the experimental search for crystalline instabilities and our conclusions regarding the extent to which this conceptual framework captures the essential underlying physics of crystal-to-amorphous phase transitions.

1.1 Crystal-to-amorphous phase transitions

Several experimental means of inducing a solid to transform from the crystalline state to an amorphous state have been discovered in the past ten years. I shall give only a brief description of the various processing methods, since the interested reader may consult one of many review articles for further details [2, 3, 4, 5, 6, 7].

1.1.1 Hydrogenation

Historically, the first report of a crystal-to-amorphous transition was noted by researchers investigating the hydrogen-storage capability and thermal stability of La–Ni hydrides [8]. After annealing various La–Ni intermetallic compounds in a hydrogen atmosphere, they observed that the x-ray diffraction Bragg peaks indicative of long-range crystalline order had disappeared! This observation and subsequent reports [9, 10, 11] of the same phenomenon in related hydrides all suffered from the inability to rule out transformation to a polycrystalline state of very small grain size (i.e., $\lesssim 2\,\mathrm{nm}$) rather than to a truly amorphous phase [12]. Convincing evidence for true hydrogen-induced amorphization of a crystalline phase was first obtained by Yeh, Samwer and Johnson [13] in 1983. They observed the gradual disappearance of Bragg peaks in x-ray diffraction scans of melt-spun crystalline ribbons of Zr_3Rh annealed in 1 atm (1×10^5 Pa) of hydrogen at temperatures in the range 150–225 °C. The radial distribution function of the amorphous Zr_3Rh hydride formed by this reaction was essentially identical to that of a sample made by hydrogenating an already-amorphous ribbon of Zr_3Rh made by rapid-quenching, thus supporting the contention that the loss of Bragg peaks corresponded to a true loss of crystalline order [14]. Hydrogen-induced amorphization has since been observed in a wide variety of intermetallic compounds with $B8_2$, C15, C23, $D0_{19}$ and $L1_2$ structures [15]. We shall encounter a specific example of this amorphization technique in Chapter 3.

1.1.2 Solid-state amorphization

Another processing method for inducing crystal-to-amorphous transformations involves an interfacial solid-state reaction between certain elemental layers. Schwarz and Johnson [16] reported in 1983 that an amorphous phase could be induced to grow in an initially crystalline diffusion couple of Au and La by a low-temperature anneal. Other binary systems, such as Ni–Zr [17], Ni–Ti [18] and Co–Sn [19], were subsequently discovered to react in a similar manner. The amorphization reaction occurs only between two elements for which (i) one element diffuses unusually rapidly in the other and whose (ii) amorphous phase has a large negative heat of formation [2, 4, 6]. For such diffusion couples an annealing treatment at relatively moderate temperatures ($\lesssim 400\,^\circ\mathrm{C}$) induces growth of an amorphous layer to a maximum thickness of $\sim 100\,\mathrm{nm}$ at the layer interface [5]. The term *solid-state amorphization reaction* (SSAR) is frequently used for this process. Thick films can be amorphized by SSAR if thin layers are deposited in alternating sequence: if the compositional wavelength of the multilayer is less than about twice the maximum amorphous interlayer thickness for that diffusion couple, then annealing can yield a completely amorphous film. The extension of the latter technique to form bulk amorphous samples is obvious: if filamentary or lamellar composites of elements known to undergo SSAR are prepared so that the individual filaments or layers have one or more nanometer-scale dimensions, such as by mechanical extrusion, drawing of powder mixtures or rolling of layered foils [20, 21, 22, 23], then annealing the composite can cause the amorphous interlayers to grow to encompass the entire bulk sample.

1.1.3 Ball milling

A related technique involves the use of a high-energy ball mill to alloy powders of two or more elements [24]. The mechanism for such mechanical alloying is poorly understood [25], but surely it must involve the severe deformation and mutual cold welding of powders trapped between colliding balls or between a ball and the container surface. Some researchers [26, 27] have claimed that during the early stages of ball milling, a lamellar structure is formed that subsequently amorphizes by SSAR (see previous section), but it is not necessary for a binary system to exhibit SSAR in order to form an amorphous phase by mechanical alloying [28]. I shall describe mechanical alloying in more detail in the next chapter (section 2.3.2). The defects introduced by ball milling (dislocations, grain boundaries and antiphase boundaries [5]) are also able to destroy the crystalline order in some intermetallic compounds, such as NiTi [29]. Here, the amorphous phase cannot result from interdiffusion but may form because the energy of defects raises the free energy of the severely deformed crystalline phase above that of the amorphous phase [24, 28].

1.1.4 Irradiation

For thin films there exist amorphization techniques roughly analogous to both mechanical alloying of initially elemental crystals and to ball milling of intermetallic phases: by directing high-energy ions at a thin-film diffusion couple or at a thin-film intermetallic compound, the initially crystalline state can frequently be driven to an amorphous state. Irradiation of layer interfaces produces collision cascades that induce atomic mixing over a length range on the order of 10 nm [3]; the cascades eventually evolve into thermal spikes that are quenched so quickly ($\lesssim 10^{-10}$ sec [30, 31]) that crystalline phases have no time to nucleate and regrow. This technique of externally driven interdiffusion induces amorphization at temperatures too low for thermal diffusion, as in SSAR. Just as with ball milling of intermetallic compounds, irradiation can also introduce enough defects, chemical disorder and topological disorder to drive a stable intermetallic phase to an amorphous state [32, 33, 34].

1.1.5 Implantation

Related to the latter case is the formation of thin-film alloys by direct implantation of solute atoms into a crystalline matrix. The concentration of solute can thereby be driven far beyond equilibrium solubility limits; for example, Linker [35] was able to implant up to ~5 at.% B into thin films of Nb, while the equilibrium solubility of B in Nb is less than 2 at.% [36]. Additional B induced the formation of amorphous regions, presumably because the strain caused by atomic-size mismatch raises the free energy of the supersaturated crystalline solid solution above that of the amorphous phase at the same composition. In subsequent chapters I shall return to this experiment and to related implantation experiments [37, 38], examining Linker's results in relation to instability theories of crystal-to-amorphous transformations.

1.1.6 Application of high pressure

A final method observed to amorphize crystalline structures is the application of high pressure. Many tetrahedrally coordinated crystals, such as SiO_2 and related structures, are known to become amorphous if held at room temperature and subjected to pressures on the order of 20 GPa [39, 40]. Other materials exhibiting this behavior include hexagonal ice [41], some molecular crystals [42] and many oxides; no metallic crystals, however, are known to amorphize in this manner.[1] Pressure-induced amorphization appears to be limited to systems in which an amorphous phase can form with a higher density than the crystalline phase of the same composition [44]. (This may explain why the phenomenon has not been observed in metals, since most metallic crystals are close-packed, or nearly so.) Upon release of the pressure, some materials remain amorphous, while others recrystallize. In fact, recent investigations [45] have found that in some materials the amorphized sample will recrystallize to the same orientation that it had before becoming amorphous! This indicates that there is a certain amount of anisotropy in the amorphous phase, enabling it to exhibit such an orientational "memory"

---

[1] Some systems that are metallic at high pressure (e.g., $Cd_{40}Sb_{60}$, $Zn_{50}Sb_{50}$ and $Al_{30}Ge_{70}$ [43]) undergo amorphization upon *de*pressurization!

[46].

1.2 Relationship between crystal-to-amorphous and crystal-to-liquid transformations

The crystal-to-amorphous phase transition shares certain characteristics with a transition with which we are much more familiar: melting! The most obvious common feature is the change from the discrete symmetry of the crystalline solid to the continuous symmetry of the liquid and amorphous phases. The similarity extends beyond symmetry change, however, to the nucleation characteristics of the transitions and to the detailed structures of the product phases.

1.2.1 Nucleation

Nucleation of the liquid phase during melting

Classical nucleation theory [47, 48, 49] dictates that there should be a nucleation barrier for first-order phase transitions like equilibrium melting. The existence of such a barrier should permit the ready superheating of solids, just as the nucleation barrier for freezing permits liquids to be undercooled, often by many tens or even hundreds of degrees [50]. To undercool a liquid one need only remove it from contact with efficient sites for heterogeneous nucleation of the crystalline phase, such as similar crystals or imperfections in the surface of the container [51]; the greatest degree of undercooling is achieved by further dividing the liquid into isolated small drops within an emulsion [52, 53]. Thus, it is the presence of heterogeneous nucleation sites—for which geometrical considerations reduce the nucleation barrier below that of homogeneous nucleation [54]—that prevents significant undercooling. The experimental fact that, contrary to expectation, solids are nearly impossible to superheat can be attributed to the surface of the solid being a heterogeneous nucleation site for the liquid phase [55, 56]. Indeed, significant superheating of a metal (~ 25 K for ~ 1 min) was first accomplished [57, 58] by encasing a single-crystal sphere of Ag in a coherent layer of Au, which has a melting point about 100 °C higher than that of Ag [59] (see Refs. [60, 61, 62] for other superheating experiments). It is also suspected that atomically disordered regions created by defects in a crystal, such as grain boundaries [63], can serve as heterogeneous nucleation sites for the liquid [64].

Nucleation of the amorphous phase during a crystal-to-amorphous transition

Heterogeneous nucleation of an amorphous phase is also observed in crystal-to-amorphous phase transitions. Yeh and Johnson [65] demonstrated that hydrogen-induced amorphization of crystalline Zr_3Rh occurs by nucleation of the amorphous phase at grain boundaries. Evidence for both heterogeneous and homogeneous nucleation of an amorphous phase was seen by Meng *et al.* [66, 67] in hydrogen-induced amorphization of Zr_3Al. Luzzi *et al.* [68] irradiated Cu_4Ti_3 with high-energy electrons and found that the amorphous phase nucleates at antiphase domain boundaries. Other irradiation studies have found heterogeneous nucleation of the amorphous phase at dislocations and free surfaces [69]. Most strikingly, solid-state amorphization experiments on bilayers of Ni on polycrystalline Zr [17] and Ni on single-crystalline Zr [70, 71, 72, 73] found, in the former case, formation of an amorphous interlayer upon annealing at temperatures as low as 250 °C, while no amorphization occurred in the latter case at annealing temperatures up to 400 °C. (At 400 °C an intermetallic compound formed at the polycrystalline Ni/single-crystalline Zr interface instead of an amorphous phase [73].) This suggests that an amorphous layer will form in the Ni–Zr bilayer only if a suitable nucleation site—such as a grain boundary—exists on the Zr surface. In fact, if the interface at the surface of the single-crystal of Zr is disordered by irradiation, then solid-state amorphization is again observed at temperatures below 350 °C [70, 71].

1.2.2 Structural change

Amorphous phases *vs.* glassy phases

Not only are the nucleation mechanisms of melting and amorphization similar, but also the structures of their product phases have several common characteristics. Any comparison of liquid and amorphous phase structures, however, is complicated by the wide range of preparation techniques for amorphous materials (section 1.1), since there is no *a priori* guarantee that the structure of an amorphous alloy made by one method will be identical to that of an amorphous alloy of the same composition made by another method. Furthermore, the amount of detailed structural analysis that has been performed on the product phases of crystal-to-amorphous transformations is much smaller than that which has been performed on amorphous phases made by the traditional technique of rapidly cooling a liquid through its glass transition (i.e., essentially cooling it so fast that its atoms or molecules become frozen in a liquid-like configuration). An amorphous solid synthesized by rapid quenching is often called a *glass.*

There is ample evidence, however, that all of the methods of amorphization of crystalline samples lead to structures substantially similar to those of glassy phases [5]. As already mentioned above (section 1.1.1), radial distribution functions of amorphous solids produced by hydrogenation of a metallic alloy or compound have been found to be essentially identical to those produced by hydrogenating a glass of the same metal atom composition [13]. Similarly, radial distribution functions of $Cu_{50}Zr_{50}$ formed by ball milling are identical to those of the same composition formed by rapid quenching [74]. Furthermore, amorphous interlayers formed in diffusion couples [72] and amorphous regions formed by irradiation of intermetallic compounds [75] produce the same kind of featureless images in high-resolution transmission electron microscopy as do metallic glasses formed by vapor deposition or splat quenching.

In recent years the apparent similarity of amorphous phases produced in crystal-to-amorphous transitions to those resulting from liquid-to-glass transitions has caused the terms *amorphous* and *glassy* to become more or less synonymous [5]. In fact, it is much more common to use the term *crystal-to-glass transition* than *crystal-to-amorphous transition* to refer to amorphization of crystalline matter. In this thesis, however, I shall maintain the original distinction between the general term *amorphous* and the more specific term *glassy* in order to avoid the possibility of confusing the underlying physics of the glass transition with that of the crystal-to-amorphous phase transition. Likewise, I shall use the term *amorphization* to refer only to those processes that disorder an initially crystalline phase rather than to those that produce amorphous solids (glasses) from a vapor or liquid initial state.

Glassy phases *vs.* liquids

Once the similarity of amorphous phases to glassy phases has been established, it remains only to elucidate the similarities of glassy phases to liquids in order to complete the link between amorphous phases and liquids. In the early 1970s, Cargill [76] established—primarily through a comparison of measured and calculated pair-correlation functions—that continuous random network models (similar to "frozen liquids") do a better job than models based on a collection of microcrystals of describing the glassy state. Subsequent studies, however, have found evidence for short-range chemical ordering in prototypical metal-metalloid glasses [5]; pair-correlation functions of these materials can be fit with models made up of prismatic building blocks of 6–9 atoms that mimic the local configuration of atoms in the associated crystalline state [77]. Further indications that the structure of glasses is not completely random have come from high-resolution transmission electron microscopy performed on the newest generation of microscopes. Image contrast has been found in metal-metalloid glasses like $Pd_{75}Si_{25}$ resembling lattice planes extending over distances of 1–2 nm [5, 78, 79, 80]. These regions are not thermodynamically stable nanocrystals, however, because they do not simply grow upon heating [5], as they would if they were already truly crystalline; rather, they crystallize through a nucleation and growth mechanism that can be distinguished from growth without nucleation by differential scanning calorimetry measurements [81].

Amorphous phases *vs.* liquid phases

The previous two sections considered together indicate a general structural similarity of amorphous phases and liquids down to a length scale of 1–2 nm. Below this length scale, the amorphous phase may tend to form short-range chemical and topological order reminiscent of the crystalline state. We must keep this length-scale dependence in mind when drawing analogies between crystal-to-amorphous and crystal-to-liquid phase transitions, since any property that is sensitive to short-range chemical and topological order may behave quite differently in the two cases.

1.3 Theories of melting

The close relationship between the phenomenological characteristics of melting and amorphization of crystalline phases—symmetry change, nucleation behavior and structural change—suggests that the underlying physics of the two types of phase transition are similar. Therefore, it may be profitable to investigate the insight into crystal-to-amorphous transformations that the standard theory of melting can offer. Unfortunately, in three dimensions there is *no* accepted theory of melting! In fact, the number of proposed mechanisms for melting is roughly equal to the number of structural lattice phenomena observed in solids: vacancies, dislocations, vibrational modes, elastic moduli and mean-square displacements, among others, have all been identified as possible causes for the ordinary crystal-to-liquid phase transition [56].

1.3.1 Two-phase theories *vs.* one-phase theories

It is certainly surprising that for centuries scientists have been baffled by a common and accessible phenomenon like melting, but it isn't for lack of trying. In fact, efforts to understand melting have been pursued in such an aggressive manner and for so long that researchers in the field have gradually established two major opposing camps. One side of the battlefield is populated by "two-phase purists," who insist that the melting point of classical thermodynamics—the temperature at which the free energies of the solid and liquid phases are equal—can only be understood after the structure, interatomic potentials, elastic moduli, enthalpy, entropy, etc., of both the crystalline and liquid phases are understood. They reject out of hand any effort to explain melting that does not place equal emphasis on the phases on both sides of the transition [56]. Their opponents, on the other hand, feel that useful information about melting—though not a complete picture—can be gleaned from the properties of the crystalline state alone [56].

The latter group's desire to focus on one side of the transition is fueled by at least two phenomenological observations about melting. First, as mentioned above (section 1.2.1), it is nearly impossible to superheat a solid, despite the significant nucleation barrier common to first-order phase transitions. I argued previously that superheating is precluded by the much smaller energy barrier for nucleation at a surface or at defects than in the bulk crystal itself; a plausible alternative explanation, however, is that significant superheating is prevented by an intrinsic instability of the crystal just above the melting point.

A second motivation for proposing an instability theory of melting is the fact that melting is observed to occur in a wide range of materials when the root-mean-square displacement $\langle u^2 \rangle^{1/2}$ of the atoms from their equilibrium positions in the crystalline lattice reaches a critical fraction $\lambda_{\rm L}$ of the interatomic spacing d:

$$\frac{\langle u^2 \rangle^{1/2}_{\rm melt}}{d} \equiv \lambda_{\rm L}, \tag{1.1}$$

where the best value for $\lambda_{\rm L}$ (typically, 0.12–0.15) depends on the symmetry of the unit cell [82]. This empirical observation is called the *Lindemann criterion* for melting [83]. The success of the Lindemann criterion, which is based on a property of the crystal alone, is further evidence that much of the underlying physics of melting may be found in the structural, mechanical and thermodynamic properties of the crystalline phase.

1.3.2 Lattice instability theories

Mechanical instabilities

Theories of melting based on an intrinsic instability of the crystalline phase may be referred to as *lattice instability* theories. Lindemann's criterion suggests an instability of the lattice with respect to large-amplitude vibrations, but it provides no compelling explanation for the universality of the critical fraction $\lambda_{\rm L}$ [56]. Others have proposed instability theories that more directly account for the structural change that occurs in melting. Motivated by the obvious difference between solids and liquids that solids can support shear forces but liquids cannot, Born [84] proposed that an elastic shear modulus of a crystal vanishes at its melting point.[2] Direct measurements of crystal shear moduli as a function of temperature, however, found that they remain finite as the melting point is approached [87, 88, 89, 90]. This bad news caused Born [91] to defect to the side of the two-phase purists!

Tallon reconsidered the Born idea as a condition for melting of a *superheated* crystal, rather than of one in equilibrium [92, 93, 94, 95, 96]. He examined the measured volume dependence of the shear moduli of many crystals and found that they extrapolate approximately to zero at the volume of the corresponding liquid phase. The crystal ordinarily melts before reaching this elastic instability point, because the additional entropy—usually called *communal entropy*—of the liquid, attributable to the ability of each atom to sample the entire volume of the material and to the volume change upon melting, lowers the liquid free energy below that of the solid with zero elastic modulus.

Thermodynamic instabilities

Thermodynamic instabilities have also been the basis of several attempts to explain melting. Herzfeld and Goeppert-Mayer [97] argued many years ago that the isothermal compressibility of a crystal diverges at the melting point. Boyer [56] linked their argument to the Born/Tallon shear instability by proposing that the shear instability triggers the compressibility divergence; he referred to this combination of instabilities as a *thermoelastic* instability because of its dual mechanical and thermodynamic origins. Fecht and Johnson [1] identified a thermodynamically determined upper bound on superheating of a crystal (see section 1.5.2). They argued that the entropy of the crystalline phase above the melting temperature increases more rapidly than that of the liquid because of the development of defects, such as vacancies [98]. If there were no limit to superheating, above a

---

[2] Similar suggestions had been made earlier by Durand [85] and Brillouin [86].

certain temperature the crystal would have a higher entropy than the liquid! The implausibility of such a state led them to propose the existence of an entropic instability at or below the equal-entropy temperature of the crystalline and liquid phases.[3]

Defect-induced instabilities

A final class of instability theories of melting encompasses those based on the influence of defects on melting—specifically, vacancies [100, 101] and dislocations [102, 103, 104, 105] (see review in Ref. [106]). The density of such defects is presumed to grow catastrophically at the melting point, resulting in collapse of the crystalline phase. For example, Cotterill has shown his dislocation theory to be consistent with the Lindemann criterion in that rms displacements of a certain critical amplitude are associated with spontaneous generation of dislocation loops [107]. Furthermore, the generation of dislocations is known to play a fundamental role in melting transitions in two-dimensional systems [108, 109, 110]. Finally, it should be noted that defect instability theories are intimately linked to mechanical instability theories through the influence of defect density on elastic properties [56, 111].

1.4 Evidence for instability theories of crystal-to-amorphous phase transitions

Given the degree of polarization of the scientific community regarding the best approach to understanding melting, one might expect the same two-phase *vs.* one-phase battlefront to separate the leading theories of crystal-to-amorphous transformations. As yet such is not the case, however, perhaps because of the

---

[3] The entropy of crystalline ^{3}He is actually higher than that of liquid ^{3}He along the solid-liquid coexistence line at temperatures below about 0.3 K [99]! The entropy difference arises from nuclear-spin alignment in the liquid phase and spin disorder in the solid phase.

greater amount of experimental evidence supporting an instability interpretation of amorphization than of melting. As noted above (section 1.2.1), heterogeneous nucleation is possibly as ubiquitous in amorphization processes as in melting, but the same argument used by members of the one-phase camp against the underlying importance of heterogeneous nucleation in melting holds for amorphization, as well: amorphization may occur preferentially at heterogeneous sites simply because the inhomogeneous conditions at such sites lead to lower nucleation barriers for transformation to the disordered state. The underlying *cause* of amorphization, however, may remain some kind of instability of the crystalline phase.

Perhaps the strongest evidence for an instability theory of amorphization comes from the success of the Egami-Waseda criterion [112, 113] in predicting glass-formation ranges in rapidly quenched and vapor-deposited alloys. Alternatively, the criterion may be viewed as a rule for predicting the maximum composition at which a supersaturated solid solution can be formed instead of an amorphous phase. It has been given a measure of theoretical justification through a calculation of the atomic-level stress created by atomic-size mismatch in substitutional binary solid solutions. The criterion states that, given a size difference between elements A and B, there is some composition $x_{\max}$ at which the crystalline alloy $A_{1-x}B_x$ is topologically unstable (with respect to a change in coordination number):

$$x_{\max} \approx \lambda_{\mathrm{EW}} \frac{V_{\mathrm{A}}}{|\Delta V|}, \tag{1.2}$$

where ΔV is the atomic volume difference $V_{\mathrm{A}} - V_{\mathrm{B}}$ and λ_{EW} is an empirically determined parameter. Approximating $x_{\max}$ by the minimum composition at which glass formation is observed in many rapidly quenched binary alloys, Egami and Waseda [112] determined that a value of 0.1 for λ_{EW} could account within experimental error for the $x_{\max}$ of most of the more than sixty binary systems that they investigated! (For vapor-deposited alloys Liou and Chien [114] found better agreement with experiment using $\lambda_{\mathrm{EW}} = 0.07$–$0.09$.) Though vapor deposition and rapid quenching of liquids are not crystal-to-amorphous processing methods, they are means of supersaturating the crystalline state, possibly up to its instability point (if, indeed, such a point exists).

If we rewrite Eq. (1.2) as

$$x_{\mathrm{max}} \frac{|\Delta V|}{V_{\mathrm{A}}} \approx \lambda_{\mathrm{EW}}, \tag{1.3}$$

we see that when the left-hand side—which is a kind of total relative size mismatch or total atomic-level stress—reaches a critical value, the crystal becomes unstable. Note the similarity of this criterion to the Lindemann criterion [Eq. (1.1)] for melting, in which crystal collapse occurs when the relative atomic root-mean-square displacement reaches a critical value. We can draw the analogy a bit further by recognizing that the atomic-size mismatch reflected in $|\Delta V|$ will lead to a *static* mean-square displacement (MSD) caused by atoms sitting at positions displaced from their ideal lattice positions [115]. Assuming atomic radii r_{A} and r_{B}, we can approximate the static MSD in an alloy $\mathrm{A}_{1-x}\mathrm{B}_x$ by [116]

$$\langle u^2 \rangle_{\mathrm{stat}} \approx Cx(1-x)\,(r_{\mathrm{A}} - r_{\mathrm{B}})^2\,, \tag{1.4}$$

where C is a symmetry-dependent constant approximately equal to 4 [117]. Inserting this expression for the (static) MSD into the Lindemann criterion [Eq. (1.1)] with interatomic spacing $d = 2\bar{r} = 2\left[(1-x)r_{\mathrm{A}} + xr_{\mathrm{B}}\right]$ yields an expression for x_{max} in terms of the empirically determined Lindemann parameter λ_{L}:

$$x_{\mathrm{max}}\,(1 - x_{\mathrm{max}}) \approx \frac{4\lambda_{\mathrm{L}}^2}{C} \left(\frac{V_{\mathrm{A}}}{|\Delta V|}\right)^2 . \tag{1.5}$$

The form of Eq. (1.5) is similar to that of the Egami-Waseda criterion [Eq. (1.2)], though the x_{max} of Eq. (1.5) turns out to be *less* restrictive than that of the Egami-Waseda criterion, probably because Eq. (1.5) ignores the thermal contribution to the total MSD that is assumed in the Lindemann criterion [Eq. (1.1)].

Other evidence for instability of the crystalline phase in crystal-to-amorphous transitions comes from the previously cited experiment of Linker [35, 37] (section 1.1.5), who was able to implant boron interstitially into thin films of Mo and Nb up to a critical composition (5–7 at.% B) at which regions of the target became amorphous. The onset of amorphization corresponded exactly to a sudden drop in the accumulated strain. This is reminiscent of Egami and Waseda's idea [112] that a solid solution (substitutional, in the case they studied) may become topologically unstable beyond a certain atomic-level stress buildup caused by size mismatch of the alloying elements. Linker and colleagues found a similar amorphization behavior in Al films implanted substitutionally with Mn [38, 118, 119, 120].

While the instability examples cited above pertain to elastic instabilities of solid solutions, there is also experimental evidence to support defect-related instabilities in crystal-to-amorphous transitions. Recall, for instance, that intermetallic compounds can be amorphized by irradiation with ion beams (section 1.1.4). It is reasonable to conjecture that amorphization occurs because the incident ion beam pumps defects into the crystal that create topological and chemical disorder until the crystal becomes unstable and collapses to the amorphous state; a similar interpretation may also hold for the amorphization of an intermetallic compound in a high-energy ball mill (section 1.1.3).

1.5 Unified instability theory of melting and amorphization

In the previous two sections we have seen various theoretical and experimental evidence for suspecting that instabilities of the crystalline phase underlie melting and amorphization, even though heterogeneous nucleation makes such instabilities difficult to detect unambiguously. In this section I shall describe a recent attempt by Fecht and Johnson [1] to unify the physics of the two phase transitions by relating them to the *same* instability. The approach of Fecht and Johnson relies on the thermodynamic properties of crystalline and liquid phases extended beyond equilibrium stability ranges into what is called the *metastable* regime. It is instructive, therefore, to preface the exposition of their theory with a discussion of metastability.

1.5.1 Metastability in thermodynamics

According to the second law of thermodynamics, the equilibrium values of the unconstrained internal parameters of a thermodynamic system are those that maximize entropy subject to a fixed total internal energy [121]. It is often convenient, however, to reformulate thermodynamics so that equilibrium corresponds to the *minimization* of an *energy* function for a given total entropy; that this definition of equilibrium is equivalent to the former one is proved in basic thermodynamics texts [121, 122]. The advantage of this approach becomes apparent when dealing with real systems in which certain externally controllable parameters, such as temperature, pressure, and magnetic field, are held constant. In these cases the equilibrium configuration is determined by minimizing a generalized energy function (often called a *thermodynamic potential*) whose form is derived from the internal energy U and the applied constraints by a Legendre transformation [121, 122]. For example, the ordinary laboratory constraints of fixed temperature T and pressure P entail that the *Gibbs free energy,* $G(T,P) = U - TS + PV$, with entropy S and volume V, is minimal at equilibrium (the generic term *free energy* usually refers to this particular thermodynamic potential). Other possible constraints include fixed temperature and volume, which corresponds to minimization of the *Helmholtz free energy,* $F(T,V) = U - TS$, and fixed temperature and chemical potential μ, which corresponds to minimization of the *grand potential* $\Omega(T,N) = U - TS - \mu N$, with number of particles N [123].

Let us now use the Gibbs free energy function—applicable to constant temperature and pressure conditions—to illustrate the meaning of *metastability;* in the following discussion we shall follow the treatment of J. W. Cahn [124]. Consider the schematic free energy curve of a crystalline alloy in Fig. 1.1. Here, the free energy G is graphed as a function of composition at fixed temperature and pressure. For overall compositions below c_0 or above c_0', the lowest free energy is achieved by a compositionally homogeneous state, but between these two compositions, the common-tangent construction (dashed line) permits the system to lower its free energy by separating into a mixture of regions with compositions given by the intersections of the tangent with the free energy curve (c_0 and c_0'). If a crystal is created by some means in a homogeneous state with uniform composition c_1, then it will have a higher free energy than the equilibrium inhomogeneous state. Is this homogeneous state at composition c_1 stable? To answer this question, we must consider the energies of the intermediate configurations between the initial homogeneous state and the final inhomogeneous state. The composition pairs AA′ and BB′ in Fig. 1.1(a) on either side of c_1 represent possible intermediate states in the compositional separation of the initially homogeneous system. The free energy of each pair is given by the point with composition c_1 on the solid line connecting the endpoints AA′ or BB′ [124]. As can be seen from the diagram, intermediate configurations AA′ and BB′ represent progressively *higher* energy states than the initially homogeneous crystal at c_1. Thus, fluctuations in composition near c_1 will tend to stop growing because of their increasing energy cost.

But what about compositional fluctuations far from c_1: won't they lower the overall energy? Indeed they will, but only at the cost of establishing an interface between regions of significantly different composition. According to nucleation theory [54], such an interface will have a positive free energy inversely proportional to the size of the fluctuation [124]. Therefore, fluctuations of small spatial extent

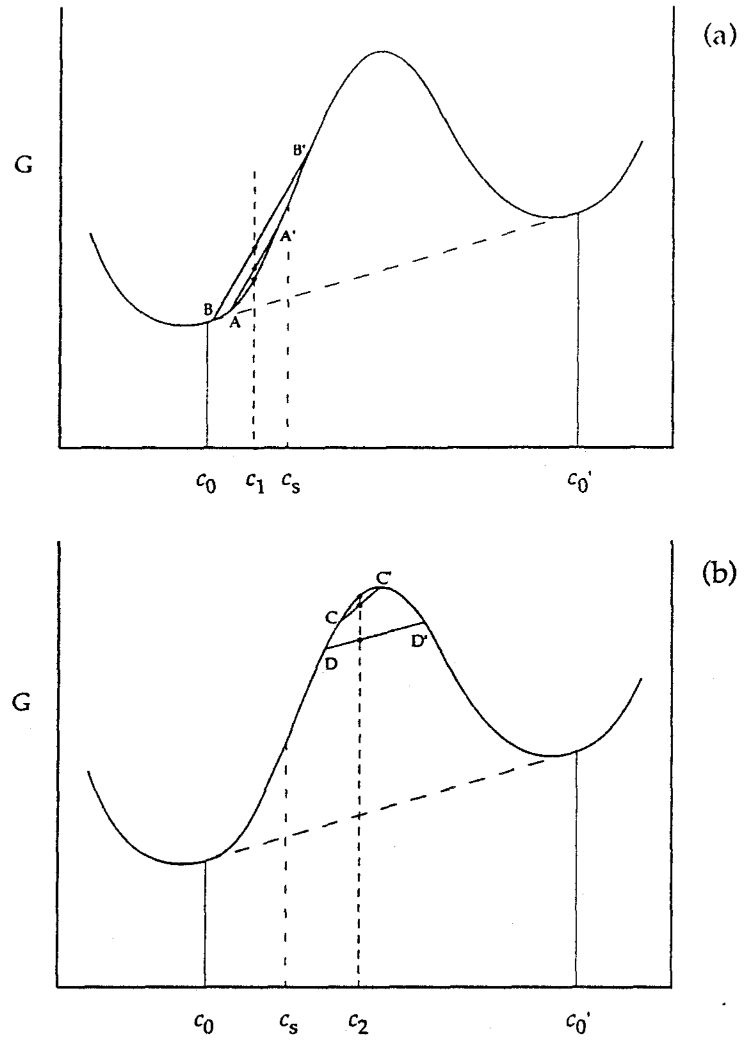

Figure 1.1: Schematic free energy curve illustrating (a) metastable and (b) unstable composition regions. Compositional fluctuations AA′ and BB′ about c_1 will die out because they raise the free energy above its level at c_1. Compositional fluctuations CC′ and DD′ about c_2 will grow without bound because they lower the free energy below its level at c_2. The composition c_s separates the metastable and unstable regions and is called the *spinodal* point. The equilibrium (lowest-energy) phase mixture is given by the dashed common-tangent line between c_0 and c_0'.

and small or large compositional magnitude result in an increase in free energy and will, therefore, be damped out. Only a statistically unlikely fluctuation of large spatial and compositional magnitude would lower the free energy and continue to grow. We say that a system in a state like c_1 is *metastable* with respect to compositional fluctuation. Metastability can be defined in a similar way with respect to phase change (as in superheating of a crystal or undercooling of a liquid), where stabilization comes from the energy barrier to nucleating the equilibrium phase.

From the construction of Fig. 1.1(a) it can be seen that metastability at c_1 requires a positive (i.e., upward) curvature of the free energy curve at c_1. This can be seen explicitly in Fig. 1.1(b) for fluctuations in a homogeneous system at c_2, where the free energy has a negative curvature: configurations CC′ and DD′ progressively lower the free energy of the system, so they will not be damped out. The interfacial energy cannot stabilize the system because the system can make compositional fluctuations of small magnitude but large spatial extent, thus reducing the interfacial energy until it is negligible [124]. Thus, there is no energy barrier to decomposition; it will occur spontaneously along with energy release. This process is commonly called *spinodal decomposition.* The inflection point c_s at which the curvature of the free energy changes sign represents the upper limit of the metastable composition region containing c_1; it is often called the *spinodal* at the temperature T to which the free energy curve corresponds. Of course, there are many ways in which a crystalline alloy can become unstable other than spinodal decomposition, such as by softening of an elastic modulus or divergence of a thermodynamic function (section 1.3.2). Any of these events may restrict a crystalline phase's metastability range more than the spinodal does. We say that a phase in a configuration beyond its metastability range is *unstable.*

1.5.2 “Inverse” Kauzmann paradox

Since a homogeneous system in a metastable state is stable with respect to fluctuations in chemical and structural order, it will have well-defined thermodynamic properties, such as entropy and enthalpy. For example, consider the crystalline and liquid phases of a one-component system, such as a metal. The thermodynamic properties of the crystalline phase are obviously well defined below the melting point, and those of the liquid are well defined above the melting point. With some care the liquid phase can be undercooled below the melting point and its entropy and enthalpy measured there [125, 126]. From the enthalpy H and entropy S functions, the free energy $G = H - TS$ may be evaluated and the other thermodynamic functions derived from it by the usual thermodynamic calculational techniques [122]. In particular, one finds from experiment that the heat capacity

$$C_P \equiv T\left(\frac{\partial S}{\partial T}\right)_P \tag{1.6}$$

of the undercooled liquid is higher than that of the crystalline phase [127] [see Fig. 1.2(a)]. Now, at the melting point T_m, the entropy of the liquid is higher than that of the crystal by $L_\mathrm{f}/T_\mathrm{m}$, where L_f is the latent heat of fusion [128], but the higher heat capacity of the undercooled liquid causes its entropy to decrease faster below T_m than that of the crystal [Fig. 1.2(b)]. That is, the entropy difference between the liquid and crystalline phases, $\Delta S \equiv S_\mathrm{L} - S_\mathrm{X}$, decreases below T_m:

$$\Delta S(T) = \frac{L_\mathrm{f}}{T_\mathrm{m}} - \int_T^{T_\mathrm{m}} \frac{(C_P)_\mathrm{L} - (C_P)_\mathrm{X}}{T'}\,dT', \quad T < T_\mathrm{m}. \tag{1.7}$$

Eventually, $\Delta S(T)$ will equal zero at a temperature T_K. Below T_K the undercooled liquid would have a lower entropy than the crystal! This makes no sense, however, since the crystal lacks the liquid's communal entropy of atomic motion (section 1.3.2). Below T_K, the liquid should be unstable with respect to crystallization [129], but at such low temperatures (usually near absolute zero), there

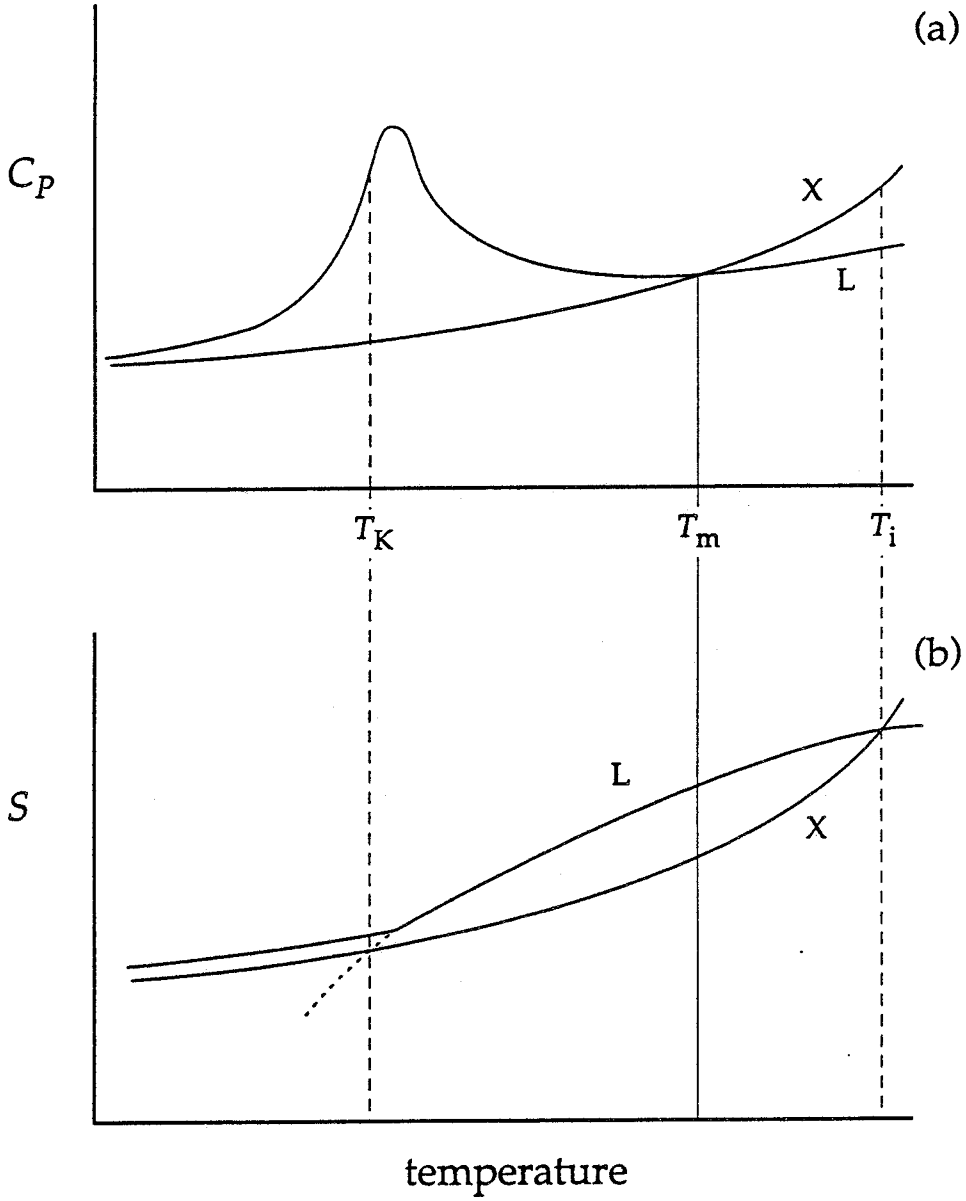

Figure 1.2: Schematic curves of (a) heat capacity C_P and (b) entropy S of crystalline and liquid phases above and below T_m. The lower isentropic point T_K is the ideal glass transition temperature, and the upper isentropic point T_i is the ultimate limit to superheating of the crystalline phase.

does not exist enough atomic mobility for crystal nucleation and growth to occur. Kauzmann [130] was the first to notice this "paradox" and suggest a solution: instead of crystallizing, the undercooled liquid simply "freezes" to a glass at or above T_{K}, a process that can occur continuously rather than through a (much more complex) nucleation and growth mechanism; we shall frequently refer to the temperature T_{K} as the *thermodynamic* or *ideal* glass transition temperature T_{g}.

In 1988 Fecht and Johnson [1] demonstrated that ΔS could vanish *above* T_{m} as well! They noted that the heat capacity of a superheated solid increases above that of the liquid because of contributions from thermal expansion, electronic heat capacity and, especially, thermal vacancy formation [Fig. 1.2(a)]. Therefore, applying Eq. (1.7) modified for $T > T_{\mathrm{m}}$ yields an isentropic temperature $T_{\mathrm{i}} > T_{\mathrm{m}}$ [Fig. 1.2(b)]. For example, Fecht and Johnson estimated the upper isentropic temperature T_{i} for aluminum to occur at ~ 1.2–$1.4\,T_{\mathrm{m}}$ using various models for the vacancy heat capacity in the superheated crystal. This temperature represents an absolute limit to metastability of the superheated state because the nucleation barrier for formation of the liquid—which is mainly proportional to ΔS [131, 132]—becomes negligibly small at T_{i}. Hence, no crystal can be superheated above its upper isentropic temperature T_{i}.

1.5.3 Polymorphous phase diagram of a binary alloy

Fecht and Johnson went on to apply this model to a binary alloy system in which chemical interdiffusion is suppressed so as to prevent phase separation; this condition is often called the *polymorphous constraint.* An alloy system has the additional variable of concentration that a single-component system lacks. For any given concentration, we can draw entropy curves just as in Fig. 1.2(b), but the isentropic points T_{g} and T_{i} are now functions of composition (Fig. 1.3). The melting point of an alloy subject to the polymorphous constraint is given by the

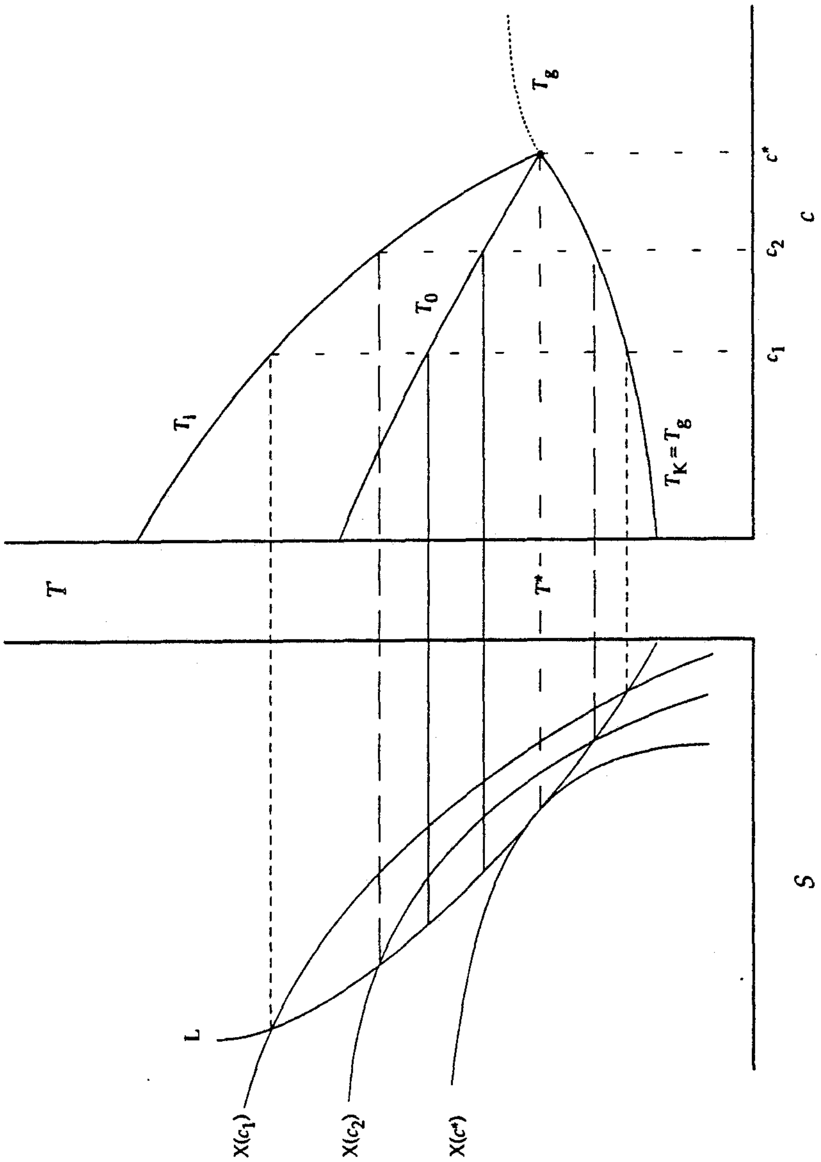

Figure 1.3: Construction of the polymorphous phase diagram for an alloy. Entropy curves shift in relative position with composition c, making the upper and lower isentropic temperatures, T_l and T_g, into functions of c. The T_0 temperature indicates equality of crystalline and liquid free energies; therefore, it is the polymorphous melting point. T_0, T_g and T_l collapse to the same value at (c^*, T^*). The dotted line is the extrapolation of T_g to higher compositions.

temperature T_0 at which the free energies of the liquid and alloy at that composition are equal [133] (see section 2.1 for a discussion of the T_0 concept). In Fig. 1.3, the T_0 temperature is identified with the point of maximum entropy difference between the liquid and crystalline phases because measurements indicate that the heat capacities of a liquid and crystal are nearly equal at the melting point [1]; regardless of the accuracy of this assignment, the T_0 temperature must, by construction, be sandwiched between the upper and lower isentropic temperatures. In many real binary alloys—particularly glass-forming alloys—the T_0 lines of the terminal solid solutions are known to plunge rapidly. Such a situation entails a corresponding rapid decrease in T_i with increasing composition c, as in Fig. 1.3. The difference between the entropy curves of the liquid and crystal keeps decreasing until the composition c^* is reached, a composition for which they meet at only one temperature T^*—here, T_g, T_0 and T_i all collapse to the same value. As discussed in the following section, under certain conditions the point (c^*, T^*) can become a thermodynamic critical point for transitions between the liquid, glass and crystalline states. For concentrations beyond c^*, the crystal has a higher entropy than the liquid at all temperatures, meaning that a homogeneous crystal with composition $c > c^*$ is absolutely unstable. Thus, c^* represents the metastable limit to (polymorphous) supersaturation of the crystalline phase.

Since rapidly cooled liquids of composition $c > c^*$ can still be quenched to a homogeneous amorphous state, the glass transition line T_g must extend beyond c^*, even though the polymorphous Kauzmann argument no longer applies in that composition region (see dotted line in Fig. 1.3). In fact, ease of glass forming appears to be greatest at regions beyond plunging T_0 lines [133, 134, 135]. We might attempt to relate the T_g line for $c > c^*$ to a Kauzmann-type argument equating the entropy of the undercooled liquid to the entropy of some crystalline phase mixture, but because the reference crystalline state is not polymorphous, the T_g

line determined in this manner would not in general connect to the polymorphous T_g line (defined for $c < c^*$) at (c^*, T^*), as we expect it should.

1.5.4 The point (c^*, T^*)

The slope of the T_0 line is readily shown to be [1]:

$$\left(\frac{\partial T_0}{\partial c}\right)_P = \frac{1}{\Delta S}\left(\frac{\partial \Delta G}{\partial c}\right)_P, \tag{1.8}$$

where ΔG is defined as the free energy difference between the liquid and crystal, $G_L - G_X$. Note that the T_0 line slope becomes infinite when $\Delta S = 0$ (as long as the numerator remains finite). By construction, the point (c^*, T^*) lies on the isentropic lines T_g and T_i; therefore, Eq. (1.8) entails that the T_0 line must be vertical there. Beyond the composition c^* at which T_0 becomes vertical, the crystalline phase is unstable—only the liquid and glass phases can exist there (above the extended T_g line and below it, respectively) as long as the polymorphous constraint is maintained (i.e., nucleation of competing crystalline phases is suppressed). At compositions below c^*, the crystalline phase is stable or metastable. Thus, we can associate homogeneous phases with distinct regions in the polymorphous phase diagram of an alloy (Fig. 1.4).

At (c^*, T^*) the crystalline, liquid and glass phases all have the same free energy and entropy. If the molar volumes of any two phases coexisting at (c^*, T^*) were identical, then a transition between the two states could be continuous: since

$$S = -\left(\frac{\partial G}{\partial T}\right)_P \quad \text{and} \quad V = \left(\frac{\partial G}{\partial P}\right)_T, \tag{1.9}$$

if ΔS and ΔV are zero at (c^*, T^*), then the first derivatives of G will be continuous through the transition [136]. In general, the molar volumes of any pair of phases at (c^*, T^*) will be equal only at certain pressures, however [137]. At a pressure P^* such that $\Delta V = 0$ for the crystalline and liquid phases, continuous (i.e.,

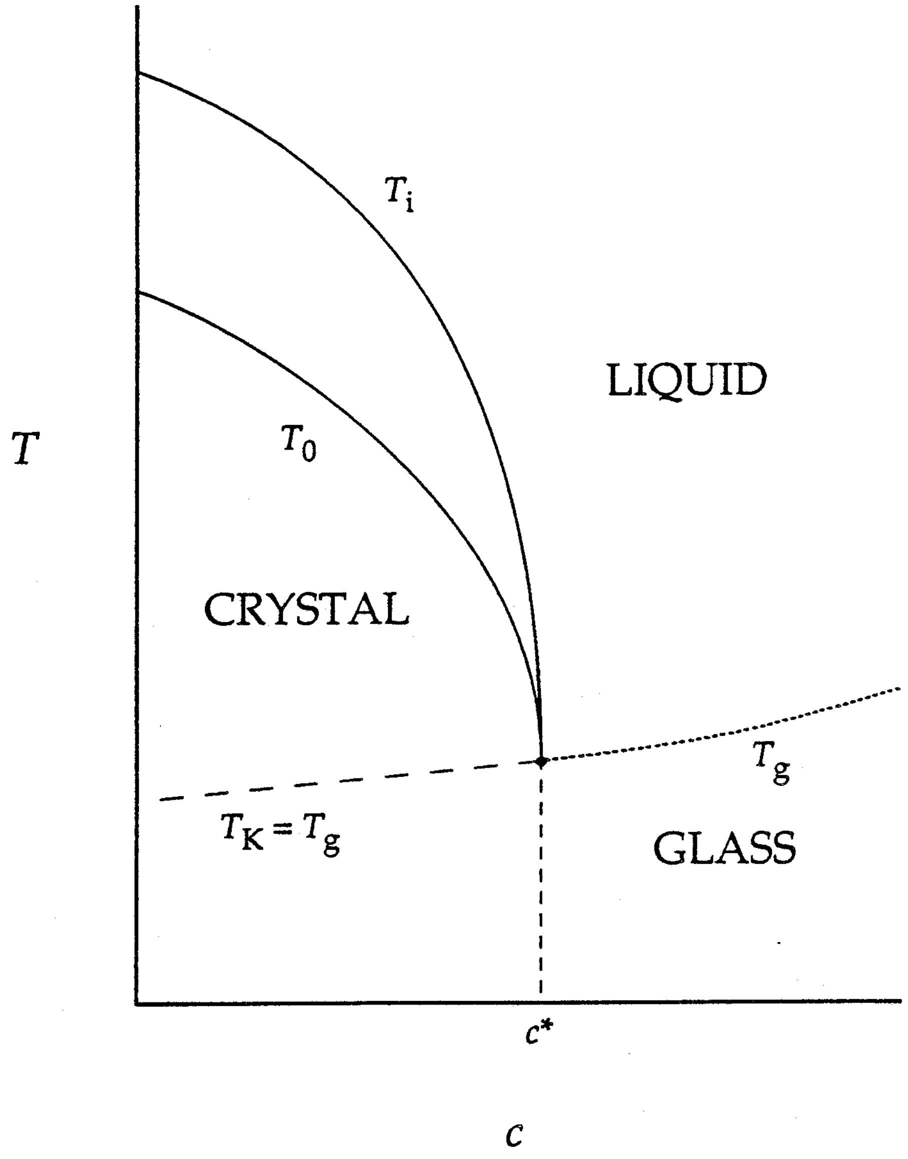

Figure 1.4: Assignment of phases to regions in the polymorphous phase diagram of an alloy. A homogeneous crystalline phase is unstable outside the boundary formed by the T_i line and the composition c^*. The liquid phase is unstable at temperatures below the T_g line, and the glass is unstable at temperatures above it.

second or higher-order) melting would be possible! An isolated point on a phase diagram at which a phase transition becomes second or higher-order is often called a *critical point;* we may refer to the point (c^*, T^*) as a *tricritical point* if continuous transitions between all three states can occur at that point.

The possibility of a continuous or nearly continuous phase transition in the polymorphous phase diagram is exciting because, unlike the case with first-order transformations, there are well-established theoretical methods (e.g., renormalization-group theories [138, 139] and field theory approaches [140, 141]) for understanding continuous phase transitions. From an experimental perspective, such transitions should exhibit measurable premelting [142, 143] or pre-amorphization [144] effects. In particular, we would expect a crystalline phase supersaturated to a composition near a continuous transition point to exhibit liquid-like properties, such as enhanced heat capacity, atomic mean-square displacements and compressibility, decreased shear modulus and diverging thermal expansion coefficient. Even if (c^*, T^*) is not a true critical point at atmospheric pressure, the necessary P^* may not be far from 1 atm (1×10^5 Pa), in which case the pre-transition effects may still be observable. This thesis describes our efforts to test the polymorphous phase diagram of Fecht and Johnson by looking for anomalous, enhanced, diverging or vanishing structural, thermodynamic and mechanical properties in supersaturated solid solutions.

1.6 Thesis overview

In order to measure the properties of a supersaturated solution near its proposed instability concentration, it is necessary to devise a process to fabricate homogeneous crystalline samples as highly supersaturated as possible. In Chapter 2, I describe the reasoning that we employed to guide our selection of promising binary alloy systems based mainly on characteristics of their equilibrium phase diagrams. Next, I examine the results of some of our initially unsuccessful attempts at synthesis and the reasons for failure in each case. The lessons that we learned from these preliminary experiments enabled us to determine and compare the strengths and weaknesses of five general sample preparation processes—first, with respect to the ability of each to supersaturate crystalline alloys and, second, with respect to the suitability of the resulting sample geometries for measuring structural, thermodynamic and mechanical properties.

Once the optimal synthetic processes have been determined, it remains only to apply them to real systems. We selected two techniques for supersaturating crystalline solids, the first being hydrogenation (or, equivalently, deuteration). In Chapter 3 I describe our investigation of the deuterated intermetallic compound $ErFe_2$. The chapter begins with an explication of the salient reasons for deuterating an intermetallic like $ErFe_2$ and then proceeds with a description of the experimental techniques utilized in the investigation. The following sections focus on the results of high-temperature elastic neutron diffraction studies and high-pressure differential scanning calorimetry scans on $ErFe_2D_{3.2}$ heated through the crystal-to-amorphous transition. In the subsequent discussion, I relate these results to a report of a "λ-type" anomaly in the heat capacity of hydrogenated $ErFe_2$ at about the temperature at which one might expect the sample to cross the T_0 line [145]. Finally, I discuss our unexpected finding of *exothermic* amorphization of $ErFe_2D_{3.2}$, devoting particular attention to the question of whether this transition is polymorphous.

The second supersaturation processing method that we employed was splat quenching (rapid cooling of a melt). I begin Chapter 4 by explaining the reasons for investigating the Nb–Pd binary alloy system and why we decided to use splat quenching to supersaturate the bcc terminal Nb phase. Next, I describe the experimental procedures that we followed in splat quenching, low-temperature neutron diffraction scans, measurements of thermal expansion and low-temperature heat capacity, and characterization by transmission electron microscopy (TEM). Since the neutron diffraction data will be found to provide the most convincing evidence of unusual properties in the supersaturated crystalline phase, the next section will explain how the diffraction data were analyzed for lattice parameter, inhomogeneous strain and atomic mean-square-displacement information. The results from the neutron diffraction analyses—when combined with the thermal expansion and heat capacity data—indicate unusual changes in the crystalline structure as it is progressively destabilized. The TEM data allow us to correlate real-space structural characteristics with the previous data derived from measurements in reciprocal space. I shall conclude the chapter by discussing these results in relation to the Lindemann criterion for melting [Eq. (1.1)], focusing in particular on the important role of static mean-square displacements.

The final chapter of the thesis attempts to assess what we have learned from the experimental results detailed in the previous two chapters. In particular, I consider two fundamental issues relevant to the use of lattice instability models for melting and amorphization. The first concerns an explicit assumption of the Fecht-Johnson approach (sections 1.5.2–1.5.4) but one which is implied in any discussion of superheating or supersaturation: what does it mean to say that a phase transition is polymorphous? We will see in the hydrogenation experiments of Chapter 3 that adherence to the polymorphous constraint can only be determined relative to a given length scale and that experimentally determined transition properties can be sensitive to violation of that constraint even when the reference length scale has atomic dimension. The prospects for testing instability theories—and, one might suspect, the prospect that they can be valid at all—depend, therefore, on the degree to which the polymorphous constraint has real meaning. The second issue to be considered concerns proper quantification of a crystalline phase's stability against melting and amorphization. I have already discussed the main candidates for a stability parameter: atomic-level stress, elastic moduli, heat capacity, mean-square displacement, etc. I conclude by assessing the degree to which each possible parameter can account for the role played by lattice instabilities in crystal-to-amorphous transitions, paying particular attention to our own results on Nb–Pd.

References

[1] H. J. Fecht and W. L. Johnson, *Nature (London)* **334**, 50 (1988).

[2] W. L. Johnson, *Prog. Mater. Sci.* **30**, 81 (1986).

[3] W. L. Johnson, *Mater. Sci. Eng.* **97**, 1 (1988).

[4] K. Samwer, *Phys. Rep.* **161**, 1 (1988).

[5] W. L. Johnson, in *Metals Handbook,* 10th ed. (ASM International, Materials Park, OH, 1990), Vol. 2, pp. 804–821.

[6] W. L. Johnson, in *Atomic-Level Properties of Interface Materials,* edited by Sidney Yip and Dieter Wolf (Chapman and Hall, London, in press).

[7] W. L. Johnson, K. Samwer and H. J. Fecht, in *Glassy Metals III,* edited by H. Beck and H. J. Güntherodt (Springer-Verlag, New York, in press).

[8] H. Oesterreicher, J. Clinton and H. Bittner, *Mater. Res. Bull.* **11**, 1241 (1976).

[9] A. M. van Diepen and K. H. J. Buschow, *Solid State Commun.* **22**, 113 (1977).

[10] S. K. Malik and W. E. Wallace, *Solid State Commun.* **24**, 283 (1977).

[11] R. H. van Essen and K. H. J. Buschow, *J. Less-Common Met.* **70**, 189 (1980).

[12] Robert C. Bowman, Jr., *Mater. Sci. Forum* **31**, 197 (1988).

[13] X. L. Yeh, K. Samwer and W. L. Johnson, *Appl. Phys. Lett.* **42**, 242 (1983).

[14] K. Samwer and W. L. Johnson, *Phys. Rev. B* **28**, 2907 (1983).

[15] K. Aoki, X.-G. Li, T. Aihara and T. Masumoto, *Mater. Sci. Eng.* **A133**, 316 (1991).

[16] R. B. Schwarz and W. L. Johnson, *Phys. Rev. Lett.* **51**, 415 (1983).

[17] B. M. Clemens, R. B. Schwarz and W. L. Johnson, *J. Non-Cryst. Solids* **61**, 817 (1984).

[18] B. M. Clemens, *Phys. Rev. B* **33**, 7615 (1986).

[19] P. Guilmin, P. Guyot and G. Marchal, *Phys. Lett. A* **109**, 174 (1985).

[20] J. Bevk, in *Annual Review of Materials Science,* edited by Robert A. Huggins, Richard H. Bube and David A. Vermilyea (Annual Reviews, Inc., Palo Alto, CA, 1983), Vol. 13, pp. 319–338.

[21] Michael Atzmon, John D. Verhoeven, Edwin D. Gibson and W. L. Johnson, *Appl. Phys. Lett.* **45**, 1052 (1984).

[22] Michael Atzmon, Karl M. Unruh and William L. Johnson, *J. Appl. Phys.* **58**, 3865 (1985).

[23] Ludwig Schultz, in *Rapidly Quenched Metals,* edited by S. Steeb and H. Warlimont (North-Holland, Amsterdam, 1985), Vol. II, p. 1585.

[24] A. W. Weeber and H. Bakker, *Physica B* **153**, 93 (1988).

[25] D. R. Maurice and T. H. Courtney, *Metall. Trans. A* **21A**, 289 (1990).

[26] R. B. Schwarz, R. R. Petrich and C. K. Saw, *J. Non-Cryst. Solids* **76**, 281 (1985).

[27] E. Hellstern and L. Schultz, *Appl. Phys. Lett.* **48**, 124 (1986).

[28] Carl C. Koch, *J. Non-Cryst. Solids* **117/118**, 670 (1990).

[29] R. B. Schwarz and C. C. Koch, *Appl. Phys. Lett.* **49**, 146 (1986).

[30] M. W. Guinon and T. H. Kinney, *J. Nucl. Mater.* **103/104**, 1319 (1981).

[31] S. Matteson and M.-A. Nicolet, in *Metastable Materials Formation by Ion Implantation,* edited by S. T. Picraux and W. J. Choyke (North-Holland, Amsterdam, 1982), p. 3.

[32] D. E. Luzzi and M. Meshii, *Scripta Metall.* **20**, 943 (1986).

[33] D. F. Pedraza and L. K. Mansur, *Nucl. Instrum. Methods B* **16**, 203 (1986).

[34] G. Martin and P. Bellon, *Mater. Sci. Forum* **15**, 1337 (1987).

[35] G. Linker, *Solid State Commun.* **57**, 773 (1986).

[36] *Binary Alloy Phase Diagrams,* edited by Thaddeus B. Massalski, Hiroaki Okamoto, P. R. Subramanian and Linda Kacprzak (ASM International, Materials Park, OH, 1990), Vol. 1, pp. 505–506.

[37] G. Linker, *Nucl. Instrum. Methods Phys. Res., Sect. B* **B19/20**, 526 (1987).

[38] A. Seidel, S. Massing, B. Strehlau and G. Linker, *Phys. Rev. B* **38**, 2273 (1988).

[39] Q. Williams, *Bull. Am. Phys. Soc.* **37**, 632 (1992).

[40] R. J. Hemley, A. P. Jephcoat, H. K. Mao, L. C. Ming and M. H. Manghnani, *Nature (London)* **334**, 52 (1988).

[41] O. Mishima, L. D. Calvert and E. Whalley, *Nature (London)* **310**, 393 (1984).

[42] Y. Fujii, M. Kowaka and A. Onodara, *J. Phys. C* **18**, 789 (1985).

[43] E. G. Ponyatovsky, *Trans. Japan Inst. Metals, Suppl.* **29**, 111 (1988).

[44] Q. Williams, presented at the 1992 March Meeting of the American Physical Society, Indianapolis, IN, 1992 (unpublished).

[45] M. B. Kruger and Raymond Jeanloz, *Science* **249**, 647 (1990).

[46] M. Grimsditch and L. E. McNeil, *Bull. Am. Phys. Soc.* **37**, 257 (1992).

[47] M. Volmer and A. Weber, *Z. Phys. Chem.* **119**, 227 (1926).

[48] R. Becker and W. Döring, *Ann. Phys. (Leipzig)* **24**, 719 (1935).

[49] D. Turnbull and J. C. Fisher, *J. Chem. Phys.* **17**, 71 (1949).

[50] R. W. Cahn and W. L. Johnson, *J. Mater. Res.* **1**, 724 (1986).

[51] David Turnbull, *Sci. Am.* **212**, 38 (1965).

[52] D. Turnbull, *J. Appl. Phys.* **21**, 1022 (1950).

[53] D. Turnbull, *J. Chem. Phys.* **20**, 411 (1952); **20**, 1824 (E) (1952).

[54] K. F. Kelton, in *Solid State Physics,* edited by Henry Ehrenreich and David Turnbull (Academic, San Diego, 1991), Vol. 45, pp. 75–177.

[55] A. R. Ubbelohde, *The Molten State of Matter: Melting and Crystal Structure,* (Wiley, New York, 1978), pp. 317–318.

[56] L. L. Boyer, *Phase Transitions* **5**, 1 (1985).

[57] J. Daeges, H. Gleiter and J. H. Perepezko, *Phys. Lett. A* **119**, 79 (1986).

[58] J. Däges, H. Gleiter and J. H. Perepezko, in *Phase Transitions in Condensed Systems—Experiments and Theory,* edited by G. Slade Cargill III, Frans Spaepen and King-Ning Tu (Mater. Res. Soc. Symp. Proc. **57**, Pittsburgh, PA, 1987), pp. 67–78.

[59] *CRC Handbook of Chemistry and Physics,* 68th ed., edited by Robert C. Weast, Melvin J. Astle and William H. Beyer (CRC Press, Boca Raton, FL, 1987), inside back flyleaf.

[60] C. J. Rossouw and S. E. Donnelly, *Phys. Rev. Lett.* **55**, 2960 (1985).

[61] J. J. Métois and J. C. Heyraud, *J. Phys. (Paris)* **50**, 3175 (1989).

[62] L. Gråbaek, J. Bohr, E. Johnson, A. Johansen, L. Sarholt-Kristensen and H. H. Andersen, *Phys. Rev. Lett.* **64**, 934 (1990).

[63] R. H. Willens, A. Kornblitt, L. R. Testardi and S. Nakahara, *Phys. Rev. B* **25**, 290 (1982).

[64] A. R. Ubbelohde, *The Molten State of Matter: Melting and Crystal Structure,* (Wiley, New York, 1978), pp. 31–32.

[65] X. L. Yeh and W. L. Johnson, in *Rapidly Solidified Alloys and Their Mechanical and Magnetic Properties,* edited by B. C. Giessen, D. E. Polk, A. I. Taub (Mater. Res. Soc. Symp. Proc. **58**, Pittsburgh, PA, 1986), p. 63.

[66] W. J. Meng, P. R. Okamoto, L. J. Thompson, B. J. Kestel and L. E. Rehn, *Appl. Phys. Lett.* **53**, 1820 (1988).

[67] W. J. Meng, P. R. Okamoto and L. E. Rehn, in *Science of Advanced Materials,* edited by H. Wiedersich and M. Meshii (ASM International, Materials Park, OH, 1990), pp. 99–119.

[68] D. E. Luzzi, H. Mori, H. Fujita and M. Meshii, *Acta Metall.* **34**, 629 (1986).

[69] D. Wolf, P. R. Okamoto, S. Yip, J. F. Lutsko and M. Kluge, *J. Mater. Res.* **5**, 286 (1990).

[70] J. F. M. Westendorp, Ph. D. thesis, University of Utrecht, 1986.

[71] A. M. Vredenberg, J. F. M. Westendorp, F. W. Saris, N. M. van der Pers and Th.H. de Keijser, *J. Mater. Res.* **1**, 774 (1986).

[72] Wen Jin Meng, Ph. D. thesis, California Institute of Technology, 1987.

[73] W. J. Meng, C. W. Nieh, E. Ma, B. Fultz and W. L. Johnson, *Mater. Sci. Eng.* **97**, 87 (1988).

[74] Dokyol Lee, J. Cheng, M. Yuan, C. N. J. Wagner and A. J. Ardell, *J. Appl. Phys.* **64**, 4772 (1988).

[75] D. E. Luzzi and M. Meshii, *J. Mater. Res.* **1**, 617 (1986).

[76] G. S. Cargill III, in *Solid State Physics,* edited by Henry Ehrenreich, Frederick Seitz and David Turnbull (Academic Press, New York, 1975), Vol. 30, pp. 227–320.

[77] P. H. Gaskell, in *Glassy Metals II: Atomic Structure and Dynamics, Electronic Structure, Magnetic Properties,* edited by H. Beck and H. J. Güntherodt (Springer-Verlag, New York, 1983), pp. 5–49.

[78] Yoshihiko Hirotsu, Naoki Imai and Takehiko Hirahara, in *Proceedings of JIMIS-5: Non-Equilibrium Solid Phases of Metals and Alloys,* supplement

to *Transactions of the Japan Institute of Metals* (Japan Institute of Metals, Sendai, Japan, 1988), Vol. 29, pp. 131–134.

[79] P. H. Gaskell, David J. Smith, C. J. D. Catto and J. R. A. Cleaver, *Nature (London)* **281**, 465 (1979).

[80] J. Zweck and H. Hoffmann, *J. Magn. Magn. Mater.* **45**, 382 (1984).

[81] L. C. Chen and F. Spaepen, *Mater. Sci. Eng.* **A133**, 342 (1991).

[82] Seung-Am Cho, *J. Phys. F* **12**, 1069 (1982).

[83] F. A. Lindemann, *Z. Phys.* **11**, 609 (1910).

[84] M. Born, *J. Chem. Phys.* **7**, 591 (1939).

[85] M. A. Durand, *Phys. Rev.* **50**, 449 (1936).

[86] L. Brillouin, *Phys. Rev.* **54**, 916 (1938).

[87] L. Hunter and S. Siegel, *Phys. Rev.* **61**, 84 (1942).

[88] F. D. Enck, *Phys. Rev.* **119**, 1873 (1960).

[89] O. D. Slagle and H. A. McKinstry, *J. Appl. Phys.* **38**, 437 (1967).

[90] O. D. Slagle and H. A. McKinstry, *J. Appl. Phys.* **38**, 451 (1967).

[91] Max Born and Kun Huang, *Dynamical Theory of Crystal Lattices,* (Clarendon Press, London, 1954), p. 413.

[92] J. L. Tallon, W. H. Robinson and S. I. Smedley, *Nature (London)* **266**, 337 (1977).

[93] J. L. Tallon, *Philos. Mag.* **39A**, 151 (1979).

[94] J. L. Tallon, *Nature (London)* **299**, 188 (1982).

[95] J. L. Tallon, *Phys. Lett.* **87A**, 365 (1982).

[96] J. L. Tallon, *Nature (London)* **342**, 658 (1989).

[97] K. F. Herzfeld and M. Goeppert-Mayer, *Phys. Rev.* **46**, 995 (1934).

[98] H. J. Fecht, *Nature (London)* **356**, 133 (1992).

[99] J. Wilks, *The Properties of Liquid and Solid Helium,* (Clarendon Press, Oxford, 1967), pp. 474–476.

[100] T. Górecki, *Z. Metallk.* **65**, 426 (1974).

[101] T. Górecki, *Scripta Metall.* **11**, 1051 (1977).

[102] R. M. J. Cotterill, *J. Cryst. Growth* **48**, 582 (1980).

[103] T. Yamamoto and T. Izuyama, *J. Phys. Soc. Jpn.* **57**, 3742 (1988).

[104] Fernando Lund, *Bull. Am. Phys. Soc.* **37**, 363 (1992).

[105] Fernando Lund, preprint (in preparation).

[106] A. R. Ubbelohde, *The Molten State of Matter: Melting and Crystal Structure,* (Wiley, New York, 1978), Chap. 11.

[107] Robert W. Cahn, *Nature (London)* **273**, 491 (1978).

[108] J. M. Kosterlitz and D. J. Thouless, *J. Phys. C* **6**, 1181 (1973).

[109] D. R. Nelson and B. I. Halperin, *Phys. Rev. B* **19**, 2457 (1979).

[110] D. R. Nelson and B. I. Halperin, *Phys. Rev. B* **21**, 5312 (1980).

[111] P. R. Couchman and W. A. Jesser, *Philos. Mag.* **35**, 787 (1977).

[112] T. Egami and Y. Waseda, *J. Non-Cryst. Solids* **64**, 113 (1984).

[113] T. Egami and S. Aur, *J. Non-Cryst. Solids* **89**, 60 (1987).

[114] S. H. Liou and C. L. Chien, *Phys. Rev. B* **35**, 2443 (1987).

[115] K. Huang, *Proc. R. Soc. London, Ser. A* **190**, 102 (1947).

[116] S. Rabinovich, A. Voronel and L. Peretzman, *J. Phys. C* **21**, 5943 (1988).

[117] A. Voronel, S. Rabinovich, A. Kisliuk, V. Steinberg and T. Sverbilova, *Phys. Rev. Lett.* **60**, 2402 (1988).

[118] A. Seidel, S. Massing, B. Strehlau and G. Linker, *Z. Phys. B* **74**, 267 (1989).

[119] A. Seidel, C. A. Majid and G. Linker, *Solid State Commun.* **69**, 769 (1989).

[120] A. Seidel and G. Linker, *Appl. Surf. Sci.* **43**, 97 (1989).

[121] Herbert B. Callen, *Thermodynamics and an Introduction to Thermostatistics,* 2nd ed. (Wiley, New York, 1985), Chap. 5.

[122] Philip M. Morse, *Thermal Physics,* 2nd ed. (Benjamin/Cummings, London, 1969), Chap. 8.

[123] Philip M. Morse, *Thermal Physics,* 2nd ed. (Benjamin/Cummings, London, 1969), p. 90.

[124] John W. Cahn, *Tran. Metall. Soc. AIME* **242**, 166 (1968).

[125] K. Ohsaka, E. H. Trinh, J. C. Holzer and W. L. Johnson, *Appl. Phys. Lett.* **60**, 1079 (1992).

[126] K. Ohsaka, J. C. Holzer, E. H. Trinh and W. L. Johnson, in *Experimental Methods for Microgravity Materials Science Research—4th International*

Symposium, TMS Symposium Proceeding (The Minerals, Metals & Materials Society, Warrendale, PA, in press).

[127] A. R. Ubbelohde, *The Molten State of Matter: Melting and Crystal Structure,* (Wiley, New York, 1978), pp. 418–428.

[128] Richard A. Swalin, *Thermodynamics of Solids,* 2nd ed. (Wiley, New York, 1972), p. 93.

[129] Robert W. Cahn, *Nature (London)* **356**, 108 (1992).

[130] W. Kauzmann, *Chem. Rev.* **43**, 219 (1948).

[131] F. Spaepen, *Acta Metall.* **23**, 729 (1975).

[132] William L. Johnson and Hans J. Fecht, *J. Less-Common Met.* **145**, 63 (1988).

[133] T. B. Massalski, in *Proceedings of the 4th International Conference on Rapidly Quenched Metals,* edited by T. Masumoto and K. Suzuki (Japan Institute of Metals, Sendai, Japan, 1982), Vol. I, pp. 203–208.

[134] W. Klement, R. H. Willens and P. Duwez, *Nature (London)* **187**, 869 (1960).

[135] M. H. Cohen and D. Turnbull, *Nature (London)* **189**, 131 (1961).

[136] A. R. Ubbelohde, *The Molten State of Matter: Melting and Crystal Structure,* (Wiley, New York, 1978), pp. 25–30.

[137] H. J. Fecht, P. J. Desré and W. L. Johnson, *Philos. Mag. B* **59**, 577 (1989).

[138] David Chandler, *Introduction to Modern Statistical Mechanics,* (Oxford University Press, New York, 1987), pp. 139–149.

[139] Humphrey J. Maris and Leo P. Kadanoff, *Am. J. Phys.* **46**, 652 (1978).

[140] Giorgio Parisi, *Statistical Field Theory,* (Addison-Wesley, Redwood City, CA, 1988).

[141] Daniel J. Amit, *Field Theory, the Renormalization Group, and Critical Phenomena,* 2nd ed. (World Scientific, Teaneck, NJ, 1984).

[142] W. Hayes, *Contemp. Phys.* **27**, 519 (1986).

[143] A. R. Ubbelohde, *The Molten State of Matter: Melting and Crystal Structure,* (Wiley, New York, 1978), Chap. 12.

[144] D. E. Luzzi, *J. Mater. Res.* **6**, 2059 (1991).

[145] H. J. Fecht, Z. Fu and W. L. Johnson, *Phys. Rev. Lett.* **64**, 1753 (1990).

Chapter 2

Synthesis of supersaturated solid solutions near T_0 boundaries

In order to test the structural, thermodynamic and mechanical properties of crystals near the instability phase boundary predicted by the polymorphous phase diagram of Fecht and Johnson [1], it is necessary to figure out how to *synthesize* crystalline material as close as possible to that boundary. This task is not a simple one, for the crystal will necessarily have a much higher free energy near its stability limit than it would have were it to assume the lowest free energy state accessible by phase separation. In this chapter I shall describe the criteria by which we chose synthesis techniques for producing the highly supersaturated solid solutions in the experiments of the following two chapters. Notice that these criteria were developed not only from theoretical considerations of the nature of solid solubility extension in metallic alloys, but also from the practical experience gained from many synthesis failures. Such is the nature of experimental science!

2.1 Properties of the T_0 line

The main feature linking the polymorphous phase diagram of Fecht and Johnson to ordinary equilibrium phase diagrams is the thermodynamic construction called the T_0 line, which we encountered briefly in Chapter 1 (section 1.5.3). At a given concentration, the T_0 *temperature* is the temperature at which the free energies of the liquid and crystalline phases, G_L and G_X, are equal. A locus $T_0(c)$ of T_0 temperatures as a function of composition c is called a T_0 *line* [2] (Fig. 2.1). A T_0 line may be extended to temperatures below the equilibrium freezing point of the liquid by equating the free energy of the crystal to the free energy of the *undercooled* liquid.

Note that such a line has two important properties. First, the T_0 line defines the temperature-composition range in which partitionless solidification can occur at a given pressure [2]. At points in temperature-composition space beyond the T_0 line, the liquid phase has a lower free energy than the single-phase crystal, so there can be no positive driving force $\Delta G = G_\mathrm{L} - G_\mathrm{X}$ for *partitionless* solidification. (There will, of course, still be a driving force for solidification *with phase separation* at all temperatures at which equilibrium crystalline phases can exist.) This has repercussions for amorphization by rapid quenching from the liquid state, for if (i) the T_0 construction indicates that partitionless crystallization is prohibited at a given temperature and composition and (ii) the cooling process is fast enough to prevent the occurrence of kinetically more difficult multiphase crystallization (such as in eutectic formation), then the liquid phase should quench to a glass upon crossing the glass-transition temperature T_g [2]. Thus, the temperature-composition region beyond a T_0 line and below T_g is a region of enhanced glass-formation ability by rapid quenching, provided that the region does not fall beneath the T_0 lines of competing crystalline phases.

Conversely, the T_0 line provides a limit for solubility extension of the crystalline phase if that phase is formed by quenching from the melt [2, 3], since there is a driving force for formation of the crystal from the liquid only in the region beneath the T_0 line. If the T_0 line becomes vertical at some composition c^* (section 1.5.4) or if it falls to absolute zero at a composition c^*, then the liquid will not be able

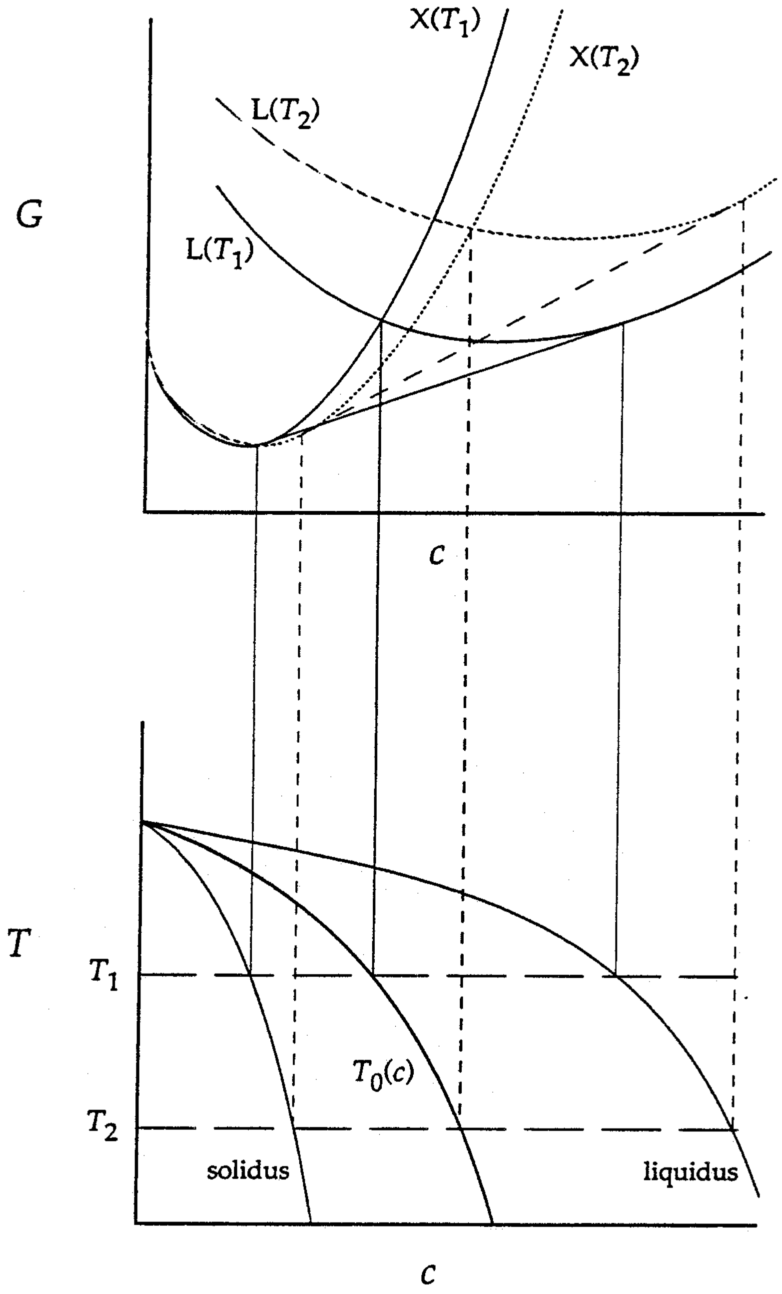

Figure 2.1: Construction of the T_0 line from free energy curves of the crystalline and liquid phases. The solidus and liquidus curves must straddle the T_0 line because of the common-tangent construction.

to be quenched to the single-phase crystal at any composition $c > c^*$, no matter how fast it is cooled.

2.1.1 Relationship of T_0 lines to phase diagrams

The usefulness of the T_0 concept in describing glass-formation ranges and limits to solubility extension is bolstered by the fact that the position of a T_0 line in an alloy system can often be inferred from its equilibrium phase diagram [4]. For temperatures at which the liquid phase exists in equilibrium, the T_0 line must pass between the corresponding solidus and liquidus lines because the common-tangent construction fixing the location of the solidus and liquidus sandwiches the crossing point of the crystal and liquid free energy curves (Fig. 2.1). Calculations of the intersection point directly from free energy curves usually find that the T_0 line lies roughly halfway between the solidus and liquidus [5, 6, 7]. As mentioned above, the T_0 line can be extended to temperatures below the equilibrium range of the liquid phase, although the shape of the phase diagram provides little information regarding the correct extrapolated line position.

While it is not possible to pin down the exact position of T_0 lines from equilibrium phase diagrams, all physically possible T_0 line shapes can be determined for any particular diagram. Three general situations are predicted from rapid quenching results on binary alloy eutectic systems [2]: (i) complete solid solubility, (ii) two-phase crystalline regions or (iii) limited single-phase crystalline regions separated by a region of at least partly amorphous material. Complete solid solubility may occur when the terminal solutions have the same crystal structure, as in the system Cu–Ag, for instance; in such cases the T_0 line is a continuous curve that never becomes vertical or intersects $T = 0\,\mathrm{K}$ [5, 8] [Fig. 2.2(a)]. Thus, the region beneath the T_0 line spans the entire composition range, and there is no solubility limit c^*. Two-phase crystalline regions may occur when the terminal solutions

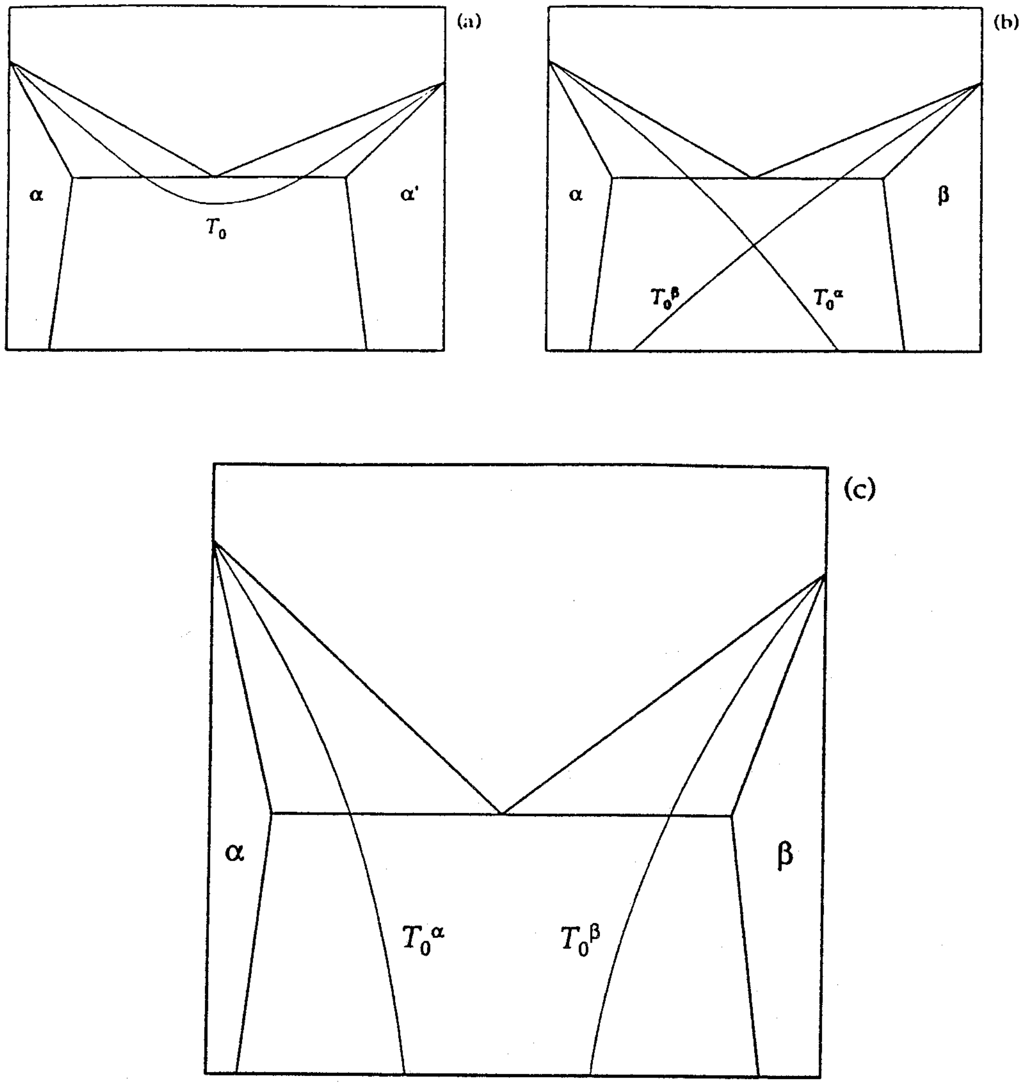

Figure 2.2: Possible T_0 line shapes for eutectic phase diagrams: (a) shallow eutectic with a continuous T_0 line, (b) shallow eutectic with crossing T_0 lines, and (c) deep eutectic with plunging, nonintersecting T_0 lines.

have different crystal structures, meaning that the T_0 line cannot be continuous as in the previous case. Instead, the T_0 lines corresponding to the different phases cross each other, creating a region that is beneath both of them [Fig. 2.2(b)]. In this region there is a driving force for partitionless solidification of the liquid to both crystalline phases. Finally, limited regions of single-phase crystals separated by an amorphous-containing region may occur when the T_0 lines of the crystalline phases plunge rapidly enough that they do not cross before intersecting the T_g line of the liquid phase [Fig. 2.2(c)]. The region between the intersections of the T_0 lines with the T_g line corresponds to the composition range in which the liquid will "freeze" to a glass instead of solidifying to a single-phase crystal as long as cooling proceeds rapidly enough to prevent crystallization with partitioning.

Since the T_0 lines are useful in predicting the results of rapid quenching from the melt, they indicate a sort of nonequilibrium phase diagram. For example, the T_0 lines superimposed on the equilibrium phase boundaries of Fig. 2.2(c) give the possible solubility regions for the terminal crystalline phases α and β and the expected glass-forming range. While such a construction ignores the kinetic constraints that must be maintained in order to form the glass or to supersaturate the crystalline phases, it at least highlights the conditions favored by the thermodynamics of the alloy. When we replace an equilibrium solidus and liquidus by a T_0 line and extend the T_0 line to temperatures below the freezing point of the liquid, we implicitly acknowledge that the results of a highly nonequilibrium synthesis process will depend on the path-dependent competition between the kinetics of processing and the underlying thermodynamics of the alloy system.

2.1.2 Limitations of the T_0 line concept

Of course, the kinetic *caveat* regarding the interpretation of metastable phase boundaries described above represents a serious limitation of the T_0 line concept.

"Violations" of nonequilibrium phase diagrams formed from T_0 lines have been observed experimentally [7]. For example, Nb–Pd exhibits a glass-forming range by vapor deposition that extends into the composition region beneath the T_0 line, whereas liquid quenching yields single-phase crystals in the same composition range (see section 2.3.2). Furthermore, accurate extrapolation of T_0 lines to low temperatures requires a good model for the free energy of the undercooled liquid. Schwarz, Nash and Turnbull [7] found that this problem is significantly underdetermined: while several different free energy models [9, 10, 11] are able to provide good fits to the solidus and liquidus of an experimentally obtained binary phase diagram, extrapolated T_0 lines calculated from the various models diverge significantly below the temperature range accessible to experiment. Schwarz *et al.* attribute the main part of the uncertainty to difficulties in modeling the entropy of undercooled liquids. The current lack of experimental data on the thermodynamic properties of undercooled liquids prevents choosing between competing models or improving on them at the present time.

2.2 T_0 line slopes

As described in the previous chapter (section 1.5.4), the critical point of the polymorphous phase diagram of Fecht and Johnson is the maximum solubility limit of solute in the crystalline phase. It is also the point at which the crystal's T_0 line has infinite slope (i.e., it is vertical). A binary alloy system appropriate for testing the validity of such a polymorphous diagram will, therefore, have a crystalline phase with a rapidly falling T_0 line that eventually becomes vertical. Our task, then, is to identify alloy systems that meet this criterion, a job made easier by the availability of a comprehensive compilation of binary alloy phase diagrams [12] and by the fact that—even without phase diagrams—we can *predict* with good accuracy which systems will exhibit steep T_0 lines.

The ability to predict T_0 slopes results from the relationship between the compositional extent of a $T_0(c)$ curve and the thermodynamically allowable extension of solid solubility of the corresponding crystalline phase. Years of metallurgical research have established which structural and electronic parameters have the greatest influence on *equilibrium* solubility ranges in binary alloy systems [13, 14]; we expect that the same parameters will influence the *metastable* solubility range reflected in the compositional extent of the T_0 line. The most significant factor governing solid solubility is the difference in atomic size of the alloy components. The so-called Hume-Rothery Size-Factor rule [13, 14] states that the equilibrium solid solubility range will become severely restricted in a binary alloy when the size difference between the component elements exceeds about 15 %. Conversely, when the size difference is much less than 15 %, one might expect solid solubility to become extensive, but in that case other factors (such as the stability of intermediate compounds and the ratio of valence electrons to the number of atoms [13, 14]) are known to have a more important influence on the solubility range, and the reliability of the size-factor rule diminishes [15]. Logically, if (i) a large size difference gives a limited equilibrium solubility range, (ii) a limited equilibrium solubility range corresponds to a limited metastable solubility range and (iii) a limited metastable solubility range corresponds to a steep T_0 line, then we would expect steep T_0 lines to occur whenever the component elements differ significantly in size.

Having confidence in the validity of postulates (i) and (ii), we can prove the conclusion of the argument by verifying that atomic-size difference does indeed have the expected influence on T_0 line slopes. In order to check this, we performed a search through the binary alloy phase diagram compilation [12] for Nb-based (bcc) and Ag-based (fcc) metallic alloys. We estimated, somewhat arbitrarily, an average T_0 slope from the slope of the line connecting the elemental melting point to the midpoint between the liquidus and solidus at the eutectic temperature T_e (Fig. 2.3). Plots of the slope of this approximate T_0 line against the atomic size ratio SR

$$SR = \frac{r_{\mathrm{metal}}}{r_{\mathrm{Nb\ or\ Ag}}}, \tag{2.1}$$

where r_{metal} is the metal atom's Goldschmidt radius (an estimate of atomic size in a 12-fold coordinated structure [16]), reveal rather high correlation between T_0 slope and atomic-size difference [Figs. 2.4(a)–2.4(b)]. Deviations from a perfectly linear dependence result from the rough nature of the approximation for T_0, from the fact that the T_0 line slope actually changes with composition and, no doubt, from ignoring the electronic and intermediate-phase effects treated by the other Hume-Rothery rules [13, 14]. Nevertheless, Figs. 2.4(a)–2.4(b) provide sufficient evidence to complete the final leg of the relationship between atomic-size difference, solubility range and T_0 slope.

A physical understanding of the origin of the size effect on solubility (and, therefore, on T_0 slope) is traditionally derived from a consideration of the lattice strain induced by size mismatch in a continuum elasticity model [17, 18]. Instead of following this approach, we shall appeal to the more recent treatment of Egami and Waseda [19] based on atomic-level stress, for they claim that their model provides a criterion for the topological instability of a supersaturated solid solution. Such a criterion may be able to predict the maximum solubility c^* of the polymorphous phase diagram of Fecht and Johnson [1], which occurs when the slope of the T_0 line becomes infinite. As discussed in the previous chapter (section 1.4) Egami and Waseda argue that a substitutional solid solution $\mathrm{A}_{1-x}\mathrm{B}_x$ will become unstable at the composition x_{max} given by

$$x_{\mathrm{max}} \approx 0.1\frac{V_{\mathrm{A}}}{|\Delta V|}, \tag{2.2}$$

where ΔV is the atomic-volume difference $V_{\mathrm{A}} - V_{\mathrm{B}}$. As the atomic-size difference

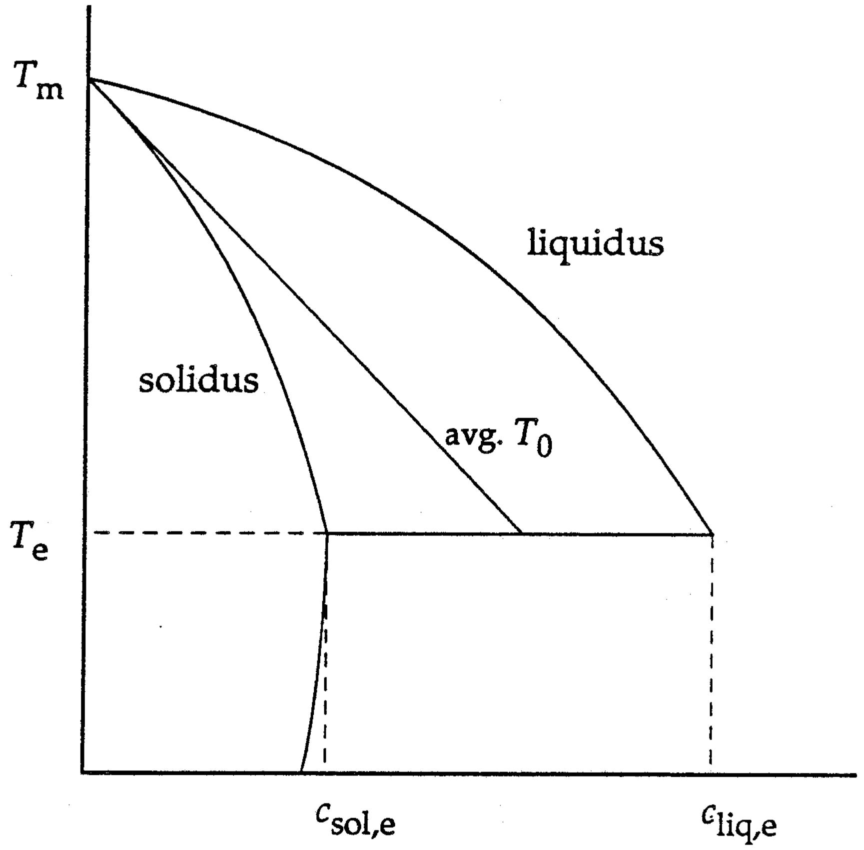

Figure 2.3: Estimation of the average T_0 line slope from the equilibrium phase diagram: we approximate the T_0 line by a line connecting the melting point of the elemental solid, $(0, T_m)$, to the midpoint between the liquidus and solidus at the eutectic temperature T_e, $\left(\frac{1}{2}(c_{sol,e} + c_{liq,e}), T_e\right)$.

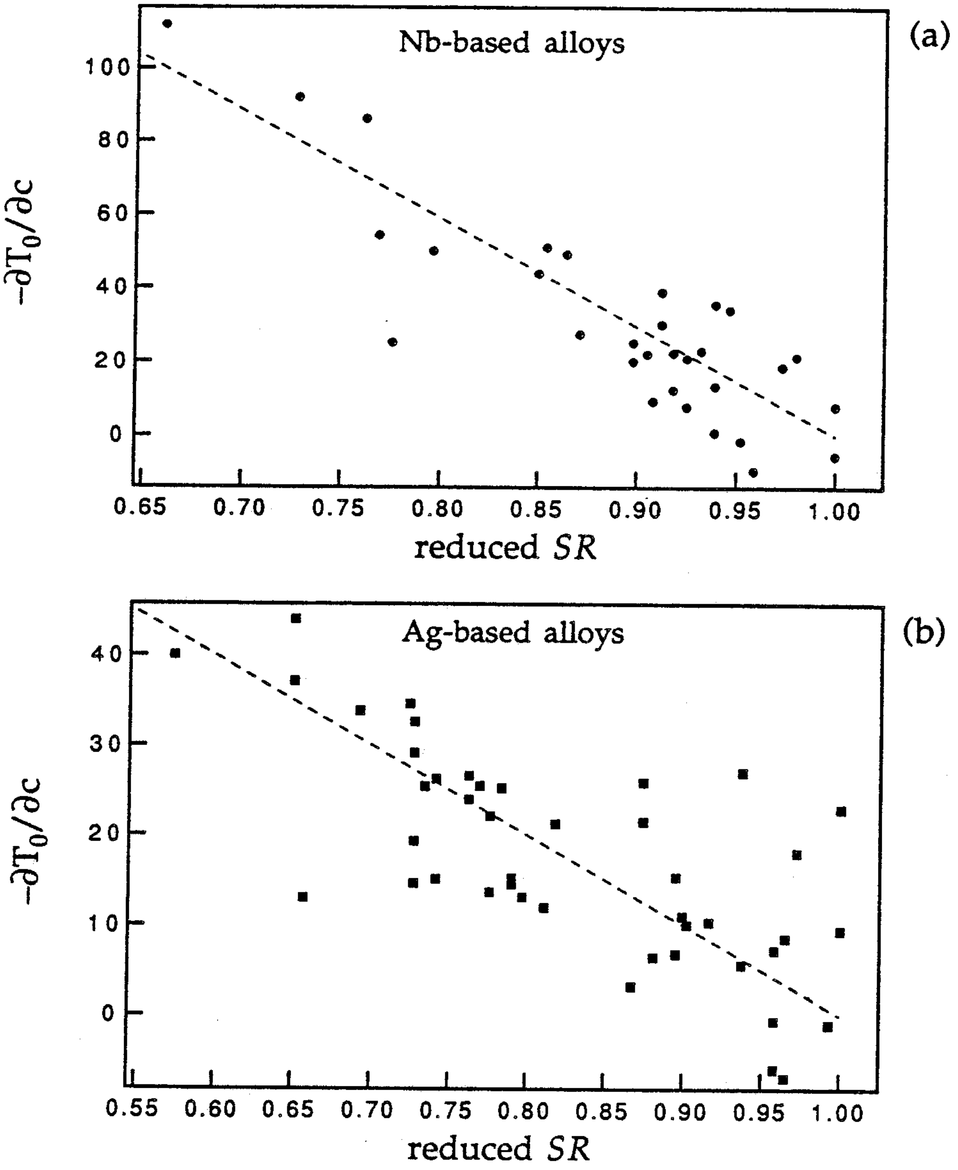

Figure 2.4: Plot of the approximate slope of the T_0 line against reduced atomic-size ratio SR for (a) Nb-based (bcc) and (b) Ag-based (fcc) metallic alloys. All SR values larger than 1.0 are reflected about 1.0 (i.e., $SR' = 2 - SR$)—hence, the qualifier *reduced*. The T_0 line slope was estimated using the construction of Fig. 2.3.

increases, x_{max} decreases, resulting in a smaller maximum solubility of B in A.

Once the correlation between atomic-size difference and T_0 slope has been established, it is easy to identify real binary alloy systems that may exhibit a critical point of the type envisioned in the Fecht-Johnson polymorphous phase diagram. Good candidates will have a large enough size difference between elemental components to have a rapidly plunging T_0 line for a terminal crystalline phase. Furthermore, since the thermodynamic and mechanical properties of the material are expected to vary strongly as the composition approaches the T_0 line, it will be preferable from an experimental point of view to investigate a system with a wide range of single-phase crystalline solubility (preferably in equilibrium) so that the sample can be studied at significantly different compositions, thus enabling the compositional dependence of the various properties to be more accurately assessed. This latter observation, however, argues for a small size difference between alloy components, since large equilibrium solubility ranges in binary alloys generally require size differences of ~5 % or less [18]. Apparently, the ideal system for testing the polymorphous phase diagram will represent a compromise between these conflicting demands.

2.3 Synthesis—considerations of kinetics

Once a suitable system has been chosen—consistent with the size difference and solubility requirements indicated in the previous paragraph—the next challenge is actually to fabricate a single-phase crystalline alloy at compositions ranging from no solute all the way up to the critical composition c^* (the point at which the T_0 line is vertical). The choice of synthetic technique is influenced by both the kinetic conditions necessary for making the sample in the desired configuration and the optimal sample geometry for the measurements that one intends to make. Let us consider the former point in this section and the latter in the following section (2.4).

2.3.1 Nature abhors the T_0 line!

Creating a crystal close to the T_0 boundary is very difficult because such a crystal would have a free energy that is nearly equal to that of the liquid phase (if $T > T_g$) or amorphous phase (if $T < T_g$) at the same composition (position 1 in Fig. 2.5). Of course, a single-phase crystal near T_0 would also have a much higher free energy than the phase-separated state indicated by the equilibrium phase diagram (position 2) and, possibly, than a phase mixture resulting from establishing "metastable equilibrium" with a metastable crystalline or amorphous phase (position 3). It is only by the imposition of kinetic constraints through a nonequilibrium fabrication process that the alloy can be prevented from accessing these lower-energy configurations. Optimal synthetic techniques can only be chosen after carefully considering the most common means by which nature conspires to avoid highly nonequilibrium states near the T_0 line during processing:

(a) by establishing phase equilibrium (either with a metastable phase or with the other equilibrium phase at that composition);

(b) by transforming to a new single phase (amorphous or crystalline);

(c) by undergoing solute segregation;

(d) by simultaneously nucleating and growing more than one phase (without establishing phase equilibrium).

Which, if any, of these means of violating the polymorphous constraint actually occurs depends on both the characteristics of the sample preparation technique and on the properties of the material being synthesized. In the following sections I shall illustrate each of the free energy-reducing processes (a) through (d) with

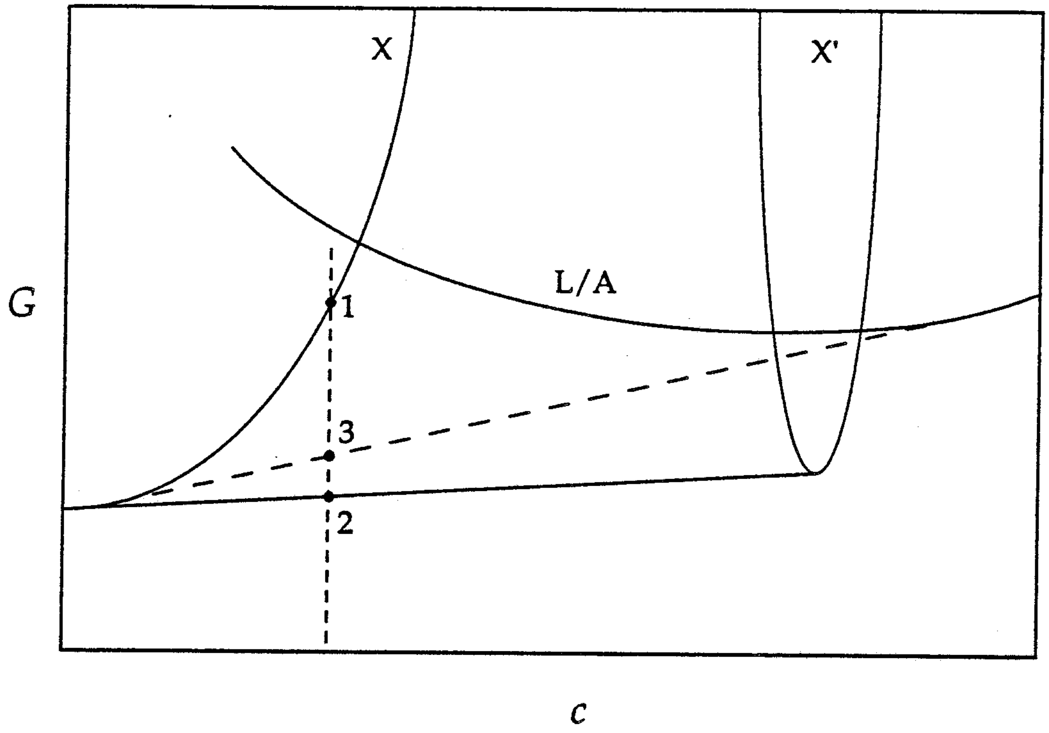

Figure 2.5: Free energy curves of a binary alloy illustrating the energy cost of approaching the T_0 line. A crystal at position 1 has a much higher energy than it would have in equilibrium (position 2) or in metastable equilibrium (position 3) with the liquid/amorphous phase.

results from our own work and attempt to indicate the synthesis-dependent and material-dependent reasons for constraint violation in each case.

2.3.2 Case studies of nonequilibrium sample preparation techniques

In the first three case studies only a brief outline of the experiments carried out will be provided in order that the main problems associated with synthesizing highly nonequilibrium alloys may be emphasized. In most cases, relevant details may be found in the pertinent references. The final case study (splat quenching of Nb–Pd and Nb–Pd–Ge) will be examined in detail because it is closely related to the subsequent discussion of supersaturated Nb–Pd solutions in Chapter 4; in this case we were able to demonstrate explicitly the connection between the T_0 lines of the Nb–Pd alloy system and the results of rapidly quenching Nb–Pd alloys from the liquid state. (From a practical standpoint, all four of these case studies helped to guide our formulation of experimental protocol in the $ErFe_2$ hydrogenation and Nb–Pd alloy experiments of Chapters 3 and 4.)

Sputter deposition of Er–Fe

The first set of experiments to be considered is the attempted fabrication of thin films of Er-rich crystals supersaturated with Fe by dc magnetron sputtering in a high-vacuum chamber [20]. Sputtering [21] is a vapor-deposition process in which ionized atoms of sputtering gas (usually Ar) are accelerated by a modest electrical potential (a few hundred volts) toward a target of the material to be deposited. The energy imparted to the surface of the target by the incoming ions knocks out neutral atoms and atom clusters of the material, which move ballistically away from the target in the low-pressure atmosphere of the chamber. Some of them land on the substrate (which usually faces the target surface), upon which they diffuse until losing most of their translational energy or becoming trapped in place by other incoming atoms and atom clusters [21]. The ability of sputter deposition—and, indeed, of all vapor deposition techniques—to produce metastable structures results from the high effective quench rate of the atoms from the vapor phase to the solid. It has been estimated that this cooling process can achieve rates as high as 10^9–10^{12} K/sec when depositing onto cooled substrates [22, 23].

For the $\mathrm{Er}_{100-x}\mathrm{Fe}_x$ system, the equilibrium phase diagram [24] (Fig. 2.6) indicates an equilibrium solubility limit of less than 0.3 at.% Fe in the terminal Er hcp solid solution [25]. The deep eutectic on the Er side of the phase diagram at $x = 31$ suggests that the T_0 line crosses the eutectic temperature at $x \approx 15$, resulting in a steeply plunging T_0 line. This is not surprising, since the Goldschmidt radius of Fe is almost 30 % smaller than that of Er ($r_{\mathrm{Fe}}/r_{\mathrm{Er}} = 0.72$) [16]. Correspondingly, the concentration of Fe estimated by the Egami-Waseda criterion [Eq. (2.2)] to cause topological instability of the terminal Er solid solution is $x_{\mathrm{max}} = 11$–14 (where we have used a prefactor of 0.07–0.09 instead 0.1, as optimized by Liou and Chien [26] for vapor-deposited alloys). We expect, therefore, that it will be impossible to deposit single-phase crystalline thin films with more than about 10–15 at.% Fe.

Diffraction patterns and dark-field images obtained by transmission electron microscopy (TEM) of $\mathrm{Er}_{100-x}\mathrm{Fe}_x$ films of thickness 15–20 nm grown on freshly cleaved crystals of KCl reveal a transition from an entirely crystalline microstructure to a mixture of crystalline and amorphous regions between $x = 9$ and $x = 16$ (Fig. 2.7). For $x \geq 26$, the dark-field images are entirely featureless, having only the 0.5–1.5 nm granularity typical of such images of amorphous materials [27].

These observations are consistent with x-ray diffraction of 600–750 nm films grown at the same compositions (Fig. 2.8). The lattice parameters of the crystalline phases—determined by Cohen's method using the extrapolation function $\cos^2\theta/\sin\theta$ [29]—do not decrease with increasing Fe content (Table 2.1), as would

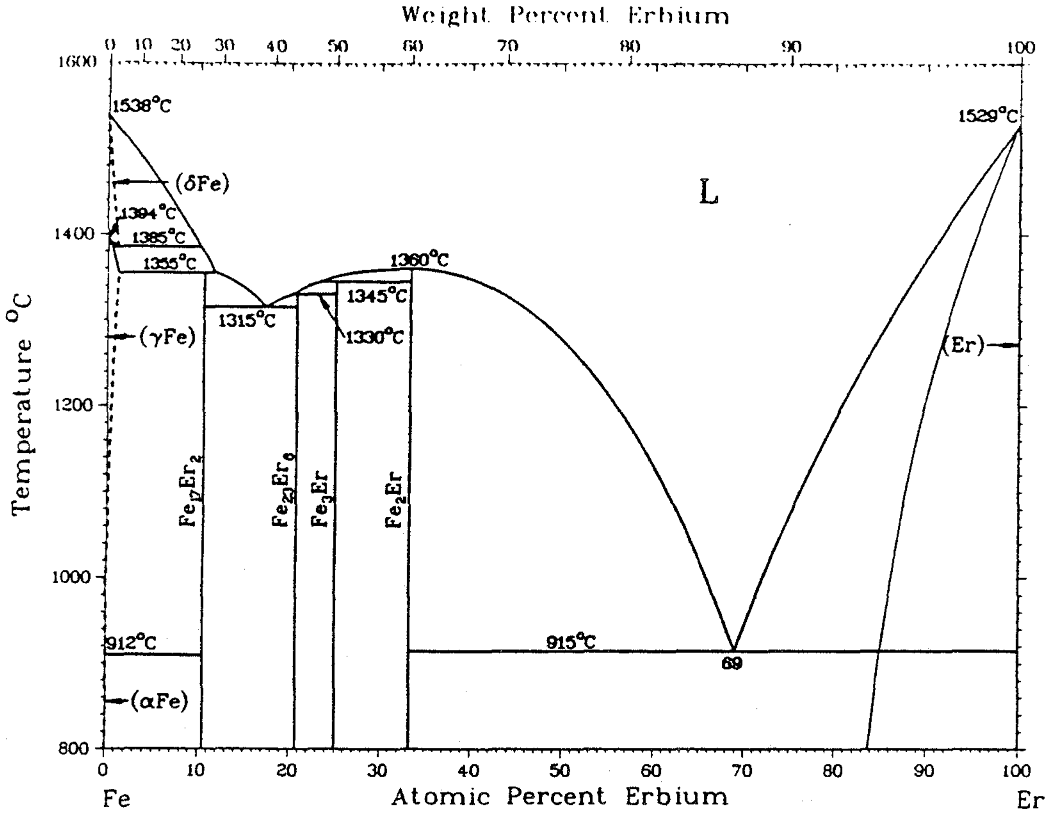

Figure 2.6: Equilibrium phase diagram of Fe–Er. The T_0 line of the terminal Er solution has been sketched in approximately midway between the solidus and liquidus. Phase diagram taken from Ref. [24].

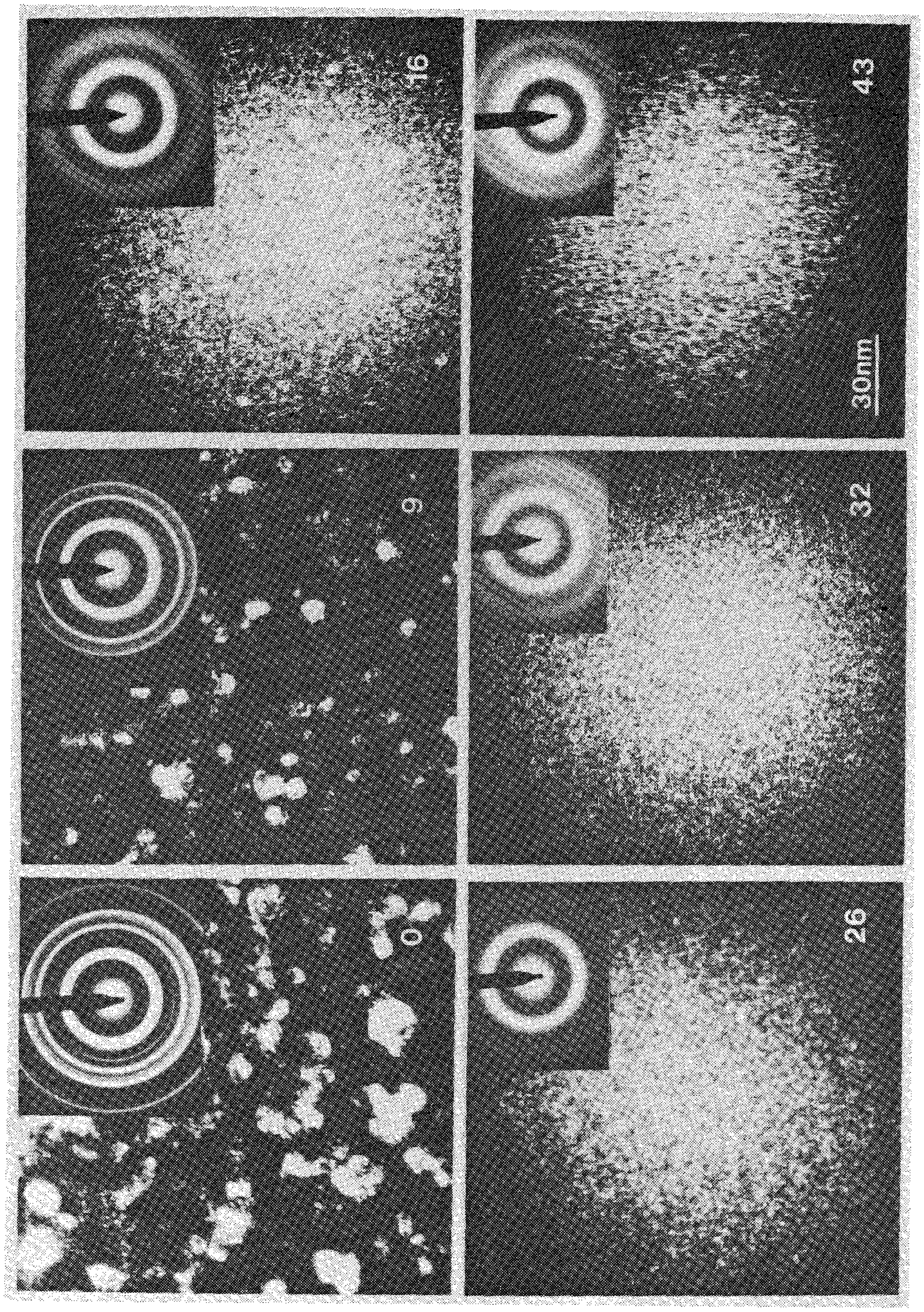

Figure 2.7: Dark-field images and diffraction patterns of $Er_{100-x}Fe_x$ thin films for $x = 0, 9, 16, 26, 32$ and 43.

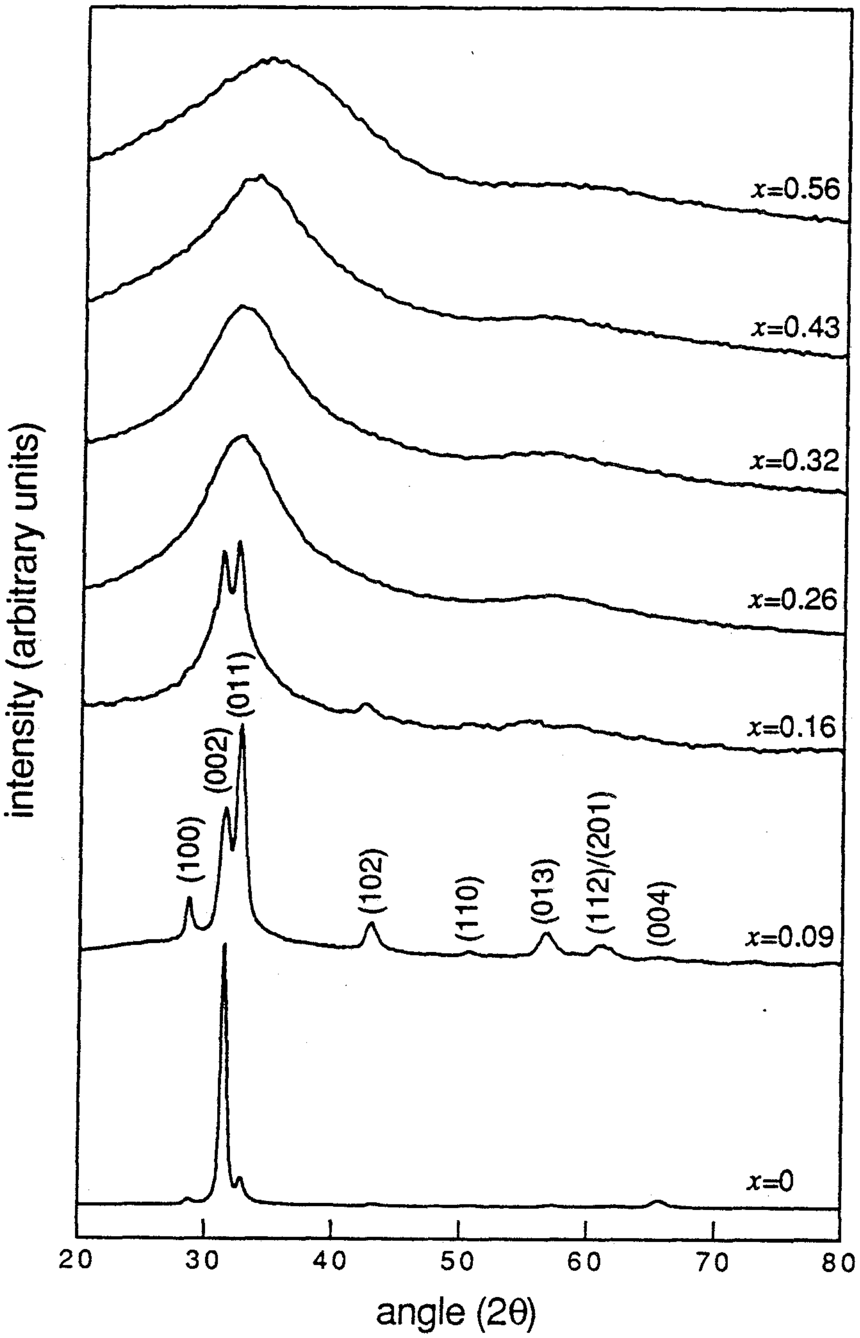

Figure 2.8: X-ray diffraction scans of $Er_{100-x}Fe_x$ thin films as a function of Fe concentration x.

be expected if the smaller Fe atoms were substituting for Er atoms in the hcp lattice, indicating that no real substitutional alloying takes place in these samples, even for $x = 9$. Instead, the Fe atoms are most likely segregated to the boundaries of the Er-rich crystals by surface diffusion during film growth. Since no peaks in addition to those of the hcp Er-rich solid solution are seen in either the electron or the x-ray diffraction scans, the segregated Fe is probably present in an amorphous state. Indeed, high-resolution TEM of a 3 nm film deposited at $x = 16$ finds crystalline regions separated by disordered boundaries (Fig. 2.9).

Thus, vapor deposition of $Er_{100-x}Fe_x$ alloys provides examples of three of the polymorphous constraint violation processes outlined above. The mixture of Er-rich crystals and an Fe-rich amorphous phase at $x = 16$ represents a kind of metastable equilibrium [process (a)]. The single-phase amorphous films found at $x \geq 26$ result from the atoms avoiding the higher-energy crystalline configuration altogether [process (b)], and the solute segregation of Fe at $x = 9$ is an example of process (c).

Sputter deposition of Nb–Pd

We carried out a similar investigation of sputter-deposited thin films of $Nb_{100-x}Pd_x$. The Nb side of the equilibrium Nb–Pd phase diagram [30, 31] (Fig. 2.10) is rather different from the Er side of the Er–Fe phase diagram, the most obvious differences being the larger equilibrium solubility range of the terminal bcc Nb-rich solid solution and its shallower T_0 line. The equilibrium solubility limit of Pd in Nb is rather large ($x_{\mathrm{max}} = 36$) at 1520 °C [32], but it drops quite a bit at room temperature ($x_{\mathrm{max}} < 20$ at temperatures below 800 °C). The large solubility range of Pd in Nb might be expected from the modest size difference between Nb and Pd atoms ($r_{\mathrm{Pd}}/r_{\mathrm{Nb}} = 0.93$ [16]), but it is surprising that the equilibrium solubility, at least at high temperature, approaches the Egami-Waseda topological instability

Fe_xEr_{1-x}	a (nm)	c (nm)
$x = 0$ (bulk)	0.35588	0.55874
$x = 0$ (film)	0.358 ± 0.001	0.567 ± 0.001
$x = 0.09$	0.360 ± 0.001	0.568 ± 0.001
$x = 0.16$	0.361 ± 0.002	0.570 ± 0.002

Table 2.1: Lattice parameters of bulk Er [28] and the terminal hcp phase of $Er_{100-x}Fe_x$ determined by x-ray diffraction using Cohen's method with extrapolation function $\cos^2\theta/\sin\theta$ [29].

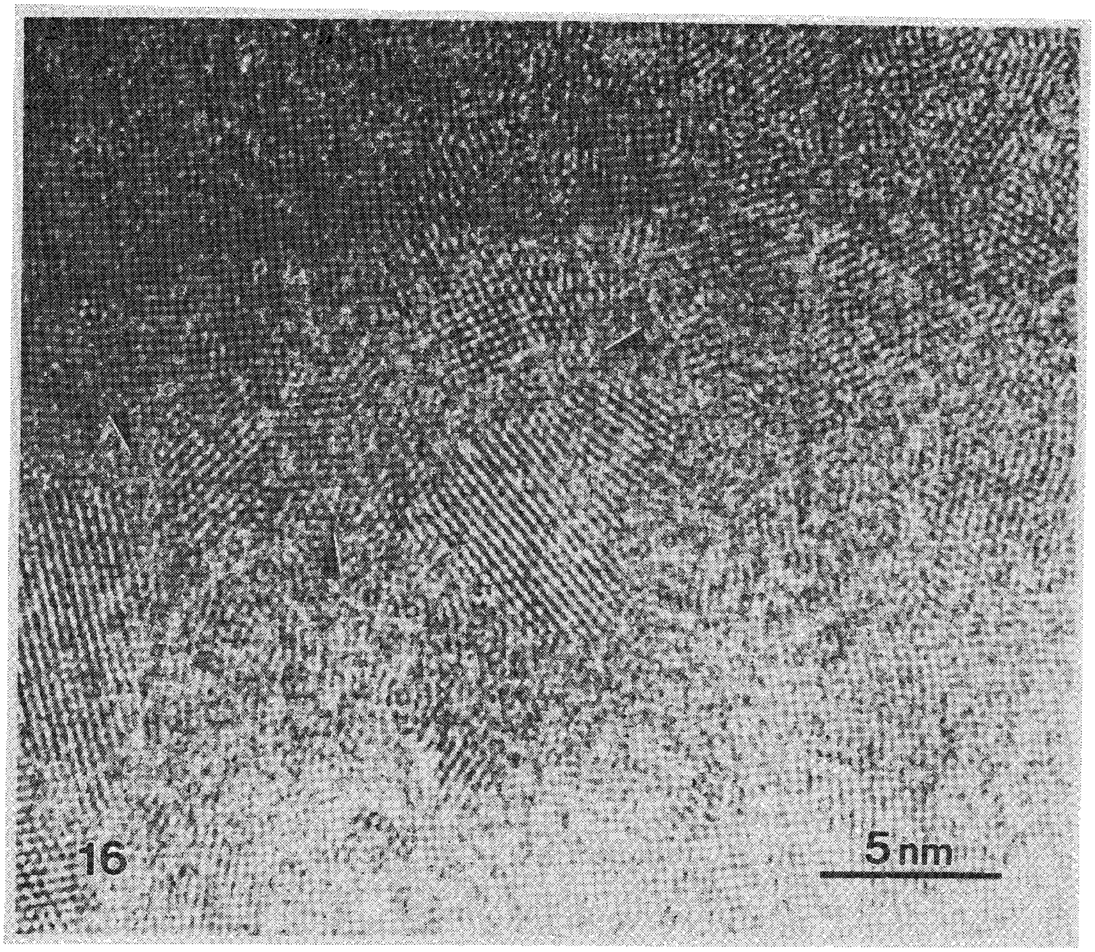

Figure 2.9: High-resolution TEM image of 3 nm thick, 16 at.% Fe film deposited on a heated (~ 80 °C) KCl substrate. Arrows indicate disordered regions possibly characteristic of Fe-rich amorphous regions between Er-rich crystals.

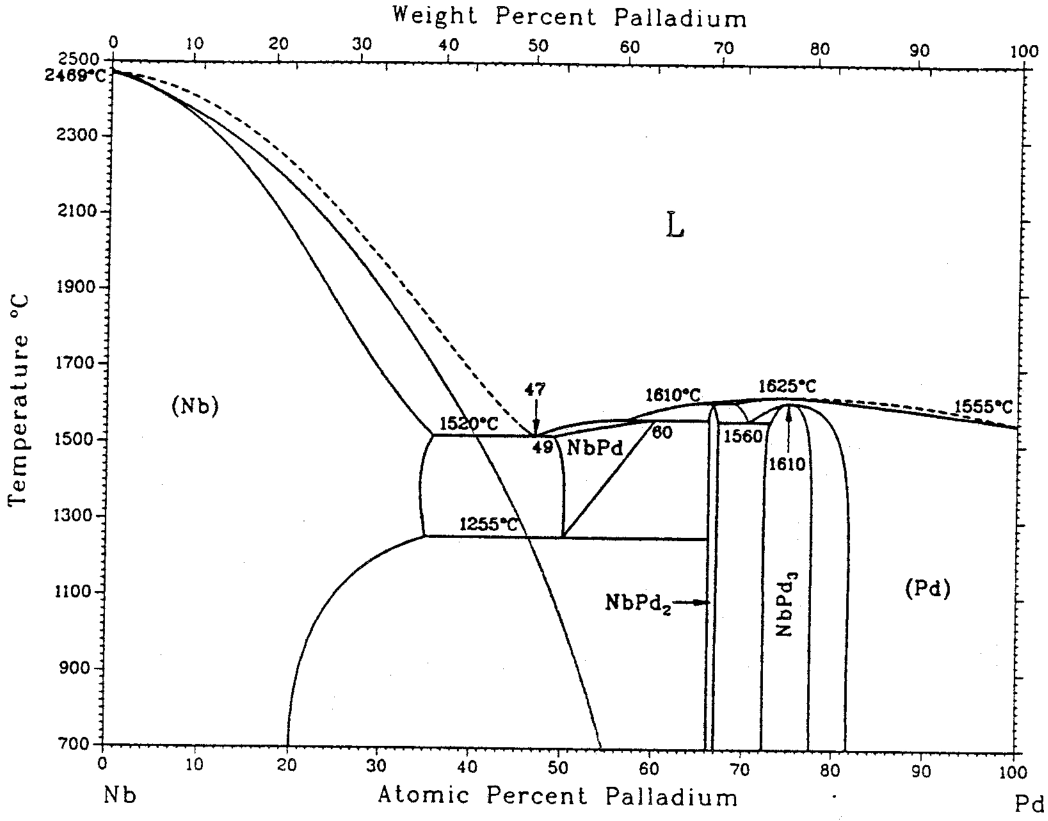

Figure 2.10: Equilibrium phase diagram of Nb–Pd. The T_0 line of the terminal Nb solution has been sketched in approximately midway between the solidus and liquidus. Phase diagram taken from Ref. [31].

of $x_{\text{max}} \approx$ 37–47 (again, using the prefactor for vapor deposition optimized by Liou and Chien [26]). In contrast to the simple eutectic on the Er-rich side of the Er–Fe phase diagram, however, in the Nb–Pd system there is a high-temperature intermetallic fcc phase (α-NbPd) that may interfere with solubility extension of the bcc terminal phase or with formation of an amorphous phase beyond the solubility limit of the bcc phase.

X-ray diffraction measurements of 500 nm thin films grown on unheated glass substrates (except for $x \approx 35$, at which a 100 nm film was grown on Si/SiO_2) reveal a progressive change from single-phase crystalline structure for $x = 0$ and $x \approx 8$ to a mixture of crystalline and amorphous phases at $x \approx 25$ and a completely amorphous film at $x \approx 35$ (Fig. 2.11). Our results are consistent with the findings of van der Kolk and colleagues [33, 34, 35] that thin films of $Nb_{100-x}Pd_x$ can be deposited in an entirely amorphous state for $40 \leq x < 60$ but not for $x = 30$. It is also another example of the success of the Egami-Waseda criterion for predicting the extent of the glass-forming range. The fact that no sign of the fcc α-NbPd phase is seen at high Pd concentrations can be attributed to the kinetic difficulties of forming the crystalline structure by surface diffusion on unheated substrates during vapor deposition.

From the standpoint of the violation of polymorphous constraints, the salient feature is that completely amorphous films grew even at compositions at which the terminal crystalline phase is stable in equilibrium, at least at high temperature [process (b)]. Certainly, at room temperature a film with $x \approx 35$ lies beneath the T_0 line of the terminal bcc solution (unless the T_0 line curves back on itself at low temperature). Indeed, we will see below that rapid quenching from the melt at the same composition yields a single-phase bcc crystalline sample. Evidently, the result of a highly nonequilibrium synthesis technique can be strongly path dependent.

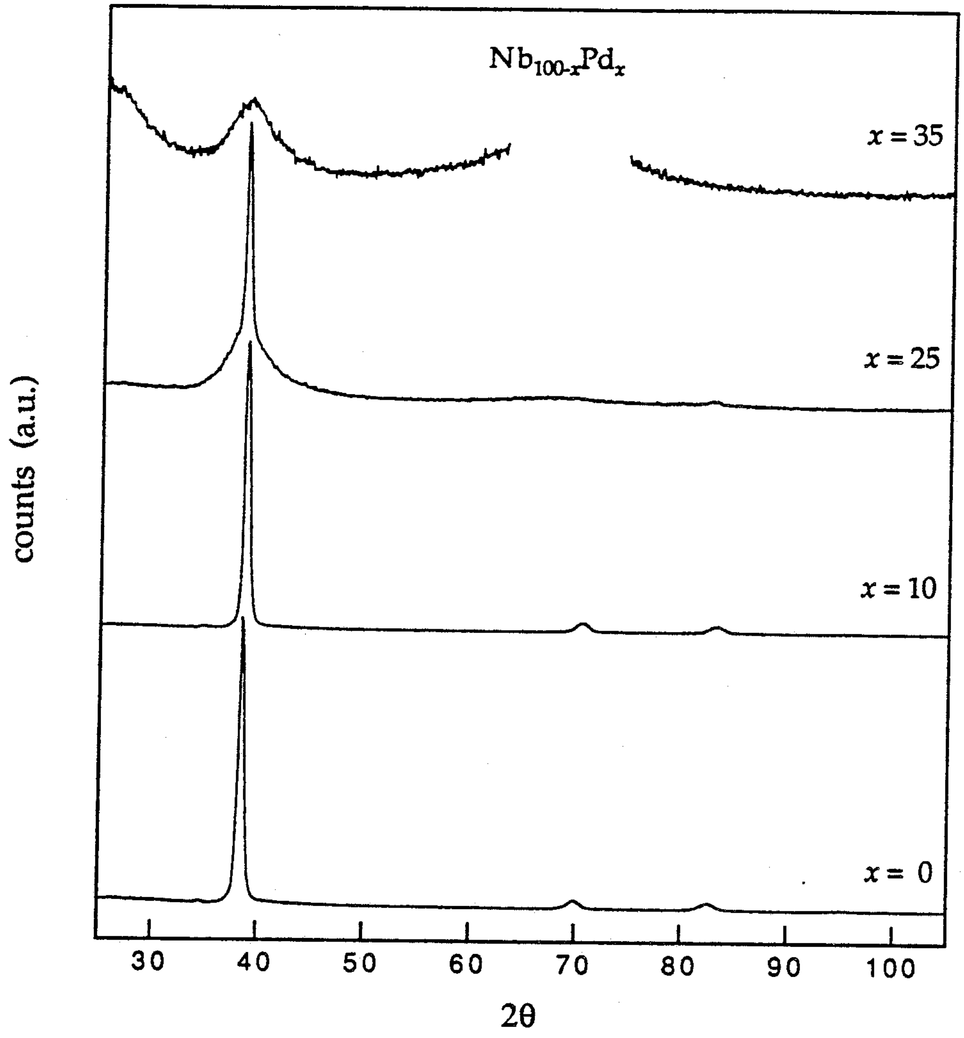

Figure 2.11: X-ray diffraction scans of $Nb_{100-x}Pd_x$ thin films deposited on unheated glass substrates, except for x = 35, which was grown on Si/SiO_2. The region in the x = 35 scan with no counts resulted from removal of a Si substrate Bragg peak.

Mechanical alloying of Nb–Pd

Another technique for making highly nonequilibrium alloys is mechanical alloying (MA) (section 1.1.3) [36]. MA is a process in which powdered components (usually elemental) are forcibly intermixed by repeated crushing together in a rapidly shaking vial filled with steel balls (or by a variation of this method [37])—hence the alternative name *ball milling*. The milling process is known to lead to complete alloying in many systems, accompanied by significant grain refinement [38], a buildup of atomic-level strain [38] and, sometimes, by complete amorphization of the powder [36]. The mechanically driven mixing is so strong that many systems with a positive heat of mixing ($\Delta H_{\mathrm{mix}} > 0$) can be alloyed [39, 40, 41]; for example, in Fe–Cu, a single-phase fcc alloy of $Fe_{50}Cu_{50}$ can be formed that releases more than 12 kJ/mol upon phase separation to equilibrium when heated in a differential scanning calorimeter [42]! The alloying process in MA can be followed most readily by the structural changes evident in x-ray diffraction scans of the powder after different milling times. For the MA machines that we used (SPEX 8000 Mixer/Mill), early milling times (< 10 hours) are characterized by rapid changes in lattice parameter (attributable to substitutional alloying), by reduction of grain size (usually to the 5–25 nm range) and by increase in internal strain (up to ~ 1.5 at.% for alloys), while later times find these properties changing much more slowly until reaching more or less steady-state values after about 20 hours. If the sample alloy is one that undergoes amorphization by ball milling, evidence can usually be found for a mixture of crystalline and amorphous material within the first 5 hours of milling, although complete amorphization may take longer than 20 hours to be achieved; it is also possible for a mixture of crystalline and amorphous powder to exist at steady state [43].

Alloys that can be made in an amorphous state by MA are generally the same ones that can be made amorphous by vapor deposition, even though the synthesis processes are so different; I know of no materials that can be amorphized by MA but not by vapor quenching. The compositional range of glass-formation by ball milling is comparable to that of vapor techniques and, consequently, is often much wider than that of rapid quenching from the melt [44].

The mechanism by which alloying takes place in the extreme experimental conditions present inside the vial is not presently understood. Electron microscopy investigations have found layered microstructures of the materials being alloyed during early milling times [45], but it is not known how these layers are subsequently mixed on an atomic scale. Yavari and Desré [46] recently proposed that the capillary pressure at nanometer-sized distorted "tips" and "necks" in the layers may provide a thermodynamic driving force for alloying, even when the bulk enthalpy of mixing is positive. Eckert *et al.* [47] have suggested that repeated deformation by ball collisions pumps a high density of dislocations into the powder grains, which in turn influences the solubility characteristics of the material through the stress fields surrounding each dislocation. Experimental evidence for the importance of dislocations in governing the properties of ball-milled materials can be found in the success of a dislocation-interaction argument [48] in explaining the minimum grain size attainable in milling of both elemental and alloyed powders [38, 47]. Finally, still others have attributed amorphization during mechanical alloying to a solid-state reaction at the interface of the alloyed elements, similar to the solid-state amorphization reaction (SSAR) observed to occur in some elemental diffusion couples (section 1.1.2), but amorphization by MA has also been observed in an alloy that does not amorphize by SSAR [43].

Since $Nb_{100-x}Pd_x$ alloys with $40 \leq x < 60$ can be made amorphous by sputter deposition, we expect amorphization to be possible by MA, as well. To test this hypothesis, stoichiometric ratios of elemental Nb (99.8 %) and Pd (99.95 %) powders with a total weight of ~ 7 g were placed in a steel milling vial along with four steel balls. The vial was sealed in an Ar atmosphere to prevent oxidation during milling; subsequent powder removal and vial resealing were also performed in an Ar-filled glove bag. The milling was accomplished on a SPEX 8000 Mixer/Mill for times typically exceeding twenty hours in order to ensure that steady-state conditions were obtained. The structure of the powder was determined by standard x-ray diffraction measurements in θ–2θ geometry.[1]

Complete alloying of the Pd into the terminal bcc Nb structure occurred for all compositions up to 40 at.% Pd, but at 40 at.% Pd, and perhaps at 35 at.% Pd as well, the Bragg peaks in the x-ray scans disappeared, leaving only the single broad maximum characteristic of an amorphous metallic alloy (Fig. 2.12). Once again, we have an example in which the energy associated with supersaturation is relieved by transformation of the crystalline phase to another phase [process (b)]. The composition at which amorphization occurs is close to that of sputter deposition, despite the manifest differences in processing characteristics. This fact supports the idea that in some instances, at least, the kinetics of processing may play a secondary role to that of thermodynamics in influencing the compositional position of the crystalline/amorphous boundary.

Splat quenching of Nb–Pd and Nb–Pd–Ge

Our final case study is an attempted supersaturation of the terminal bcc Nb phase in Nb–Pd by rapid quenching from the melt [50]. Rapid cooling of a liquid phase can extend solubility beyond equilibrium limits, quench the melt to a metastable crystalline phase—such as a high-temperature phase or one that does not appear in the equilibrium phase diagram—or quench the melt to an amorphous state by

---

[1] Most of the following experimental results were obtained by Mr. Steve Hwang as part of his summer 1990 research project [49].

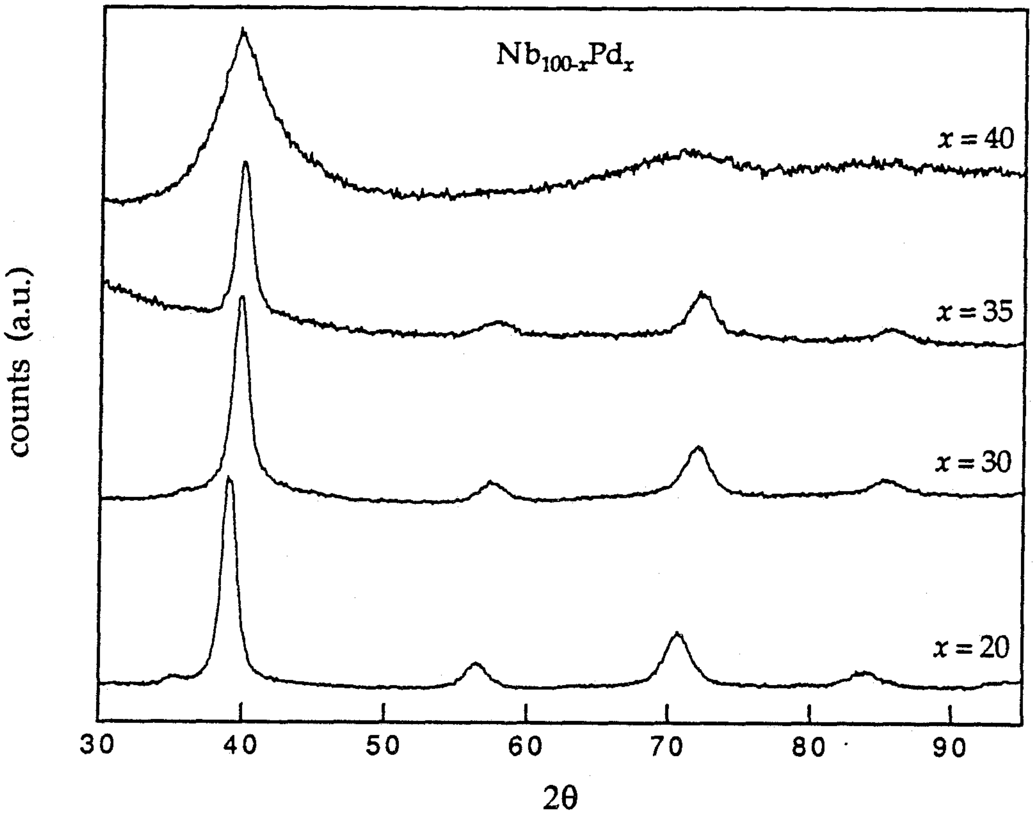

Figure 2.12: X-ray diffraction scans of $Nb_{100-x}Pd_x$ alloys ball milled for at least 20 hours in Ar. For $x = 40$ the scan has the single broad intensity maximum characteristic of amorphous metallic alloys.

suppressing the nucleation and growth of crystalline phases [51, 52, 53]. The cooling rates of the common rapid-quenching techniques—melt spinning and piston-and-anvil quenching—are several orders of magnitude slower than that of vapor deposition [22, 23], a fact that is reflected in the very restricted glass-formation ranges by rapid quenching of most binary metallic alloys. Rather than being a disadvantage, this slower cooling rate will be seen to produce a *wider* supersaturation range of the bcc terminal Nb phase in Nb–Pd than found by vapor deposition or mechanical alloying.

Splat quenching The particular rapid-quenching technique that we employed is called *twin-piston splat quenching,* a process in which a small piece of the material to be quenched is levitation melted in an argon-filled chamber above the centerline of an opposing pair of pistons (Fig. 2.13). When the rf power to the levitation coil is turned off, the melt falls through the bottom of the coil and passes a photocell detector, which triggers the pistons to fire. By setting the trigger delay properly, the pistons can be made to strike both sides of the falling drop nearly simultaneously, causing the sample to be cooled at 10^4–10^6 K/sec [54]. The resulting foil has a thickness ranging from 5 to 300 μm, with the center usually about 50–100 % thicker than the edge [54]; due to heat flow considerations, the cooling rate of a local region of the foil is approximately inversely proportional to its final thickness [55].

Nb–Pd results X-ray diffraction scans of the foil centers found only the bcc terminal Nb phase for Pd concentrations up to 42 at.%, an extension of about 6 at.% Pd beyond the equilibrium solubility limit at high temperature and more than 20 at.% Pd beyond the room-temperature limit (bottom row of Fig. 2.14). A mixture of bcc and fcc phases is found for 44–48 at.% Pd, and single-phase fcc

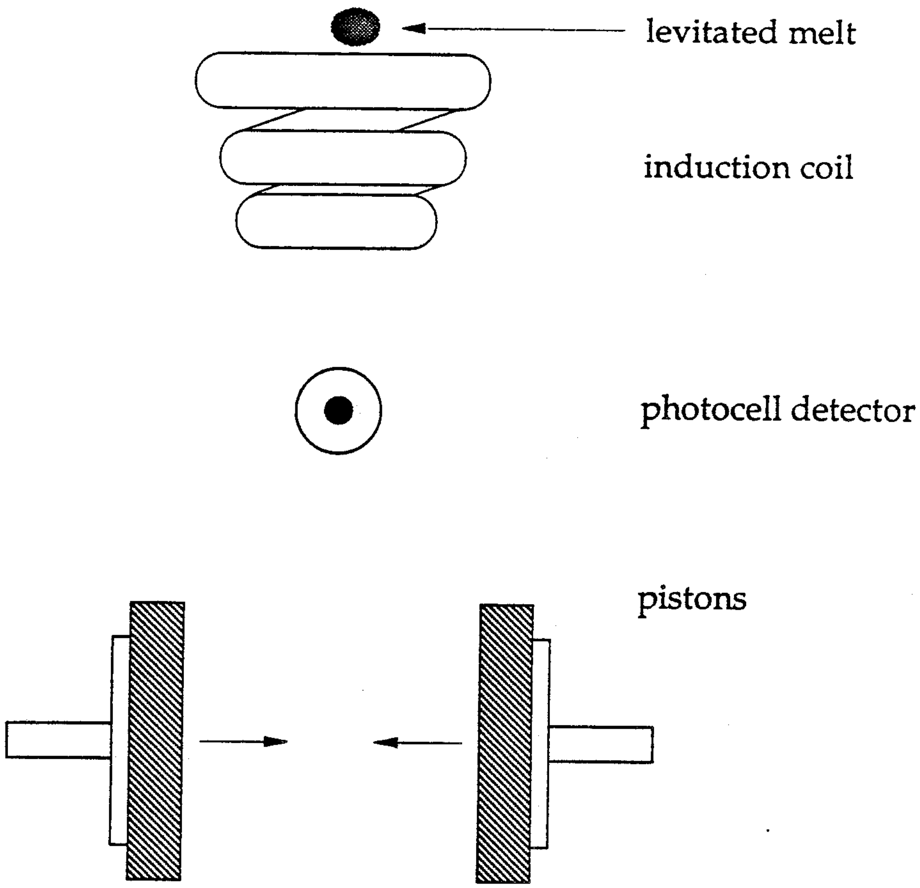

Figure 2.13: Schematic diagram of a twin-piston splat quencher. The sample is levitation melted in an rf coil and then dropped past the photocell detector, which triggers the pistons to close.

foils are obtained for Pd concentrations of 50 at.% and higher. The fcc phase has the expected lattice parameter of the high-temperature α-NbPd phase—an extension of the terminal Pd solution—seen in the equilibrium phase diagram (Fig. 2.10). No amorphous phase is found at any Pd composition despite the noncrystalline phase formed at 40 at.% Pd by both sputter deposition and mechanical alloying (see above). Neither is the nearest room-temperature intermetallic phase, $NbPd_2$, found in any of the splats. The relative amount of fcc phase to bcc phase, as judged from the relative intensities of the respective x-ray diffraction Bragg peaks, increases from 0 % to 100 % as the Pd content is increased from 42 at.% to 50 at.%, indicating that a kind of lever rule governs the quenching process in that composition range; here is another example [process (d)] of how nature—by following more than one synthetic path at the same time—can conspire to avoid respecting a polymorphous constraint that we try to impose.

Nb–Pd–Ge results Once one has determined the behavior of an alloy during quenching, one can try to exploit its own characteristics to keep it in line! A possible way to extend the bcc phase to higher Pd concentrations would be to add a third element that, if forcibly alloyed with the sub-critical nuclei of the bcc and fcc phases during rapid quenching, would destabilize the fcc nuclei—thus preventing them from growing into fcc crystals—without seriously affecting the bcc nuclei. Ideally, this third element would be incorporated substitutionally into the bcc lattice without changing its dimensions, so that the bcc structure is not destabilized by size-mismatch-induced strains. We chose Ge for this task because (i) its Goldschmidt radius (0.139 nm) is almost identical to that of Pd (0.137 nm) [16] and (ii) its solubility in Pd (less than 0.5 at.%) is lower than in Nb (11.5 at.% at 1900 °C and more than 3 at.% at room temperature) [56, 57, 58, 59]. Since Ge atoms are so similar in size to Pd atoms, we expect the Ge atoms to substitute one for one with Pd atoms in both the bcc and fcc lattices. Furthermore, since α-NbPd is an extension of the terminal fcc Pd phase, we expect Ge to have a lower solubility in α-NbPd than in the Nb-rich bcc solution. Since the equilibrium solubility limit reflects, in part, the stability of the solid solution, a lower solubility limit implies a higher energy state at a given composition. If this is true, then there should be a certain range of Ge concentration that the bcc phase can tolerate but the fcc phase cannot.

The effect of Ge addition to Nb–Pd alloys is readily apparent in x-ray scans, where the relative amount of fcc α-NbPd is always decreased by the incorporation of more Ge into the foil. In Fig. 2.14 we plot the structure of the rapidly-quenched foils as a function of Ge and Nb concentrations (Nb concentration was used for the horizontal axis instead of Pd concentration because to a first-order approximation the Ge substitutes for the Pd). Replacing 3 at.% Pd with Ge extends the range of bcc phase formation to 50 at.% Nb, and further increasing the Ge concentration completely suppresses the fcc phase, even for Nb concentrations as low as 45 at.%. The single-phase bcc region, however, can be extended only by about 2 at.%. Germanium concentrations higher than 6 at.% increase the relative amount of the bcc phase but also result in quenching of an amorphous phase. At 15 at.% Ge the foils are entirely amorphous (as determined by x-ray diffraction scans). The boundary of the single-phase amorphous region was much less composition dependent than that of the single-phase bcc and fcc regions.

The compositions indicated in Fig. 2.14 are the stoichiometric ratios present in the pre-alloyed ingots before splat quenching. While the overall composition of a quenched sample is certainly close to its pre-alloyed composition, there is no guarantee that the phases present in the multi-phase foils have the same composition as the overall composition. By examining the lattice parameters of the crystalline phases, however, we can estimate their compositions, because their

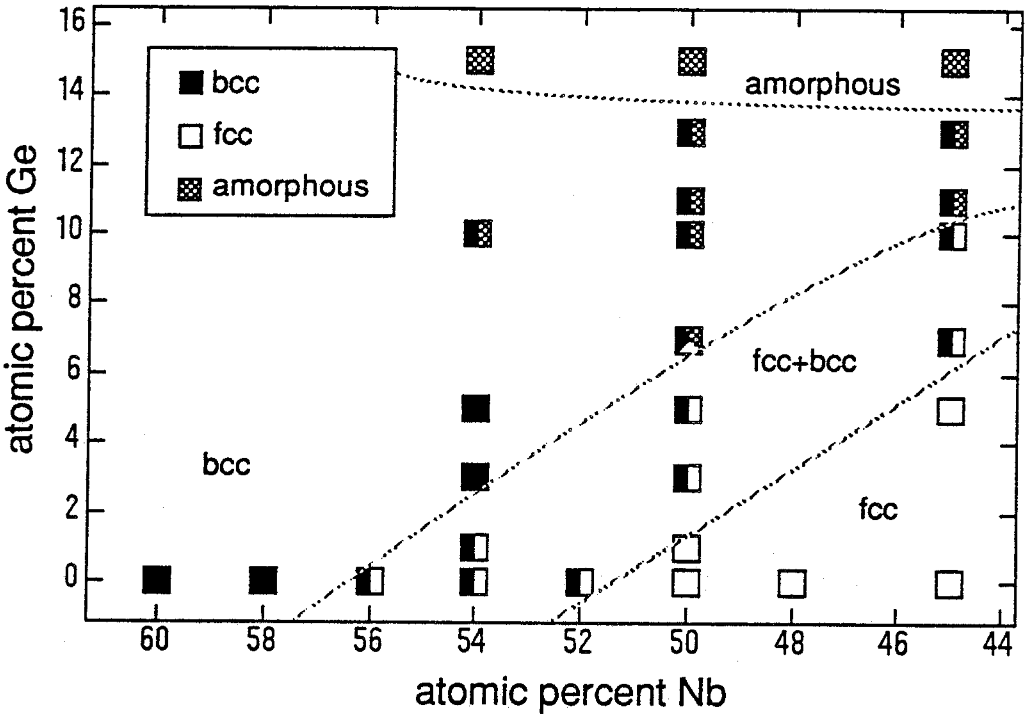

Figure 2.14: Phase diagram of splat-quenched foils of Nb–Pd–Ge. The solid squares represent the bcc Nb-rich phase, the open ones indicate fcc α-NbPd, and the shaded ones represent an amorphous phase. Squares with more than one type of marking indicate a phase mixture.

unit cell sizes will vary with the relative amount of Nb and (Pd+Ge) that they contain. Figure 2.15 is a plot of the bcc and fcc lattice parameters determined by x-ray diffraction (refined using Cohen's method and the extrapolation function $\cos^2\theta/\sin\theta$ [29]). The size of the bcc unit cell varies more rapidly with composition that that of the fcc unit cell. Replacing Pd with Ge at a fixed Nb concentration causes the bcc lattice parameter to increase slightly but not above the size expected from an extrapolation of the higher-Nb-content lattice parameters (dashed line). Even at (45 at.% Nb,10 at.% Ge) the bcc phase formed (in a mixture with fcc) has about the expected lattice parameter. If a significant amount of solute segregation had occurred, such as the bcc phase becoming Nb rich and the fcc phase Pd rich, then a plot of lattice parameter against concentration would deviate from the nearly linear curve without chemical segregation. That does not appear to occur with these foils, indicating that the quenching process was fast enough to prevent significant concentration fluctuations.

Finally, the average grain size of the crystalline phases was estimated from the broadening of the x-ray diffraction peaks using the variation of the full width at half maximum with scattering angle [60]. Grain sizes for both bcc and fcc phases ranged from 20 to 50 nm. Most significantly, the grain sizes of bcc and fcc phases *present in the same foil* were about the same within the error ($\sim 20\,\%$) of the estimation technique. Thus, the *growth* rates of each phase do not differ significantly in the multi-phase compositional range; differences in *nucleation* rates, rather than in growth rates, must give rise to the compositional dependence of the volume ratio of bcc and fcc crystalline phases.

Phase diagram and T_0 lines In Fig. 2.16 we have reproduced the Nb-rich side of the Nb–Pd phase diagram [30, 32] and sketched in approximate T_0 lines for the bcc Nb-rich and fcc α-NbPd phases using the fact the the T_0 line will

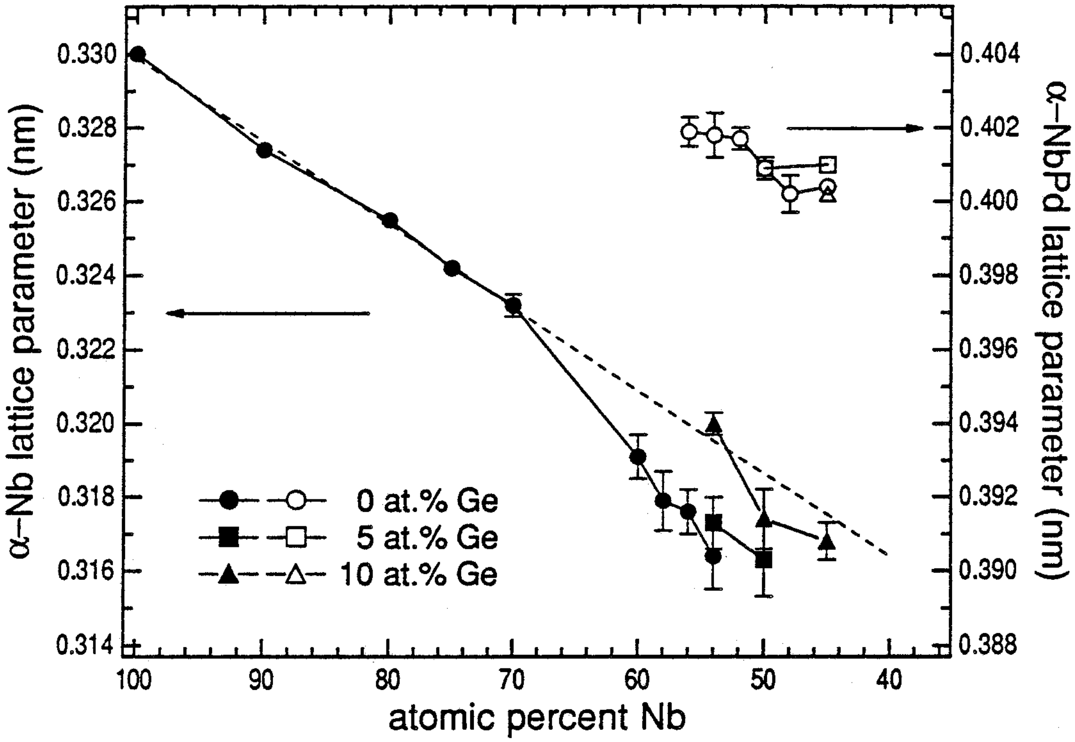

Figure 2.15: Lattice parameters of the bcc α-Nb phase (left axis) and the fcc α-NbPd phase (right axis) determined by x-ray diffraction. (The three data points between 75 and 90 at.% Nb come from Ref. [32].) The dashed line is a least-squares fit to the first five points. The horizontal axis indicates the Nb content of each sample, with the remainder being Pd and Ge.

pass approximately halfway between the liquidus and solidus (section 2.1.1). The relevance of this thermodynamic construction is justified by the observation that the constraint of uniform chemical composition is maintained during quenching, even though more than one phase may nucleate and grow. Although there is a large amount of uncertainty in the extrapolations of the bcc and fcc T_0 lines at temperatures well below the eutectic (1520 °C), the point of most interest to us—the crossing point of T_0^{bcc} and T_0^{fcc}—requires only a small amount of extrapolation and, consequently, is constrained fairly closely to ~42 at.% Pd; note that this is approximately the same limit we found for single-phase bcc extension at 0 at.% Ge by rapid quenching (Fig. 2.14). Slightly higher Pd concentrations result in a mixture of bcc and fcc phases rather than single-phase fcc samples, even though the melt crosses the fcc T_0 line first during the rapid quench. As the T_0 lines move further apart at 50 at.% Pd and higher, however, the quench results in single-phase fcc foils.

Nucleation rates and T_0 lines The T_0 line is a thermodynamic construct useful for predicting the possible phases resulting from a polymorphous quench, but determining the outcome near a crossing point of two T_0 lines requires an understanding of the kinetics governing crystal nucleation and growth. As mentioned above, lattice parameter data strongly suggest that the competition between bcc and fcc phases in the Nb–Pd–Ge ternary system is controlled by the relative nucleation—rather than growth—rates of the two phases. We can model this competition in a rough way using classical nucleation theory, which approximates the steady-state homogeneous nucleation rate as [61]:

$$I = A^* \exp\left(-\frac{16\pi}{3k_{\mathrm{B}}} \cdot \frac{{T_{\mathrm{m}}}^2}{T\Delta T^2} \cdot \frac{\sigma^3}{\Delta H_{\mathrm{f}}^2}\right), \tag{2.3}$$

where I is the nucleation rate at temperature T, σ is the liquid-crystal interfacial energy, ΔH_{f} is the heat of fusion, T_{m} is the melting point and ΔT is the

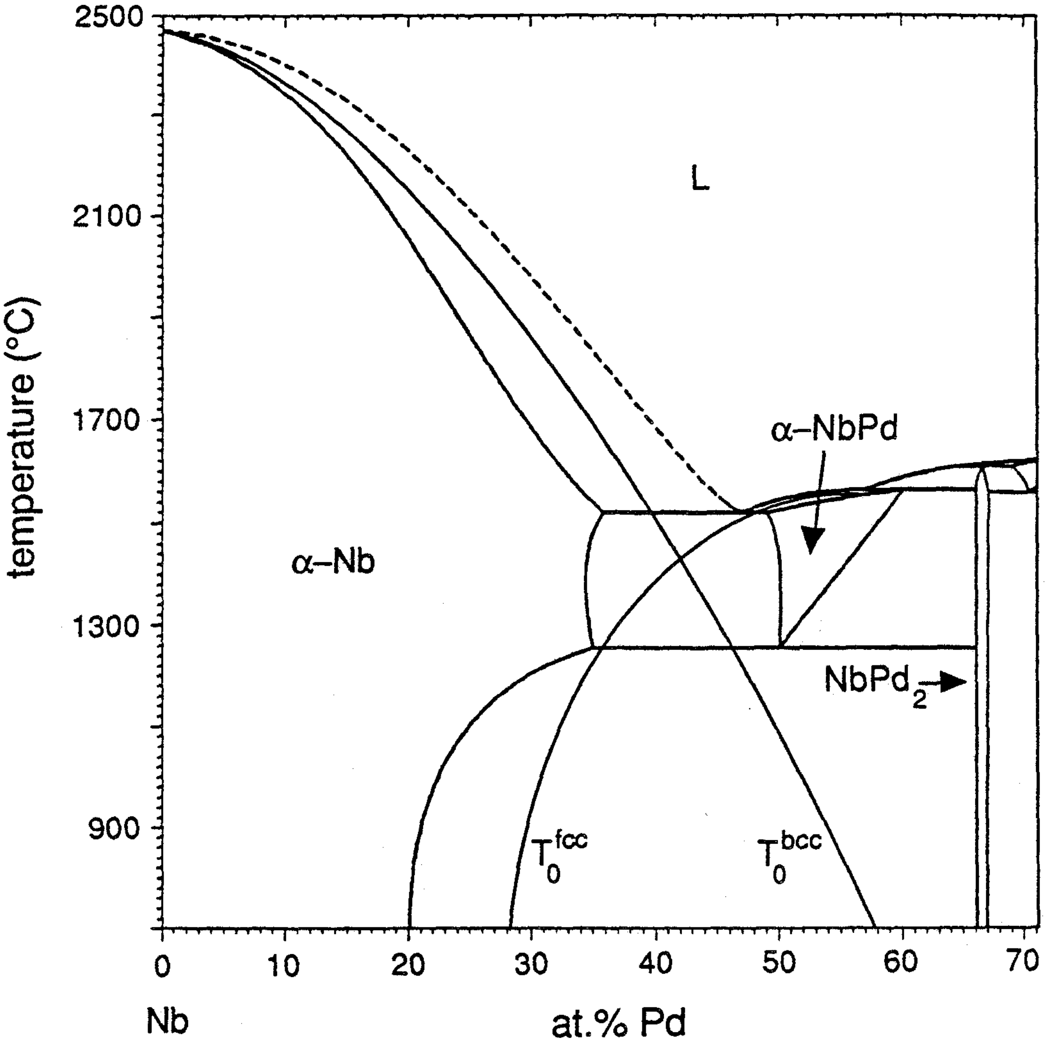

Figure 2.16: Nb-rich side of the equilibrium Nb–Pd phase diagram. T_0 lines for the bcc α-Nb and fcc α-NbPd phases have been sketched in by eye. (Equilibrium diagram taken from Ref. [30].)

undercooling at which the nucleation takes place. This general analysis will apply even if the dominant nucleation process during the rapid quench is heterogeneous, rather than homogeneous, because the heterogeneous nucleation rate differs from the homogeneous rate only by a geometrical factor in the argument of the exponential of Eq. (2.3) [61]. Since it is empirically found that $\sigma_g/\Delta H_f \approx 0.4$–$0.5$, where σ_g is the gram-atomic interfacial energy ($\sigma_g = \sigma N^{1/3} V^{2/3}$) [62], we can set $\sigma = K\Delta H_f$, where K is a composition-dependent proportionality factor. Furthermore, if chemical composition is held uniform, then the melting point T_m is given by the T_0 line. Making these substitutions gives

$$I = A^* \exp\left[-K'(T) \cdot \left(\frac{T_0}{T - T_0}\right)^2 \cdot \Delta H_f\right], \tag{2.4}$$

where $K'(T)$ is a positive function only of composition and T. At fixed composition and temperature T ($< T_0^{\mathrm{bcc}}, T_0^{\mathrm{fcc}}$) it follows that

$$\frac{I^{\mathrm{bcc}}}{I^{\mathrm{fcc}}} = \frac{A^{*,\mathrm{bcc}}}{A^{*,\mathrm{fcc}}} \exp\left\{K'(T)\left[\left(\frac{T_0^{\mathrm{fcc}}}{T - T_0^{\mathrm{fcc}}}\right)^2 \Delta H_f^{\mathrm{fcc}} - \left(\frac{T_0^{\mathrm{bcc}}}{T - T_0^{\mathrm{bcc}}}\right)^2 \Delta H_f^{\mathrm{bcc}}\right]\right\}. \tag{2.5}$$

In general, we expect the exponential term to vary with composition much more rapidly than the prefactor term. The nucleation rate ratio then is a function primarily of the heats of fusion and of the T_0 values at a given composition.

This expression is consistent with the results that we obtained for 0 at.% Ge: for Nb concentrations several atomic percent greater than the T_0 crossing point at 58 at.%, $T_0^{\mathrm{bcc}} > T_0^{\mathrm{fcc}}$. This yields a more positive argument of the exponential due to the large denominator in the negative term, giving $I^{\mathrm{bcc}} \gg I^{\mathrm{fcc}}$. Likewise, for Nb concentrations several atomic percent less than the crossing point, $T_0^{\mathrm{bcc}} < T_0^{\mathrm{fcc}}$, giving $I^{\mathrm{bcc}} \ll I^{\mathrm{fcc}}$. Very close to the crossing point, $T_0^{\mathrm{bcc}} \approx T_0^{\mathrm{fcc}}$, and the resulting ratio depends sensitively on the relative size of the heats of fusion and on the ratio of the prefactors. At fixed Nb concentration the increase of $I^{\mathrm{bcc}}/I^{\mathrm{fcc}}$ with Ge concentration suggests that the replacement of Pd with Ge decreases $\Delta H_f^{\mathrm{bcc}}$ more than $\Delta H_f^{\mathrm{fcc}}$ and/or causes $T_0^{\mathrm{bcc}} - T_0^{\mathrm{fcc}}$ to increase.

Since the relative nucleation rate is so sensitive to the amount of undercooling, $|T - T_0|$, the compositional dependence of $I^{\mathrm{bcc}}/I^{\mathrm{fcc}}$ suggests that the effect of Ge addition is to pull the fcc phase's T_0 line to lower temperature more rapidly than it pulls down the bcc phase T_0 line (Fig. 2.17). It is as if the Nb terminal solution's T_0 line were convoluted with the moderately steep one of the terminal Nb solution in Nb–Ge and the α-NbPd T_0 line were convoluted with the nearly vertical one of the terminal Pd solution in Pd–Ge. This would make the T_0 line of α-NbPd appear to twist downward to a greater extent than the T_0 line of the bcc Nb-rich solution, thereby shifting the crossing point of the T_0 lines to lower niobium content. This extends the single-phase bcc solubility region a small amount while simultaneously creating a deep eutectic in the polymorphic phase diagram, encouraging quenching of the amorphous phase [63, 64]. Thus, we see how a rather detailed understanding of kinetics during nonequilibrium processing can be gained from simple thermodynamic ideas derived from equilibrium phase diagrams.

2.4 Synthesis—considerations of sample geometry

In addition to the conditions that must obtain in order to maintain polymorphous constraints when synthesizing supersaturated solutions near the T_0 line, the resulting samples must meet certain geometrical criteria so that it is possible to measure relevant properties. Not only do we need to determine structural parameters like the lattice parameter, strain, density and atomic mean-square displacement, we might also want to measure thermodynamic and mechanical properties like the thermal expansion coefficient, heat capacity, shear modulus and Young's modulus. The only type of sample suitable for *all* of these measurements would be a cubic-centimeter single crystal! Unfortunately, no known processing technique

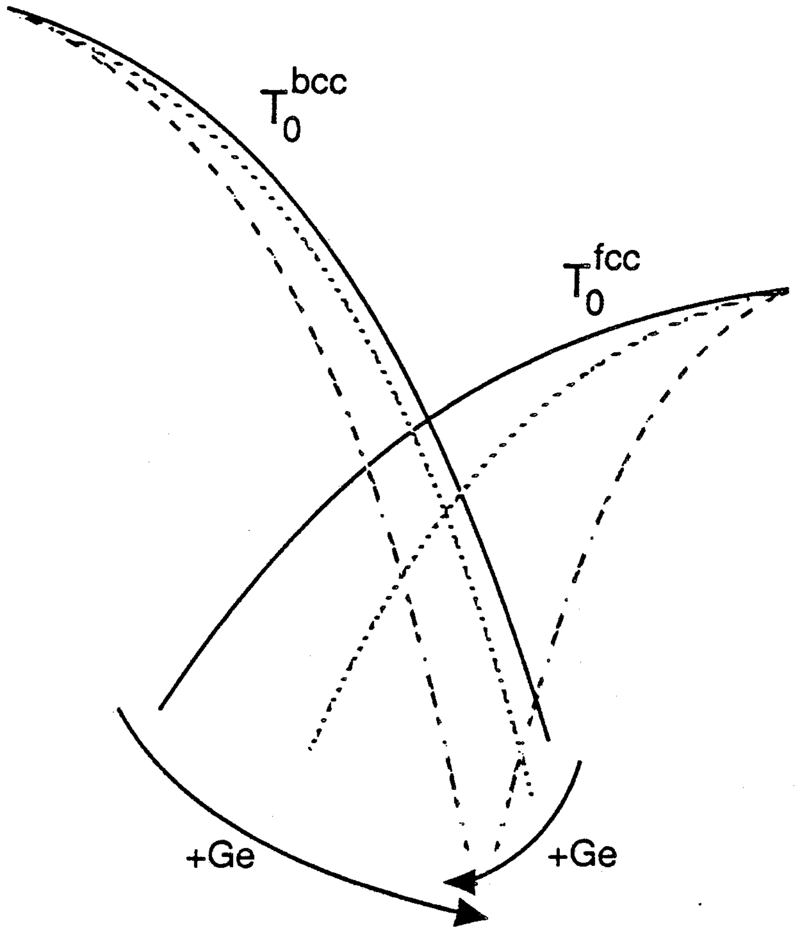

Figure 2.17: Possible influence of Ge concentration on T_0 lines of the bcc and fcc phases. Greater T_0^{fcc} depression causes the crossing point to move to lower Nb concentration (to the right in this diagram). Large Ge concentrations pull both T_0 lines down into a deep eutectic, enabling the amorphous phase to be quenched.

can fabricate such a sample in a nonequilibrium state. Instead, we must make a compromise, choosing one or more sample preparation techniques to produce samples appropriate for as many experimental investigations as possible. Table 2.2 indicates the degree to which the common nonequilibrium synthesis techniques lend themselves to producing samples suitable for each desired measurement. It is evident that splat quenching, hydrogenation and mechanical alloying produce samples amenable to all of the desired nonmechanical tests, but of these three techniques only the samples yielded by splat quenching lend themselves to simple mechanical testing. Unfortunately, the shear modulus, which I shall discuss in the last chapter of the thesis as a quantitative measure of crystalline stability against amorphization, can be determined readily only in vapor-deposited thin films (by Brillouin scattering [65, 66]) and possibly in splat-quenched foils (section 2.5.1), although directionally averaged phonon dispersion curves of a powder sample can be measured by inelastic neutron scattering [67].

2.5 Assessment of synthesis techniques of supersaturated solid solutions

In the following few sections I will review the advantages and disadvantages of the common nonequilibrium crystal processing methods in regard to their ability to fabricate supersaturated solid solutions. Three of the techniques (vapor deposition, splat quenching and mechanical alloying) were described in section 2.3.2, while the remaining two (implantation and hydrogenation) will be introduced in the appropriate section below and, in the case of hydrogenation, explained in more detail later in the thesis (Chapter 3). The synthesis methods are grouped according to the mechanism by which they accomplish supersaturation. A tabular comparison of the strengths and weaknesses of each technique is found in Table 2.3.

Property	Nonequilibrium alloy synthesis techniques				
	Vapor Deposition	Splat Quenching	Implantation	Hydrogenation	Mechanical Alloying
lattice parameter	+	+	+	+	+
strain	•	+	•	+	+
atomic MSD[a]	−	•	•	+	+
thermal expansion	•	+	•	−	•
heat capacity	−	+	−	•	•
shear modulus	•	−	•	−	−
Young's modulus	•	•	•	−	−

[a] MSD = mean-square displacement

Table 2.2: Rating of synthesis techniques with respect to the suitability of the sample geometry for measurement of the indicated structural, thermodynamic and mechanical properties. Plus (+) signifies that the sample lends itself to the corresponding measurement, minus (−) indicates that it does not, and dot (•) means that such a measurement would be difficult but possibly feasible.

Technique	Advantages[a]	Disadvantages[a]
vapor deposition	A, B, C	d1, d2, e, f
splat quenching	A, B, D1, D2, E	c, f
implantation	A, B, F, G	c, d1, d2
hydrogenation	B, C, D2, F, G	a, d1
mechanical alloying	A, D2, F	b, c, d1, e

[a]KEY:

Advantages		Disadvantages	
A.	wide range of alloy combinations	a.	limited range of alloy combinations
B.	minimal impurity concentration	b.	significant impurity concentration
C.	good microstructure uniformity	c.	poor microstructure uniformity
D1.	convenient sample geometry for mechanical property measurements	d1.	inconvenient sample geometry for mechanical property measurements
D2.	convenient sample geometry for nonmechanical property measurements	d2.	inconvenient sample geometry for nonmechanical property measurements
E.	slow quench rate avoids glass formation	e.	quench rate so fast that supersaturation is limited by amorphous phase formation
F.	start from crystalline state ⇒ can extend beyond T_0 line	f.	must nucleate crystal from noncrystalline state ⇒ cannot extend beyond T_0 line
G.	fast interdiffusion at low temperature avoids amorphous phase formation		

Table 2.3: Assessment of synthesis techniques for preparing highly supersaturated solid solutions.

2.5.1 Methods exploiting time-scale differences

Rapid cooling: vapor deposition and splat quenching

If a liquid or vapor is cooled rapidly enough, the atoms may not have enough time to segregate by diffusion or organize themselves collectively into separate phases before losing their mobility; instead, they may crystallize into the one phase that is easiest to form for kinetic and/or thermodynamic reasons. Rapid cooling often leads to supersaturation because the nucleation and growth of a crystalline phase from a vapor condensing on a thin-film surface or in an undercooled liquid can be so much faster than the atomic diffusion necessary for solute segregation, since partitionless crystallization requires no long-range atomic diffusion. Both vapor deposition and splat quenching can be used on an almost unlimited variety of alloy systems, and the samples that each produces are generally free of contamination by impurities. Vapor-deposited thin films usually have uniform thickness and a columnar microstructure oriented perpendicular to substrate that is caused by self-shadowing effects at the film surface [68]. The shadowing creates regions between the columns of lower density than those within the columns but having the same chemical composition, so this effect does not influence the amount of supersaturation or most bulk properties. Splat-quenched foils typically have a more complicated microstructure caused by the gradation of cooling rate across the sample and as a function of foil thickness [55]. The slower cooling rate of splat quenching in comparison to that of vapor deposition, on the other hand, often prevents glass formation, thus extending the supersaturation range. The maximum supersaturation attainable by either technique is limited by the T_0 line because the crystalline phase must be nucleated and grown from a noncrystalline phase (except possibly if it can be grown epitaxially on a crystalline substrate)—if the composition is beyond that given by the T_0 line, there will be no driving force for nucleation and growth of the crystalline phase, and a glass will be formed (if phase separation is suppressed). Finally, as indicated in Table 2.2 of the previous section, the thin-film sample geometry of vapor deposition is poorly suited to density and heat capacity measurements and can present a challenge for mean-square displacement evaluation (from the Debye-Waller factor) because of significant texturing. Splat-quenched foils are suitable for all of the measurements of Table 2.2, although determining their elastic moduli is difficult: while the Young's modulus can be evaluated with some care by the vibrating-reed technique [69], determination of the shear modulus by ultrasonic techniques [70] would require a shear transducer of extremely high frequency ($\gtrsim 50\,\mathrm{MHz}$ [71]) and special high-speed detection equipment. The technique used to measure shear moduli of thin films, Brillouin scattering, is not well adapted for use with foils because signals passing through the foil and bouncing off the other side become too attenuated by the greater travel distance. It may be possible, however, to adapt a technique developed by R. B. Schwarz at Los Alamos involving a frequency-modulated magnetostrictive coating to measure both shear and Young's moduli in splat-quenched foils [72].

Diffusion asymmetry: implantation and hydrogenation

Instead of trying to find the "window" of cooling rates in which quenching is fast enough to prevent solute segregation but slow enough to avoid glass formation, one can take an alternative approach in which solute atoms are introduced into a solvent matrix in such a way that they incorporate themselves directly into the crystal structure rather than segregating into separate phases. Two experimental realizations of this approach are implantation and hydrogenation: in both cases, the diffusion rate of solute atoms is many orders of magnitude higher than that of the matrix atoms under the sample preparation conditions. In *implantation,* solute atoms are accelerated to high velocity and shot—like bullets from a gun—

into a sample (usually a thin film) made of the matrix element(s). Depending on considerations of both kinetics and thermodynamics [73], the incoming atoms can come to rest in interstitial sites of the lattice, or they can replace matrix atoms substitutionally. It is experimentally found that upon reaching a critical concentration, the incident atoms can cause the film to become partially or completely amorphous (see section 1.1.5). *Hydrogenation* works in a similar manner as implantation but avoids the problems associated with radiation damage to the matrix. Since hydrogen atoms are so much smaller than metal atoms, hydrogen atoms diffuse much more rapidly in metals than metals themselves do [74, 75], enabling the hydrogen atoms to incorporate themselves into interstitial sites in the lattice of the host metal at temperatures too low to permit metal atom diffusion. If there is no barrier to hydrogen on the surface of the metal matrix, then the host crystal can be saturated with hydrogen merely by annealing it at low temperature in an atmosphere of hydrogen gas at high pressure; the higher the gas pressure, the higher will be the hydrogen concentration in the crystal because the chemical potential of hydrogen in the solid must equilibrate to that of the gas (see section 3.2.4). Certain materials become amorphous upon absorbing high concentrations of hydrogen during anneals at rather modest temperatures [76], a phenomenon that is studied in detail in the following chapter.

The main advantage that these supersaturation techniques hold over vapor deposition and splat quenching is that implantation and hydrogenation start with the desired crystalline structure already formed. They do not need to nucleate and grow it from a phase with different symmetry. Thus, they can in principle achieve supersaturations beyond the T_0 line (though not beyond the postulated critical composition c^* at which the T_0 line has vertical slope) because there is no need to have a driving force in the form of a free energy difference for nucleation and growth of the crystal from another phase. Furthermore, fast solute diffusion in a crystal held at temperatures too low to permit thermally activated matrix atom diffusion avoids the competing process of glass formation that limits supersaturation ranges in vapor deposition and splat quenching. Implantation and hydrogenation introduce little or no impurities during sample preparation. While there are no fundamental limitations on alloy combinations suitable for implantation, the usefulness of hydrogenation is limited to those alloys and intermetallic compounds that have nonzero hydrogen solubilities; otherwise, the increase in hydrogen concentration attainable by raising the gas pressure during annealing will be too small to measure. The microstructure of a hydrogenated crystal is quite uniform because of the ease with which hydrogen atoms can diffuse to smooth out concentration fluctuations; such solute diffusion is not possible in implanted crystals once the incident solute atoms have lost their translational energy and settled into a lattice position, making sample homogeneity a sensitive function of the dose profile. To supersaturate regions that are thicker than the profile of a single dose requires overlapping of subsequent doses, which increases the difficulty of creating a homogeneous sample. Finally, the thin-film sample geometry of supersaturated solid solutions made by implantation is inconvenient for both mechanical and nonmechanical measurements, especially given the further complication of sample inhomogeneity. Making mechanical tests on samples supersaturated with hydrogen can be difficult because of their generally brittle nature; in fact, most crystals break up into a fine powder upon hydrogen absorption because of the strain energy induced by the volume expansion needed to accommodate the interstitial hydrogen atoms. Such a powder presents no problems for nonmechanical testing, however, as long as the hydrogen stays in the powder at the temperatures of interest; if it does not, then the measurements can be made with the powder in sealed containers (see sections 3.2.3 and 3.2.4) or the surfaces can, perhaps, be oxidized or otherwise "poisoned" in order to form a barrier preventing hydrogen escape [77].

2.5.2 Method employing mechanical intermixing

The last common synthetic technique for extending solubility limits is mechanical alloying. As described above (sections 1.1.3 and 2.3.2), this process achieves alloying by forcing interdiffusion between two components in the solid state through severe deformation and mutual cold welding, but the exact mechanism for the alloying is not presently understood. There are no fundamental limitations on alloy combinations that can be made by milling, though harder elements and intermetallics are always contaminated by wear debris from the milling vial and balls [78]. While mechanical alloying shares the advantage with implantation and hydrogenation of having the desired crystal structure present from the start, the range of amorphous phase formation by ball milling in many binary systems is as wide as that of vapor deposition [44], resulting in little or no additional supersaturation of crystalline phases over that achieved by vapor deposition [cf. ball milling of Nb–Pd (section 2.3.2)]. Furthermore, sample uniformity is particularly suspect in ball-milled powders: the range of grain sizes is quite wide (at least one order of magnitude) even after the average has stopped changing [79] and both alloyed and unalloyed wear debris is found in increasing concentration as the milling progresses [38]. The limitations imposed by powder samples on measurements are the same as described above with hydrogenated powders: not well suited for mechanical measurements but fine for structural analysis, heat capacity determination and thermal expansion measurement (by diffraction only).

2.5.3 Optimized sample preparation

Comparison of the various supersaturation techniques (Tables 2.2 and 2.3) points to the general superiority of splat quenching for our particular experimental purposes. The solubility extension attainable by splat quenching may be limited by the modest cooling rate (in comparison to that of vapor deposition, for instance), but this characteristic serves to avoid equally undesirable glass formation. Most importantly, splat-quenched foils are suitable for a wider variety of measurements than the samples produced by any other technique. A detailed study of the properties of supersaturated Nb–Pd alloys prepared by splat quenching is found in Chapter 4.

While limited to far fewer systems than splat quenching, hydrogenation has the significant advantage of starting from the crystalline phase already present, thus avoiding the problem of nucleating and growing it at high supersaturation. This makes it possible, at least in theory, to extend solubility limits beyond the T_0 line. As a complement to the splat quenching of Nb–Pd alloys, we performed a study of hydrogenated $ErFe_2$ and its stability against amorphization (Chapter 3).

References

[1] H. J. Fecht and W. L. Johnson, *Nature (London)* **334**, 50 (1988).

[2] T. B. Massalski, in *Proceedings of the 4th International Conference on Rapidly Quenched Metals,* edited by T. Masumoto and K. Suzuki (Japan Institute of Metals, Sendai, Japan, 1982), Vol. I, pp. 203–208.

[3] J. W. Cahn, S. R. Coriell and W. J. Boettinger, in *Laser and Electron Beam Processing of Materials,* edited by C. W. White and P. S. Peercy (Academic, New York, 1980), pp. 89–103.

[4] L. Katgerman, *J. Mater. Sci. Lett.* **2**, 444 (1983).

[5] K. N. Ishihara and P. H. Shingu, *Scripta Metall.* **16**, 837 (1982).

[6] P. Gressin, N. Eustathopoulos and P. Desre, *Scripta Metall.* **17**, 711 (1983).

[7] R. B. Schwarz, P. Nash and D. Turnbull, *J. Mater. Res.* **2**, 456 (1987).

[8] William C. Giessen, *Bull. Alloy Phase Diagrams* **1**(1), 43 (1980).

[9] L. Kaufman, *CALPHAD* **2**, 117 (1978).

[10] J. L. Murray, *Bull. Alloy Phase Diagrams* **4**, 81 (1983).

[11] N. Saunders, *CALPHAD* 9, 297 (1985).

[12] *Binary Alloy Phase Diagrams,* edited by Thaddeus B. Massalski, Hiroaki Okamoto, P. R. Subramanian and Linda Kacprzak (ASM International, Materials Park, OH, 1990).

[13] T. B. Massalski, in *Physical Metallurgy,* 3rd ed., edited by R. W. Cahn and P. Haasen (Elsevier, Amsterdam, 1983), Part 1, Chap. 4.

[14] J. A. Alonso and N. H. March, *Electrons in Metals and Alloys,* (Academic, New York, 1989), pp. 265–285.

[15] J. T. Waber, K. A. Gschneidner, A. C. Larson and M. Y. Prince, *Trans. Metall. Soc. AIME* **227**, 717 (1963).

[16] A. Taylor, *X-ray Metallography,* Wiley (New York, 1961, pp. 332–336).

[17] T. B. Massalski, in *Physical Metallurgy,* 3rd ed., edited by R. W. Cahn and P. Haasen (Elsevier, Amsterdam, 1983), Part 1, pp. 176–178.

[18] J. A. Alonso and N. H. March, *Electrons in Metals and Alloys,* (Academic, New York, 1989), pp. 265–268.

[19] T. Egami and Y. Waseda, *J. Non-Cryst. Solids* **64**, 113 (1984).

[20] C. E. Krill III, presented at the SCANNING '89/EM West joint conference, Long Beach, CA, April 1989 (unpublished).

[21] W. D. Westwood, *MRS Bull.* **13**(12), 46 (1988).

[22] S. R. Elliott, *Physics of Amorphous Materials,* 2nd ed. (Longman Scientific & Technical, Essex, England, 1990), p. 18.

[23] David Turnbull, *Metall. Trans. A* **12A**, 695 (1981).

[24] *Binary Alloy Phase Diagrams,* edited by Thaddeus B. Massalski, Hiroaki Okamoto, P. R. Subramanian and Linda Kacprzak (ASM International, Materials Park, OH, 1990), Vol. 2, pp. 1580–1581.

[25] V. E. Kolesnikov, V. F. Trekhova and E. M. Savitskii, *Izv. Akad. Nauk SSSR, Neorg. Mater.* **7**, 495 (1971) [*Inorg. Mater. (USSR)* **7**, 433 (1971)].

[26] S. H. Liou and C. L. Chien, *Phys. Rev. B* **35**, 2443 (1987).

[27] P. H. Gaskell, L. A. Freeman and David J. Smith, in *Proceedings of the Fourth International Conference on Rapidly Quenched Metals,* edited by T. Masumoto and K. Suzuki (Japan Institute of Metals, Sendai, Japan, 1982), Vol. I, pp. 439–442.

[28] P. Villars and L. D. Calvert, *Pearson's Handbook of Crystallographic Data for Intermetallic Phases,* (ASM, Metals Park, OH, 1985), Vol. 3, p. 2098.

[29] Harold P. Klug and Leroy E. Alexander, *X-ray Diffraction Procedures for Polycrystalline and Amorphous Materials,* 2nd ed. (Wiley, New York, 1974), Chap. 8.

[30] M. S. Chandrasekharaiah, *Bull. Alloy Phase Diagrams* **9**, 449 (1988).

[31] *Binary Alloy Phase Diagrams,* edited by Thaddeus B. Massalski, Hiroaki Okamoto, P. R. Subramanian and Linda Kacprzak (ASM International, Materials Park, OH, 1990), Vol. 3, pp. 2751–2753.

[32] B. C. Giessen, N. J. Grant, D. P. Parker, R. C. Manuszewski and R. M. Waterstrat, *Metall. Trans. A* **11A**, 709 (1980).

[33] R. Coehoorn, G. J. van der Kolk, J. J. van den Broek, T. Minemura and A. R. Miedema, *J. Less-Common Met.* **140**, 307 (1988).

[34] G. J. van der Kolk, T. Minemura and J. J. van den Broek, *J. Mater. Sci.* **24**, 1895 (1989).

[35] T. Minemura, G. J. van der Kolk and J. J. van den Broek, *J. Less-Common Met.* **153**, 151 (1989).

[36] A. W. Weeber and H. Bakker, *Physica B* **153**, 93 (1988).

[37] D. R. Maurice and T. H. Courtney, *Metall. Trans. A* **21A**, 289 (1990).

[38] J. Eckert, J. C. Holzer, C. E. Krill III and W. L. Johnson, *J. Mater. Res.* (in press).

[39] T. Fukunaga, K. Nakamura, K. Suzuki and U. Mizutani, *J. Non-Cryst. Solids* **117/118**, 700 (1990).

[40] T. Fukunaga, M. Mori, K. Inou and U. Mizutani, *Mater. Sci. Eng. A* **134**, 863 (1991).

[41] K. Uenishi, K. F. Kobayashi, S. Nasu, H. Hatano, K. N. Ishihara and P. H. Shingu, *Z. Metallk.* **83**, 132 (1992).

[42] J. Eckert, R. Birringer, J. C. Holzer, C. E. Krill III and W. L. Johnson, in *Structure and Properties of Interfaces in Materials,* edited by W. A. T. Clark, C. L. Briant and U. Dahmen (Mater. Res. Soc. Symp. Proc. **238**, Pittsburgh, PA, in press).

[43] Carl C. Koch, *J. Non-Cryst. Solids* **117/118**, 670 (1990).

[44] K. Matsuki, A. Inoue, H. M. Kimura and T. Masumoto, *Mater. Sci. Eng.* **97**, 47 (1988).

[45] E. Hellstern and L. Schultz, *Appl. Phys. Lett.* **48**, 124 (1986).

[46] A. R. Yavari, P. J. Desré and T. Benameur, *Phys. Rev. Lett.* **68**, 2235 (1992).

[47] J. Eckert, J. C. Holzer, C. E. Krill III and W. L. Johnson, *J. Appl. Phys.*, (submitted).

[48] T. G. Nieh and J. Wadsworth, *Scr. Metall. Mater.* **25**, 955 (1991).

[49] Steve Hwang, report on 1990 SURF research project (unpublished).

[50] C. E. Krill III and W. L. Johnson, in *Kinetics of Phase Transformations,* edited by Michael O. Thompson, Michael J. Aziz and G. Brian Stephenson (Mater. Res. Soc. Symp. Proc. **205**, Pittsburgh, PA, 1992), pp. 313–318.

[51] R. W. Cahn, in *Physical Metallurgy,* 3rd ed., edited by R. W. Cahn and P. Haasen (Elsevier, Amsterdam, 1983), Part 2, Chap. 28.

[52] H. Jones and C. Suryanarayana, *J. Mater. Sci.* **8**, 705 (1973).

[53] C. Suryanarayana, *Rapidly quenched metals: a bibliography, 1973–1979,* (IFI/Plenum, New York, 1980).

[54] S. J. Savage and F. H. Froes, *J. Met.* **36**(April), 20 (1984).

[55] H. Jones, *Rapid Solidification of Metals and Alloys,* (The Institution of Metallurgists, London, 1982).

[56] J. L. Jorda, R. Flükiger and J. Müller, *J. Less-Common Met.* **62**, 25 (1978).

[57] *Binary Alloy Phase Diagrams,* edited by Thaddeus B. Massalski, Hiroaki Okamoto, P. R. Subramanian and Linda Kacprzak (ASM International, Materials Park, OH, 1990), Vol. 2, pp. 1981–1982.

[58] K. Khalaff and K. Schubert, *Z. Metallk.* **65**, 279 (1974).

[59] *Binary Alloy Phase Diagrams,* edited by Thaddeus B. Massalski, Hiroaki Okamoto, P. R. Subramanian and Linda Kacprzak (ASM International, Materials Park, OH, 1990), Vol. 2, pp. 1971–1972.

[60] Harold P. Klug and Leroy E. Alexander, *X-ray Diffraction Procedures for Polycrystalline and Amorphous Materials,* 2nd ed. (Wiley, New York, 1974), Chap. 9.

[61] K. F. Kelton, in *Solid State Physics,* edited by Henry Ehrenreich and David Turnbull (Academic, San Diego, 1991), Vol. 45, pp. 75–177.

[62] D. Turnbull, *J. Appl. Phys.* **21**, 1022 (1950).

[63] W. Klement, R. H. Willens and P. Duwez, *Nature (London)* **187**, 869 (1960).

[64] M. H. Cohen and D. Turnbull, *Nature (London)* **189**, 131 (1961).

[65] John R. Dutcher, Sukmock Lee, Jeha Kim, John A. Bell, George I. Stegman and Charles M. Falco, *Mater. Sci. Eng.* **B6**, 199 (1990).

[66] P. R. Okamoto, L. E. Rehn, J. Pearson, R. Bhadra and M. Grimsditch, *J. Less-Common Met.* **140**, 231 (1988).

[67] C. Stassis, in *Neutron Scattering,* Part A, edited by Kurt Sköld and David L. Price, Methods of Experimental Physics, Vol. 23 (Academic, New York, 1986), Chap. 6.

[68] A. G. Dirks and H. J. Leamy, *Thin Solid Films* **47**, 219 (1977).

[69] Lowell Hazelton, Ph. D. thesis, California Institute of Technology, 1985.

[70] E. R. Fuller, Jr., A. V. Granato, J. Holder and E. R. Naimon, in *Solid State Physics,* edited by Robert Vincent Coleman, Methods of Experimental Physics, Vol. 11 (Academic, New York, 1974), Chap. 7.

[71] Panametrics, 221 Crescent St., Waltham, MA 02154-3497, (617) 899-2719 (private communication).

[72] R. B. Schwarz (private communication).

[73] J. A. Alonso and N. H. March, *Electrons in Metals and Alloys,* (Academic, New York, 1989), pp. 281–285.

[74] K. W. Kehr, in *Hydrogen in Metals I,* edited by G. Alefeld and J. Völkl, Topics in Applied Physics, Vol. 28 (Springer-Verlag, New York, 1978), Chap. 8.

[75] J. Völkl and G. Alefeld, in *Hydrogen in Metals I,* edited by G. Alefeld and J. Völkl, Topics in Applied Physics, Vol. 28 (Springer-Verlag, New York, 1978), Chap. 12.

[76] Robert C. Bowman, Jr., *Mater. Sci. Forum* **31**, 197 (1988).

[77] G. E. Fish, J. J. Rhyne, S. G. Sankar and W. E. Wallace, *J. Appl. Phys.* **50**, 2003 (1979).

[78] C. E. Krill III, APh 141 final project, 7 June 1991 (unpublished).

[79] C. E. Krill III (unpublished).

Chapter 3

Amorphization of $ErFe_2D_{3.2}$

3.1 Why deuterate $ErFe_2$?

As discussed in the previous chapter, hydrogenation is a promising method for preparing highly nonequilibrium metallic solutions because hydrogen atoms can diffuse into the matrix at temperatures much lower than those at which the metal atoms may move, thus preserving the desired crystalline structure. The small size of hydrogen atoms permits them to occupy interstitial sites in the metal lattice, but not without inducing some volume expansion. The energy needed to expand the lattice is derived from the energy gained from metal-hydrogen bonds. Above a certain hydrogen concentration, however, the lattice can no longer maintain the expanded crystalline structure—consequently, it transforms to another structure or separates into multiple phases.

Surprisingly, upon annealing in a hydrogen atmosphere at temperatures between 25 °C and 250 °C, many intermetallic compounds of the form $A_{1-x}B_x$, where A is a hydride-forming metal and B is a non-hydride-forming metal, collapse to an amorphous phase rather than to one or more crystalline phases (section 1.1.1). Many intermetallic compounds transform directly from the crystalline state with no hydrogen to a hydrogenated amorphous state, while some others first pass through an intermediate crystalline hydride state before becoming amorphous

[1, 2]. $ErFe_2$ is a member of the latter class of compounds: upon being heated in a hydrogen atmosphere, $ErFe_2$ transforms to a crystalline hydride at $\sim 50\,^{\circ}C$ and then to an amorphous phase at $\sim 220\,^{\circ}C$ [2, 3]. If the amorphization of this crystalline hydride occurs at a definite temperature rather than spread over a wide temperature range, then the observed crystal-to-amorphous transformation might provide an experimental manifestation of instability-induced amorphization, as predicted by the polymorphous phase diagram of Fecht and Johnson, for instance [4].

It was these considerations that motivated Fecht, Fu and Johnson [3] to investigate the enthalpy change associated with hydrogen-induced amorphization of $ErFe_2$. They placed a small amount of the crystalline hydride in a sealed capsule and measured the enthalpy change upon heating in a differential scanning calorimeter (DSC). To their surprise, they observed an unusual λ-shaped endothermic signal at $\sim 200\,^{\circ}C$ that seemed to be at least partially reversible. Analysis of the sample by transmission electron microscopy after cooling back to room temperature revealed the presence of amorphous regions, suggesting that the so-called "λ-anomaly" is associated with the crystal-to-amorphous transformation of the crystalline hydride. It is this claim that motivated us to devise experiments to observe the structure of the hydride both below and above the anomaly; our results [5, 6]—while not confirming those of Fecht *et al.*—shed some light on the mechanism of hydrogen-induced amorphization and on the assumptions implicit in the polymorphous phase diagram of Fecht and Johnson.

I begin the chapter by describing how we prepared the crystalline $ErFe_2$ hydride starting material and the methods we chose to study its structure and properties as a function of temperature. Then I briefly discuss the relationship between the crystal structure of $ErFe_2$ and its various hydride phases. In the next section I present the results of a combined DSC and high-temperature neutron diffraction study of the crystal-to-amorphous transition of deuterated $ErFe_2$. The discussion that concludes the chapter addresses the origin of the "λ-anomaly" in the experiment of Fecht *et al.* and then relates our findings to the mechanism of the crystal-to-amorphous phase transition.

3.2 Experimental details

3.2.1 Ingot and deuteride synthesis

Ingots of $ErFe_2$ weighing ~ 5 g were prepared from sublimed, dendritic Er lump (REacton grade, 99.99 %) and vacuum-remelted, low-oxygen Fe lump (REacton grade, 99.99 %) obtained from AESAR/Johnson Matthey [7]. Stoichiometric amounts were weighed out and alloyed by induction melting on a silver boat in an argon atmosphere. Each ingot was subsequently turned over and remelted at least three more times to improve homogeneity. Each ingot was then sealed in helium in a fused silica tube with a piece of titanium to act as an oxygen getter and annealed at $\sim 850\,^\circ$C for at least two days, causing the $ErFe_2$ grain size to grow to a typical diameter of $\gtrsim 200\,\mu$m. The ingot was ground up with a mortar and pestle in an argon atmosphere into a fine powder of particle size $< 44\,\mu$m by sifting through a #325-mesh sieve; since the particle size is smaller than the average grain size, a majority of particles will be single crystals of $ErFe_2$. (This step was performed to guard against possible distortion of enthalpy signals arising from grain boundaries.) The powder particles were then placed in a fused-silica tube connected to a cylinder of deuterium (C.P. grade 99.5 % or research grade 99.99 %)—deuterium was used instead of hydrogen to improve the signal-to-background level in neutron diffraction (section 3.2.3). After repeated evacuation and purging of the tube with deuterium, the gas pressure was raised to approximately 85 psi (5.9×10^5 Pa), and a tube furnace was placed around the silica tube. The deuterium pressure was maintained at 85 psi while the temperature of the powder in the tube was raised to 180–200 °C for at least eight hours and then cooled slowly to room temperature. Uptake of deuterium was observed to occur very quickly, often even at room temperature. Although oxidation of the surface of the deuterated powder upon exposure to air renders the powder stable with respect to deuterium desorption at room temperature (as confirmed by direct measurement—see section 3.2.4), the powder was kept in a sealed container at all times as a precautionary measure. Chemical analysis of the deuterium concentration in samples prepared by this procedure found ~ 3.2 D atoms per $ErFe_2$ formula unit.

3.2.2 X-ray diffraction characterization

X-ray diffraction was used to characterize the $ErFe_2$ powder before and after deuteration. Diffraction scans with excellent signal-to-background ratios were obtained from an INEL 120° (2θ) position-sensitive detector mounted in Debye-Scherrer geometry [8] with monochromated Co Kα radiation. Cobalt radiation ($\lambda = 0.17903\,\mathrm{nm}$ [9]) is a better choice for these samples than the more commonly used Cu radiation because Co-Kα photons do not excite fluorescence radiation in Fe, as those of Cu do [10]. For the diffraction measurements powder samples were mounted on glass slides with Formvar$^{\mathrm{TM}}$ and held at a fixed incident angle of ~ 15°. Bragg peaks from both $ErFe_2$ and $ErFe_2D_{3.2}$ were very sharp, confirming the presence of large grains [11]. No evidence for any secondary phases could be found in the $ErFe_2$ scans or in most taken of $ErFe_2D_{3.2}$; a second deuteride phase in one batch of $ErFe_2D_{3.2}$ was made to disappear by repeating the anneal in a deuterium atmosphere.

3.2.3 High-temperature elastic neutron diffraction

At temperatures above $\sim 160\,^\circ\mathrm{C}$ the surface oxide of the $\mathrm{ErFe_2D_{3.2}}$ powder breaks down, allowing deuterium to escape from the solid (section 3.2.4); therefore, the only way that deuterium can be kept in the solid during high-temperature measurements is by containing the powder in a closed cell. This experimental constraint makes high-temperature x-ray diffraction almost impossible, since the candidate materials for making a sample enclosure—materials that scatter x-rays only weakly, such as beryllium or other elements with low atomic number—are either structurally rather weak or difficult to machine into a leak-tight container. In contrast, neutrons, which have much smaller scattering cross-sections than x-rays and, consequently, longer penetration depths, place no serious restrictions on cell construction. The desire to study the structure of $\mathrm{ErFe_2D_{3.2}}$ near the "λ-anomaly" at $\sim 200\,^\circ\mathrm{C}$ thus led us to perform elastic neutron diffraction on the deuterated powder enclosed in a stainless-steel sample cell to be described below.

We made the elastic neutron diffraction measurements on the powder diffractometer at the Missouri University Research Reactor (MURR) utilizing neutrons of wavelength 0.154720 nm and a position-sensitive detector arranged in Debye-Scherrer geometry [8] that covered a 2θ angular range of 20°. Normalization of individual 20° scan sections for later combination into a wide-range scan is facilitated by the ease of measuring the incident neutron flux I_0: a low-efficiency detector is placed in the incident beam to measure a fixed fraction of I_0 during data collection at a given PSD position; because of the weak interaction between neutrons and the detector material, the incident beam is not seriously attenuated by the detector. Once the number of detected neutrons in the incident beam reaches a preset value, the goniometer is rotated by 20°, the data from the previous scan are stored and a new scan is begun. By this method, diffraction scans from 5° to 105° 2θ could be measured in a sequence of five steps.

Another advantage of neutron diffraction over x-ray diffraction for our purposes is the fact that neutrons scatter from light elements (i.e., those with atomic number $Z \lesssim 6$) with roughly the same amplitude as from heavy elements [12], while the amplitude of x-ray scattering is proportional to Z [13]. The difference is most pronounced with hydrogen, for which position determination by x-ray diffraction is practically impossible. Unfortunately, the common isotope of hydrogen (atomic mass number $A = 1$) is difficult to study by neutron diffraction, as well, because nuclear spin incoherence of H leads to a high background level, thus swamping out Bragg peaks from the sample in the noise from the counting statistics. The problem is especially acute with $ErFe_2H_x$, since for $x \approx 3$, the density of hydrogen in the solid is greater than that in liquid hydrogen! This difficulty can be sidestepped by replacing the hydrogen atoms with their heavier isotope, deuterium ($A = 2$), which has a much smaller incoherent neutron scattering cross section [12, 14, 15]. This is why we studied deuterated $ErFe_2$ rather than hydrogenated $ErFe_2$, as in the original experiment of Fecht *et al.* The effect of such a substitution on sample properties is often negligible; for example, the isotope effect on the pressure-composition isotherms of hydrogenated $ErFe_2$ was found to be quite small [16].

As mentioned above, it was necessary to seal the deuterated powder in order to prevent loss of deuterium in the sample during diffraction scans at temperatures above ~160 °C. To accomplish this, we constructed a sample holder able to withstand the buildup of pressure that may accompany the increase in chemical potential of the solid-phase deuterium with temperature. This pressure rise can conceivably be enormous: for a sample density of $8\,\mathrm{g/cm^3}$, volume packing fraction of 10 %, temperature of 200 °C and drop in number of deuterium atoms per $ErFe_2$ formula unit from 3.2 to 2.8, simple application of the ideal gas law predicts a pressure increase in excess of 20 atmospheres (2.03×10^6 Pa)! With this in mind, we designed the sample cell sketched in Fig. 3.1. The construction of the container not only had to be strong, but also the materials had to be impervious to deuterium gas when heated as high as 300 °C. For these purposes, we chose 1/8″ (3.18 mm) o.d. 304 stainless steel tubing with a wall thickness of 0.020″ (0.51 mm) and had it heli-arc welded to a mounting block on one end and to a "mini" [1.33″ (3.38 cm) diameter] Conflat$^{\mathrm{TM}}$ flange on the other, both also made of 304 stainless. The flange was sealed using a copper gasket. When the sample holder was filled to tap density, it held approximately 850 mg of $\mathrm{ErFe_2D_{3.2}}$. Because the sample holder is located next to the sample powder, a diffraction scan of the sample will include strong Bragg peaks from the stainless steel, most of which could be distinguished from those of the sample by their much greater intensity. In order to identify weaker stainless steel diffraction peaks, we made a scan of the empty sample holder.

The heating unit surrounding the sample holder was designed by the staff at MURR. It consisted of two resistance heating coils that surrounded the upper and lower portions of the sample holder, a vanadium tube that acted as a heat shield to improve temperature homogeneity and an aluminum case that enabled the interior to be evacuated. Temperature measurement was made with a Chromel-Alumel (type K) thermocouple in contact with the bottom of the sample holder. The temperature controller could keep the cell within ±2 °C of the setpoint, but only after the unit was allowed to equilibrate. Unfortunately, equilibration took from one to two hours in the temperature region in which we operated and was often impossible to achieve at temperatures below 100 °C. Upon changing the temperature setpoint, the controller always caused an overshoot of 10 °C or more, even for small setpoint changes, though the magnitude of temperature oscillations dropped off steadily after the initial overshoot. While the long equilibration time

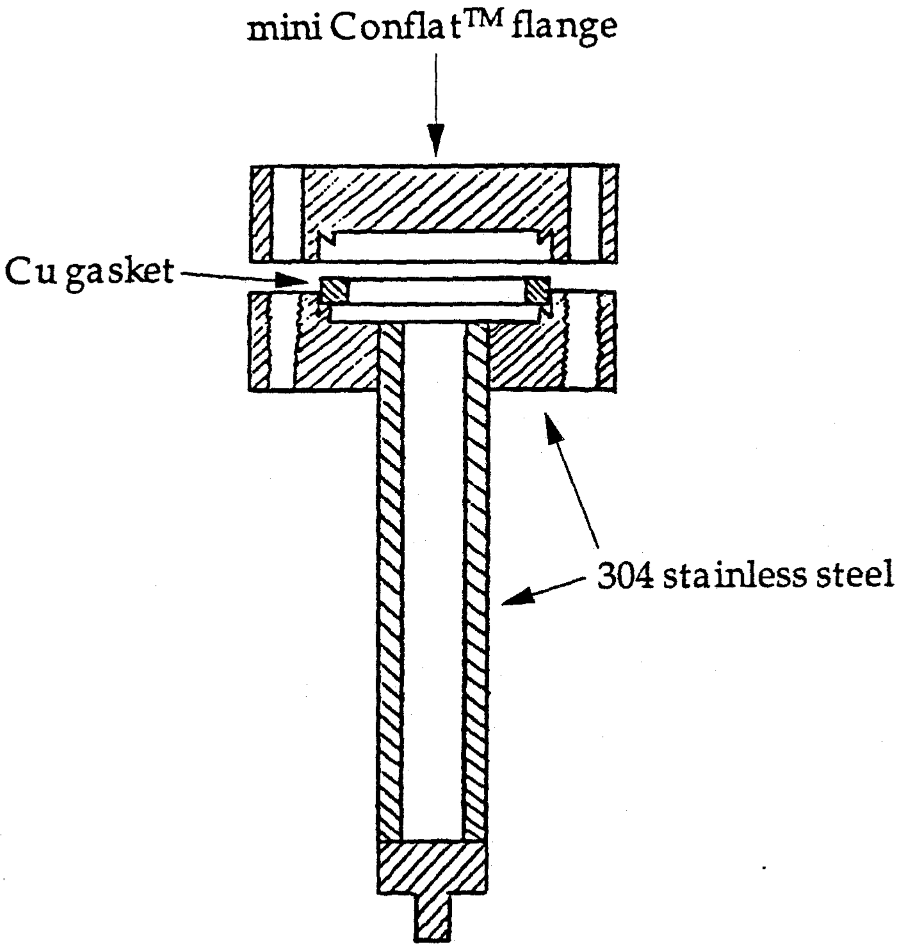

Figure 3.1: Stainless-steel sample cell for neutron diffraction of deuterium-containing powders at elevated temperature. Neither the stainless steel housing nor the copper gasket react with deuterium at the temperatures of interest.

and the overshoot problem affect the *relative* accuracy of temperature difference measurements, the main causes of uncertainty in the *absolute* temperature are the inefficiency of radiation heating in vacuum and the use of only one thermocouple to measure temperature at the sample holder. For these reasons, I estimate that the relative error of our temperature measurements was five degrees or less for differences less than about 100 °C, while the *absolute* uncertainty probably increased from 10 °C at a setpoint of about 100 °C to 20 °C or 30 °C at setpoints above 200 °C. Fortunately, the large magnitude of these uncertainties did not invalidate the high-temperature neutron diffraction measurements when assessed in conjunction with the differential scanning calorimetry results, for which the temperature is much more accurately calibrated.

For the actual neutron diffraction measurements, approximately 850 mg of $ErFe_2D_{3.2}$ powder was sealed in the high-pressure stainless steel sample holder of Fig. 3.1 under a helium atmosphere in a glove bag. Measurements were performed at progressively higher temperatures from $\sim 70\,^\circ C$ to $\sim 250\,^\circ C$. Typically, the sample holder was equilibrated for approximately 30 minutes upon reaching a new temperature, and then a 30–180 minute neutron diffraction scan was measured covering an angular range of 40–80° 2θ. The 30-minute equilibration time was sufficient to reduce the temperature fluctuation of the sample holder to within ±5 °C, although the initial overshoot was usually on the order of 10 °C above the setpoint.

3.2.4 DSC of volatile samples

Another analytic technique that is highly sensitive to transitions in a specimen is differential scanning calorimetry (DSC). *Calorimetry* is the measurement of enthalpy H stored in a material relative to a reference state [for example, a typical reference state used by chemists is standard temperature and pressure (STP):

$0\,^\circ$C and 1 atm (1.01×10^5 Pa) pressure]. *Scanning* refers to the fact that the enthalpy is measured as a function of temperature by raising or lowering the temperature of the sample. Since the temperature is changed at a constant rate, the quantity directly measured is the rate of change of H with time t : dH/dt. Finally, the technique is called *differential* because the actual sample dH/dt is not measured directly; instead, the difference in dH/dt of the sample and of a reference material is measured. This quantity, $d\Delta H/dt = d(H_{\text{sample}} - H_{\text{reference}})/dt$, can be determined very precisely by comparing the power needed to heat the sample and the reference at the same rate. Since the reference material (typically a noble metal like Au) is chosen not to undergo any phase transitions in the temperature range of study, $d\Delta H/dt$ will differ from dH_{sample}/dt only by a continuous, nearly constant function, which can be subtracted away easily.

I performed all DSC measurements on a Perkin-Elmer DSC4 operating between $35\,^\circ$C and temperatures as high as $425\,^\circ$C. Perkin-Elmer DSC's maintain the sample and the reference at identical temperatures by independently adjusting the power input to the heaters of the sample and reference pans. The difference in power supplied to each pan is directly proportional to $d\Delta H/dt$, and the constant of proportionality is determined by integrating the area under the endothermic melting peaks of standard samples with known latent heats of fusion $L_f = (\Delta H)_{\text{melt}}$:

$$(\Delta H)_{\text{melt}} = \int_{T_1}^{T_2} \left(\frac{dH}{dt}\right)_P \left(\frac{dT}{dt}\right)^{-1} dT, \tag{3.1}$$

where T_1 is the onset temperature of the melting transition and T_2 is the completion temperature. Enthalpy uptake (endothermic reaction) or release (exothermic reaction) by the sample between any two temperatures can then be calculated from the measured DSC scan according to the same formula.

Ordinarily, DSC measurements are made on samples in open pans, resulting in measurements of enthalpy change at constant pressure. When the sample contains a volatile component, however, the evolution of gas must be suppressed because (i) the strongly endothermic signal from outgassing may mask other transitions in the sample and (ii) if only one component of the sample is volatile, such as deuterium in $ErFe_2D_{3.2}$, then the composition of the sample will change irreversibly in the DSC during the first heating cycle. Both points (i) and (ii) must be considered when searching for enthalpy changes in $ErFe_2D_{3.2}$ by DSC. For example, Fig. 3.2 shows the open-pan DSC scan of $ErFe_2D_{3.2}$. X-ray diffraction of the sample after cooldown finds a reduced lattice parameter characteristic of pure $ErFe_2$; therefore, we can attribute the large endotherm to evolution of deuterium from the sample. The lack of an endothermic signal at temperatures below $\sim 160\,^{\circ}\mathrm{C}$ confirms that the surface barrier of the powder that prevents the deuterium from escaping remains intact until temperatures well above room temperature are reached.

One method for overcoming the problems caused by the volatility of hydrogen is to place the sample and reference in a deuterium atmosphere of high enough pressure to exceed the vapor pressure of deuterium in the sample throughout the temperature range studied. This is the approach taken by Aoki and colleagues [17, 18, 19] using a high-pressure differential thermal analyzer (DTA). (A DTA instrument performs the same function as a DSC instrument but in a different manner: a DTA maintains a constant heating power to both sample and reference and measures the temperature difference between the two, in contrast to the opposite process used in a DSC.) Lacking such a high-pressure DTA unit, one can maintain a fairly constant sample deuterium concentration by placing the sample in a sealed DSC pan. A small amount of gas evolution will cause a rapid buildup in the deuterium pressure above the sample in the cell until the chemical potential of the gas equilibrates with the chemical potential of the deuterium in the solid. Thus, gas evolution is reduced to the rate necessary to maintain equilibrium as the sample temperature is changed.

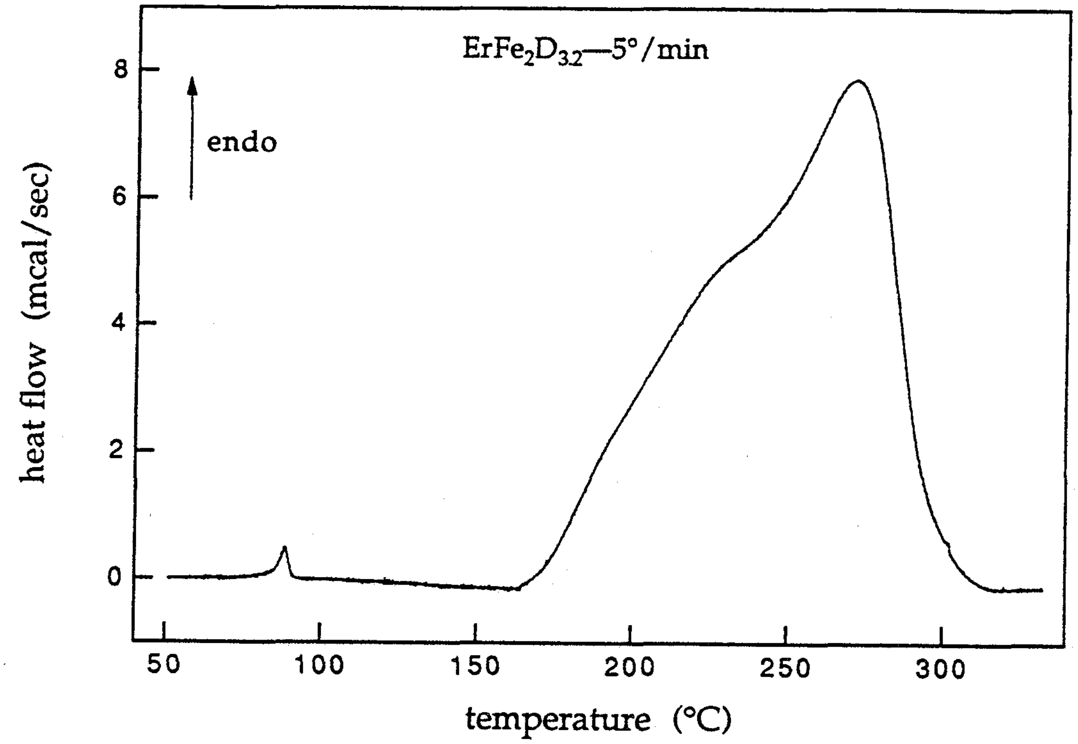

Figure 3.2: DSC trace of $ErFe_2D_{3.2}$ powder in an open aluminum pan. The large exothermic signal is the heat needed to evolve deuterium from the solid phase to the vapor phase. The small bump at low temperature will be explained in section 3.4.1.

It is the latter method that Fecht, Fu and Johnson [3] adopted in their search for the enthalpy signal of amorphization in $ErFe_2H_{3.4}$. They sealed their DSC pans (Perkin-Elmer No. 0219-0062) by pressure-welding the aluminum base and lid; however, such a construction has an interior overpressure rating of only 2 atm (2×10^5 Pa) [20]. As suggested by the calculation in section 3.2.3, a 2 atm increase in pressure in the cell results in only a small change in sample hydrogen concentration; unfortunately, the vapor pressure of $ErFe_2H_{3.4}$ climbs to nearly 10 atm (1×10^6 Pa) at 80 °C [21]! This precludes DSC measurements of $ErFe_2H_{3.4}$ in the pans used by Fecht *et al.* unless some property of the material (such as a surface layer of oxide from reaction with air [22] or with an oxidizing gas like SO_2 [21] or CO [23]) acts as a barrier to hydrogen evolution. As we saw in Fig. 3.2, breakdown of the air-induced oxide layer present on my samples (and on those of Fecht *et al.*) occurs at ~ 160 °C.

Fortunately, Perkin-Elmer manufactures two other models of high-pressure DSC pans: one rated to 25 atm (2.5×10^6 Pa) and the other rated to 150 atm (1.5×10^7 Pa) [24]. We decided for reasons of ease of use [25] to try the 25 atm pans (Perkin-Elmer No. 0319-0218) sketched in Fig. 3.3. The lid and base are constructed of 304 stainless steel and sealed together by a Viton$^{\text{TM}}$ O-ring. The seal is actually made by squeezing the close-fitting lid over the base and O-ring using a hand-held press; since the compressed metal opposes the force generated by internal overpressure, the O-ring must be capable of withstanding only a small force at the seal. Temperature limits of the pan are determined by the glass transition of the Viton rubber at -40 °C [26] and the observed decomposition of the rubber at temperatures $\gtrsim 425$ °C. While no leakage was ever detected from such a pan, it was observed that the pan lid would irreversibly deform when the internal pressure reached a high value, bowing out noticeably. The heat generated by deforming the pan is exactly canceled by the cooling of the gas inside the pan upon expansion

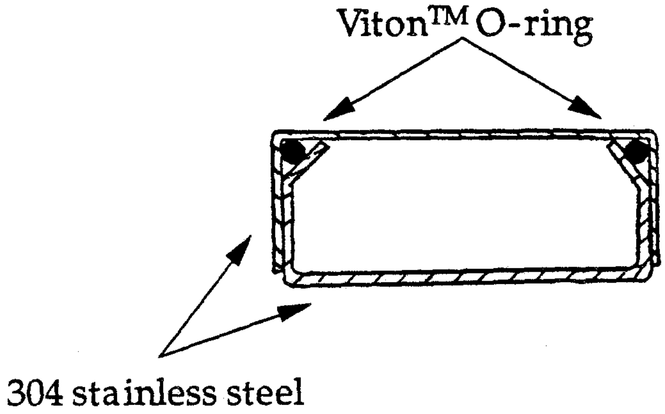

Figure 3.3: High-pressure (25 atm) stainless-steel DSC pan. The usable temperature range is limited by the thermal properties of the Viton O-ring, which makes the seal when compressed between the base and lid. The cell volume exceeds 75 μl.

of the internal volume. Nevertheless, a net endothermic signal (Fig. 3.4) occurs because more gas must be evolved to re-establish equilibrium with the chemical potential of the remaining gas in the solid. When the weight of $ErFe_2D_{3.2}$ powder in the 25-atm DSC pan exceeded $\sim 75\,\mathrm{gm}$, the pan often exploded. Such an event is easily detected in the DSC as an almost instantaneous jump in dH/dt above the range of the most endothermic signal measurable! Since the pressure in the pan is established by equilibration of the deuterium chemical potential in the gas and in the solid, it may seem surprising that explosion of the pan would depend on the amount of sample, since vapor pressure is an intensive quantity characteristic of a material. One must remember, however, that the deuterium in the gas that establishes the gas-solid chemical potential equilibrium must evolve from the solid. Once it leaves the solid, the chemical potential of the hydrogen in the solid decreases, since $\mu_{\mathrm{D}} = (\partial G/\partial N_{\mathrm{D}})_{T,P}$ [27], where N_{D} is the number of deuterium atoms, and this derivative of G generally increases with N_{D}. The less material in the pan, the more the chemical potential will be lowered by the equilibration process, because the concentration change in the solid will be proportionally larger. The chemical potential of the deuterium gas is a monotonically increasing function of pressure P:

$$\mu_{\mathrm{D}_2} = k_{\mathrm{B}}T\left[\log\left(\frac{P}{k_{\mathrm{B}}Tn_Q}\right) - \log Z_{\mathrm{int}}\right], \tag{3.2}$$

where $n_Q = \left(Mk_{\mathrm{B}}T/2\pi\hbar^2\right)^{3/2}$, M is the deuterium mass, and Z_{int} is the partition function of the internal degrees of freedom (rotational and vibrational) [28]. Therefore, a smaller deuterium chemical potential in the solid means a lower equilibrium gas pressure for a given temperature T. Let us now turn the argument around by considering what happens at the pan's pressure limit P_{max}: The temperature at which the gas reaches P_{max} will depend on the chemical potential of the deuterium in the solid. The higher the chemical potential in the solid, the

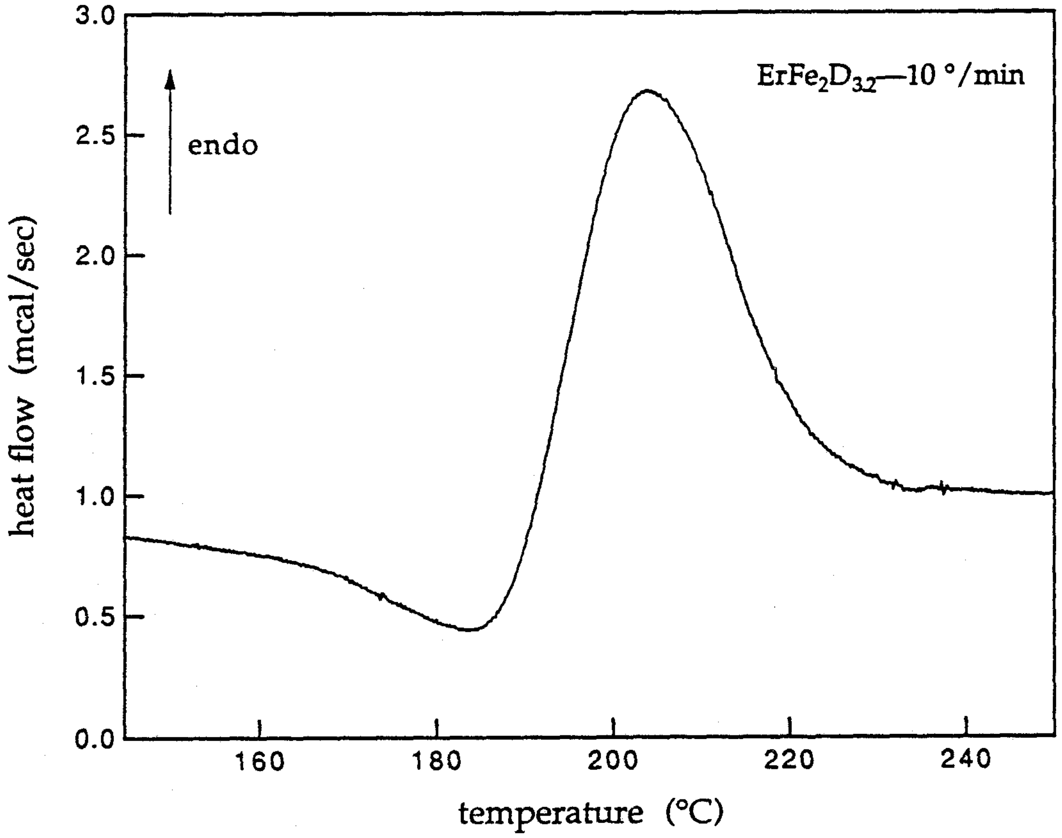

Figure 3.4: Endothermic signal from deformation of a high-pressure DSC pan in response to the buildup of internal pressure upon heating $ErFe_2D_{3.2}$ powder. No such peak is observed on subsequent scans. Pan deformation is concentrated mostly in the lid but does not lead to seal failure until much higher pressures are reached.

lower the temperature at which the gas reaches P_{max}. Since the chemical potential of the deuterium in the solid scales with the amount of sample in the pan, a larger amount of powder in the pan will cause the gas to reach P_{max} at a lower temperature (i.e., more material in the pan means that the equilibrium gas pressure starts out closer to P_{max}).

The experimental protocol followed for each DSC scan was quite simple: First, the 25-atm DSC pan bases and lids were pre-annealed under vacuum to remove volatile surface impurities. Second, from 10 to 100 mg of $ErFe_2D_{3.2}$ powder was sealed in a pan in a helium-filled glove bag; no grease was used on the O-ring. Third, the sample was scanned in the DSC with an empty 25-atm pan base+lid (no O-ring) as a reference. Scanning rates usually ranged from 5–20 °C, though some slower and faster scans were performed as part of a Kissinger analysis (section 3.4.4). Despite the relatively thick pan walls and the relatively poor thermal conductivity of stainless steel, checking the melting point of elemental standards in a 25-atm pan verified that no additional scan rate correction was needed beyond that determined for the standard aluminum DSC pans, even for the fastest scan (80 °C/min) of the Kissinger analysis sequence.

3.3 Structure of $ErFe_2$ and its hydrides

Experiments have demonstrated that the structure of the hydride phases of $ErFe_2$ is strongly influenced by the topology of interstitial sites in its crystal structure [23, 29, 30, 31]. Measurement of the rate of hydrogen evolution from $ErFe_2H_x$, $0 < x \lesssim 4$, found three distinct peaks for $x \gtrsim 3$, implying that hydrogen sites of at least three different binding energies exist in the lattice [23]. While it is conceivable that hydrogen atoms could substitute for metal atoms in the $ErFe_2$ lattice, the fact that x-ray and neutron diffraction experiments find simply an expanded lattice as x increases from 0 to ~ 3 indicates that hydrogen occupies only interstitial sites in the $ErFe_2$ lattice. $ErFe_2$ has the cubic C15 Laves structure ($cF24$) [32] shown in Fig. 3.5 with lattice parameter 0.728 nm [33]. The many interstitial sites available for hydrogen occupation are indicated in Table 3.1. All sites of a given nearest-neighbor quadruple are identical thanks to the cubic symmetry of $ErFe_2$.

Pressure-composition isotherm measurements have detected at least five distinct phases of $ErFe_2H_x$ for $0 < x \lesssim 4$ [16, 35]. There are at least three expanded C15 Laves structure phases for $x \lesssim 3.2$, one rhombohedrally distorted C15 phase for $3.2 \lesssim x \lesssim 4$ and another expanded C15 phase for $x \gtrsim 4$. The hydrogen evolution measurements mentioned above, coupled with recent neutron diffraction work [23, 29, 30, 31], conclude that for $x \lesssim 3$, hydrogen atoms occupy only A_2B_2 sites in a random manner, as expected from the fact that the A_2B_2 sites are larger than the AB_3 and B_4 interstitial sites [30]. Even though the various A_2B_2 sites of a cubic structure are identical, two distinct evolution peaks are found for $1 \lesssim x \lesssim 3$, presumably resulting from the filling geometry of the A_2B_2 sites in the lattice: for $1 < x \leq 2$ each A_2B_2 site that is occupied by a hydrogen atom can be separated by at least a sixth-nearest-neighbor distance, but for $2 < x < 3$, the minimum separation of occupied A_2B_2 drops to a fifth-nearest-neighbor distance [29]. When $x \gtrsim 3.2$, the AB_3 site begins to be populated [23, 29, 30]. The rhombohedral distortion ($\alpha = 91.2°$ [30]) found at this composition breaks the equivalence of the AB_3 sites, resulting in some being larger and the others smaller than in the expanded C15 structure. The hydrogen atoms in AB_3 sites preferentially occupy the larger sites for energetic reasons (less strain energy). Thus, the loss of cubic symmetry enables the crystal to lower its overall strain energy by ordering the AB_3 hydrogens. As x approaches 4, however, the amount of rhombohedral distortion is observed to decrease [23, 29] until at $x \approx 4$, the lattice is cubic once again, probably because some of the smaller AB_3 sites must be filled in order to accommodate the extra hydrogen.

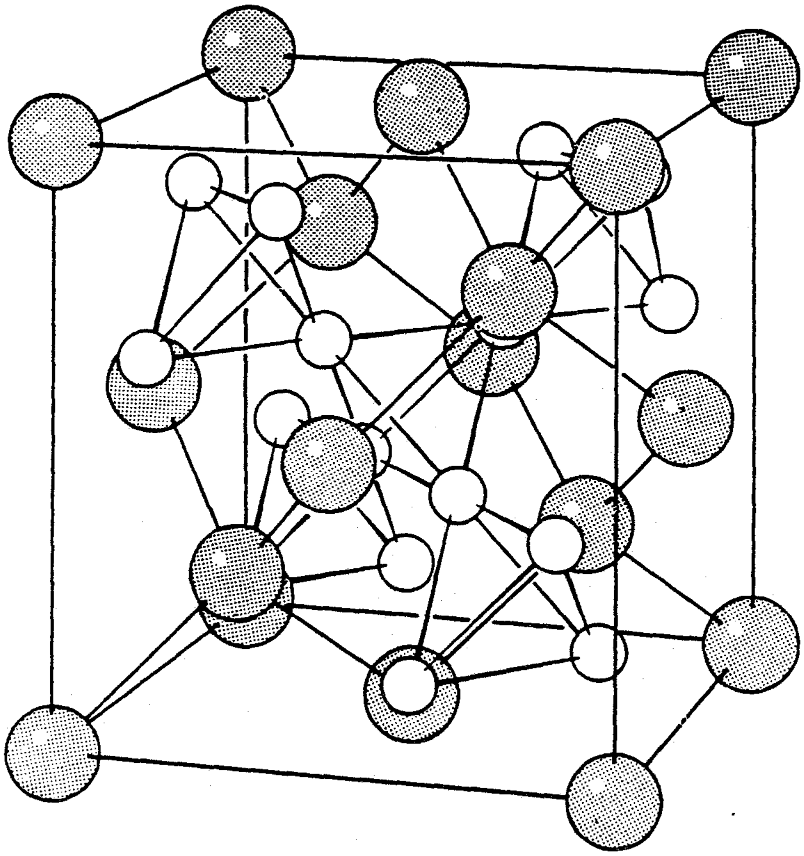

Figure 3.5: Unit cell of the C15 Laves structure. The large spheres represent Er atoms and the small ones represent Fe atoms. Diagram taken from Ref. [34].

Number per $ErFe_2$ formula unit	Surrounding atoms	Nearest neighbors (formula unit AB_2)
12	2 Er + 2 Fe	A_2B_2
4	1 Er + 3 Fe	AB_3
1	4 Fe	B_4

Table 3.1: Interstitial sites in the C15 Laves structure of $ErFe_2$ (from Ref. [23]). The size of the site decreases from top to bottom of the table.

3.4 Results

3.4.1 Enthalpy signals in sealed-pan DSC measurements of $ErFe_2D_{3.2}$

Neutron diffraction and DSC measurements of sealed $ErFe_2D_{3.2}$ at elevated temperatures were performed to settle questions about the "λ-anomaly" found in the DSC scans of Fecht, Fu and Johnson [3]. Four signals were observed in sealed-pan DSC scans from 35–400 °C (Fig. 3.6): two reversible endothermic peaks with onset temperatures of approximately 90 °C and at 200 °C and two irreversible exothermic peaks with onsets at approximately 280 °C and 360 °C. Let us consider what high-temperature neutron diffraction reveals about each of them.

Endothermic peak at ~ 90 °C

Elastic neutron diffraction scans at ~ 70 °C and at ~ 100 °C revealed that the crystalline structure changes from rhombohedral below the transition to cubic above it (Fig. 3.7). We may understand such a rhombohedral-to-cubic transition in terms of a change in interstitial site occupancy by deuterium atoms: Recall that the rhombohedral distortion of the cubic C15 Laves structure occurs because hydrogen atoms order in the AB_3 (1 Er + 3 Fe) interstitial sites [23, 30]. Above a certain temperature, it is reasonable that the hydrogen atoms might gain enough energy to jump between AB_3 sites, thus occupying all of them with the same probability. Equal occupation of all AB_3 sites forces the lattice back into the cubic configuration, as also occurs when the deuterium concentration approaches 4 deuterium atoms per $ErFe_2$ formula unit. Thus, we conclude that the endothermic peak at ~ 90 °C results from a reversible order-disorder transition of the deuterium atoms in the AB_3 sites of the C15 Laves structure. The DSC scans of this transition are usually quite asymmetric (though the trace shown in Fig. 3.6

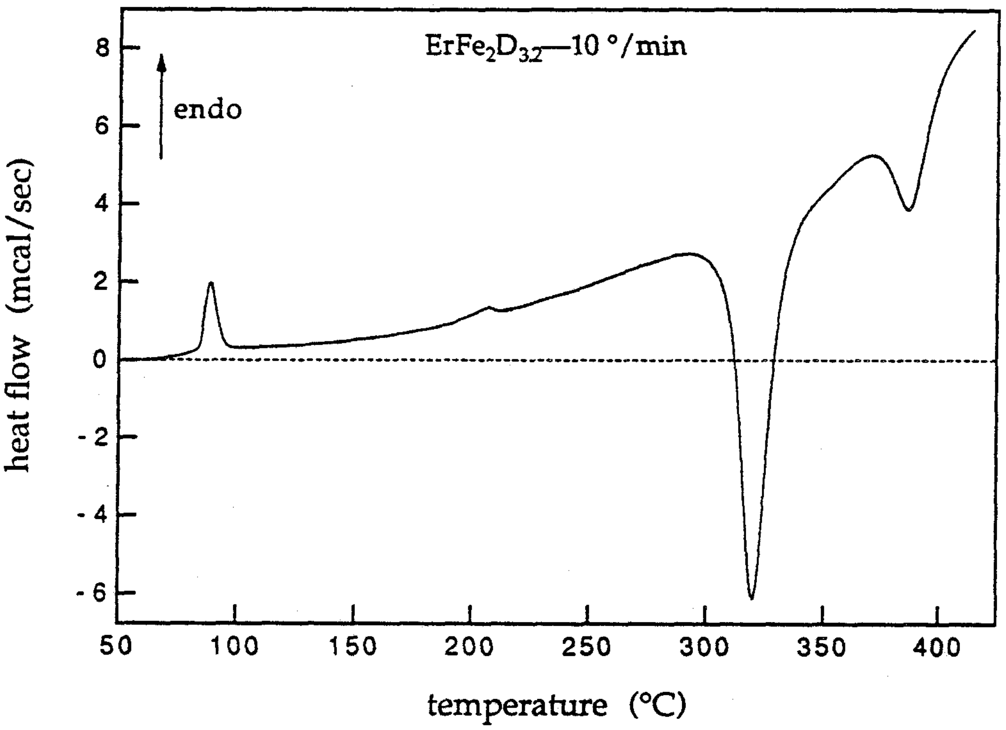

Figure 3.6: DSC scan of $ErFe_2D_{3.2}$ sealed in a 25-atm pan. The signal from the pan itself was removed by subtracting a DSC scan of an empty pan performed under identical conditions, and the high-pressure deformation signal (Fig. 3.4) was removed by first scanning up to 250 °C and then cooling back to room temperature. Since the two endothermic signals are reversible, this preliminary heating cycle has no effect on the resulting scan except to remove the deformation endotherm. The two exothermic signals are irreversible. At temperatures above about 425 °C, the seal fails and the deuterium leaks out.

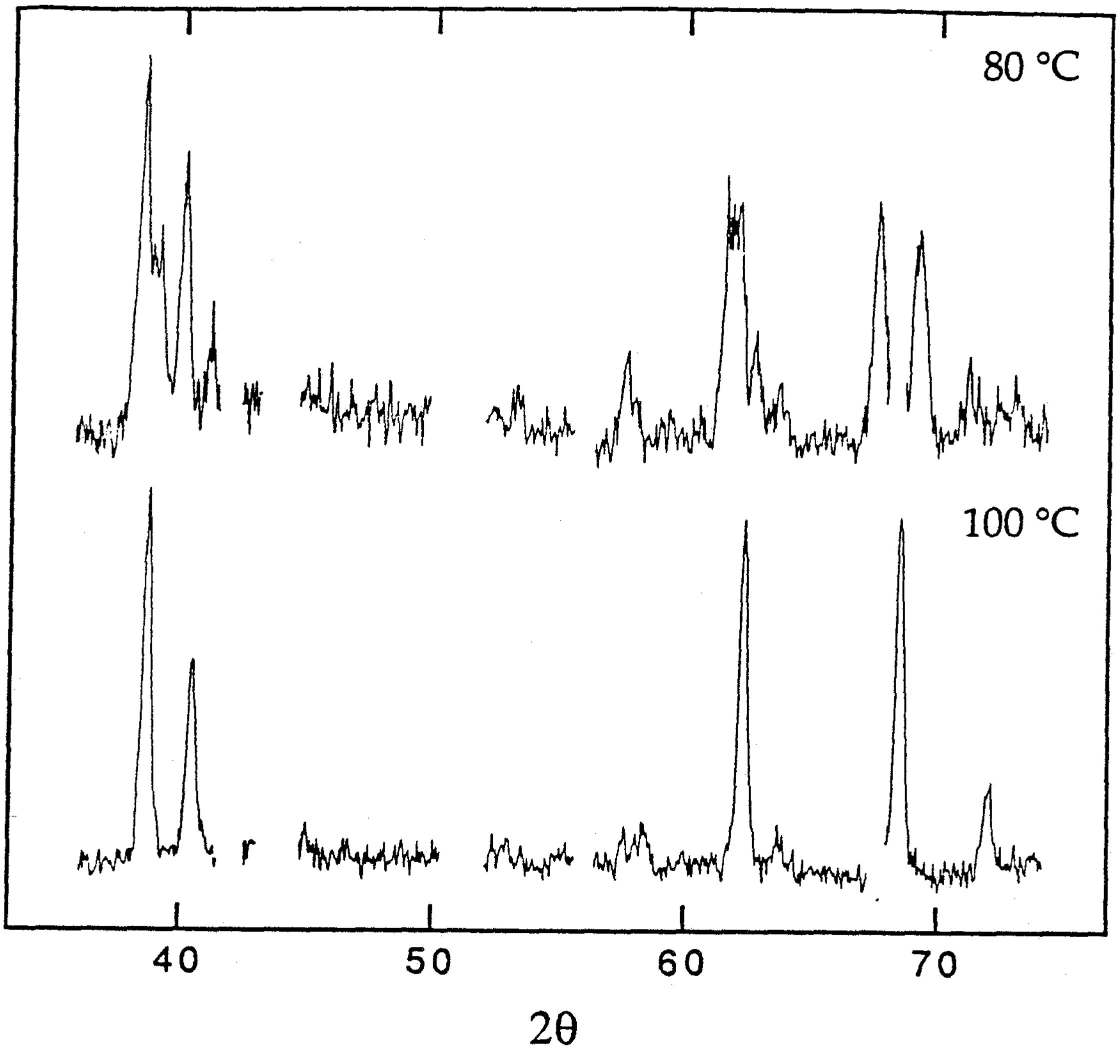

Figure 3.7: Elastic neutron diffraction scans of the sample below and above the endothermic peak at ~ 90 °C. Transition from a rhombohedral to a cubic structure is signaled by the lack of peak splitting at the higher temperature. Regions with no data result from deletion of Bragg peaks from the stainless-steel sample holder.

is an exception)—see, for example, the scan of Fig. 3.8. Such asymmetry suggests that the order-disorder transition may not be a first-order transition, an interpretation that will be strengthened by the attempt to determine the activation energy for the transition from a Kissinger analysis (section 3.4.4). Similar asymmetric calorimetric signals caused by hydrogen rearrangement have been observed in Ta_2H [36, 37].

Endothermic peak at ~200 °C

Our elastic neutron diffraction data find no structural change in the metal lattice of $ErFe_2D_{3.2}$ upon passing through this reversible peak (Fig. 3.9). As with the endothermic DSC trace at ~90 °C, the asymmetric shape of this transition (Fig. 3.10) and the Kissinger analysis results suggest a higher-order phase transition—possibly another order-disorder transition of the deuterium atoms. More likely, however, the peak is just the Curie transition of the cubic C15 structure formed at ~90 °C: neutron diffraction measurements on $ErFe_2D_x$ with $x \approx 3.5$ and C15 structure claimed to find a Curie transition temperature of 167 °C [33]; the same authors measured the Curie transition of unhydrogenated $ErFe_2$ to be 301 °C. Assuming as a first approximation that the Curie temperature depends linearly on x, we would expect to find the Curie transition of $ErFe_2D_{3.2}$ at ~180 °C. Given the crude approximations inherent in this estimate and given the uncertainty of the deuterium concentration in the sample measured in Ref. [33] and in our sample at elevated temperature, the agreement appears to be rather close. Furthermore, we found that the rhombohedrally distorted room-temperature $ErFe_2D_{3.2}$ powder was attracted to a magnet at room temperature, meaning that it is at least ferrimagnetic there (measurements have confirmed the ferrimagnetism of $ErFe_2H_x$, $x \approx 3$ [29, 33]), but this does not necessarily mean that the cubic C15 phase of the same composition is also ferrimagnetic between

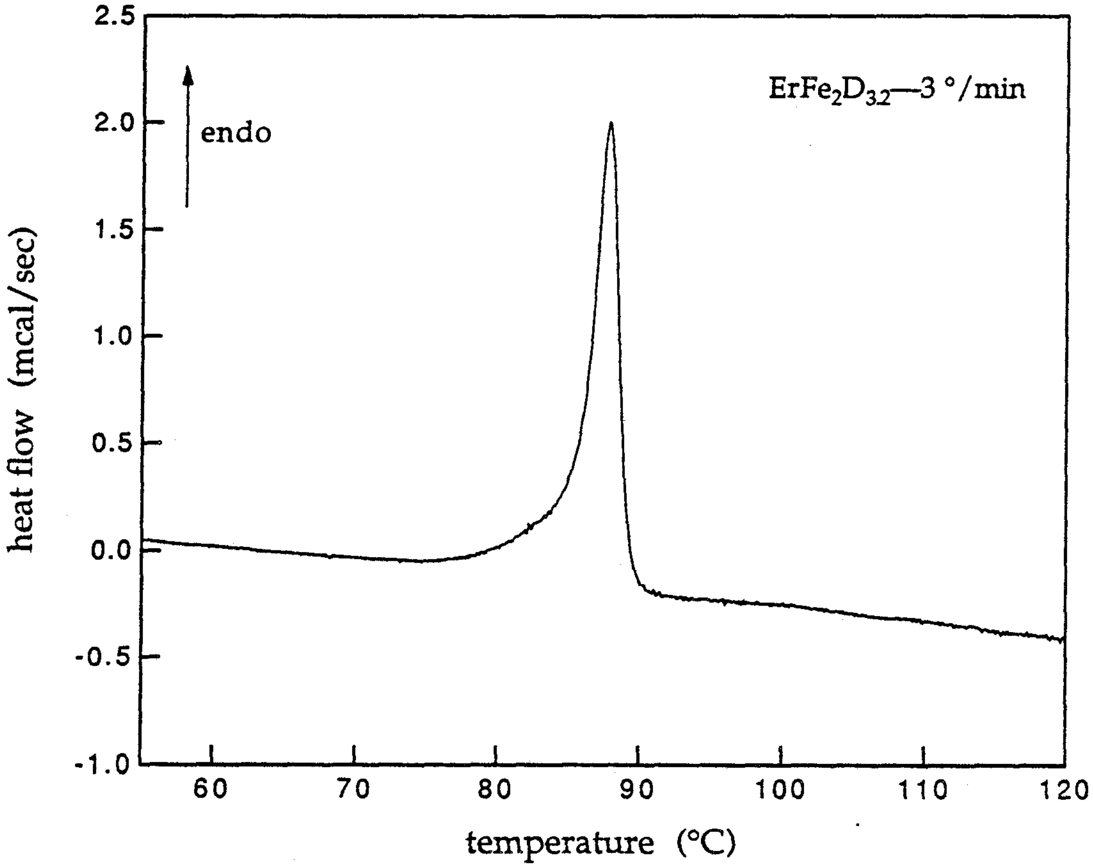

Figure 3.8: DSC scan of reversible rhombohedral-to-cubic transition in $ErFe_2D_{3.2}$. Asymmetry suggests that the phase transformation is not first order.

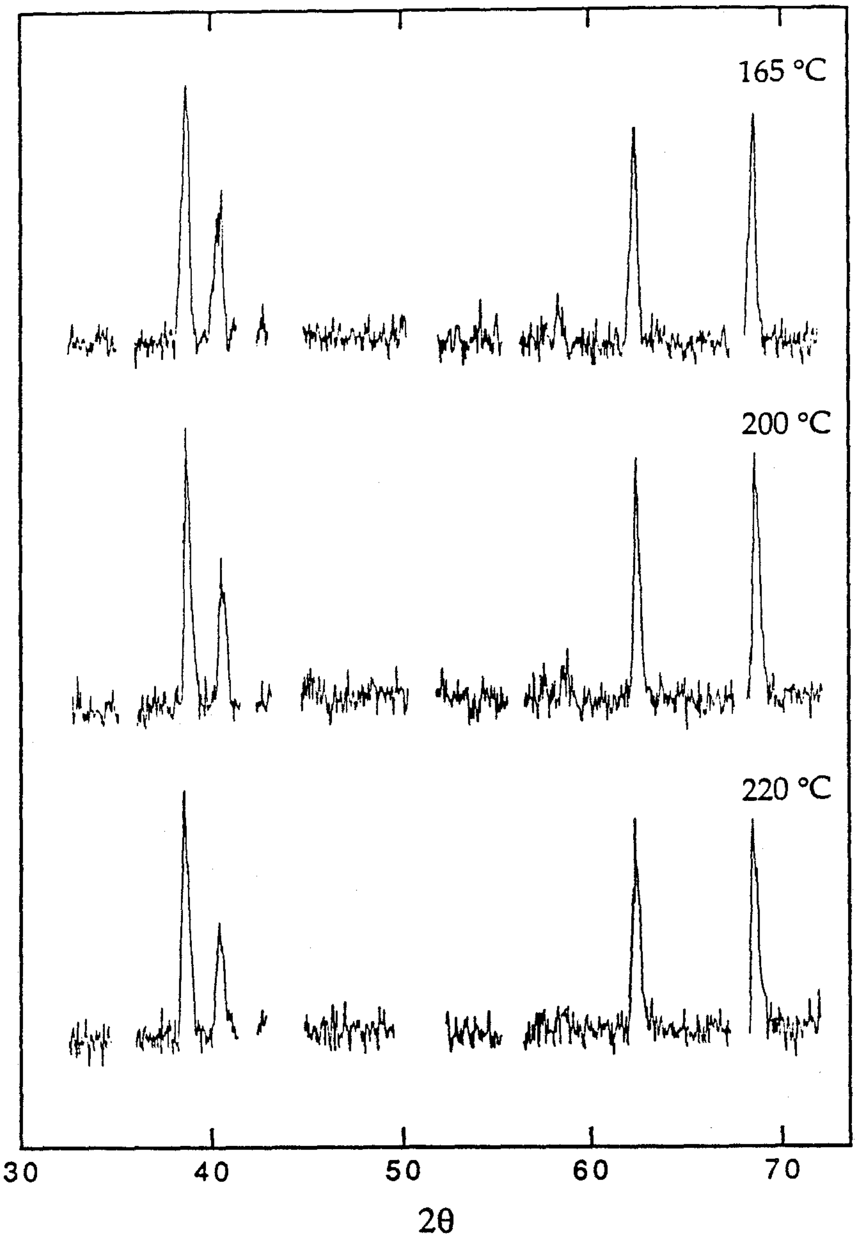

Figure 3.9: Elastic neutron diffraction scans of the sample below, at and above the endothermic peak at ∼200 °C. No change in the C15 Laves structure of the metal atoms is detected. Regions with no data result from deletion of Bragg peaks from the stainless-steel sample holder.

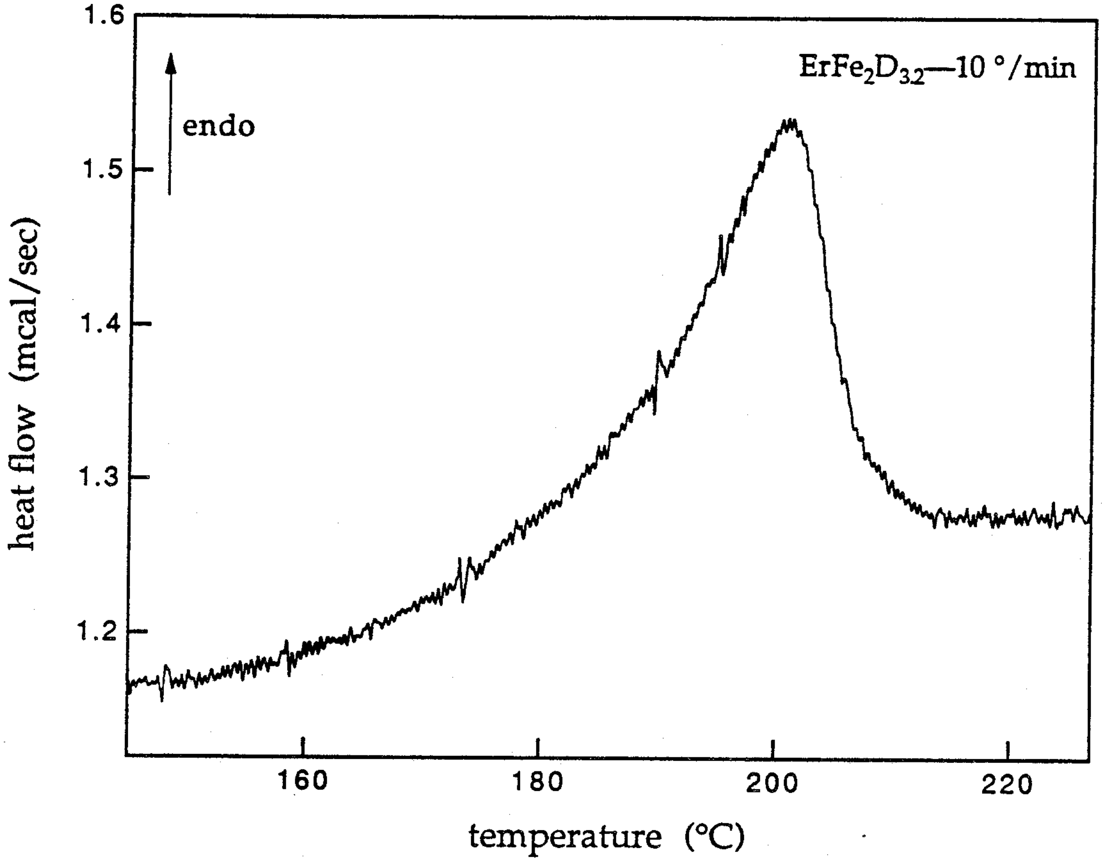

Figure 3.10: DSC scan of reversible transition at ~200 °C in $ErFe_2D_{3.2}$. Asymmetry suggests that the phase transformation is not first order; it may be just the Curie transition.

its formation at ~70 °C and the endothermic transition at 200 °C. Performing a DSC scan with the sample pan in a strong magnetic field created by a large (and heavy!) permanent magnet held nearby didn't affect the peak position, probably because the magnetic field was not strong enough to saturate the sample magnetization.

Evidence of a change in the magnetic properties of the sample might have been derived from the neutron diffraction data had our diffraction scan included the (111) Bragg peak at ~20° 2θ, for the contribution of scattering from the Fe magnetic moment to the integrated intensity of the (111) peak is stronger than its contribution to any other Bragg peak [33]. Unfortunately, our counting statistics were not good enough to detect the smaller magnetic contributions to the intensities of higher-angle peaks.

Finally, it must be admitted that the shape of this transition resembles that of the "λ-anomaly" found by Fecht *et al.* at nearly the same temperature in $ErFe_2H_{3.4}$. The enthalpy per mole derived from the integrated area of our DSC signal [58 J/mol(atoms)] is much smaller, however, than that of the "λ-anomaly" [~440 J/mol(atoms)], suggesting that the peaks do not share a common origin. In any event, no sign of amorphization was seen upon heating through this transition, in contradiction to the claims of Fecht *et al.* I shall return to the issue of the origin of the "λ-anomaly" below (section 3.5.1).

Exothermic peak at ~280 °C

This prominent exothermic peak is not reversible; upon cooldown to room temperature, the powder's x-ray diffraction scan is found to have no Bragg peaks, implying that the signal corresponds to amorphization of the sample (Fig. 3.11). In the high-temperature neutron diffraction measurements, the Bragg peaks of crystalline $ErFe_2D_{3.2}$ were observed to disappear between 220 °C and 240 °C (Fig. 3.12),

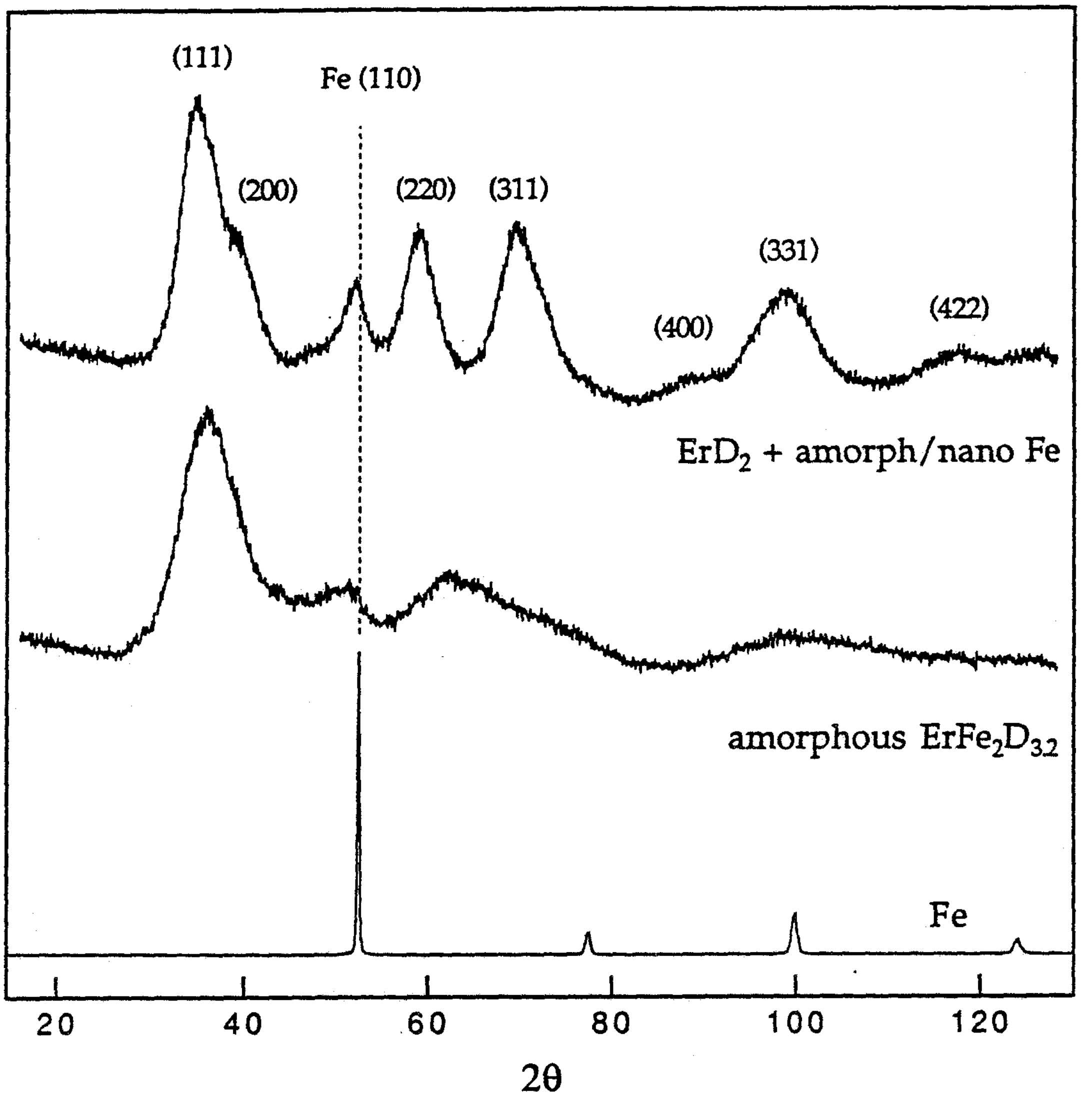

Figure 3.11: X-ray diffraction scans of $ErFe_2D_{3.2}$ heated above the first exothermic peak at ~280 °C (middle) and above the second exothermic peak at ~360 °C (top). Unlike the middle scan, the top scan has intensity maxima at the expected locations for ErD_2, indicating that ErD_2 has crystallized from the amorphous phase. The peak at about 53° 2θ in both deuteride scans is close to, but slightly shifted from, the position of the Fe (110) peak (bottom).

which is $\sim 50\,^\circ$C lower than the onset of the corresponding DSC signal. This discrepancy in amorphization temperature could result from temperature control problems (such as overshoot, calibration inaccuracy, etc., discussed above in section 3.2.3) and to the difference in time at which the sample is held at elevated temperature in the DSC and in the neutron diffraction sample holder. We will discuss the latter point below in connection with an activation energy for amorphization (section 3.4.4). The enthalpy release upon heating through this transition obtained by integrating the area of the exothermic peak[1] is ~ 6.7 kJ/mol(atoms), which is comparable in magnitude to the heat of fusion that one would estimate (using Richard's Rule [38]) for melting of the crystal at the amorphization temperature: 5–9 kJ/mol(atoms). Chemical analysis reveals a change in (room-temperature) deuterium concentration from $ErFe_2D_{3.2}$ to $ErFe_2D_{2.8}$, which is in good agreement with the composition of the amorphous hydrogenated $ErFe_2$ formed directly by annealing $ErFe_2$ in a hydrogen atmosphere at 240 °C [3].

Exothermic peak at $\sim 360\,^\circ$C

Since no neutron diffraction scans were recorded above 250 °C, we had to determine any associated structural changes using x-ray diffraction of the powder after it had been heated through this irreversible transition in the DSC and cooled back down to room temperature. The x-ray diffraction scan has broad peaks similar to those of the amorphous sample of the previous section, but the peaks of the sample heated through the transition at $\sim 360\,^\circ$C can be indexed to the expected Bragg peaks of ErD_2 and also, perhaps, to Fe (Fig. 3.11). The precipitation of ErD_2 should leave Fe-rich clusters, but only a peak near the strong (110) Fe position is obvious; there are none corresponding to higher-order Fe reflections. Even

---

[1] Technically, this area is not exactly equivalent to ΔH because the pressure inside the sealed pan is not constant during the transition. Unfortunately, there is no easy way to measure the pressure change in the DSC pan.

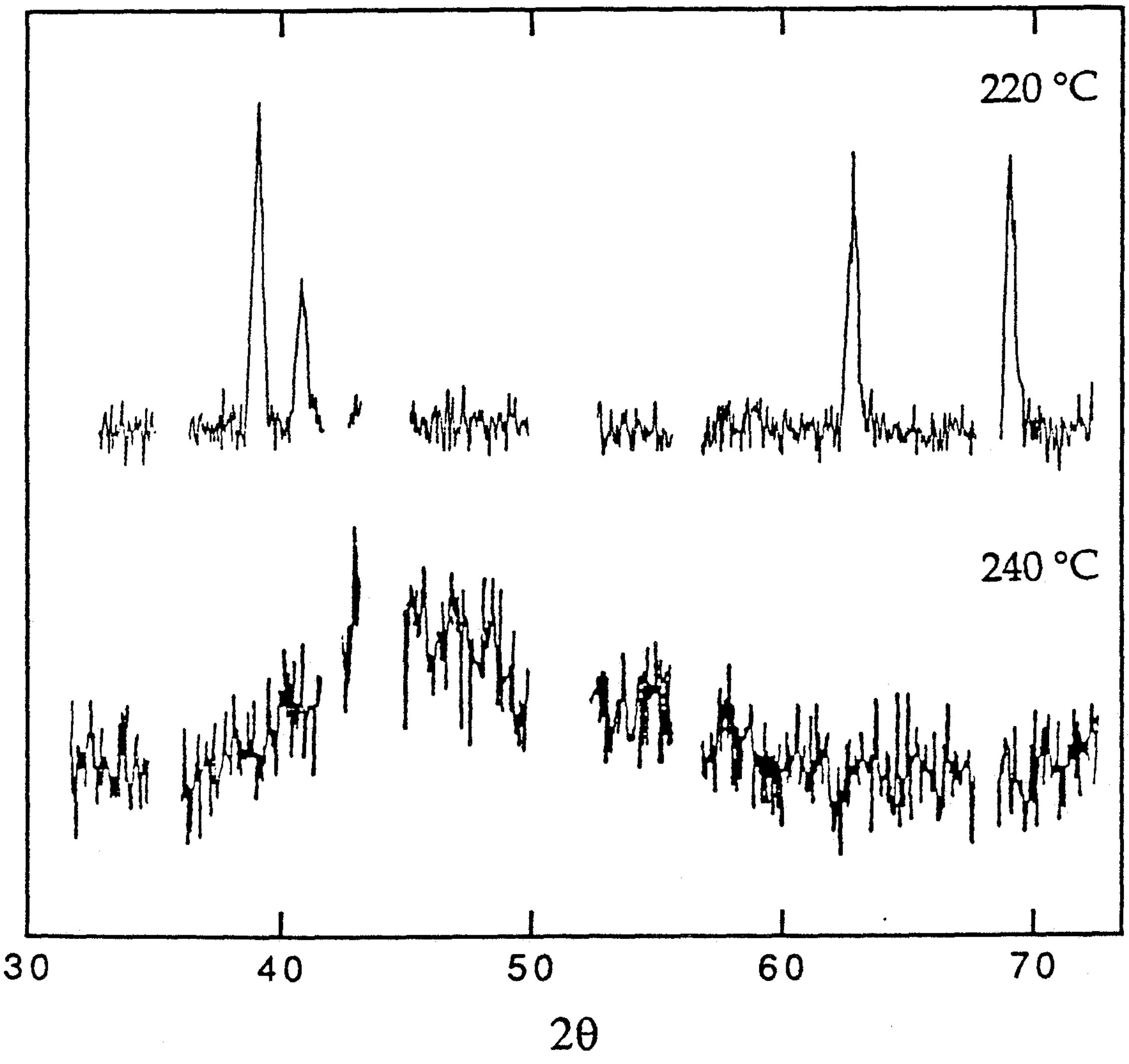

Figure 3.12: Elastic neutron diffraction scans of $ErFe_2D_{3.2}$ measured at ~220 °C and ~240 °C. Peaks from the C15 Laves structure of the metal atoms vanish between the two temperatures, leaving only a broad intensity maximum characteristic of an amorphous phase. No recovery of the crystalline phase was observed upon cooling back to 220 °C or to lower temperatures. Subsequent x-ray diffraction scans of the amorphous powder were identical to those of the $ErFe_2D_{3.2}$ powder heated above ~280 °C in the DSC (Fig. 3.11).

the possible Fe (110) peak is noticeably displaced from its position in bulk Fe, though this could reflect lattice expansion due to interstitial D or to alloying with Er. Analysis of the similar crystalline hydride $GdFe_2H_x$ in a high-pressure DTA by Aoki *et al.* found separate exothermic peaks corresponding to precipitation of GdH_2 and Fe [19]. This suggests that the "(110)" peak is actually the nearest-neighbor peak arising from amorphous Fe. Application of the Scherrer formula [11] for the effect of small grain size on peak width suggests that the precipitated ErD_2 grains are quite small:

$$L \approx \frac{0.9\,\lambda}{B\cos\theta_B} \approx 2\,\mathrm{nm}, \tag{3.3}$$

where λ is the x-ray radiation wavelength (0.17903 nm for the Co-Kα radiation used in the scan of Fig. 3.11) and B is the full width at half maximum of the diffraction peak at $2\theta_B$.

3.4.2 Outgassing of deuterium

We have seen that the deuterium evolution found in the open-pan DSC scan of $ErFe_2D_{3.2}$ (Fig. 3.2) necessitates the use of high-pressure DSC pans when investigating phase transitions in this material. Placing the sample in a sealed pan does not, of course, prevent *all* deuterium evolution from occurring. As discussed above, deuterium will leave the sample until the chemical potential of deuterium in the gas phase is equal to that of the remaining deuterium in the solid; thus, some concentration change in the solid must occur as a function of temperature. The continuous outgassing of deuterium can, in fact, be observed in the increase of the baseline of Fig. 3.6, in which the signal due to the pan has been subtracted (the baseline increase begins *below* 160 °C in this scan because I first heated the sample to ~200 °C to break the oxide surface layer). The heat needed to "boil off" deuterium from the solid represents an endothermic contribution to the enthalpy change per unit time dH/dt measured by the DSC. As this is a continuous process (as long as deuterium remains to evolve from the solid), it will cause the $ErFe_2D_{3.2}$ signal to rise above that of an empty pan (assuming "up" corresponds to "endothermic"), which is exactly what we observe.

3.4.3 Concentration dependence of signal temperatures

If we suppose that the ease of amorphization in $ErFe_2D_{3.2}$ is influenced by the concentration of the deuterium still in the solid or by the pressure on the solid, then we would expect the temperature at which amorphization occurs to depend on the *packing fraction* of powder in the DSC cell or in the neutron sample holder, where packing fraction is defined as the ratio of sample volume to container volume. This is in fact what is observed: the onset temperature of amorphization decreases as the packing fraction is increased (Fig. 3.13). An opposite temperature dependence of ErD_2 precipitation on packing fraction is also found. The onset temperature of the endothermic order-disorder transition at ~ 85 °C does not have a noticeable packing-fraction dependence; unfortunately, the signal from the possible Curie transition at ~ 200 °C was masked by the endothermic peak associated with pan deformation (section 3.2.4). The lack of temperature dependence in the order-disorder case may be due to the fact that at low temperatures there is less difference in deuterium concentration for different packing fractions than at high temperatures, while the opposite temperature dependences of the exothermic transitions can be explained by the atomic-level mechanisms for amorphization and crystallization.

Since the packing fraction of the neutron sample holder was ~ 0.14, we would expect from Fig. 3.13 that the onset of amorphization in the neutron diffraction experiments would occur at ~ 280 °C. This prediction is still ~ 50 °C higher than the temperature actually observed; as promised above (section 3.4.1) we will now investigate to what extent the temperature offset can be explained as an effect of

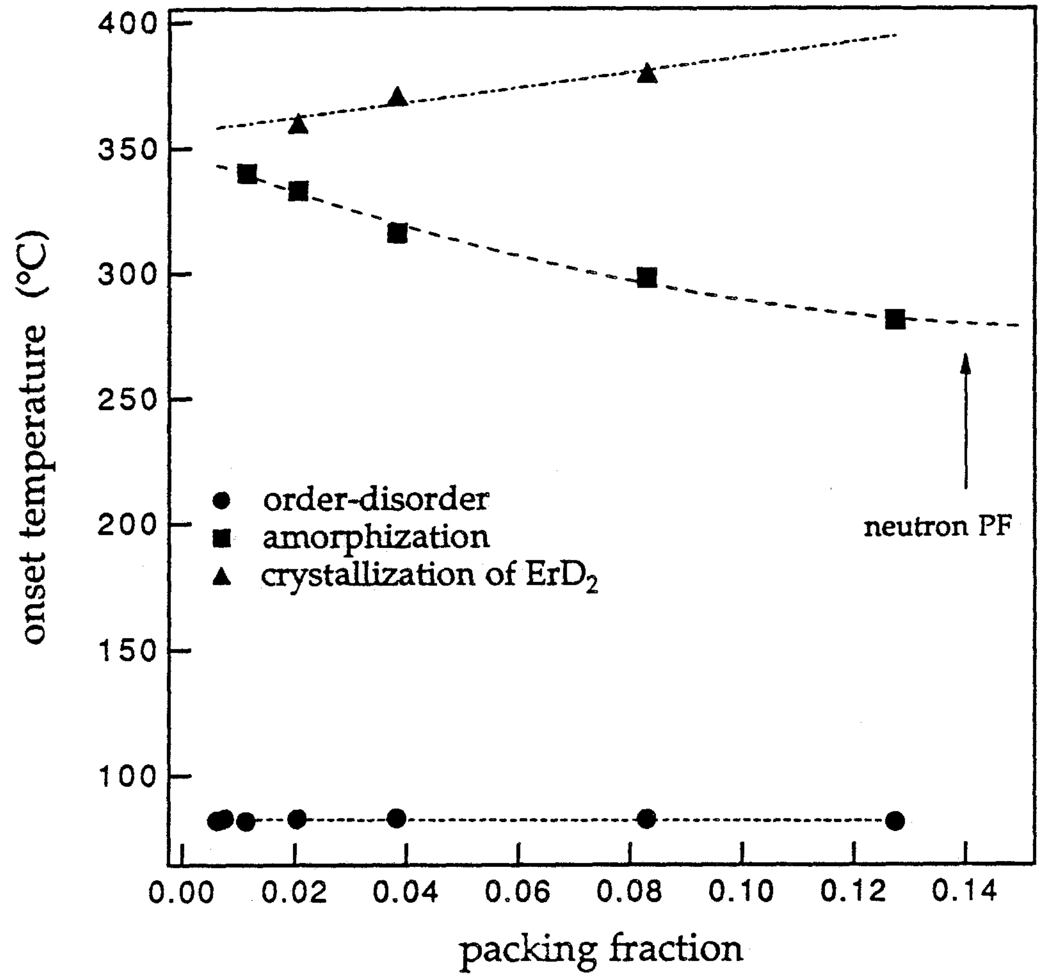

Figure 3.13: DSC transition temperature onsets *vs.* packing fraction of $ErFe_2D_{3.2}$ powder in a sealed 25 atm sample cell. The endothermic transition at ~200 °C was obscured by the much stronger pan deformation signal. Note that the $ErFe_2D_{3.2}$ amorphization and ErD_2 crystallization temperatures have opposite dependences on packing fraction.

an activation energy for amorphization.

3.4.4 Kissinger analysis-derived activation energies

According to Kissinger [39], the activation energy E_a of a single, thermally activated endothermic or exothermic first-order transition seen in a DSC trace can be estimated from the dependence of the transition peak temperature T_p on scanning rate r according to the equation:

$$\frac{d\left(\ln \frac{r}{T_\mathrm{p}^2}\right)}{d\left(\frac{1}{T_\mathrm{p}}\right)} = -\frac{E_\mathrm{a}}{k_\mathrm{B}}. \tag{3.4}$$

This expression is accurate only when the reaction is dominated by one thermally activated process with an Arrhenius temperature dependence; if, for instance, both nucleation and growth occur during the reaction, the analysis may give a spurious result [40, 41]. In particular, for a higher-order transition, which has no nucleation barrier, T_p will be independent of r. Application of Eq. (3.4) to such a situation will result in unphysically high estimates of E_a. Kissinger plots for the two endothermic and two exothermic reactions seen in the DSC scans are given in Figs. 3.14(a)–3.14(c). The slope of the line provides an estimate for E_a, and the error of the least-squares fit provides a measure of the statistical uncertainty in E_a. The deuterium order-disorder reaction at 90 °C has an apparent activation energy of 16 eV/atom at slower scan rates and 2 eV/atom at faster scan rates; this unphysical behavior (especially the high activation energy at slower scan rates) supports our interpretation (section 3.4.1) of the peak's asymmetric shape as an indication of a higher-order phase transition. A similar conclusion follows from the poor fit and high activation energy of ~5 eV/atom for the possible Curie transition at 200 °C.

The exothermic amorphization reaction at ~280 °C has an activation energy of 1.02 ± 0.04 eV/atom, although the deviation of the data points from a straight

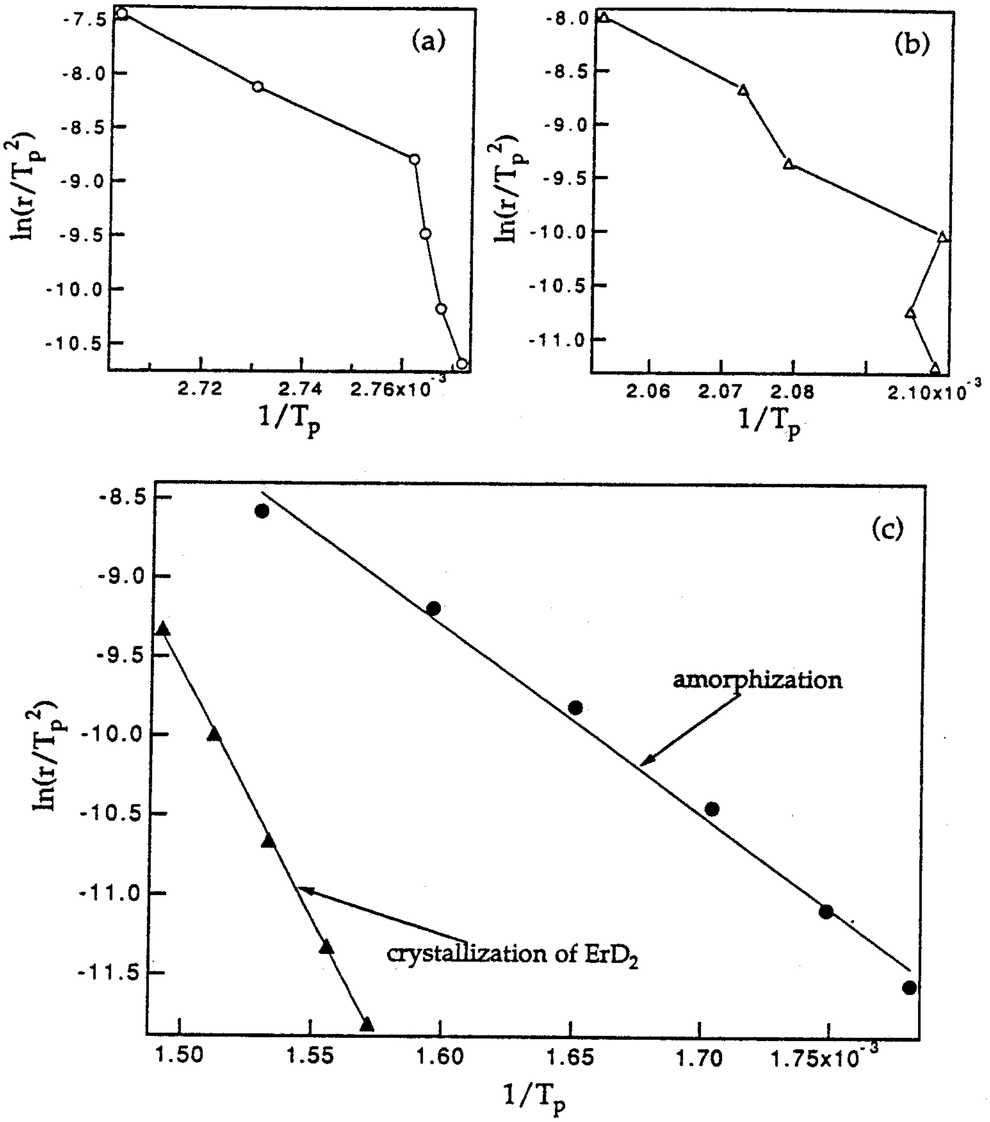

Figure 3.14: Kissinger plots of $\ln(r/T_p^2)$ *vs.* $1/T_p$ for the (a) rhombohedral-to-cubic transition, (b) possible Curie transition and (c) exothermic transitions (amorphization and crystallization of ErD_2). The scanning rate r ranged from 3 °C/min to 80 °C/min. T_p is the peak of the transition as measured in the DSC.

line indicates that one or more of the assumptions necessary for the success of Eq. (3.4) has broken down. The problem likely arises from interference of activated growth with the signal from nucleation of the amorphous phase. Hence, the value derived for E_a should be viewed as only an approximation to the true value. The Kissinger analysis estimate of the activation energy for crystallization of ErD_2 is 2.65 ± 0.04 eV/atom. In section 3.5.2, I shall discuss the proper interpretation of these energies in light of an atomic mechanism for both transitions.

Finally, the fact that a reaction has an associated nucleation barrier results in a time dependence of the reaction temperature. In other words, the (apparent) onset temperature at which a reaction occurs will depend on the time at which the sample is left at that temperature: depending on the activation energy a reaction may take, for instance, one hour to complete at 150 °C but only a minute at 175 °C. The activation energy $E_a \approx 1$ eV/atom for amorphization allows us to calculate how long amorphization would require at the temperature at which it was seen in neutron diffraction (230 °C), given that it takes ~ 3 min to complete starting from an onset of 280 °C in the DSC (at the packing fraction of the neutron diffraction sample holder—see Fig. 3.13). To make such an estimate, we need only use the standard empirical expression for the diffusion coefficient D [42]:

$$D = D_0 \exp\left(-E_a/k_B T\right), \tag{3.5}$$

where D_0 and E_a may vary with composition but not with temperature. Since the units of D are $[\text{Length}]^2[\text{Time}]^{-1}$, the characteristic length L_0 over which diffusion occurs in a time t at a temperature T_1 is just $\sqrt{D(T_1)t(T_1)}$. Thus, the time required for diffusion over the same distance L_0 at a different temperature T_2 is just:

$$t(T_2) = t(T_1) \exp\left[\frac{E_a}{k_B}\left(\frac{1}{T_2} - \frac{1}{T_1}\right)\right]. \tag{3.6}$$

Inserting the above numbers into Eq. (3.6) yields a time required for amorphization at 230 °C of 24 minutes, which is about the same as the minimum equilibration time spent between neutron diffraction measurements. This provides a reasonable explanation for the temperature offset between the neutron and DSC amorphization reactions.

3.5 Discussion

3.5.1 Is the "λ-anomaly" associated with amorphization?

The results described above make it highly unlikely that the apparent "λ-anomaly" in the DSC trace of $ErFe_2H_{3.4}$ seen by Fecht, Fu and Johnson [3] is related to a reversible amorphization reaction. Not only was (irreversible) amorphization found in the high-temperature neutron diffraction experiments at a temperature at least 30 °C above that of the "λ-anomaly," but the signal from the deformation of the stainless-steel DSC pan (Fig. 3.4), which was found at about the same temperature as the "λ-anomaly," would be expected to occur in response to a much higher internal pressure than the 2 atm (2×10^5 Pa) rating of the sealed aluminum pans used by Fecht *et al.* That is, the pans used by Fecht *et al.* could not have remained intact upon heating through the endothermic transition that we saw at $\sim 200\,^\circ$C, because their seals would have broken upon reaching the temperature at which outgassing from the powder begins.

In fact, it is reasonable to suppose that the "λ-anomaly" is simply the deformation peak of a sealed aluminum pan: the low-temperature edge would rise for the same reasons as with the deformation peak of the stainless-steel pans (gas evolution from the sample necessary for re-establishing equilibrium) and the quick drop-off on the high-temperature side might result from a sudden ceasing of the deformation. That is, the deformation of the aluminum might proceed rapidly until reaching a point at which further deformation can only occur by breaking the seal, a process that may require significantly more internal pressure than that needed for the initial deformation. Indeed, several scans of $ErFe_2D_{3.2}$ in the same sealed aluminum DSC pans used by Fecht *et al.* produced "λ-like" signals just before seal failure [Fig. 3.15(a)]. The temperature at which the anomaly occurs is the same as the temperature at which the oxide layer is broken and deuterium begins to evolve from the powder. We could even reproduce the "partial reversibility" found by Fecht *et al.:* if the sample is heated to a point above the "λ-like" signal but below the temperature at which the sample pan breaks open, then cooled back to room temperature and reheated, a second "λ-like" signal can be observed that is weaker in magnitude than the first and displaced to a lower temperature [Fig. 3.15(b)]. This result is consistent with pan deformation, since once the surface oxide layer is broken and deuterium evolution can occur—as seen in the first scan's "λ-anomaly"—then deuterium evolution will begin at a significantly lower temperature, so the pressure buildup will occur faster during the second scan than the first. The smaller magnitude of the signal is probably related to the smaller amount by which the aluminum pan can deform a second time before breaking.

Lastly, we must question the finding by Fecht *et al.* of amorphous regions in TEM images of $ErFe_2H_{3.4}$ heated through the "λ-anomaly" and cooled back down to room temperature. We saw no amorphous regions in x-ray diffraction scans of $ErFe_2D_{3.2}$ heated to just below the amorphization exotherm. Perhaps the amorphous regions seen by Fecht *et al.* were an artifact of TEM sample preparation or were caused by the influence of the electron beam and degassing of the sample in the microscope.

3.5.2 Exothermic amorphization

Convincing evidence that hydrogen-induced amorphization is exothermic in RE–Fe_2 compounds (RE = rare earth) was first obtained by Aoki and coworkers using

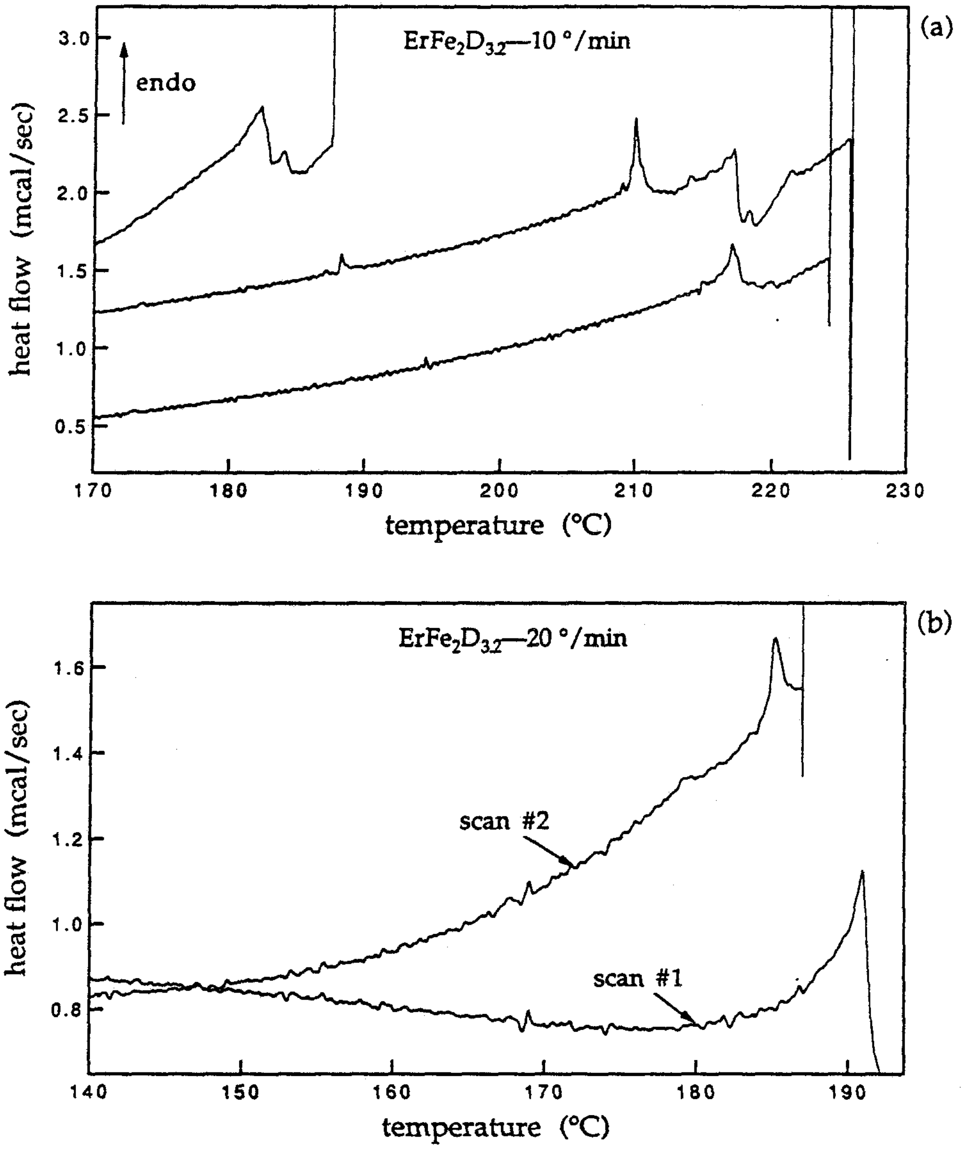

Figure 3.15: DSC scans of $ErFe_2D_{3.2}$ in sealed aluminum pans of the type used by Fecht *et al.* [3]. Scans from several individual runs terminating in pan failure are found in (a). In (b), the first scan was stopped before the pan failed; the second scan from room temperature indicates both a rise in the baseline (caused by outgassing of deuterium at lower temperature, since the oxide layer was broken during the first scan) and a "λ-like" peak displaced to lower temperature. Fecht *et al.* suggested that this was evidence for partially reversible amorphization.

a high-pressure DTA [17, 18, 19]. Their study of $GdFe_2H_x$ [19], which has an expanded C15 Laves structure like that of $ErFe_2D_{3.2}$ (above the order-disorder transition), found the same sequence of transitions that we obtained in $ErFe_2D_{3.2}$: first, amorphization occurred, then precipitation of the rare-earth dihydride, and, finally, crystallization of pure Fe to achieve the equilibrium mixture of RE-H_2 + α-Fe. (Temperature limitations of our high-pressure DSC pans prevented us from measuring the Fe crystallization step in $ErFe_2D_{3.2}$.) The measured dependence of $GdFe_2$ hydride amorphization and crystallization temperatures on ambient hydrogen pressure in the DTA was qualitatively the same as the transition-temperature dependence on packing fraction (section 3.4.3) for both transitions in $ErFe_2D_{3.2}$. Using the Kissinger analysis technique, Aoki *et al.* also determined the activation energies for each transition, again finding similar values to those we obtained for $ErFe_2D_{3.2}$ (Table 3.2).

If polymorphous amorphization is thermodynamically similar to melting—as we claimed in Chapter 1—and if thermally induced amorphization of a hydrogenated crystalline intermetallic compound is polymorphous—as we would expect it to be, since it occurs at low temperatures, where the metal atoms lack mobility—then the enthalpy signal upon amorphization should be *endothermic,* not strongly exothermic as we measured!

Atomic-level structural change upon amorphization

This counterintuitive result can be understood from an analysis of the change in the atomic-level structure of the sample during the amorphization transition. The majority of information that we have about the amorphous phase is found in its x-ray diffraction scan, which has an unusual amount of structure for a diffraction scan of an amorphous solid. To first approximation, we can ask if any of the intensity maxima in the amorphous diffraction scan correspond to a

Transition	E_a	
	$ErFe_2D_x$ (eV/atom)	$GdFe_2H_x$ (eV/atom)
amorphization	1.02 ± 0.04	1.2
hydride crystallization	2.65 ± 0.04	2.1

Table 3.2: Activation energies for amorphization of $ErFe_2D_{3.2}$ and $GdFe_2H_{4.2}$ and for crystallization of the rare-earth hydride as measured by the Kissinger analysis technique. All data on $GdFe_2H_{4.2}$ taken from Aoki *et al.* [19].

reasonable interatomic distance in the solid. For an intensity maximum centered on a diffraction angle $2\theta_{\mathrm{m}}$, the corresponding interatomic spacing d_{m} is given by Ehrenfest's formula [43]:

$$d_{\mathrm{m}} = K \frac{\lambda}{2 \sin \theta_{\mathrm{m}}}, \tag{3.7}$$

where λ is the wavelength of x-ray radiation and K is a constant equal to 1.1–1.2. Keeping in mind that the assumptions made in deriving this formula render it useful only for order of magnitude predictions in most cases [43, 44], we get distances of $d_{\mathrm{m}} \approx 0.35$ nm for the lowest-angle maximum and $d_{\mathrm{m}} \approx 0.25$ nm for the next-highest-angle maximum in Fig. 3.16. In $\mathrm{ErFe_2}$, the Fe–Fe bond distance is 0.257 nm, Er–Fe is 0.301 nm and Er–Er is 0.314 nm [45]. It is tempting to identify the first intensity maximum with the Er–Er bond length and the second maximum with the Fe–Fe bond length. These peaks can be distinguished only if the amorphous phase has relatively few Er–Fe nearest neighbors; otherwise, overlap with the signal from Er–Fe bonds—which would fall between the other two maxima—would result in one broad intensity maximum in the diffraction scan. That the amorphous solid has relative few Er–Fe nearest neighbors strongly implies the existence of short-range clustering of Er and Fe atoms with other atoms of the same kind.

This clustering explanation for the structure of the amorphous diffraction scan has been placed on a firm foundation by comparison of the radial distribution function (RDF) of amorphous $\mathrm{ErFe_2}$ with that of hydrogenated amorphous $\mathrm{ErFe_2}$ [45].[2] The difference in partial coordination numbers (Table 3.3) between crystalline $\mathrm{ErFe_2}$ and amorphous $\mathrm{ErFe_2}$ (prepared without hydrogen by thin-film de-

---

[2] For the RDF measurements of Ref. [45], the hydrogen-containing amorphous phase was obtained by hydrogenating an *already amorphous* film of $\mathrm{ErFe_2}$ rather than by inducing a crystal-to-amorphous phase transition in the crystalline hydride, as we did with $\mathrm{ErFe_2D_{3.2}}$. We believe that both techniques should lead to the same amorphous structure, however, since comparative studies of hydrogenation of amorphous and crystalline $\mathrm{Zr_3Rh}$ found no significant structural differences in the final states [46, 47].

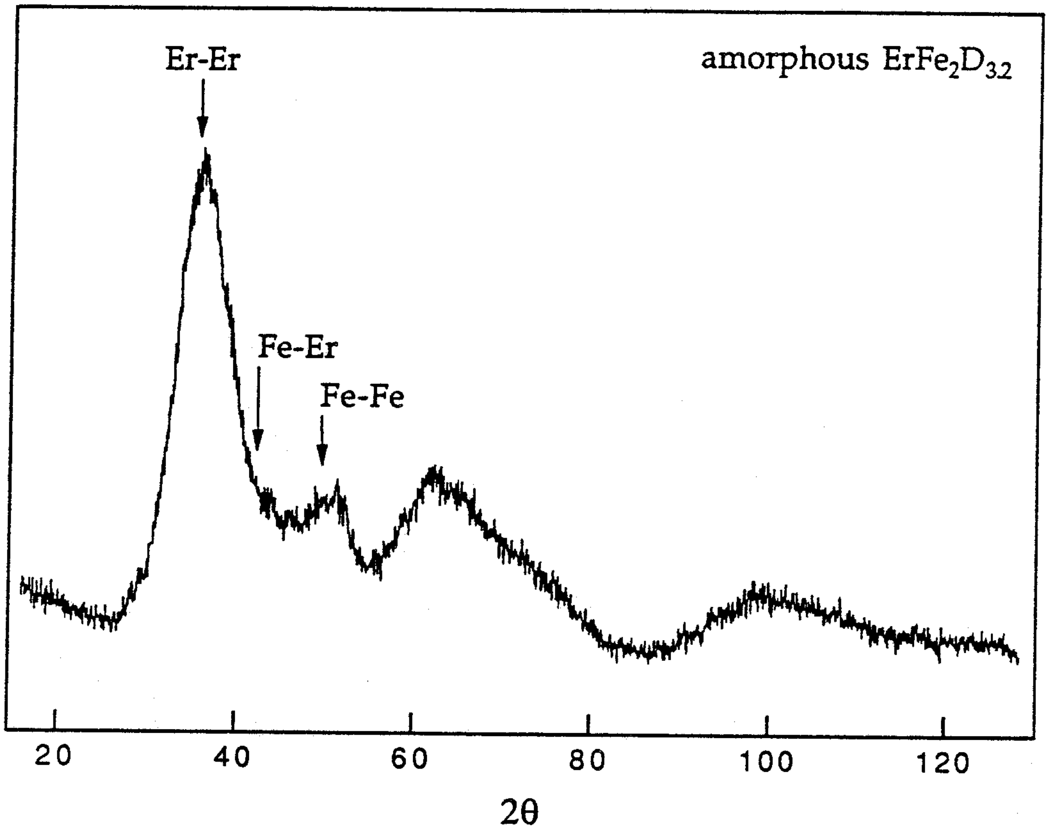

Figure 3.16: X-ray diffraction scan of amorphous $ErFe_2D_{2.8}$. The unusual split first intensity maximum can be identified with Er–Er and Fe–Fe interatomic spacings, while the lack of intensity in between these peaks can be attributed to a dearth of Fe–Er nearest-neighbor bonds in the amorphous structure. Intensity maxima positions predicted by use of Eq. (3.7).

position) provides evidence for a moderate increase in Fe–Fe and Er–Er clustering in the amorphous state. The clustering becomes almost complete, however, with the addition of hydrogen: the partial correlation number of Fe–Er drops from 6 in the crystal to 3.1 in a-$ErFe_2$ to 1.1 in the hydrogenated glass! It is no surprise, then, that a contribution to the nearest-neighbor amorphous peak from Fe–Er interatomic distances is missing from the x-ray diffraction scan.

The increase in Er–Er nearest-neighbor distance upon amorphization (Table 3.3) suggests that amorphization relieves the compression of the rare-earth spacing characteristic of the Laves phase [29, 48]: compare the Er–Er interatomic distance in pure Er (0.3468 nm [49]) to that in $ErFe_2$ (0.314 nm) and in the hydrogenated glass (0.361 nm). Neither amorphization nor subsequent hydrogenation have much effect on the Fe–Fe or Fe–Er spacings. Hydrogen atoms in the amorphous phase must be be found almost entirely in the Er clusters, since the Er–Er spacing increases upon hydrogenation while the Fe–Fe spacing does not [45]. This is not surprising, given the relatively high solubility of hydrogen in rare-earth metals and the large, negative heat of mixing of hydrogen with Er. The Er–Er spacing measured in hydrogenated amorphous $ErFe_2$ is quite close to the distance that we estimated from the Ehrenfest equation; clearly, it corresponds to a reasonable position for the lowest-angle amorphous intensity maximum in Fig. 3.16.

Diffusional activation energy for clustering

An activation energy $E_a \approx 1.0\,\mathrm{eV/atom}$ for amorphization of $ErFe_2D_{3.2}$ was determined by the Kissinger method. This energy must correspond to the barrier hindering atomic rearrangement from the expanded C15 Laves phase of crystalline $ErFe_2D_{3.2}$ to the clustered amorphous state of $ErFe_2D_{2.8}$. The change in short-range configuration found in the RDF analysis requires some diffusion of metal atoms to occur. We expect Fe atoms to diffuse much more rapidly in

Bond	Interatomic distance[a]			Coordination number[a]		
	d_x (nm)	d_a (nm)	d_h (nm)	n_x	n_a	n_h
Fe–Fe	0.257	0.257 ± 0.005	0.262 ± 0.005	6	7.2 ± 0.2	10.5 ± 0.2
Fe–Er	0.301	0.299 ± 0.005	0.305 ± 0.005	6	3.1 ± 0.2	1.1 ± 0.2
Er–Er	0.314	0.341 ± 0.005	0.361 ± 0.005	4	7.0 ± 0.2	9.6 ± 0.5

[a] Subscript key: x = crystalline $ErFe_2$, a = amorphous $ErFe_2$,
h = hydrogenated amorphous $ErFe_2$.

Table 3.3: Partial coordination numbers and nearest-neighbor spacings in crystalline $ErFe_2$, amorphous $ErFe_2$ and hydrogenated amorphous $ErFe_2$. All data from Matsuura *et al.* [45].

$ErFe_2D_{3.2}$ than Er atoms, because the Fe atoms are much smaller than the Er atoms. While there are no known measurements of the activation energy for Fe diffusion in $ErFe_2D_{3.2}$ (Goldschmidt radius $r_{\mathrm{Fe}} = 0.126\,\mathrm{nm}$ [50]) or even in bulk Er ($r_{\mathrm{Er}} = 0.175\,\mathrm{nm}$), we can get an idea of its value from the measured E_{a} for the diffusion of Au ($r_{\mathrm{Au}} = 0.144\,\mathrm{nm}$) in Er: 0.66 eV/atom parallel to the *c*-axis of Er and 1.0 eV/atom perpendicular to it [51]. The activation energy for Au diffusion in $ErFe_2D_{3.2}$ would probably be higher, since the "average metal atom" is smaller in $ErFe_2D_{3.2}$ than in pure Er, but Fe atoms are smaller than Au atoms, which would tend to lower the activation energy, so it is reasonable to assign the activation energy $E_{\mathrm{a}} \approx 1.0$ to Fe diffusion.

Enthalpy release and concentration dependence of amorphization

The proposed clustering mechanism of amorphization in $ErFe_2D_{3.2}$ successfully accounts not only for the intensity maxima seen in the diffraction scan of the amorphous phase and for the activation energy determined by Kissinger analysis, but also for the large enthalpy release associated with amorphization and for the packing fraction dependence of its transition temperature. First, the exothermic heat release can be seen to arise from the change in local environment of the deuterium atoms in the solid. Instead of having at most two Er nearest neighbors—to which an interstitial deuterium atom is limited in the C15 crystalline structure (see Table 3.1)—the deuterium atoms in the amorphous phase can surround themselves almost entirely with Er atoms by occupying interstitial sites in and around the Er-rich regions. The clustering enables the deuterium atoms to avoid energetically unfavorable Fe neighbors. The enthalpy release gained from this favorable change in deuterium environment provides the energy to drive the atomic-level decomposition of the crystalline phase (through Fe diffusion) that results in amorphization. Hydrogen-induced amorphization has long been attributed to the energetically advantageous hydrogen environments present in the amorphous phase [52]; we have succeeded in directly measuring the sizeable enthalpy release associated with the energetic driving force for amorphization.

Second, the fact that the amorphization transition temperature *decreases* as the packing fraction (PF) in the sealed DSC pans *increases* (Fig. 3.13) can be attributed to a concentration dependence of the amorphization mechanism. Recall that for a given temperature, a higher PF corresponds to a higher concentration of deuterium in the crystalline phase. Also, the more deuterium present in the solid, the larger the lattice parameter of the C15 unit cell will be, meaning that the metal atoms will be farther apart. The greater the spacing between metal atoms, the easier it will be for the Fe atoms to diffuse out of their crystalline positions—hence, the lower temperature required for amorphization at higher PF. The same argument explains the pressure dependence of the amorphization temperature and activation energy in $GdFe_2H_{4.2}$ observed by Aoki *et al.* [19]. Decrease of the transition temperature and of the activation energy with higher ambient hydrogen pressure can both be attributed to the expanded crystalline lattice resulting from the increase in hydrogen concentration in the solid phase with pressure.

Diffusional activation energy for ErD_2 crystallization

The activation energy for crystallization of ErD_2 in amorphous $ErFe_2D_{2.8}$ determined by Kissinger analysis is $E_a \approx 2.7\,\mathrm{eV/atom}$. This value is much higher than the E_a for amorphization, which implies that a different mechanism governs crystallization of ErD_2. It is reasonable to assume that a certain amount of atomic rearrangement in the Er+D clusters will be necessary for crystallization to occur. Therefore, the measured activation energy may correspond to Er diffusion, which would likely be the rate-limiting step in the crystallization process; not surprisingly, the activation energy for ErD_2 crystallization is close to that of

Er self-diffusion (3.1 eV/atom [53]). Furthermore, the observed *increase* in the crystallization temperature with PF can be attributed to the higher deuterium concentration in the Er+D clusters hindering Er rearrangement. Aoki *et al.* [19] found a similar increase in the GdH_2 crystallization temperature with increasing ambient hydrogen pressure.

Finally, no activation energy could be measured for crystallization of the amorphous Fe regions because it occurs at a temperature higher than the maximum at which the high-pressure DSC pans remain sealed (the Viton O-ring begins to decompose around 425 °C). No activation energy for Fe precipitation in amorphous $GdFe_2H_{3.2}$ was reported by Aoki *et al.,* either.

3.5.3 Violation of the polymorphous constraint

The clustering of Er and Fe during amorphization of $ErFe_2D_{3.2}$ described in the previous section occurs without apparent phase separation, at least as phase separation is traditionally considered. The clusters of Er and Fe are probably smaller than the $\sim$2 nm ErD_2 regions that crystallize at a higher temperature (section 3.4.1). Thus, the chemical composition profile of the amorphous phase is essentially uniform except when considered at an almost atomic length scale! If we did not know about the short-range clustering, we might think that the deuterium-induced amorphization of $ErFe_2$ occurred polymorphously.

But polymorphous amorphization—just like polymorphous melting—should be endothermic: At the polymorphous transition temperature T_0, $G_A - G_X = \Delta H - T_0 \Delta S = 0$, which means that $\Delta H = T_0 \Delta S$. Since the amorphous phase has a higher entropy than that of the crystal (except at the critical point of the polymorphous phase diagram of Fecht and Johnson [4]), $\Delta H > 0$. But we measured $\Delta H < 0$ for amorphization of $ErFe_2D_{3.2}$. Hence, the transition could not have occurred at the polymorphous melting point T_0. Apparently, the clustering observed in the amorphous phase, despite the very short range over which it occurred, was enough to change the thermodynamics of the amorphization transition from what one would expect of a polymorphous transition to one that is *completely* different. If the amorphization is not truly polymorphous, then ΔG need not be zero at the transition. For the reaction to occur spontaneously at a given temperature $T_{\rm a}$, it is necessary for the free energy to drop (i.e., $\Delta G < 0$). This requires only that $\Delta H - T_{\rm a}\Delta S < 0$ or $\Delta H < T_{\rm a}\Delta S$. A negative enthalpy change and a positive entropy change are certainly consistent with this relation; in fact, both help to satisfy it. Thus, from this perspective the exothermic heat release upon amorphization merely indicates that amorphization occurred nonpolymorphously at a temperature $T_{\rm a} < T_0$.

Superheating with respect to the clustered state

Since $\Delta H \ll 0$ and $\Delta S > 0$ (clustering could make ΔS negative, but that tendency is offset by the topological disorder of the clustered regions), $\Delta G = \Delta H - T_{\rm a}\Delta S \ll 0$. Thus, before amorphization the crystal is in a highly superheated state! It is so superheated, in fact, that it is almost certainly heated beyond the "inverse Kauzmann" temperature proposed by Fecht and Johnson [4], if one could define the entropy of the clustered liquid corresponding to the experimentally obtained clustered amorphous state. The free energy curves drawn in Fig. 3.17 illustrate this superheating as a function of deuterium concentration. The concave free energy curve accounts for the tendency of the amorphous phase to decompose into clustered regions of different composition. This diagram is also consistent with the compositional dependence of the amorphization temperature as inferred from its packing-fraction (PF) dependence. The higher the PF, the higher the concentration of deuterium in the sample at a given temperature. Since the driving force for amorphization, ΔG, increases as the amount of deuterium

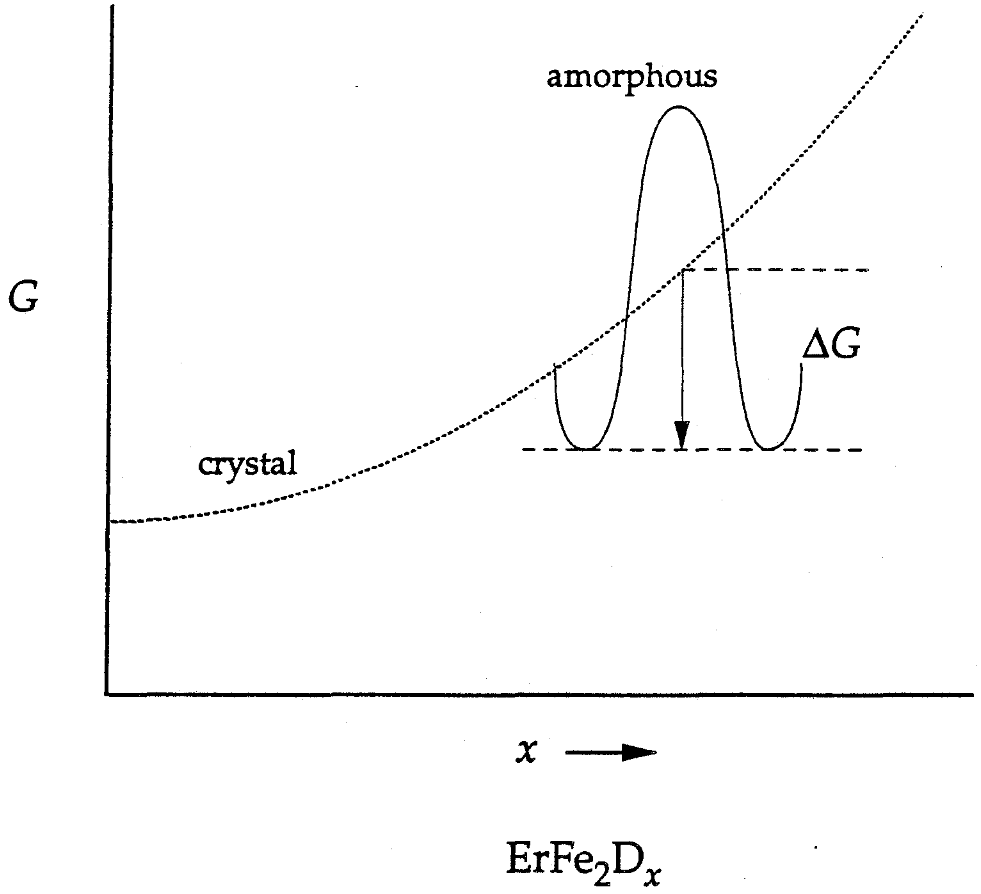

Figure 3.17: Schematic free energy curves of crystalline and amorphous phases of $ErFe_2D_x$ as a function of deuterium concentration x. The driving force for amorphization *with clustering* is given by the downward arrow. The concave free energy curve of the amorphous phase accounts for its tendency to decompose into clustered regions of different composition.

in the solid increases, the amount of additional thermal energy needed to cause the amorphization reaction to proceed will decrease with increasing deuterium concentration. Thus, the reaction temperature goes down with increasing PF.

Phase diagram of $ErFe_2$+D

Using schematic free energy curves as in Fig. 3.17, we can infer a possible phase diagram for the deuterated $ErFe_2$ system having an unusual feature (Fig. 3.18). A miscibility gap appears in the amorphous phase at a temperature T^* due to development of a region of negative curvature in the associated free energy curve G_{A}; below T^* the homogeneous amorphous phase decomposes into clustered states with compositions at the minima of G_{A}. At still lower temperatures, the free energy curve of the crystalline phase drops below that of the amorphous phase, passing first through a eutectic-like condition at T_{e^*}, at which the two amorphous phases and the crystalline phase simultaneously satisfy the chemical potential equilibrium conditions (as indicated by the common-tangent construction). Below T_{e^*}, which may be negative, the crystalline phase opens up into an equilibrium phase field. Upon heating of a sample with composition c_{e^*} from the single-phase crystalline region to a temperature above T_{e^*}, the system transforms into two liquid-like phases—a sort of inverse analogue to eutectic solidification, in which a single-phase liquid transforms into two crystalline phases. (For this reason, we have given it the name *inverse eutectic.*) The T_0 line for the crystalline phase is sketched into the phase diagram, as well. Just as with the polymorphous phase diagram of Fecht and Johnson (section 1.5.3) the T_0 line indicates a boundary to superheating and supersaturation of the crystalline phase. It is improbable that the crystalline phase of such a diagram could melt or amorphize polymorphously because the T_0 line is located entirely within the miscibility gap of the amorphous phase—only if the crystal were somehow driven intact beyond the T_0 line could it

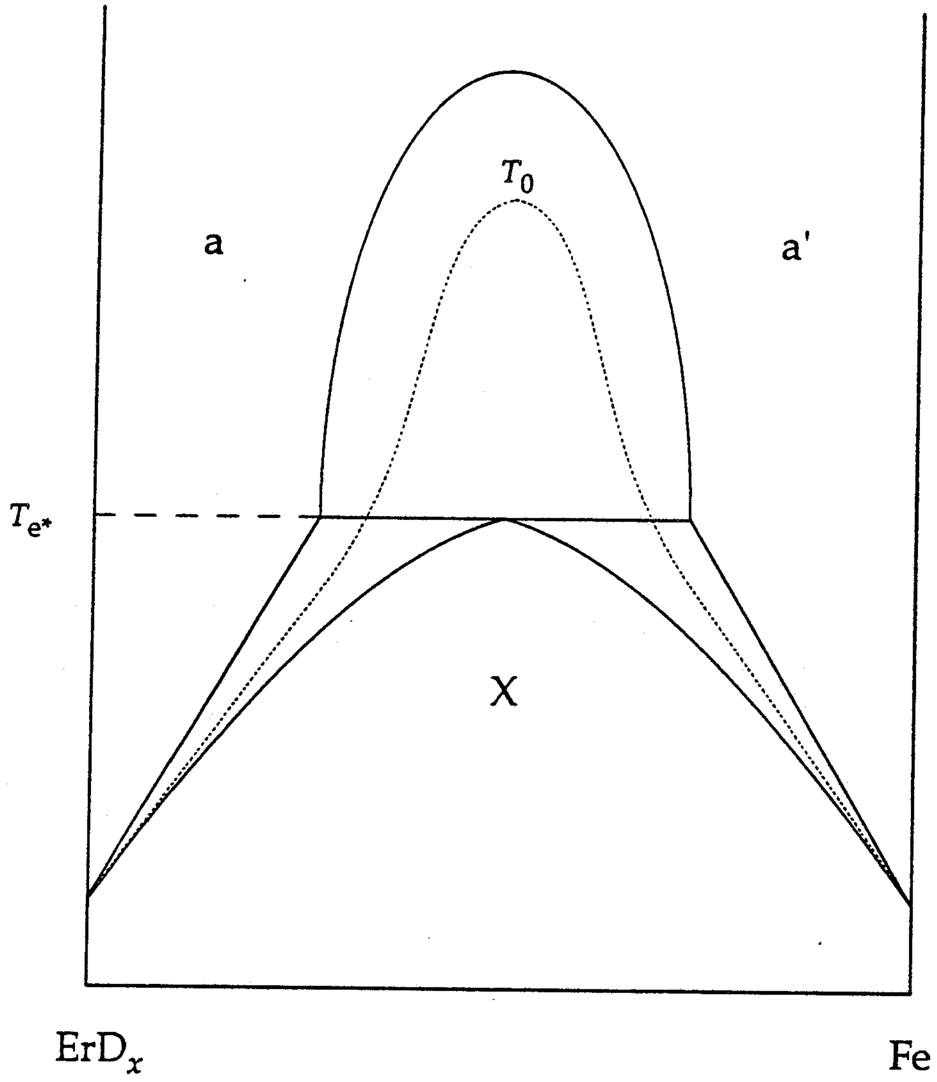

Figure 3.18: Possible phase diagram for $ErFe_2$+D derived from free energy curves of the type in Fig. 3.17. The crystalline phase opens up into a phase field below the temperature T_{e^*}. Heating from this crystalline region to a temperature above T_{e^*} causes a crystalline phase to transform to two amorphous phases—a sort of inverse to eutectic solidification, in which a liquid phase transforms into two crystalline phases.

then transform to a uniform amorphous phase.

The prediction of this schematic phase diagram regarding the unlikelihood of observing polymorphous amorphization in $ErFe_2D_{3.2}$ is probably true of all known examples of hydrogen-induced amorphization. The clustering mechanism that we have deduced from the structure of amorphous deuterated $ErFe_2$ may be a universal feature of such crystal-to-amorphous transitions, regardless of whether the material first forms a crystalline hydride or transforms directly to the amorphous phase. When discussing the topological change in a crystal upon hydrogen-induced amorphization, Dubois [54] has emphasized the importance of the role of preferential chemical bonding (such as between a rare-earth element and hydrogen) and the unsuitability of simple disorder parameters like atomic-size mismatch or atomic mean-square displacement for describing this particular crystal-to-amorphous transition. In this respect, hydrogen-induced amorphization may be better understood as a chemical reaction than as an instability-induced thermodynamic phase transition.

References

[1] U-In Chung, Yong-Gyoo Kim and Jai-Young Lee, *Philos. Mag. B* **63**, 1119 (1991).

[2] K. Aoki, A. Yanagitani, X.-G. Li and T. Masumoto, *Mater. Sci. Eng.* **97**, 35 (1988).

[3] H. J. Fecht, Z. Fu and W. L. Johnson, *Phys. Rev. Lett.* **64**, 1753 (1990).

[4] H. J. Fecht and W. L. Johnson, *Nature (London)* **334**, 50 (1988).

[5] C. E. Krill III, J. Li, W. L. Johnson and W. B. Yelon, *Bull. Am. Phys. Soc.* **37**, 258 (1992).

[6] C. E. Krill III, J. Li, C. Ettl, K. Samwer, W. B. Yelon and W. L. Johnson, to be presented at the Eighth International Conference on Liquid and Amorphous Metals, Vienna, 31 August–4 September 1992.

[7] Address: P.O. Box 8247, Ward Hill, MA 01835-0747.

[8] Harold P. Klug and Leroy E. Alexander, *X-ray Diffraction Procedures for Polycrystalline and Amorphous Materials,* 2nd ed. (Wiley, New York, 1974), Chap. 4.

[9] B. D. Cullity, *Elements of X-ray Diffraction,* 2nd ed. (Addison-Wesley, Menlo Park, CA, 1978), p. 511.

[10] Harold P. Klug and Leroy E. Alexander, *X-ray Diffraction Procedures for Polycrystalline and Amorphous Materials,* 2nd ed. (Wiley, New York, 1974), p. 493.

[11] B. D. Cullity, *Elements of X-ray Diffraction,* 2nd ed. (Addison-Wesley, Menlo Park, CA, 1978), p. 102.

[12] Valery F. Sears, in *Neutron Scattering,* Part A, edited by Kurt Sköld and David L. Price, Methods of Experimental Physics, Vol. 23 (Academic, New York, 1986), Appendix.

[13] B. D. Cullity, *Elements of X-ray Diffraction,* 2nd ed. (Addison-Wesley, Menlo Park, CA, 1978), p. 112.

[14] G. Kostorz and S. W. Lovesey, in *Neutron Scattering,* edited by G. Kostorz, Treatise on Materials Science and Technology, Vol. 15 (Academic, New York, 1979), pp. 4–8.

[15] K. Sköld, M. H. Mueller and T. O. Brun, in *Neutron Scattering,* edited by G. Kostorz, Treatise on Materials Science and Technology, Vol. 15 (Academic, New York, 1979), p. 425.

[16] T. B. Flanagan, J. D. Clewley, N. B. Mason and H. S. Chung, *J. Less-Common Met.* **130**, 309 (1987).

[17] K. Aoki, A. Yanagitani and T. Masumoto, *Appl. Phys. Lett.* **52**, 2122 (1988).

[18] K. Aoki, X.-G. Li and T. Masumoto, *Mater. Sci. Eng.* **A133**, 565 (1991).

[19] K. Aoki, X.-G. Li and T. Masumoto, *Acta Metall. Mater.* **40**, 221 (1992).

[20] *Perkin-Elmer Thermal Analysis and Supplies Catalog,* No. T-1, The Perkin-Elmer Corporation, 761 Main Avenue, Norwalk, CT 06859-0156, 1990, p. 9.

[21] H. A. Kierstead, P. J. Viccaro, G. K. Shenoy and B. D. Dunlap, *J. Less-Common Met.* **66**, 219 (1979).

[22] A. Seiler, L. Schlapbach and H. Scherrer, *Surf. Sci.* **121**, 98 (1982).

[23] Jong-Man Park and Jai-Young Lee, *Scripta Metall.* **23**, 1525 (1989).

[24] *Perkin-Elmer Thermal Analysis and Supplies Catalog,* No. T-1, The Perkin-Elmer Corporation, 761 Main Avenue, Norwalk, CT 06859-0156, 1990, pp. 8 and 10.

[25] Colin J. Williams, Senior Field Technical Specialist: Thermal & Elemental Analysis, The Perkin-Elmer Corporation, 10 Faraday, Irvine, CA 92718-2769, (714) 458-7262 (private communication).

[26] Instruction sheet No. 993-9115 for Perkin-Elmer No. 0319-0218 LVC capsules (unpublished).

[27] Philip M. Morse, *Thermal Physics,* 2nd ed. (Benjamin/Cummings, London, 1969), p. 94.

[28] Charles Kittel and Herbert Kroemer, *Thermal Physics,* 2nd ed. (W. H. Freeman, New York, 1980), p. 170.

[29] T. de Saxcé, Y. Berthier and D. Fruchart, *J. Less-Common Met.* **107**, 35 (1985).

[30] D. Fruchart, Y. Berthier, T. de Saxce and P. Vuillet, *J. Less-Common Met.* **130**, 89 (1987).

[31] D. Fruchart, Y. Berthier, T. de Saxce and P. Vuillet, *J. Solid State Chem.* **67**, 197 (1987).

[32] W. B. Pearson, *The Crystal Chemistry and Physics of Metals and Alloys,* (Wiley, New York, 1972), p. 42.

[33] G. E. Fish, J. J. Rhyne, S. G. Sankar and W. E. Wallace, *J. Appl. Phys.* **50**, 2003 (1979).

[34] David A. Porter and Kenneth E. Easterling, *Phase Transformations in Metals and Alloys,* (Van Nostrand Reinhold (International), London, 1981), p. 28.

[35] Henry A. Kierstead, *J. Less-Common Met.* **70**, 199 (1980).

[36] W. G. Saba, W. E. Wallace, H. Sandmo and R. S. Craig, *J. Chem. Phys.* **35**, 2148 (1961).

[37] W. E. Wallace, *J. Chem. Phys.* **35**, 2156 (1961).

[38] D. R. Gaskell, in *Physical Metallurgy,* 3rd ed., edited by R. W. Cahn and P. Haasen (Elsevier, Amsterdam, 1983), Part 1, p. 278.

[39] Homer E. Kissinger, *Anal. Chem.* **29**, 1702 (1957).

[40] K. F. Kelton (private communication).

[41] D. W. Henderson, *J. Non-Cryst. Solids* **30**, 301 (1979).

[42] Paul Shewmon, *Diffusion in Solids,* 2nd ed. (The Minerals, Metals & Materials Society, Warrendale, PA, 1989), p. 74.

[43] A. Guinier, *X-Ray Diffraction in Crystals, Imperfect Crystals, and Amorphous Bodies,* (W. H. Freeman, San Francisco, 1963), p. 73.

[44] Harold P. Klug and Leroy E. Alexander, *X-ray Diffraction Procedures for Polycrystalline and Amorphous Materials,* 2nd ed. (Wiley, New York, 1974), pp. 847–850.

[45] M. Matsuura, K. Fukamichi, H. Komatsu, K. Aoki, T. Masumoto and K. Suzuki, *Mater. Sci. Eng.* **97**, 223 (1988).

[46] X. L. Yeh, K. Samwer and W. L. Johnson, *Appl. Phys. Lett.* **42**, 242 (1983).

[47] R. C. Bowman, Jr., J. S. Cantrell, K. Samwer, J. Tebbe, E. L. Venturi and J. J. Rush, *Phys. Rev. B* **37**, 8575 (1988).

[48] W. B. Pearson, *The Crystal Chemistry and Physics of Metals and Alloys,* (Wiley, New York, 1972), pp. 52–61.

[49] *CRC Handbook of Chemistry and Physics,* 68th ed., edited by Robert C. Weast, Melvin J. Astle and William H. Beyer (CRC Press, Boca Raton, FL, 1987), p. F-161.

[50] A. Taylor, *X-ray Metallography,* Wiley (New York, 1961, pp. 332–336).

[51] M. P. Dariel, L. Kornblit, B. J. Beaudry and K. A. Gschneidner, *Phys. Rev. B* **20**, 3949 (1979).

[52] K. Samwer and W. L. Johnson, *Phys. Rev. B* **28**, 2907 (1983).

[53] F. H. Spedding and K. Shiba, *J. Chem. Phys.* **57**, 612 (1972).

[54] Jean-Marie Dubois, *J. Less-Common Met.* **145**, 309 (1988).

Chapter 4

Precursors of instability in Nb–Pd solid solutions

In the previous chapter we saw that supersaturation of $ErFe_2$ by hydrogenation led to a violation of the polymorphous constraint on an almost atomistic length scale and caused amorphization to occur in a completely different manner than expected from the polymorphous phase diagram. Instead of being reversible and endothermic, the amorphization was irreversible and strongly exothermic. We discussed reasons for suspecting that all hydrogen-induced amorphization transitions will share these characteristics. The anisotropic bonding behavior of the hydrogen (strongly favoring the rare-earth atoms over the transition metal atoms) leads to the clustering that results in a fundamental change in the short-range order of the material, rendering the polymorphous diagram inapplicable.

A way to avoid the asymmetric bonding problem of a ternary system—especially of one involving hydrogen—is to disorder a binary alloy simply by changing the relative concentrations of its components. In order to get an accurate measure of the variation of alloy properties as the composition nears the postulated stability limit of the crystalline phase, it must be possible to change the composition over a rather extended range (say, 15 at.% or more) without changing the symmetry of the crystalline phase. Solid solutions with such an extended solubility range tend to occur only when the relative size difference of the component atoms is less than 5%, but as discussed in section 2.2, the T_0 line that corresponds to such a small atomic size difference usually has a very shallow slope, making it uncertain whether it will ever become vertical. On the other hand, steep T_0 lines correspond to large relative atomic size differences, but according to the empirically well-founded Hume-Rothery Size-Factor rule [3], such alloys do not have extended solubility ranges. As is frequently the case, the requirements of experiment and theory are at loggerheads.

4.1 Why Nb–Pd?

A promising compromise, however, is found in the Nb–Pd binary system [1, 2]. The phase diagram (see Fig. 2.10) [4, 5] reveals a solid solubility range of the terminal Nb (bcc) phase (also called α-Nb) out to ~36 at.% Pd at 1520 °C as well as narrowly spaced liquidus and solidus lines that allow the position of the T_0 line to be estimated fairly accurately. The far edge of the equilibrium single-phase bcc phase field approaches within ~7 at.% Pd of the T_0 line at 1520 °C) (see Fig. 2.16). While $Nb_{100-x}Pd_x$ has an fcc phase at $49 \le x \le 60$ (called α-NbPd), it is unstable below 1255 °C; at room temperature the nearest intermetallic to α-Nb is $NbPd_2$, which has a body-centered orthorhombic $MoPt_2$-type structure.

Previous studies described in Chapter 2 (section 2.3.2) found that vapor deposition is not able to extend the solubility range of α-Nb out to the T_0 line because of the formation of an amorphous phase. The effective quench rate of techniques like rapid quenching, on the other hand, is much slower than that of vapor deposition [6], resulting in little or no trapping of atoms in an amorphous phase [1]. Splat quenching was able to extend the α-Nb phase out to nearly 42 at.% Pd, which is 6 at.% beyond the high-temperature limit for α-Nb and at least 22 at.% beyond its solubility range at room temperature! No sign of the intermetallic $NbPd_2$ was found at any composition studied. The fcc α-NbPd phase, on the other hand, was found at Pd concentrations of 42 at.% and higher. The formation of α-NbPd is difficult to avoid because of its high-temperature equilibrium solubility range; this presents a formidable barrier to extension of the bcc Nb-rich phase because a liquid solution with 49 at.% Pd or more must be cooled through a temperature range of 200–300 °C where nucleation and growth of the fcc phase is favored.

Another salient feature of the Nb–Pd phase diagram is the relative extent to which the T_0 line falls before reaching the eutectic temperature: it drops to 65 % of the melting point of pure Nb at $\sim$41 at.% Pd. Extrapolating the T_0 line to higher Pd concentrations on the Nb–Pd equilibrium phase diagram suggests that the T_0 line may become vertical between 50 and 60 at.% Pd, implying that we can perhaps supersaturate Nb with Pd to within $\sim$15 at.% of the postulated instability concentration c^*.

4.2 Experimental details

4.2.1 Ingot preparation

Ingots of various compositions were prepared by arc melting Nb wire (ESPI, 99.995 %) and Pd foil (Materials Research Corporation, 99.99 %). While compositions stated denote the nominal stoichiometry before arc melting, mass changes during melting were negligible. A particular problem for purification of Nb is separating it from tantalum. Typical Ta concentrations in the best Nb are 300–1000 ppm [7]; only with expensive electron-beam processing can the Ta content be reduced below 300 ppm. While the vendor claimed that the Ta content of the Nb wire used in these experiments was 300 ppm, no independent measurement of this quantity was attempted. Regardless, any effect that the Ta impurity could have on these experiments would probably be overshadowed by that of nonmetallic impurities, such as oxygen, but we found no evidence for oxidation of either the ingot before splat quenching or the quenched foils in x-ray or neutron diffraction scans.

4.2.2 Splat quenching

The arc-melted ingots were broken into 100–200 mg pieces, which were levitation melted in a high-frequency rf field and subsequently quenched into thin foils in an argon-filled Bühler twin-piston rapid quencher (see Fig. 2.13). The typical cooling rate for this process is 10^5–10^7 K/sec at the freezing point, slowing by an order of magnitude or greater as ambient temperature is approached [8]. Due to heat flow considerations, the cooling rate is inversely proportional to the thickness of the resulting foil [9]. Foil thicknesses ranged from 50 to 80 μm at the center to as thin as 30 μm at the edge. The homogeneity of the splats was checked by x-ray diffraction using a Philips diffractometer operating in θ–2θ mode with Cu Kα radiation. Due to the opposing-piston geometry of the rapid quencher, one side of the splat is always cooled at a somewhat faster rate than the other: the falling liquid metal drop makes contact first with one piston and then collides with the opposing piston. The quench rate on the side of the splat hit by the second piston is faster than that hit by the first piston because the splat is in contact with the second piston for a shorter amount of time. (This had a noticeable effect on the relative amount of bcc α-Nb and fcc α-NbPd phase in splats of $\mathrm{Nb}_{100-x}\mathrm{Pd}_x$ with $42 \leq x \leq 50$. In that region, the faster the quench, the greater is the relative proportion of bcc α-Nb that would nucleate and grow in the splat [1].) At 42 at.% Pd a small amount of the undesired fcc phase was always detected on both sides of the splat by x-ray diffraction, implying that a certain amount of fcc α-NbPd was distributed throughout the sample.

4.2.3 Low-temperature elastic neutron diffraction characterization

The use of elastic neutron diffraction to study samples at temperatures elevated above room temperature was described in the previous chapter (section 3.2.3). Neutron diffraction is also a convenient tool for characterization of samples held at low temperatures. The long penetration depth of neutrons facilitates the construction of low-temperature cryostats that do not cause a prohibitive amount of beam attenuation. We performed elastic neutron diffraction measurements at the Missouri University Research Reactor (MURR) on Nb–Pd alloy samples held at 12 K, 100 K, 200 K and 300 K in a cryorefrigerated cold head unit (Fig. 4.1). The sample pieces were held in a vanadium tube that was attached to one of the inside faces of an aluminum cylinder filled with helium gas. The high thermal conductivity of He gas helps to equilibrate the temperature of the sample, as does the fact that the aluminum cylinder acts as a large heat shield around the sample; since the boiling point of He is 4.2 K [10], it remains gaseous even at the lowest temperature reached by the cold head. The temperature was held constant to within ±1 K by a Lake Shore cryogenic temperature controller connected to a thermocouple and resistance heaters in the cold head. All other details of operation of the neutron powder diffractometer, including data acquisition, were identical to those described above for the high-temperature sample holder (section 3.2.3) with the exception that in this case no extraneous Bragg peaks resulted from the sample holder because vanadium has an extremely small coherent scattering cross section for neutrons [11]. (The aluminum cylinder and cold-head housing contributed no peaks because they are located so far from the sample.)

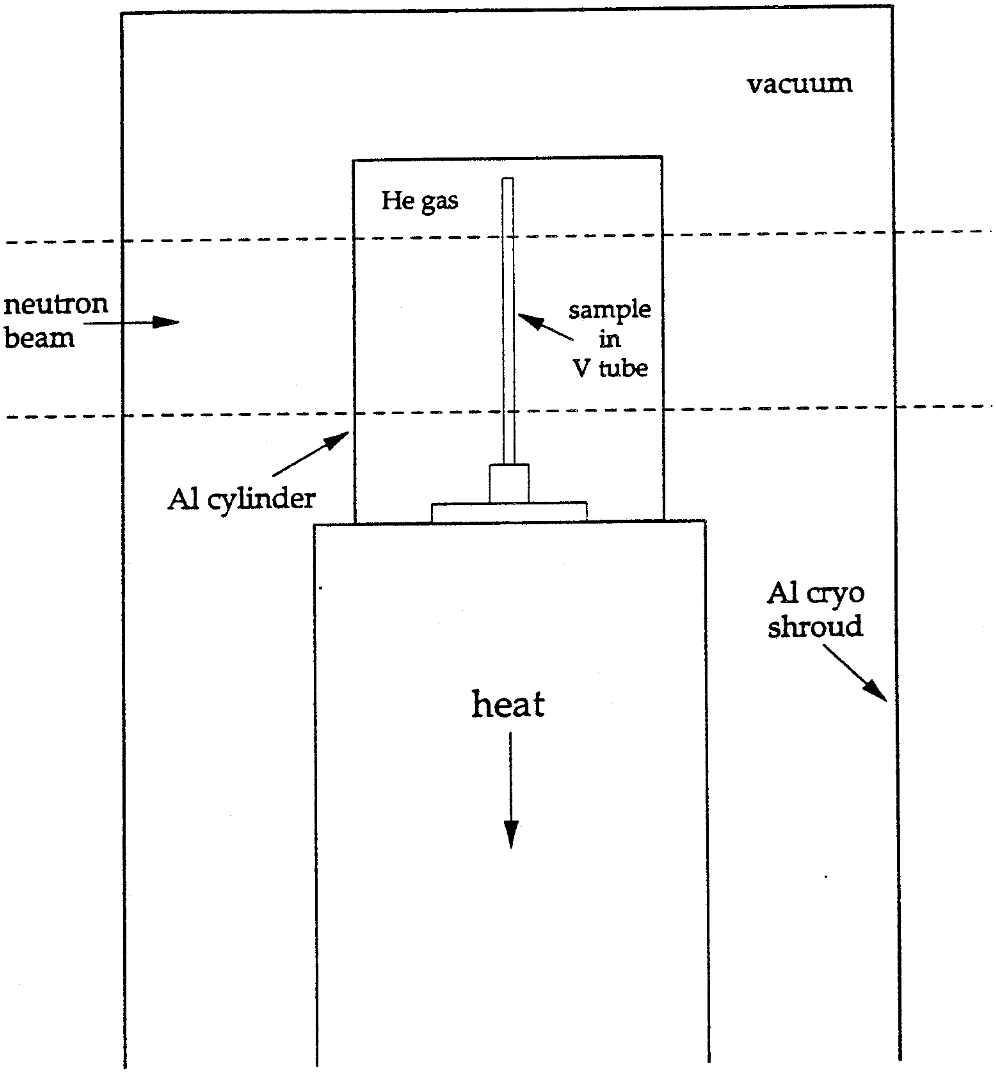

Figure 4.1: Schematic diagram of cryorefrigerated cold head sample holder for low-temperature neutron diffraction. When mounted on the powder diffractometer at MURR, the entire unit is upside down in comparison to this diagram.

4.2.4 Thermal expansion measured by dilatometry

Since thermal expansion of a solid occurs only because of the anharmonic shape of the interatomic potential [12], change in a material's thermal expansion coefficient signifies modification of the shape of the potential function. The linear thermal expansion coefficient α_L is defined as:

$$\alpha_\mathrm{L} \equiv \frac{1}{L}\left(\frac{\partial L}{\partial T}\right)_P = \frac{1}{a}\left(\frac{\partial a}{\partial T}\right)_P, \tag{4.1}$$

where L is the length of the specimen, T is temperature, P is pressure and a is the unit cell parameter. (The latter equality holds for cubic materials.)

One method for measuring α_L is to determine the change in lattice parameter a as a function of temperature. Values for the lattice parameter are easy to obtain from elastic x-ray or neutron diffraction, but the precision with which they can be determined is often too low to determine α_L with an uncertainty of less than 10–20 %. This problem is especially acute with metastable materials of small grain size and/or high strain, for their rather broad Bragg peaks increase the uncertainty in a significantly. A simple calculation suffices to illustrate the problem: for a temperature change of 300 K, a lattice parameter of $a = 0.3\,\mathrm{nm}$ and a minimum uncertainty in the change in a of 0.0001 nm (usually δa is known only to within 0.0003 nm or so), the resultant uncertainty in α_L is approximately

$$\delta\alpha_\mathrm{L} \simeq \frac{\delta a}{a\Delta T} = 1 \times 10^{-6}. \tag{4.2}$$

Typical values for α_L are 7.3×10^{-6} for Nb at room temperature [13] and 11.8×10^{-6} for Pd at room temperature [14], so the relative error in determining α_L by diffraction is about 10 % even under ideal conditions.

Much better results can be obtained from measurements of the overall length L of a specimen, since then the absolute change is much larger and easier to measure. For example, a piece of Nb that is 1 cm at room temperature will increase in length by more than 20 μm upon heating by 300 °C. Instruments constructed to measure such length changes—called *dilatometers*—can easily determine such distances with a relative error of less than 5 %. Making this kind of measurement on splat samples is subject to further complications due to geometrical considerations, but if the splats are self-supporting when stood on edge, the thermal expansion coefficient parallel to the plane of the splat can be measured quite reliably. The α_L of our samples—6 mm × 3 mm pieces cut from the center of splat-quenched foils—were measured by Manfred Klingel, a graduate student at the laboratories of Prof. Dr. H. Gleiter [15], from 150 K to room temperature using a dilatometer (Fig. 4.2). Uncertainties arising from flexing of the splats in the dilatometer necessitated three or four temperature scans for each sample to reduce the relative uncertainty in α_L to ~ 3 %.

4.2.5 Low-temperature heat capacity measurements

Low-temperature heat capacity measurements enable accurate determination of a sample's Debye temperature θ_D, which we will find to be an important parameter for estimating elastic properties and the dynamic mean-square displacements of atoms about their ideal lattice points. At temperatures $T \ll \theta_\mathrm{D}$, the heat capacity of a metal may be written as a sum of the electronic and lattice contributions: $C_P = \gamma T + AT^3$, where γ is a constant characterizing the electronic heat capacity and A is a constant characterizing the vibrational heat capacity [16]. Thus, the vibrational heat capacity can be isolated by fitting a straight line to a plot of C_P/T against T^2: the slope will give A and the intercept will give γ. The Debye temperature is determined from the $T = 0$ K expression for A evaluated with the Debye model for the phonon density of states:

$$A = \frac{12\pi^4}{5} \cdot \frac{Nk_\mathrm{B}}{\theta_\mathrm{D}^3}, \tag{4.3}$$

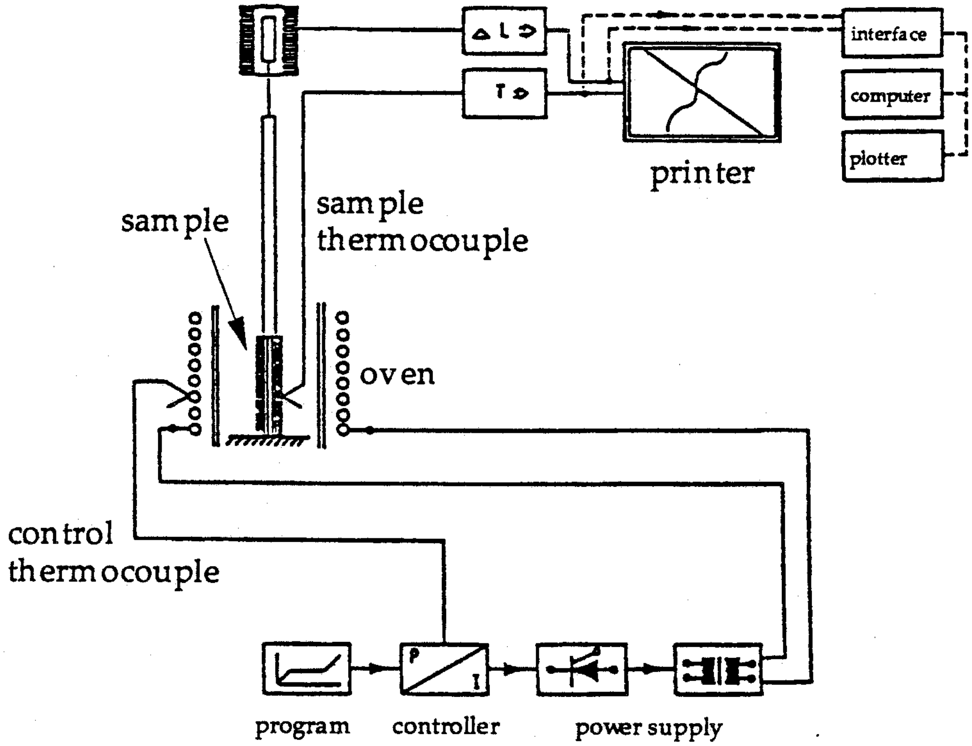

Figure 4.2: Schematic of dilatometer used to determine the thermal expansion coefficient α_L. Operating temperatures range from 150 K to room temperature. The thin-foil sample is stood on edge at the bottom of the apparatus as indicated. Its length is sensed by a carefully balanced rod pressing against it from above.

where N is the number of atoms in the sample [17].[1]

The Debye temperatures of Nb–Pd alloys of several compositions were measured by Christoph Ettl, a graduate student at the laboratories of Prof. Dr. K. Samwer [18]. He used a modified heat-pulse method to measure C_P between 1.5 K and 9 K [20, 21]. In this method, C_P is calculated from the duration and decay of the heat pulse according to the formula:

$$C_P = \frac{W\tau}{\Delta T}(1 - e^{-\Delta t/\tau}), \tag{4.4}$$

where W is the power of the heat pulse, Δt is its duration, ΔT is the maximum temperature change of the sample in response to the pulse and τ is the sample's temperature decay constant. The samples (individual splats) were fixed with grease onto a small sapphire plate having an evaporated Au heater and a Si chip for temperature measurement attached to its back. The entire apparatus was held in a ^{4}He cryostat (Fig. 4.3) and cooled to temperatures below 4.2 K by pumping on a small liquid ^{4}He bath. Temperatures above 4.2 K were achieved by heating with a manganese heater. A plot of C_P *vs.* T for $Nb_{70}Pd_{30}$ is given in Fig. 4.4(a) and determination of A is indicated in Fig. 4.4(b). Note the transition to superconductivity at about 2.2 K.

4.2.6 Sample preparation for TEM

In order to investigate the microstructure of the splats by transmission electron microscopy (TEM), it is necessary to thin them enough to allow penetration of the electron beam. While several rather involved techniques have been developed to thin semiconductor, polymer and bulk metal samples [22], sample preparation of splats is simplified by the fact that they already have one thin dimension [23].

---

[1] Actually, this formula for A is derived from the low-temperature expression for C_V (not C_P), but $C_P - C_V \to 0$ as $T \to 0$ because $C_P - C_V = 9\alpha_L{}^2 BVT$, where B is the bulk modulus [19].

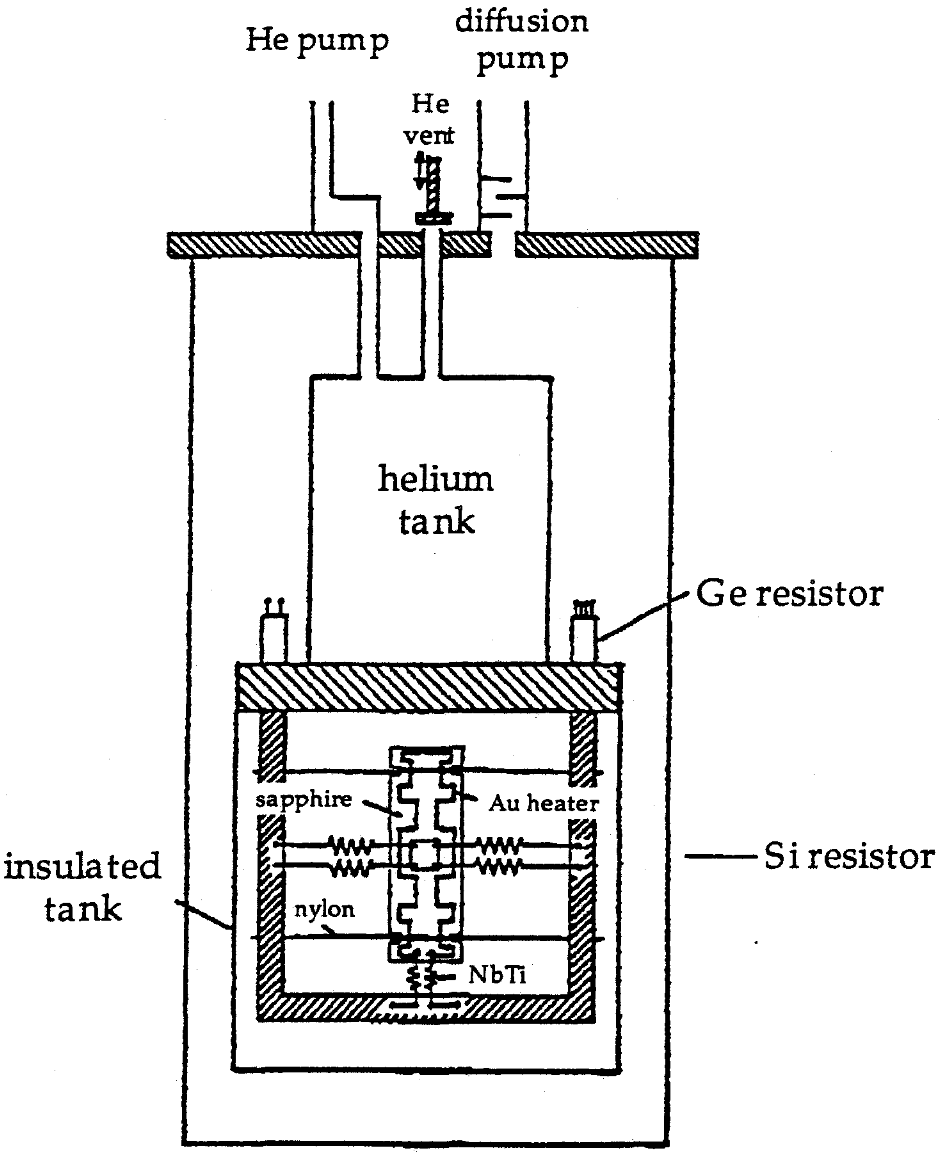

Figure 4.3: Schematic of apparatus for measuring low-temperature heat capacity by a modified heat-pulse method. The sample is mounted on the sapphire plate and heated by the evaporated Au strip. The nylon wires help to isolate thermally the sapphire plate from the ^{4}He bath. The heat-pulse voltage is delivered by the superconducting NbTi wires. Operating temperatures range from 1.5 K to 9 K.

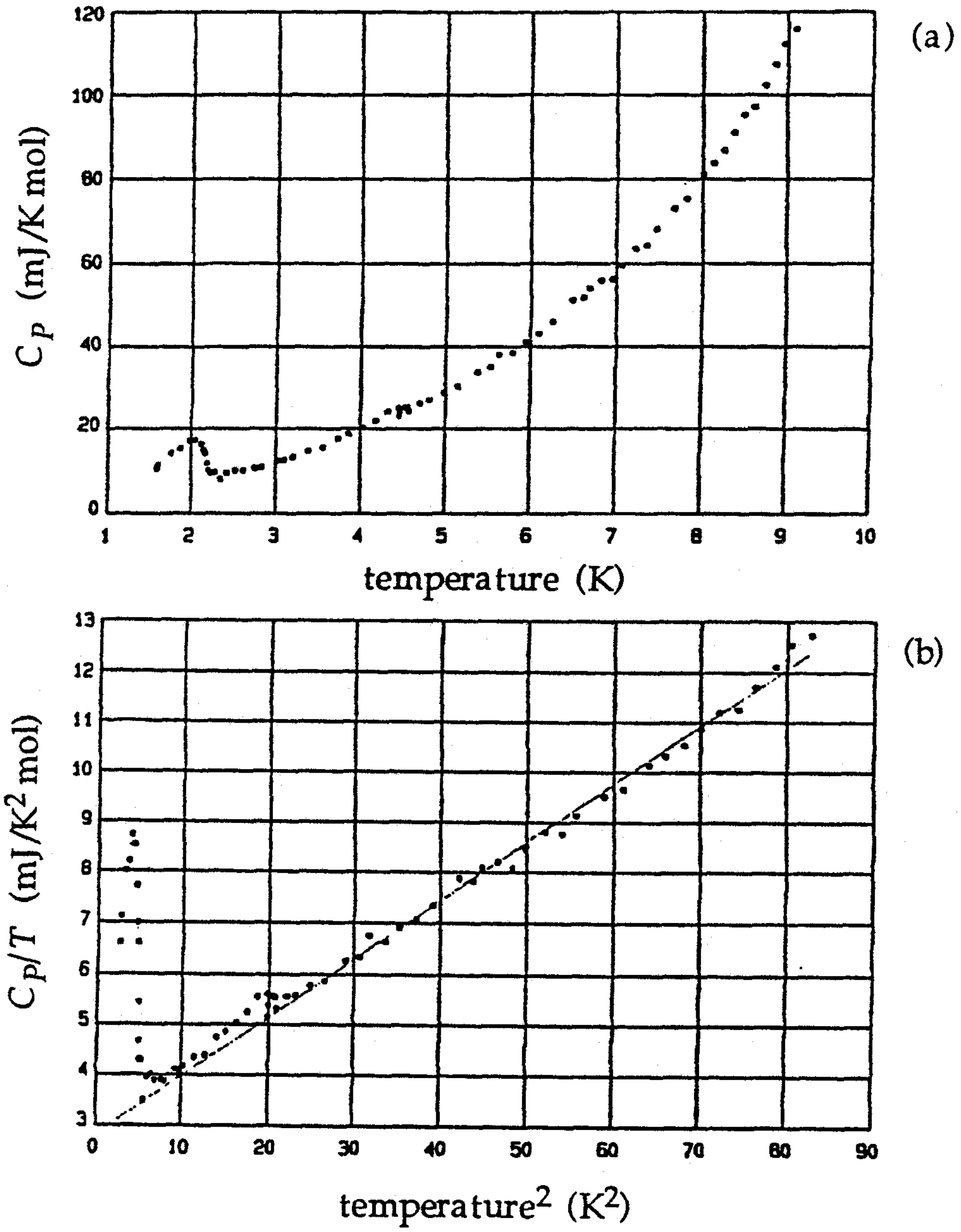

Figure 4.4: Low-temperature heat capacity measurement for $Nb_{70}Pd_{30}$: (a) C_P *vs.* T and (b) C_P/T *vs.* T^2. An estimate for A is obtained from a least-squares fit of a straight line to (b). The Debye temperature is then calculated from A using Eq.(4.3).

Three-millimeter-diameter disks were punched out of the splat foils and then attached to a Teflon^{TM} holder with paraffin. The wax acts as a mask to prevent the acid from attacking the edges of the disk. The standard etch for Nb is a roughly 2:1 solution of nitric acid (HNO_3) and hydrofluoric acid (HF) [24], and nitric acid also etches Pd [25]. By dipping the holder in a beaker of the above acid solution at room temperature for 15–30 seconds, rinsing the specimen in water and then looking for holes under an optical microscope, it was possible to produce areas thin enough for TEM analysis in about 20–30 minutes. This etch was adequate for all compositions of $Nb_{100-x}Pd_x$ studied ($0 \leq x \leq 42$).

4.3 Analysis of neutron diffraction data

The theoretical framework for describing the elastic scattering of neutrons from atoms of a condensed phase is formally identical to that which describes the elastic scattering of x-rays [26]. The only necessary modification to the structure factor describing the scattering amplitude is the replacement of the atomic form factor f appropriate for x-ray scattering with the scattering length b appropriate for neutron scattering, reflecting the difference between scattering from the electron cloud of the atom (x-rays) and from the atomic nucleus (neutrons). In both cases, the intensity $I_{\mathbf{G}}$ of the scattered diffraction probe at a reciprocal lattice point $\mathbf{G}$ is proportional to the square magnitude of the structure factor: $I_{\mathbf{G}} \propto |F_{\mathbf{G}}|^2 = F_{\mathbf{G}} F_{\mathbf{G}}^*$, where the proportionality factor is a function of such factors as the scattering geometry, the instrumental broadening and the multiplicity of the Bragg peak. All of the structural information about the sample—atomic positions, mean-square displacements and site occupancy probabilities—is found in the structure factor, however.

4.3.1 Structure analysis by powder diffraction

Hence, the determination of sample structure from x-ray or neutron diffraction must focus on careful measurement of the structure factors $F_{\mathbf{G}}$. Ideally, the sample in question is a single crystal large enough to provide a measurable diffracted beam intensity, since the theory of perfect-crystal diffraction is well-developed [27, 28], as are techniques for single-crystal structural refinement by either x-ray or neutron diffraction [29, 30]. Many kinds of samples, such as metals rapidly quenched from the melt, can be prepared only in polycrystalline form, however; structural determination of such samples is more difficult than of single crystals but often still feasible because all of the possible Bragg reflections from the sample will be present in any given diffraction scan (assuming more-or-less random crystallite orientation). Traditionally, structural refinement of such so-called "powder" samples is performed by integrating the measured Bragg peaks to gain an estimate for $|F_{\mathbf{G}}|^2_{\mathrm{meas}}$ and comparing this to a calculated $|F_{\mathbf{G}}|^2_{\mathrm{calc}}$ based on assumed atomic positions $\{\mathbf{r}\}$ in the unit cell and known atomic form factors or neutron scattering lengths [31]. Refinement of the atomic positions $\{\mathbf{r}\}$ is then accomplished by adjusting the atomic positions to minimize the R-factor:

$$R = \frac{\sum_{\mathbf{G}} \left| |F_{\mathbf{G}}|_{\mathrm{meas}} - |F_{\mathbf{G}}|_{\mathrm{calc}} \right|}{\sum_{\mathbf{G}} |F_{\mathbf{G}}|_{\mathrm{meas}}}, \tag{4.5}$$

or, alternatively,

$$R = \sum_{\mathbf{G}} w_{\mathbf{G}} \left(|F_{\mathbf{G}}|_{\mathrm{meas}} - |F_{\mathbf{G}}|_{\mathrm{calc}} \right)^2, \tag{4.6}$$

where $w_{\mathbf{G}}$ is a weighting factor determined by the relative accuracy of the corresponding diffraction intensity measurement. The same technique can be used to optimize the atomic mean-square displacements and the site occupancy probabilities in ordered solutions.

This traditional method breaks down frequently because of overlap of Bragg peaks in powder diffraction patterns, thus preventing the isolation of individual

$|F_{\mathbf{G}}|^2_{\text{meas}}$ values by peak integration [32]. An elegant way around that problem was developed by Rietveld in the late 1960s [33, 34]. His so-called "profile refinement" technique, which has become the standard structural refinement tool in neutron crystallography, assumes a peak profile function for the Bragg reflections, calculates the *entire* diffraction scan from a given set of atomic positions, mean-square displacements and site occupancies, and then compares the calculation to the observed diffraction scan in order to refine the structural parameters. Thus, peak overlaps pose no problem as long as the peak profile function is reasonably accurate. Standard nonlinear least-squares refinement techniques are used to minimize the quantity

$$M = \sum_k w_k \left(I_k^{\text{meas}} - I_k^{\text{calc}} \right)^2, \tag{4.7}$$

where I_k is the background-corrected intensity at the 2θ-point k and w_k is a weighting factor determined by the minimization scheme. I_k^{calc} is computed from all of the Bragg peaks of the given structure that contribute to the intensity at the point k. Labeling a Bragg reflection by its associated reciprocal-lattice vector $\mathbf{G}$, we have [32, 35]

$$I_k^{\text{calc}} = S \sum_{\mathbf{G}} |F_{\mathbf{G}}|^2 \, j_{\mathbf{G}} \, L_{\mathbf{G}} \, H(2\theta_k - 2\theta_{\mathbf{G}}), \tag{4.8}$$

where

S = scale factor,

$j_{\mathbf{G}}$ = multiplicity of reflection $\mathbf{G}$,

$L_{\mathbf{G}}$ = Lorentz factor,

$2\theta_{\mathbf{G}}$ = calculated 2θ position of $\mathbf{G}$,

$H(2\theta_k - 2\theta_{\mathbf{G}})$ = peak profile in 2θ-space.

The structure factor $F_{\mathbf{G}}$ is computed from the atomic unit cell positions $\{\mathbf{r}\}$, the site occupancy probabilities $p_{\mathbf{r}}$ and the isotropic temperature factor U_{iso} [36, 37]:

$$F_{\mathbf{G}} = \sum_{\mathbf{r}} p_{\mathbf{r}}\, b_{\mathbf{r}}\, e^{i\mathbf{G}\cdot\mathbf{r}} \exp\left(-\frac{8\pi^2}{3} U_{\mathrm{iso}} \frac{\sin^2\theta}{\lambda^2}\right), \tag{4.9}$$

where $b_{\mathbf{r}}$ is the neutron scattering length for the atom at site **r** and λ is the neutron wavelength. (The refinement can be carried out with an anisotropic temperature parameter if the symmetry of the crystal allows it.)

4.3.2 *GSAS:* Generalized Structure Analysis System

The actual refinement package that we used in analyzing the elastic neutron diffraction data from Nb–Pd splat-quenched alloys was *GSAS*, an acronym for *Generalized Structure Analysis System. GSAS* is an integrated set of computer programs [38], written and assembled by Allen C. Larson and Robert B. Von Dreele of Los Alamos National Laboratory, for performing single-crystal or powder Rietveld analyses on x-ray or neutron diffraction data. *GSAS* is written in VAX FORTRAN and runs under the VMS operating system on any of a number of graphics terminals. The current version can handle all diffraction effects except magnetic scattering, though future versions of *GSAS* will reportedly include this important component of neutron diffraction.

As an interactive data analysis package, *GSAS* presents the experimenter with several choices regarding the selection and complexity of functions for background subtraction and peak-profile modeling. I shall describe the functions upon which we settled by trial-and-error after a significant number of data analyses. Following this discussion I will briefly describe the manner in which we refined the temperature factor U_{iso}, since that will turn out to play an important role in our subsequent analysis of the structural changes accompanying supersaturation of the Nb-rich bcc phase of Nb–Pd.

Background subtraction

We used a cosine Fourier series function for background subtraction of the form:

$$I_{\text{back}} = B_1 + \sum_{j=2}^{n} B_j \cos[2\theta(j-1)], \tag{4.10}$$

where $B_1, B_2, \ldots, B_n$ are refinable coefficients and n is an integer up to 12. We used $n = 6$ for all compositions except pure Nb and $Nb_{93}Pd_7$, for which we used $n = 3$. The advantage of Eq. (4.10) is that it is always rather flat: it has enough curvature to fit any slight curvature in the background due to thermal diffuse scattering, but it does not follow background oscillations of short period [35]. All of the raw diffraction scans of the Nb–Pd alloys had very flat backgrounds—so flat in the case of pure Nb and $Nb_{93}Pd_7$ that more than three refinable coefficients led to no noticeable improvement in the fit.

Peak profile function

All of our analyses were performed using the standard Gaussian peak profile modified by Rietveld [34] for peak asymmetry. This function has the form:

$$H(2\theta_k\text{-}2\theta_{\mathrm{G}}) = \frac{1}{\sqrt{2\pi\sigma^2}} \left(1 - \frac{\Delta T\,|\Delta T|\,A_s}{\tan\theta}\right) e^{-(\Delta T)^2/2\sigma^2}, \tag{4.11}$$

where

$$\Delta T = 2\theta_k - 2\theta_{\mathrm{G}} + \frac{F_1}{\tan 2\theta}, \tag{4.12}$$

$$\sigma^2 = U\tan^2\theta + V\tan\theta + W + \frac{F_2}{\tan^4\theta}, \tag{4.13}$$

and U, V, W, A_s, F_1 and F_2 are refinable parameters. We refined all six parameters for each composition except pure Nb, for which F_1 and F_2 did not improve the fit.

The Gaussian function Eq. (4.11) fit the measured diffraction peak shapes very well except at the base of the lowest-angle (110) reflection, the tails of which fell off slightly more slowly than the Gaussian function would permit; nevertheless, the "missing" intensity was in all cases only a small fraction of the total area under the (110) peak. It is possible to improve the fit in such cases by replacing the Gaussian peak profile function with the more sophisticated *Voigt function,* which is a convolution of Lorentzian and Gaussian peak shape functions [39, 40, 41], but only at the expense of having still more refinable parameters. Once the number of refinable parameters becomes large, the nonlinear refinement program tends to adjust some of them to nonphysical values, indicating that the diffraction data has too little information to determine properly so many parameters. Our simple bcc diffraction scans are an example of just such a case, since unphysical parameter values resulted every time that we tried to fit the data with the Voigt diffraction profile.

Temperature parameter

The refinable temperature parameter U_{iso} appears in one of the exponential terms of Eq. (4.9); this term is commonly called the *Debye-Waller factor* [42]. It accounts for the reduction in intensity associated with the fact that with increasing temperature, the diffracting atoms in a crystal oscillate with greater amplitude about their ideal lattice positions. If we let the instantaneous position of a given atom be $\mathbf{r}(t)$ and its ideal position be $\mathbf{r}_0$, then its instantaneous displacement vector can be defined as $\mathbf{u}(t) \equiv \mathbf{r}(t) - \mathbf{r}_0$. If the amplitudes of the various $\mathbf{u}(t)$'s for all of the atoms are small or have a Gaussian distribution, then for monatomic cubic crystals it can be shown that U_{iso} is equal to the time-averaged mean-square displacement (MSD) $\langle u^2 \rangle$ [42, 43]. In the case of cubic crystals with more than one type of atom, to be strictly correct one must assign a different MSD to each atom type, but for practical purposes this is usually not necessary, since at high temperature ($T \gtrsim \theta_{\mathrm{D}}$) the MSD is independent of atomic weight [44].[2]

In a random solid solution there is no way to determine the relative contribution to the overall Debye-Waller parameter from each atomic component because all of the lattice sites giving rise to the diffraction signals have the same occupancy probability. Therefore, in bcc Nb–Pd alloys, the Debye-Waller factor gives a MSD averaged over the Nb and Pd contributions, $U_{\mathrm{iso}}^{\mathrm{Nb}}$ and $U_{\mathrm{iso}}^{\mathrm{Pd}}$; we expect $U_{\mathrm{iso}}^{\mathrm{Nb}}$ and $U_{\mathrm{iso}}^{\mathrm{Pd}}$ to be equal at high temperatures and to differ by no more than the difference of the inverse atomic weights of Nb and Pd ($\sim 13\,\%$) at low temperatures. Thus, it should not be a bad approximation to assume $U_{\mathrm{iso}}^{\mathrm{Nb}} \approx U_{\mathrm{iso}}^{\mathrm{Pd}}$. Furthermore, because of the cubic symmetry of the bcc lattice, the MSD of the "average atom" must be isotropic [46]. These considerations led us to refine an isotropic temperature parameter U_{iso} in Eq. (4.9) subject to the constraint that $U_{\mathrm{iso}}^{\mathrm{Nb}} = U_{\mathrm{iso}}^{\mathrm{Pd}}$.

Neutrons hold a distinct advantage over x-rays in refining the value of the temperature parameter, because the scattering potential for neutrons has a smaller spatial extent ($\sim 10^{-15}\,\mathrm{m}$ [47]) than that of the x-ray scattering potential ($\sim 10^{-10}\,\mathrm{m}$). Thus, the neutron scattering potential is better represented by a delta function than is that of x-ray scattering, resulting in more accurate structural information (especially with regard to thermal vibrations) [48].

GSAS provides estimates for the uncertainty in each refined parameter from the corresponding entry in the error matrix of the multivariable nonlinear least-squares fit [49]. Such error estimates properly take into account correlations between refinement parameters, but the estimates can provide a measure only of the uncertainty due to statistical fluctuations in the data and to inadequacy of fit—that is, such uncertainty values do not take into account the many potential

---

[2] At low temperature ($T \ll \theta_{\mathrm{D}}$), however, the MSD will vary roughly inversely with atomic weight [45].

sources of systematic error. The errors that we quote in the data of the next section are the one-standard-deviation values resulting from the *GSAS* fit without any additional estimated systematic error. Since we will mostly be investigating *relative* changes between measurements made in an as nearly identical fashion as possible, the systematic error should have minimal effect on our analysis and conclusions.

Figure 4.5 illustrates the ability of *GSAS* to fit one of our raw diffraction scans. The solid line running through the data points is the calculated diffraction scan, and the roughly flat scan below it is the difference curve between the measured and calculated diffraction intensities. Note how well the Rietveld analysis is able to fit the raw data.

4.4 Results

According to the polymorphous phase diagram of Fecht and Johnson [50], near the supersaturation limit a solid solution may exhibit "pre-amorphization" effects in one or more structural, thermodynamic or mechanical properties. Such anomalies should be easiest to recognize as deviations in the temperature or compositional dependence of the properties in question. As part of the search for these effects, we performed elastic neutron diffraction on a series of $\mathrm{Nb}_{100-x}\mathrm{Pd}_x$ alloys ($x = 0,\ 7,\ 15,\ 30$ and 42) at temperatures of 12 K, 100 K, 200 K and 300 K. We determined the lattice parameter, thermal expansion coefficient, inhomogeneous strain and atomic mean-square displacement from each diffraction scan using the program *GSAS* described in the previous section. Direct measurements of the thermal expansion coefficient from 150 K to 270 K by dilatometry and of the Debye temperature θ_{D} by low-temperature heat capacity supplement the information derived from neutron diffraction.

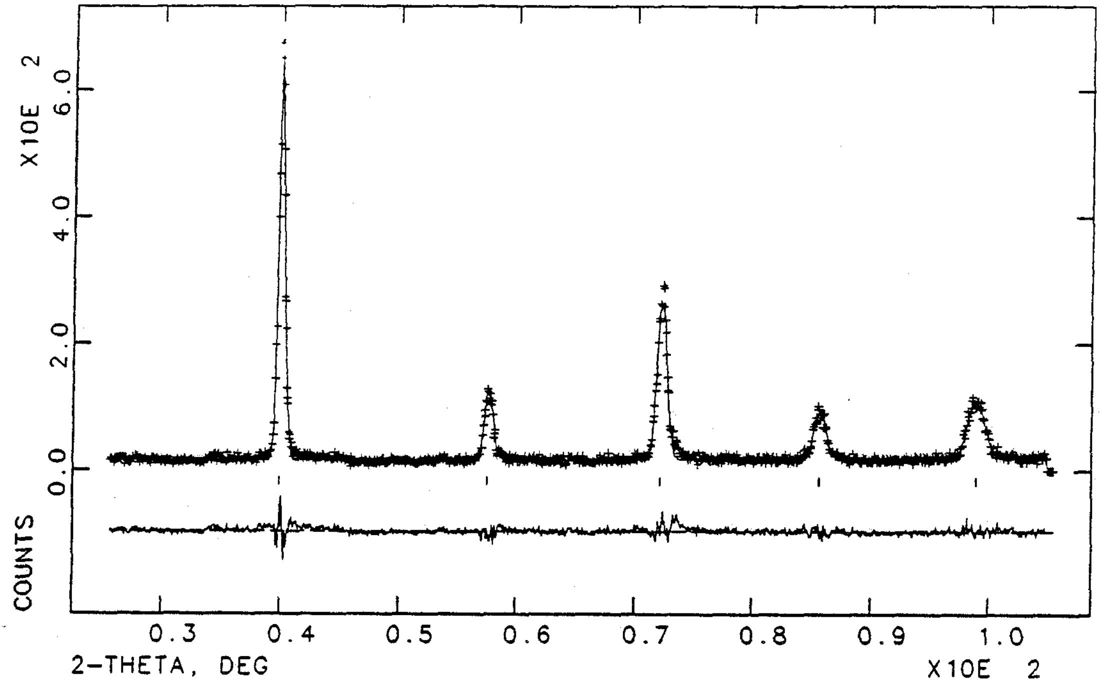

Figure 4.5: Example of Rietveld profile-refinement fit to raw elastic neutron diffraction data taken of $Nb_{70}Pd_{30}$ at 200 K. The solid line passing through the data points (crosses) in the upper scan is the calculated diffraction scan for the refined structural parameters, profile parameters and background coefficients. The lower scan is the difference curve between the measured and calculated intensities.

4.4.1 Lattice parameter

The bcc unit cell side length a is plotted against Pd concentration at each temperature in Figure 4.6. The lattice parameter varies nearly linearly with composition in accordance with Vegard's law [51, 52] until about 42 at.% Pd, at which composition a is larger than expected, implying either that (i) some solute segregation has occurred (i.e., the bcc crystals have less Pd than the overall composition would dictate) or that (ii) the true a *vs.* Pd concentration relationship is somewhat curved. X-ray analysis of a series of bcc Nb–Pd and Nb–Pd–Ge alloys found no evidence, however, for solute segregation, even at Pd concentrations above 42 at.% (see section 2.3.2) [1]; furthermore, deviations from Vegard's law are so numerous [53] that now they are considered the rule rather than the exception!

4.4.2 Thermal expansion coefficient

From the temperature variation of a at each alloy composition [Fig. 4.7(a)], we can estimate that the thermal expansion of bcc $Nb_{100-x}Pd_x$ alloys increases with x. By fitting a straight line to the data of Fig. 4.7(a), we can determine an "average" α_L for each composition using Eq. (4.1) [Fig. 4.7(b)].[3] The increase in α_L at $x = 42$ suggests that the crystal might be exhibiting growing anharmonicity as a precursor to instability—that is, the crystal could be nearing a point of divergence in α_L. Unfortunately, the uncertainty in a arising from the diffraction statistics increases with x because of significant peak broadening at high Pd concentrations. When substituted into Eq. (4.2), the uncertainties in a produce such large error bars ($> 20\,\%$) at all data points (especially at $x = 42$) that no significant compositional trend in α_L can be inferred from Fig. 4.7.

Since dilatometry can provide much more accurate determination of α_L than

---

[3] The thermal expansion coefficient is roughly constant at high temperature but varies as T^3 for $T \ll \theta_D$ [54].

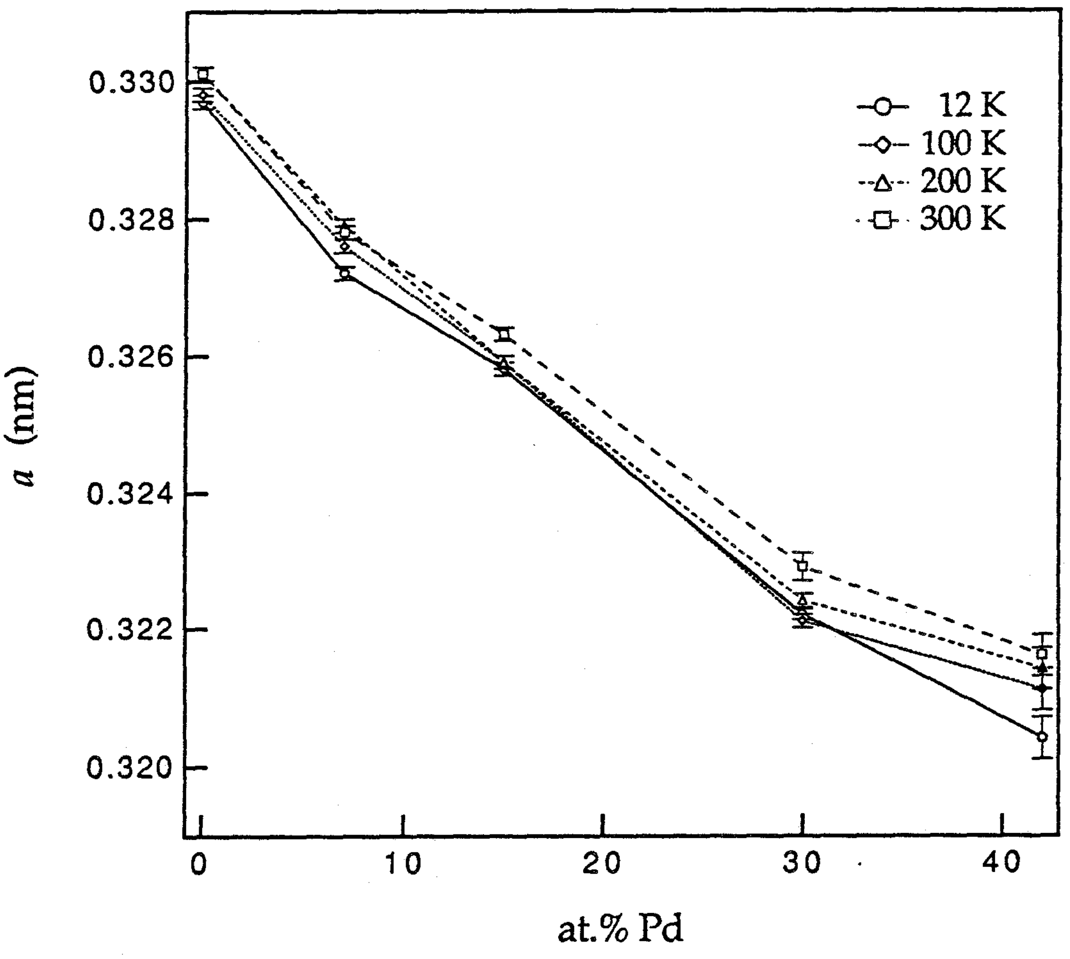

Figure 4.6: Lattice parameter *a* *vs.* Pd concentration in Nb–Pd alloys at several temperatures. Error bars are plus or minus one standard deviation, as provided by the *GSAS* fitting.

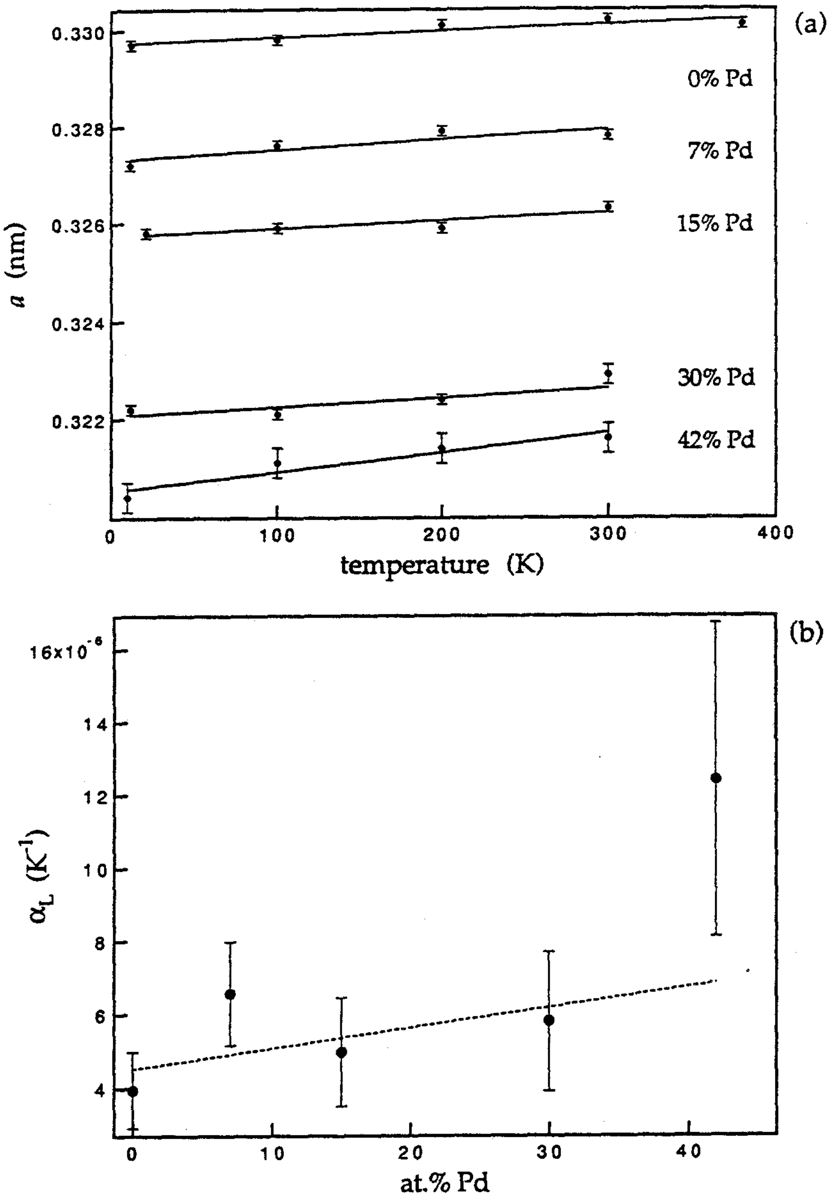

Figure 4.7: (a) Lattice parameter *vs.* temperature in Nb–Pd alloys at several compositions, and (b) average linear thermal expansion coefficient α_L estimated from the slopes in (a). The error bars in (b) are determined from the uncertainty of the least-squares fit to the data points in (a), taking into account the individual uncertainties associated with each data point.

diffraction can (see section 4.2.4), we arranged for several alloys of Nb–Pd to be measured in this manner from 150–270 K (Fig. 4.8). In Fig. 4.9 we compare the value of α_{L} at 150 K to the "average" α_{L} determined from neutron diffraction between 12 K and 300 K; evidently, the anharmonic collapse suggested by the neutron diffraction data is an artifact of statistical fluctuation. Plotting α_{L} against at.% Pd demonstrates that a roughly linear relationship exists across the entire composition range, even though the 52 at.% Pd and the pure Pd samples have fcc structure rather than bcc. Thus, we have no way of deciding whether the increase in α_{L} with Pd content in the bcc samples indicates significant destabilization of the crystalline structure or just a kind of weighted average of the anharmonicity in the interatomic potentials that cause thermal expansion (a Vegard's law for α_{L}?).

In retrospect, it is not surprising that α_{L} gives no sign of diverging as the crystalline phase nears its supposed stability limit with respect to amorphization. If we define an overall *Grüneisen parameter* γ_{g}, we can write (ignoring electronic effects) [55, 56]:

$$\alpha_{\mathrm{L}} = \frac{\gamma_{\mathrm{g}} C_V}{3VB}, \tag{4.14}$$

where C_V is heat capacity, V is the volume of the sample and B is its bulk modulus. The Grüneisen parameter is a constant having a typical value between one and two for most materials [56], and—as we shall argue in the next chapter (section 5.2.3)—the bulk modulus of elemental solids extrapolates smoothly through the melting transition, so B would not be expected to diverge upon amorphization, either. At temperatures above θ_{D}, the heat capacity at constant volume of the crystalline phase reaches the Dulong-Petit limit, so we would expect it to remain roughly constant until the amorphization or melting transition were to occur. Thus, we should not expect α_{L} to be a sensitive measure of pre-amorphization effects.

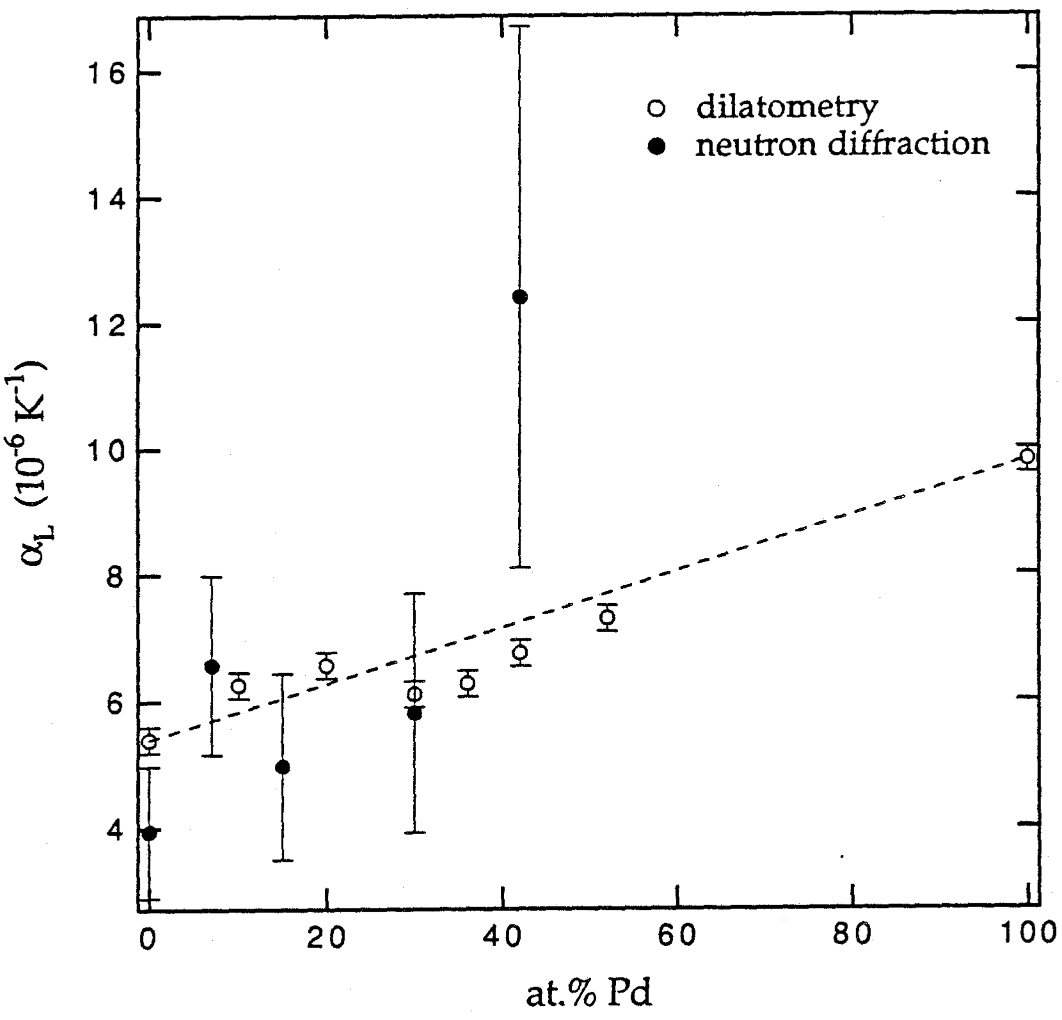

Figure 4.8: Linear thermal expansion coefficient α_L of Nb–Pd alloys determined by dilatometry between 150 K and 270 K. The samples with 42 at.% Pd or less have bcc structure, and those with 52 at.% Pd or more have fcc structure. The value of α_L at 150 K is roughly equivalent to the "average" α_L determined by neutron diffraction between 12 K and 300 K [Fig. 4.7(b)].

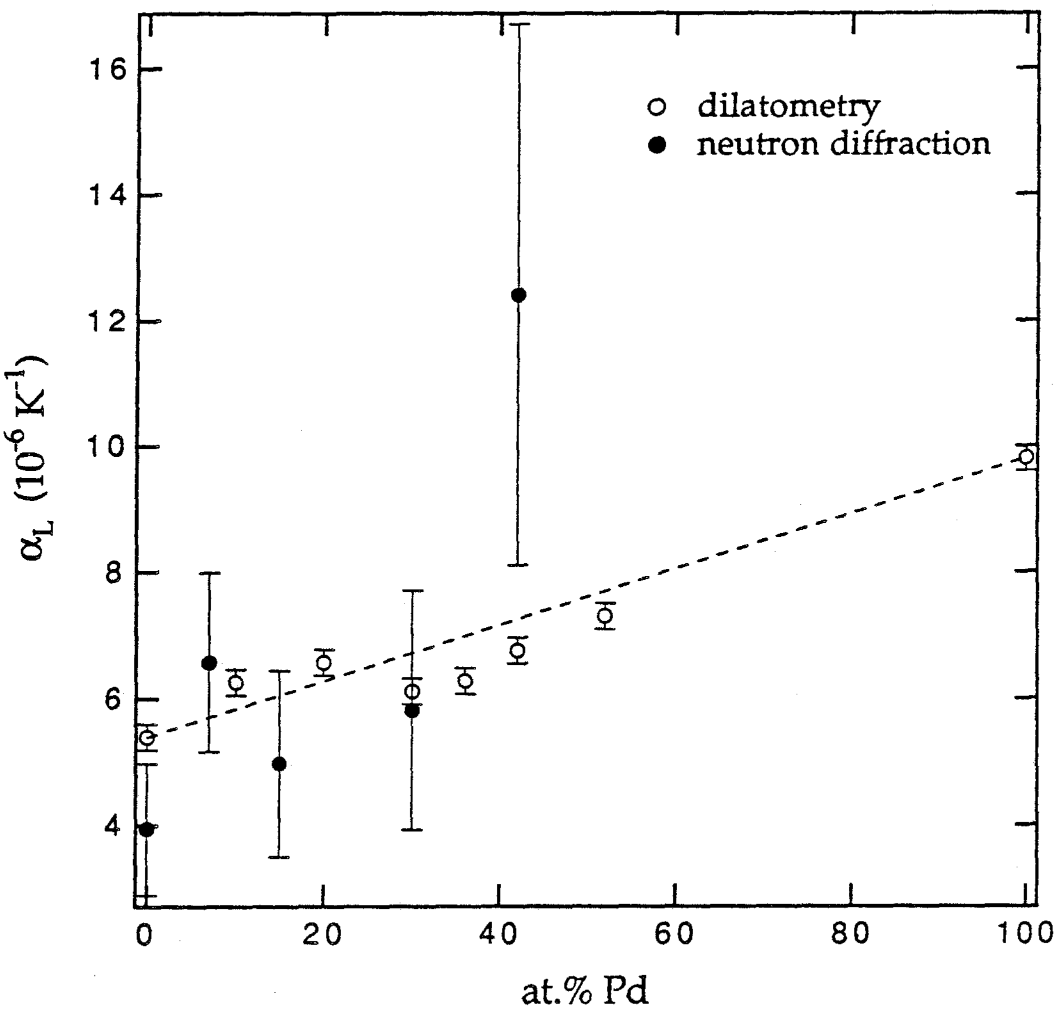

Figure 4.9: Linear thermal expansion coefficient of Nb–Pd alloys at 150 K determined by dilatometry and the "average" α_L determined by neutron diffraction *vs.* Pd concentration. Obviously, the apparent anharmonic enhancement of α_L at 42 at.% Pd in the neutron data is a result of the large uncertainty for that data point. The roughly linear dependence of α_L on Pd concentration extends from pure Nb to pure Pd.

4.4.3 Inhomogeneous strain

We can estimate the root-mean-square inhomogeneous strain $\langle\epsilon^2\rangle^{1/2}$ of the crystalline phase from the angular dependence of the full width at half maximum (FWHM) of the Bragg peaks [57]. If we let $\delta(2\theta)_s$ represent the FWHM of a diffraction peak (in radians) caused by strain broadening, then it can be shown that [57]

$$\delta(2\theta)_s = 5\langle\epsilon^2\rangle^{1/2}\tan\theta. \qquad (4.15)$$

Since a Gaussian peak profile of the form given in Eq. (4.11) has FWHM $= \sqrt{(8\ln 2)\sigma^2}$, it follows from Eq. (4.13) that

$$(\text{FWHM})^2 = 8\ln 2\left(U\tan^2\theta + V\tan\theta + W + \frac{F_2}{\tan^4\theta}\right). \qquad (4.16)$$

The only term on the right-hand side of Eq. (4.16) having the same angular dependence as $\delta(2\theta)_s^2$ is $(8\ln 2)U$. Subtracting off U_{inst}—the contribution of instrumental broadening to U—yields

$$\langle\epsilon^2\rangle^{1/2} = \frac{\sqrt{8\ln 2}}{5}\left(U - U_{\text{inst}}\right)^{1/2}. \qquad (4.17)$$

The variation of $\langle\epsilon^2\rangle^{1/2}$ in the $Nb_{100-x}Pd_x$ alloys over the temperature range that we studied was statistically insignificant, but the variation with Pd concentration (Fig. 4.10) was dramatic. From $x = 0$ to $x = 30$, $\langle\epsilon^2\rangle^{1/2}$ increases rapidly to the rather high value of $\sim 0.6\,\%$. But at $x = 42$, the apparent strain resulting from the profile refinement is 2.4 %! While such a value is unphysically high, it may be a sign that the incorporation of 42 at.% Pd drives the bcc phase into a highly nonequilibrium state. Breakdown of this strain analysis method probably occurred because of failure to satisfy one or more of the conditions for validity of Eq. (4.15).

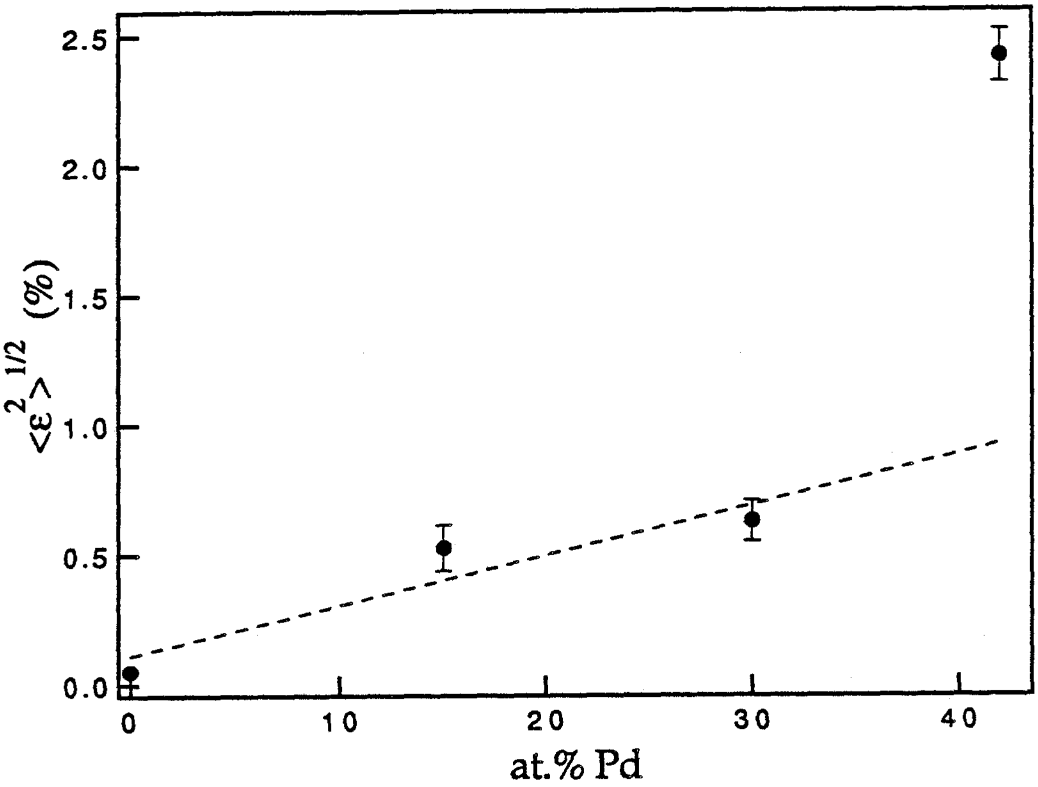

Figure 4.10: Root-mean-square strain plotted against Pd concentration. The inhomogeneous strain was estimated from the peak profile fitting parameter U (not to be confused with the temperature parameter $U_{\rm iso}$) according to Eq. (4.17). The value for 42 at.% Pd is unphysically high, indicating a breakdown in one or more of the assumptions made in deriving Eq. (4.15).

4.4.4 Atomic mean-square displacement

We plot the total atomic mean-square displacement (MSD) $\langle u^2\rangle_{\mathrm{tot}}$—which is just the isotropic temperature parameter U_{iso}—against temperature for several $\mathrm{Nb}_{100-x}\mathrm{Pd}_x$ compositions in Fig. 4.11. From the plot it is evident that $\langle u^2\rangle_{\mathrm{tot}}$ has a roughly linear dependence on temperature and can be fit by a function of the form:

$$\langle u^2\rangle_{\mathrm{tot}} \approx \langle u^2\rangle_0 + \left(\frac{\partial\langle u^2\rangle_{\mathrm{tot}}}{\partial T}\right)_{P,x} T. \tag{4.18}$$

By fitting a straight line to the data in Fig. 4.11, we can estimate $\langle u^2\rangle_0$ and $\partial\langle u^2\rangle_{\mathrm{tot}}/\partial T$ for each composition x. A plot of $\langle u^2\rangle_0$ against Pd concentration [Fig. 4.12(a)] reveals a nearly linear dependence of the $T = 0\,\mathrm{K}$ part of $\langle u^2\rangle_{\mathrm{tot}}$ on composition, a fact that will be seen to violate theoretical considerations (see section 4.5.1). The behavior of the slope of $\langle u^2\rangle_{\mathrm{tot}}$ [Fig. 4.12(b)] is even more unusual: it goes *down* as x increases. This is unexpected because

$$\left(\frac{\partial\langle u^2\rangle_{\mathrm{tot}}}{\partial T}\right)_{P,x} \propto \frac{1}{\theta_{\mathrm{D}}^2} \tag{4.19}$$

in the Debye approximation.[4] Thus, a decreasing MSD slope implies an increasing Debye temperature, which is exactly *opposite* to what we would expect of a lattice becoming progressively more unstable.

4.4.5 Direct measurement of θ_{D}

In order to resolve this paradox, we arranged for the direct determination of θ_{D} as a function of composition by low-temperature heat capacity measurement. Actually, the θ_{D} found in the Debye model for atomic displacements [from which Eq. (4.19) is derived] is not the same Debye temperature as that used to model the low-temperature heat capacity of solids. The difference arises because the

---

[4] Obtained by assuming that the temperature-dependent part of $\langle u^2\rangle_{\mathrm{tot}}$ may be represented by $\langle u^2\rangle_{\mathrm{dyn}}$ as given in Eq. (4.20) below and differentiating with respect to temperature.

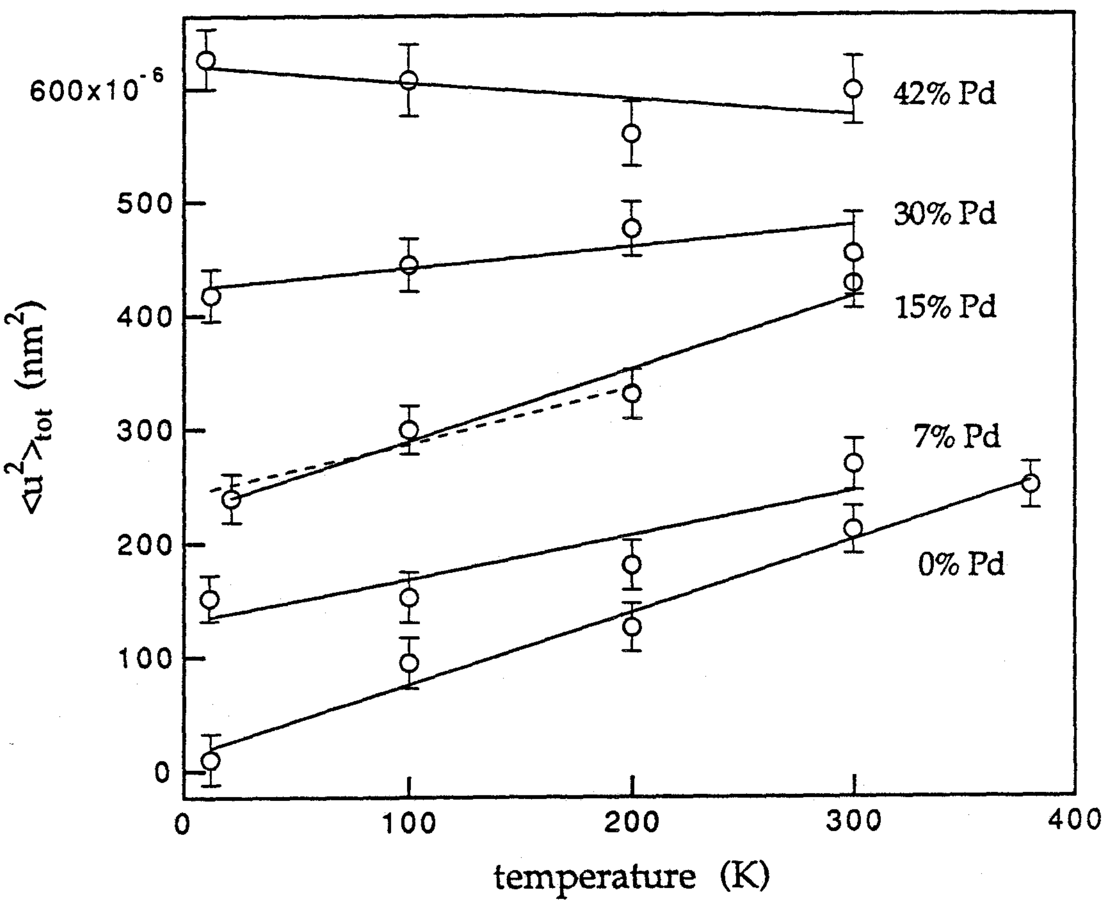

Figure 4.11: Total atomic MSD $\langle u^2\rangle_{\rm tot}$ plotted against temperature for several Nb–Pd compositions. Straight lines fit to the data points provide estimates for $\langle u^2\rangle_0$ and $\partial\langle u^2\rangle_{\rm tot}/\partial T$ [Eq. (4.18)]. (At 15 at.% Pd, the dashed line was used because the highest temperature data point seems anomalously large.)

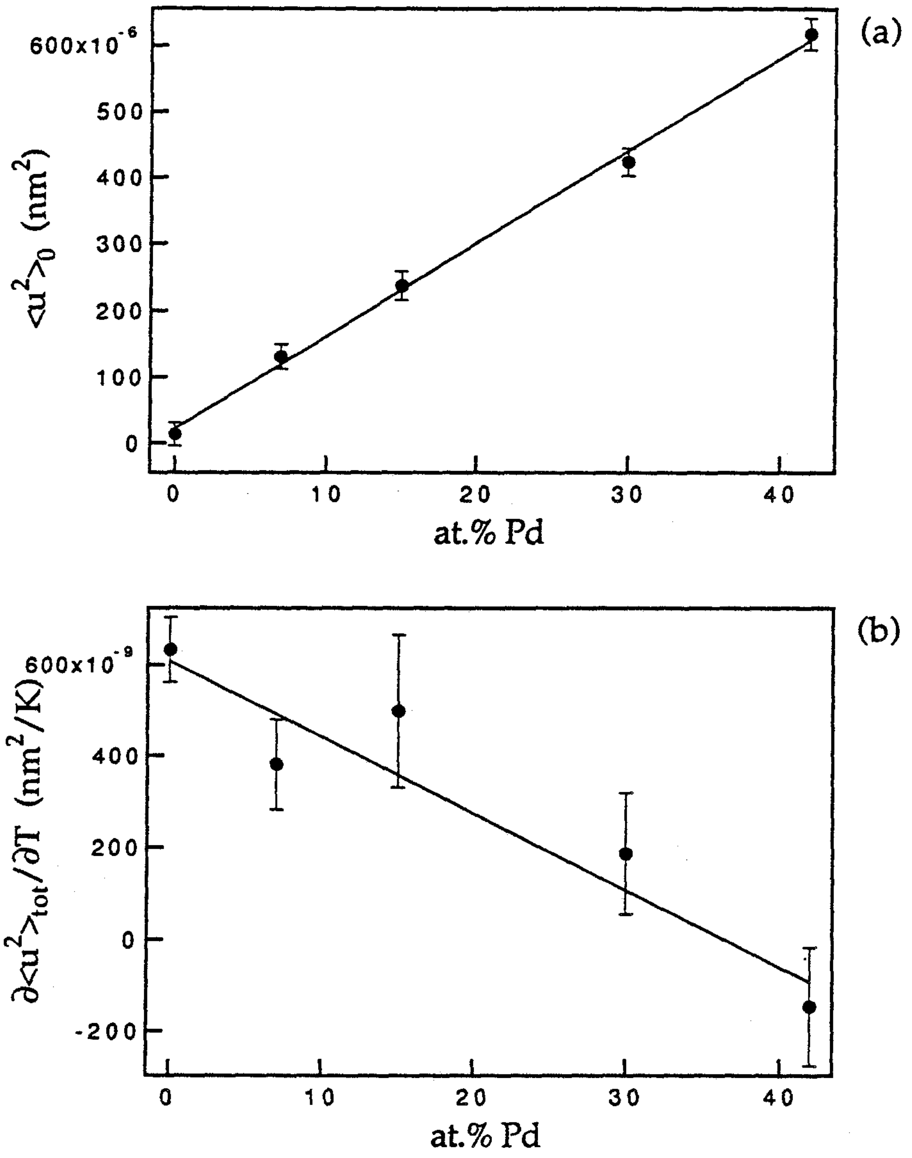

Figure 4.12: (a) $T = 0\,\mathrm{K}$ MSD plotted against Pd concentration, and (b) $(\partial\langle u^2\rangle_{\mathrm{tot}}/\partial T)_{P,x}$ plotted against Pd concentration for Nb–Pd splat-quenched alloys. The data points are obtained from least-squares, straight-line fits to the data in Fig. 4.11. Both the linear concentration dependence in (a) and the decreasing slope in (b) violate general expectations regarding MSD's in highly concentrated binary alloys.

Debye models for atomic displacements and for heat capacity involve different averages over the phonon frequency spectrum (for instance, the low frequencies are relatively more important than high frequencies to mean-square displacements, but they are equally important to the heat capacity for $T \gtrsim \theta_{\mathrm{D}}$ [59]). The difference is ordinarily not very large [60], however, so it is usually acceptable to replace the diffraction-measured Debye temperature with that derived from heat capacity measurements (higher accuracy can be obtained by making corrections using experimentally determined elastic constants and infrared/Raman frequencies [45]).

As is evident in Fig. 4.13, θ_{D} of $\mathrm{Nb}_{100-x}\mathrm{Pd}_x$ alloys decreases by about 15 % from $x = 0$ to $x = 42$, while at $x = 52$, for which the sample has fcc structure, θ_{D} is even higher than for pure Nb or pure Pd. The falling Debye temperature is reminiscent of the measured and extrapolated decrease in θ_{D} in bcc alloys like Ti–Mo and Ti–Cr as the solute concentration approaches the martensitic transition range [61]. That is, the decrease in θ_{D} may signal a significant softening of one of the elastic moduli of the bcc crystal; we shall derive an explicit connection between the Debye temperature and the shear modulus in Chapter 5. Along with the inhomogeneous strain data, this drop in θ_{D} suggests an impending instability in the bcc Nb–Pd phase with increasing Pd concentration.

4.4.6 Static and dynamic decomposition of $\langle u^2 \rangle_{\mathrm{tot}}$

Such a decrease in θ_{D} is also exactly opposite to what we expect from the composition dependence of $\partial\langle u^2 \rangle_{\mathrm{tot}}/\partial T$! Recall that the decrease in the MSD slope as Pd concentration increases implied that θ_{D} should go up rather than down. A possible resolution of the contradiction lies in a somewhat subtle assumption made when dividing $\langle u^2 \rangle_{\mathrm{tot}}$ into its “static” and “dynamic” parts: $\langle u^2 \rangle_{\mathrm{stat}} + \langle u^2 \rangle_{\mathrm{dyn}}$. The conventional approach assigns temperature dependence only to the dynamic term, which

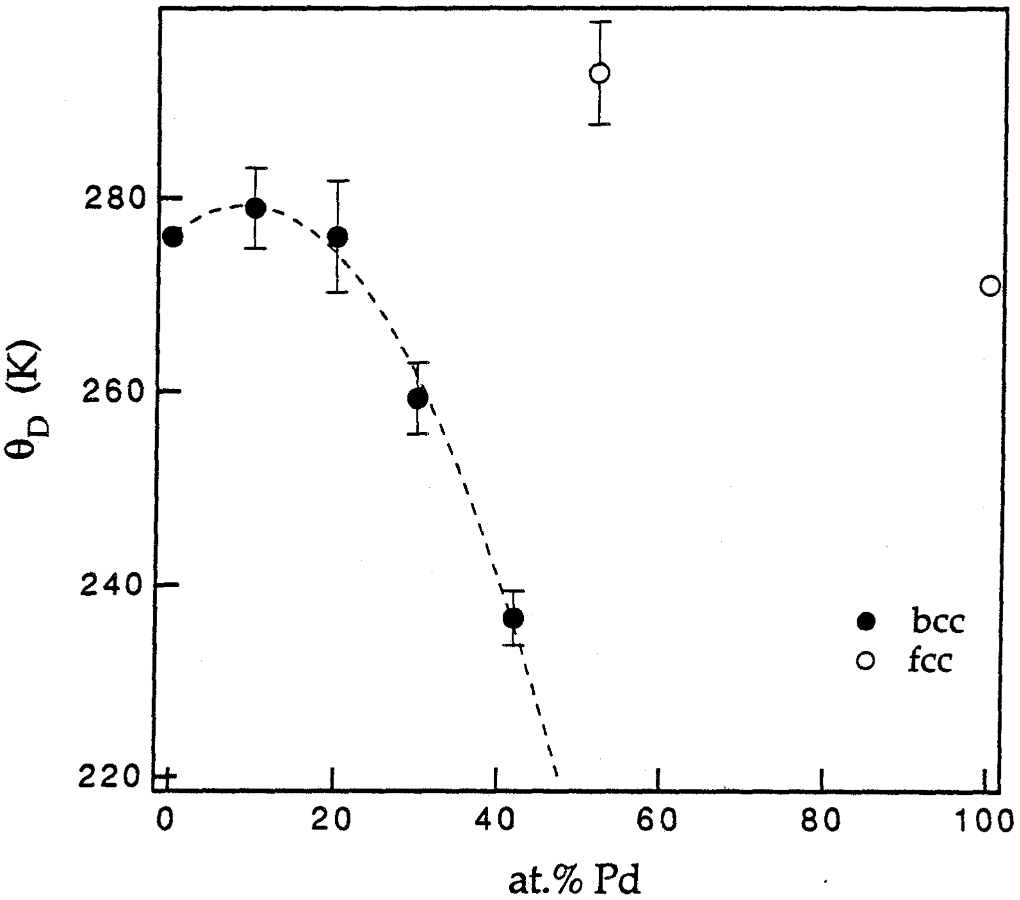

Figure 4.13: Debye temperature θ_{D} *vs.* Pd concentration for several Nb–Pd alloys. The pure Nb and Pd Debye temperatures are taken from Ref. [58]. The samples with up to 42 at.% Pd have bcc structure, and those with more Pd have fcc structure. Note the discontinuity in θ_{D} between the bcc and fcc phase fields. Low-temperature heat capacity measurements were used to determine all θ_{D} values in this plot.

accounts for the contribution of the vibrational motion of the atoms to $\langle u^2\rangle_{\text{tot}}$. The vibrations obviously increase in amplitude as the temperature increases. The remaining part of $\langle u^2\rangle_{\text{tot}}$, which includes the static atomic displacements,[5] is assumed not to depend on temperature. There is no *a priori* reason to believe, however, that the static MSD's of an alloy must remain independent of temperature—they could decrease with increasing temperature, for instance, if increasing vibrational amplitudes enable adjacent atoms to correlate their motion in such a way that each on average remains closer to its ideal lattice site.

Indeed, this may be occurring to $\langle u^2\rangle_{\text{stat}}$ in the Nb–Pd alloys with high Pd content. We can calculate $\langle u^2\rangle_{\text{stat}}$ as a function of temperature for each composition by subtracting $\langle u^2\rangle_{\text{dyn}}$ from the $\langle u^2\rangle_{\text{tot}}$ measured by neutron diffraction. In the Debye approximation [63],

$$\langle u^2\rangle_{\text{dyn}} = \frac{9\hbar^2}{M k_{\text{B}} \theta_{\text{D}}} \left[\frac{T}{\theta_{\text{D}}} \Phi\left(\frac{\theta_{\text{D}}}{T}\right) + \frac{1}{4} \right], \tag{4.20}$$

where M is the (average) atomic mass and $\Phi(x)$ is defined as

$$\Phi(x) \equiv \frac{1}{x} \int_0^x \frac{t}{e^t - 1}\, dt. \tag{4.21}$$

Using the Debye temperatures of Fig. 4.13 in Eq. (4.20), we are able to subtract off the calculated vibrational contribution to $\langle u^2\rangle_{\text{tot}}$ to get an estimate for $\langle u^2\rangle_{\text{stat}}$ at each composition and temperature (Fig. 4.14). As expected, $\langle u^2\rangle_{\text{stat}}$ is approximately zero for pure Nb at all temperatures, and it assumes a higher value as the Pd concentration increases. At 30 at.% Pd there is a hint of a decrease in $\langle u^2\rangle_{\text{stat}}$ with increasing temperature, and at 42 at.% Pd the downward slope becomes statistically significant. Such a decrease of "static" displacement with

---

[5] The remainder of $\langle u^2\rangle_{\text{tot}}$ also includes the zero-point motion of the atoms [62], which can be significant at temperatures below θ_{D}, but in the case of $\text{Nb}_{100-x}\text{Pd}_x$ alloys is entirely negligible for $x \geq 7$. Compare, for instance, the extrapolated MSD at $T = 0\,\text{K}$ for pure Nb in Fig. 4.11, which is entirely due to zero-point motion, to the other extrapolated MSD's in the figure—even the static MSD of the sample with 7 at.% Pd is much larger than the zero-point contribution.

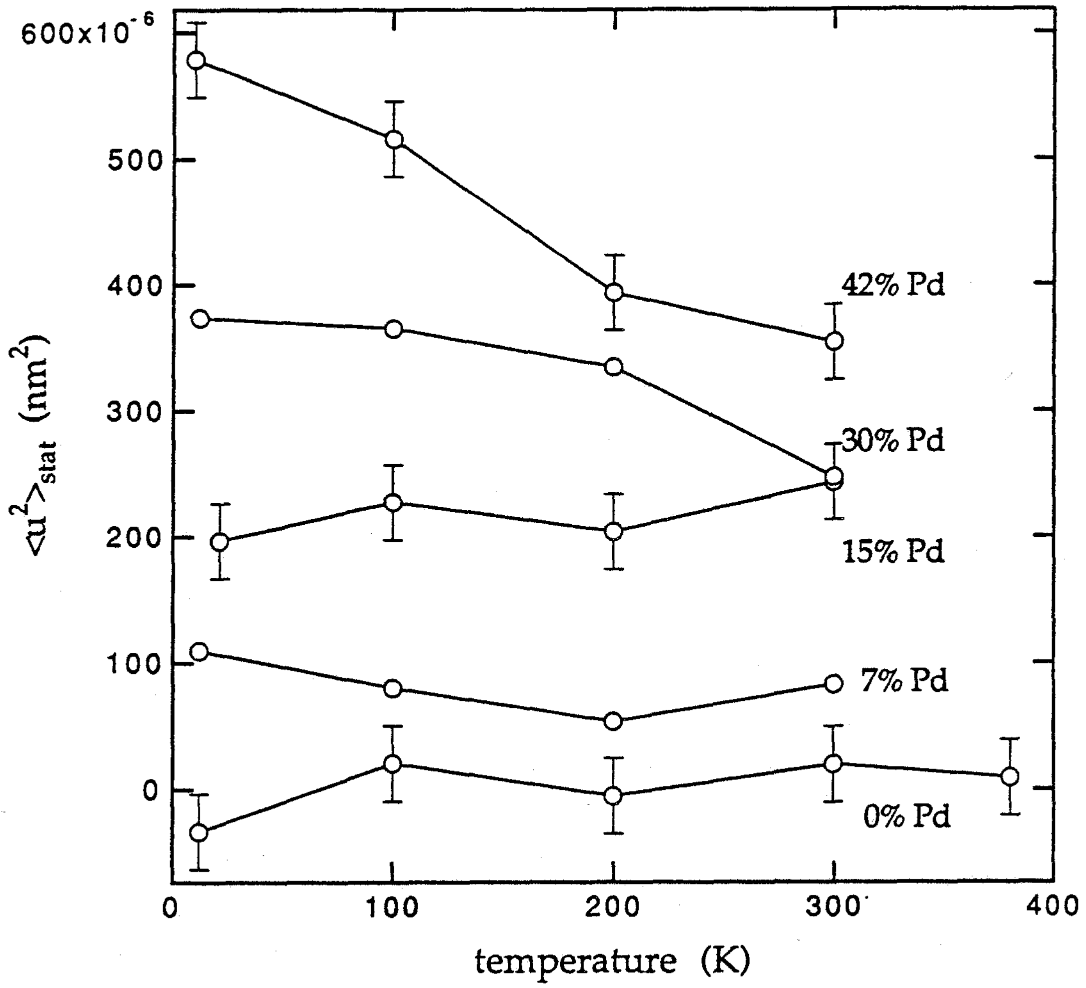

Figure 4.14: Static MSD $\langle u^2 \rangle_{\text{stat}}$ *vs.* temperature for several Pd concentrations. The static MSD was determined by subtracting $\langle u^2 \rangle_{\text{dyn}}$, as determined by Eq. (4.20), from the $\langle u^2 \rangle_{\text{tot}}$ measured at each composition and temperature by neutron diffraction (Fig. 4.11). The downward slope of $\langle u^2 \rangle_{\text{stat}}$ with increasing temperature at 30 and 42 at.% Pd suggests that the atoms are able to reduce the amplitude of their static displacements using the thermal energy available at the higher temperatures.

increasing temperature suggests a "melting" of distortions in the highly nonequilibrium crystal that were "frozen in" at low temperature. That is, it appears as if the atoms can exploit their greater mobility at higher temperatures to improve their topological packing, but at low temperatures they become trapped in positions rather far from their corresponding ideal sites.

4.4.7 Transmission electron microscopy

To study the issue of the "static" distortions in the high-Pd-content alloys, we decided to examine the samples in the electron microscope, looking in particular for bands of diffuse scattering in the diffraction pattern arising from static disorder [64]. Unfortunately, the crystals in the sample with 42 at.% Pd were too small to permit isolation of the diffracted signal from just one crystal using the smallest SAD (selected area diffraction) aperture in the microscope. But to our surprise, bright-field/dark-field image pairs and high-resolution images revealed a strikingly anisotropic structure: when viewed down the $\langle 100\rangle$ or $\langle 110\rangle$ zone axes, the crystals have a "tweed"-like structure reminiscent of martensitic decomposition [Fig. 4.15(a) and 4.15(b)], whereas when viewed down the $\langle 111\rangle$ zone axis [Fig. 4.15(c)], the crystals appear to have a uniform substructure! Crystals in the samples with 30 at.% Pd were large enough to permit recording sharp diffraction patterns in the electron microscope, and the "tweed" microstructure was still present when viewed along all zone axes except $\langle 111\rangle$ [Figs. 4.16(a)–4.16(c)], though the cross-hatched contrast was perhaps not as distinct as in the case of 42 at.% Pd. The fine scale of the microstructure is visible in a high-resolution image of $Nb_{70}Pd_{30}$ taken down the $\langle 100\rangle$ zone axis (Fig. 4.17). One explanation for the zone-axis dependence of the contrast is that the atomic displacements responsible for the "tweed" structure occur only along the $\langle 111\rangle$ real-space direction. A common displacive transition seen in many bcc alloys in which relative atomic dis-

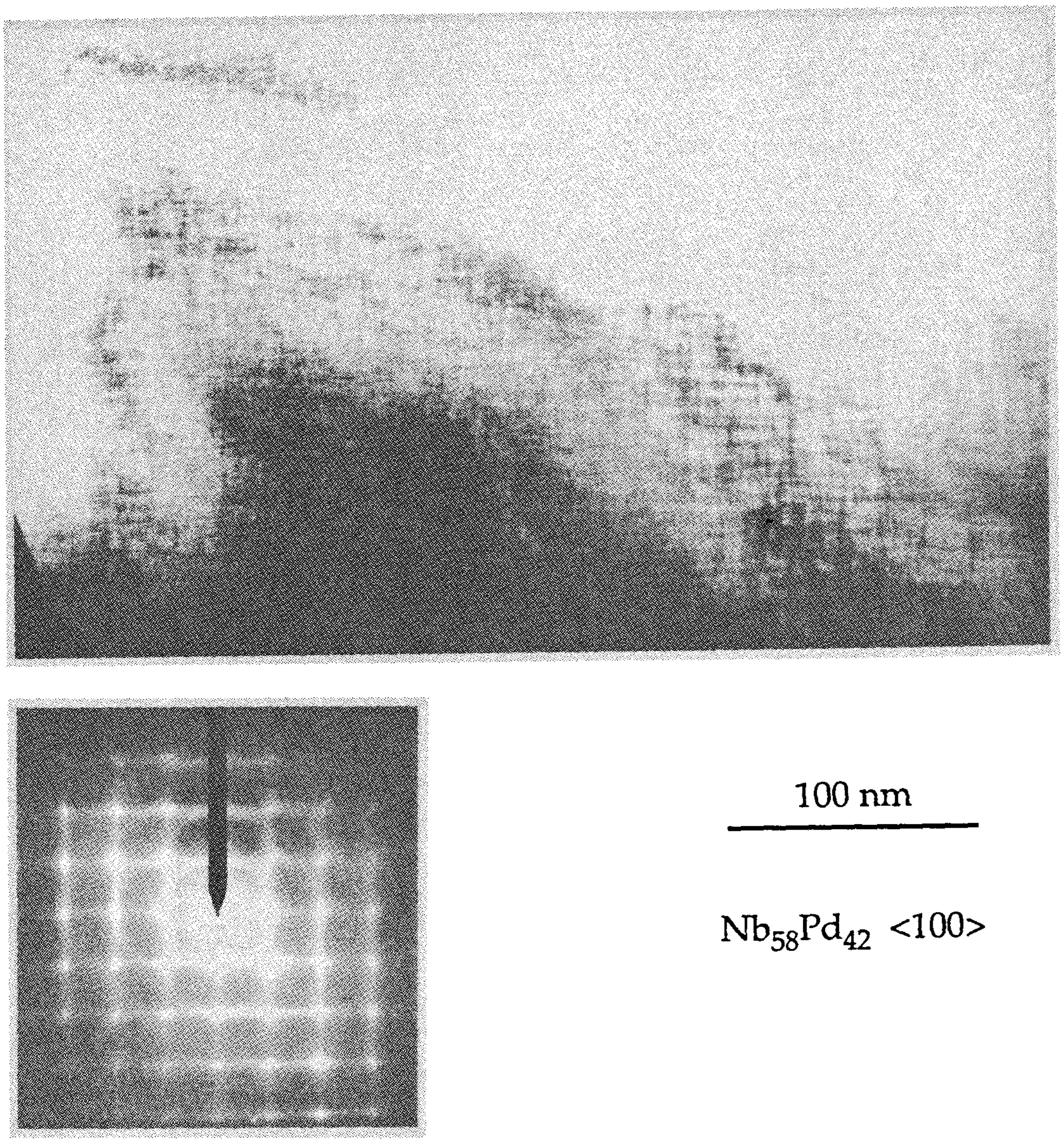

Figure 4.15(a): Bright-field TEM image and corresponding diffraction pattern of $Nb_{58}Pd_{42}$ taken down the $\langle 100 \rangle$ zone axis. Note the cross-hatched "tweed" microstructure characteristic of martensitic and ω-phase decomposition.

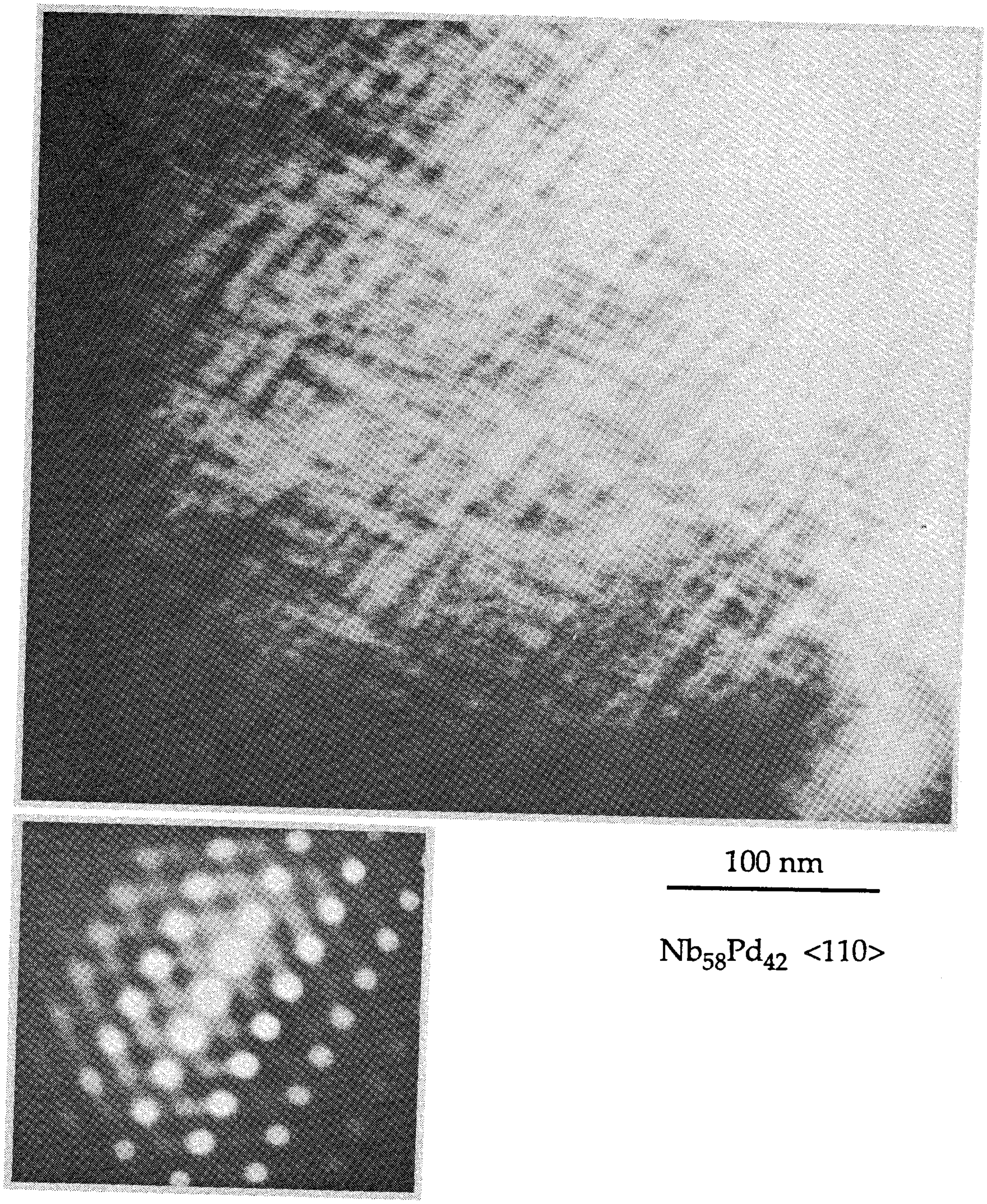

Figure 4.15(b): Bright-field TEM image and corresponding diffraction pattern of $Nb_{58}Pd_{42}$ taken down the $\langle 110 \rangle$ zone axis. Note the cross-hatched "tweed" microstructure characteristic of martensitic and ω-phase decomposition.

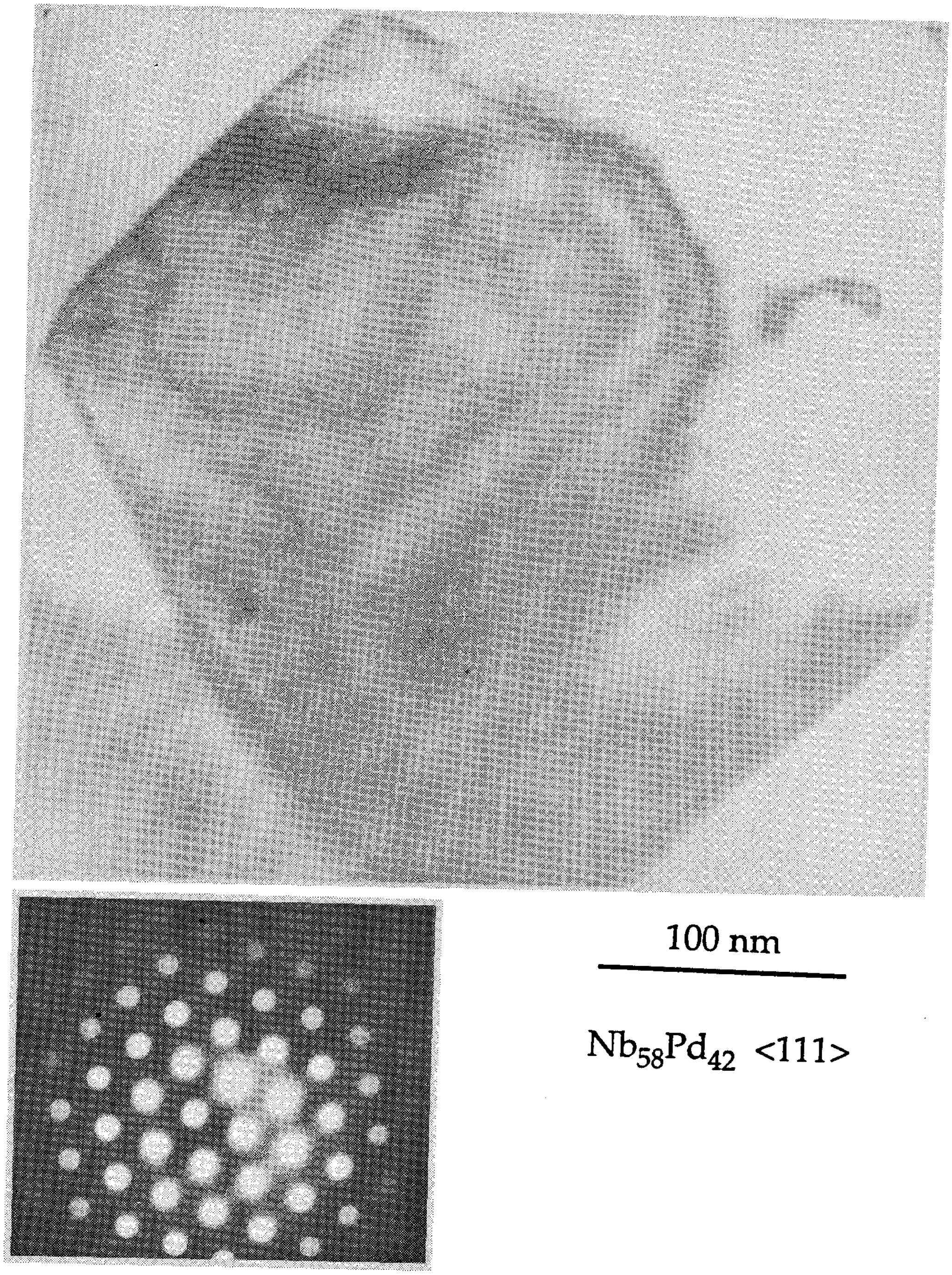

Figure 4.15(c): Bright-field TEM image and corresponding diffraction pattern of $Nb_{58}Pd_{42}$ taken down the $\langle 111 \rangle$ zone axis. Note the lack of a cross-hatched "tweed" microstructure as seen along the $\langle 100 \rangle$ and $\langle 110 \rangle$ zone axes.

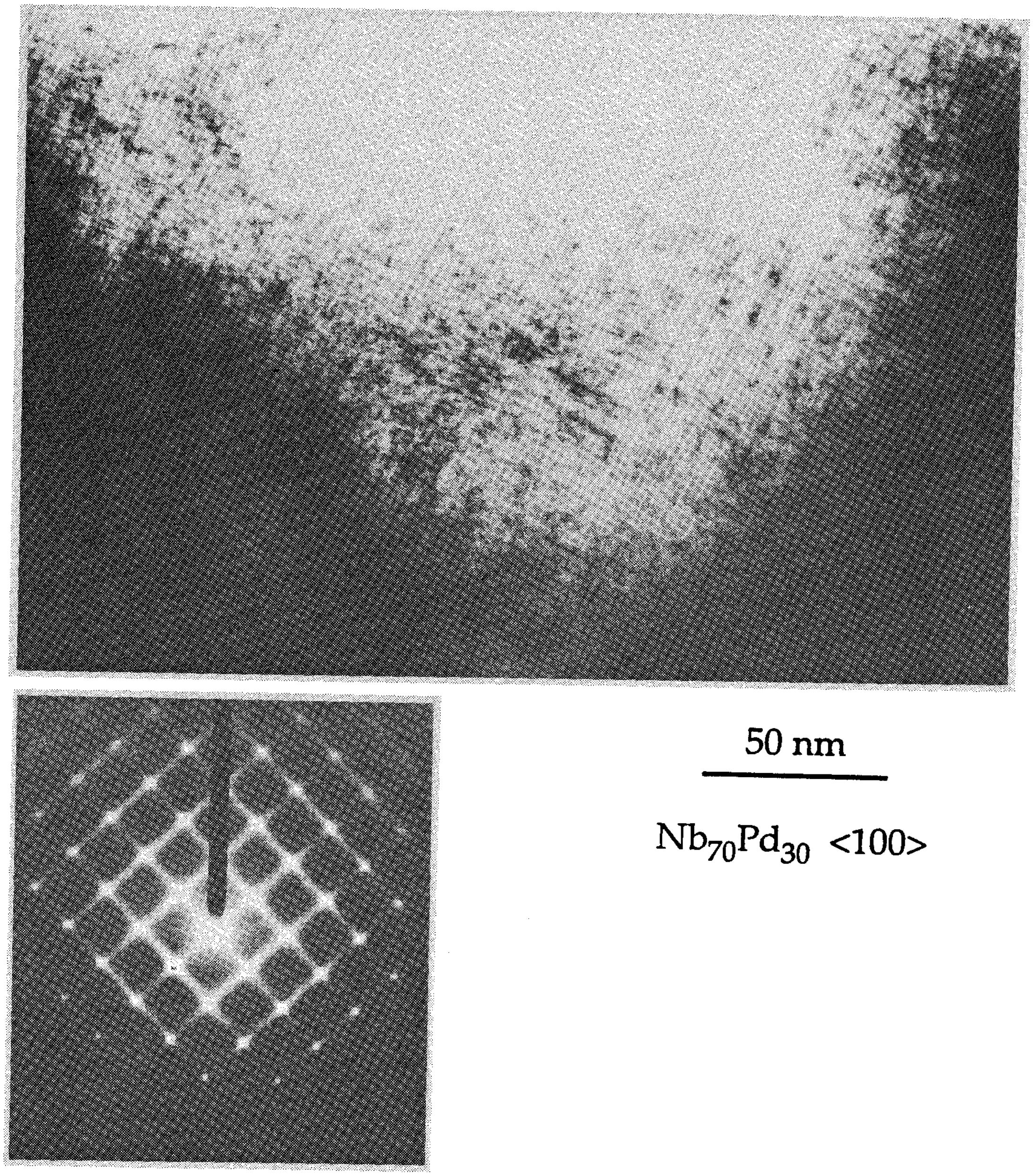

Figure 4.16(a): Bright-field TEM image and corresponding diffraction pattern of $Nb_{70}Pd_{30}$ taken down the $\langle 100 \rangle$ zone axis. Note the cross-hatched "tweed" microstructure and the strong lines of diffuse scattering intensity in the diffraction pattern.

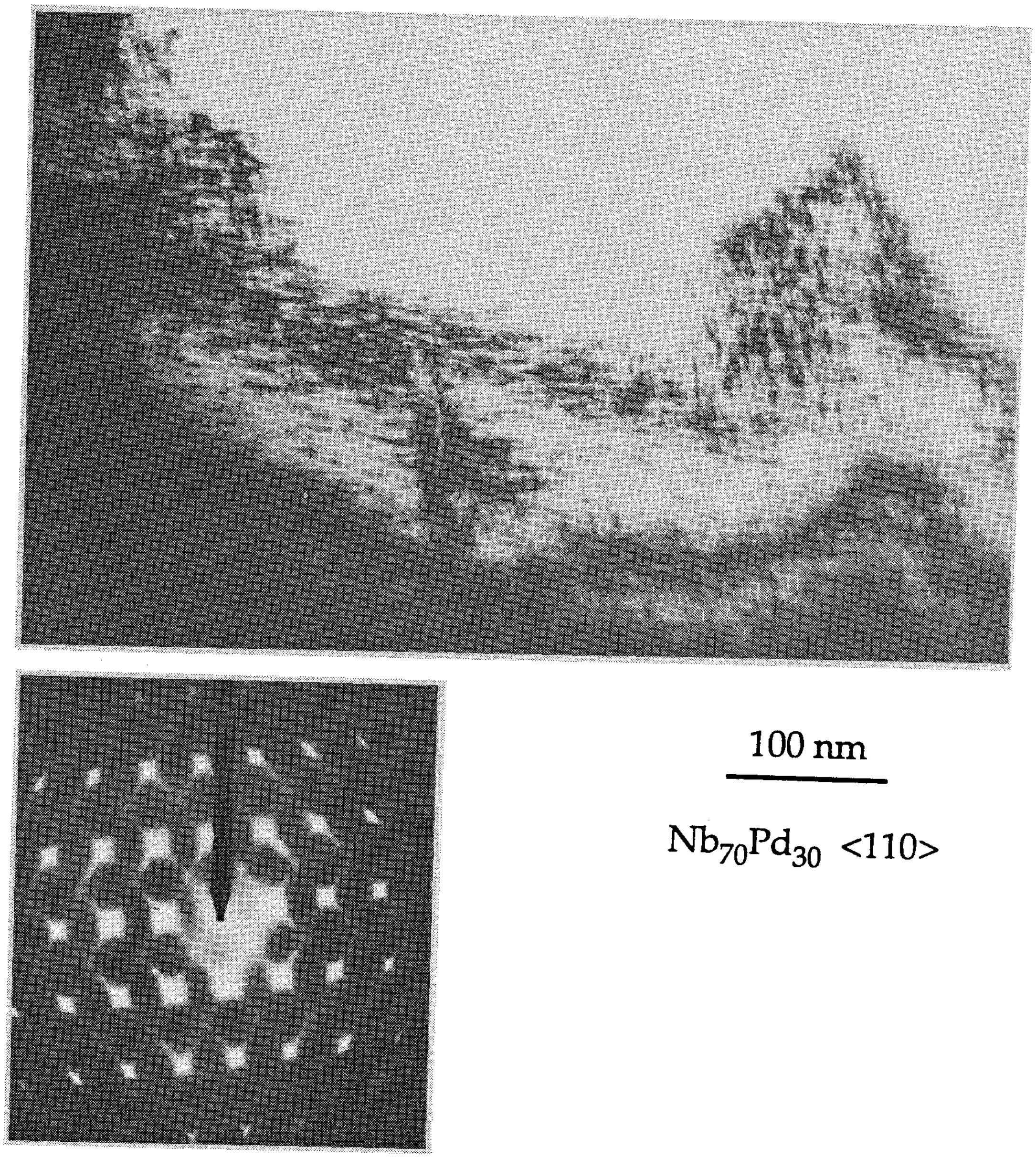

Figure 4.16(b): Bright-field TEM image and corresponding diffraction pattern of $Nb_{70}Pd_{30}$ taken down the ⟨110⟩ zone axis. Note the cross-hatched "tweed" microstructure and the lines of diffuse scattering intensity in the diffraction pattern.

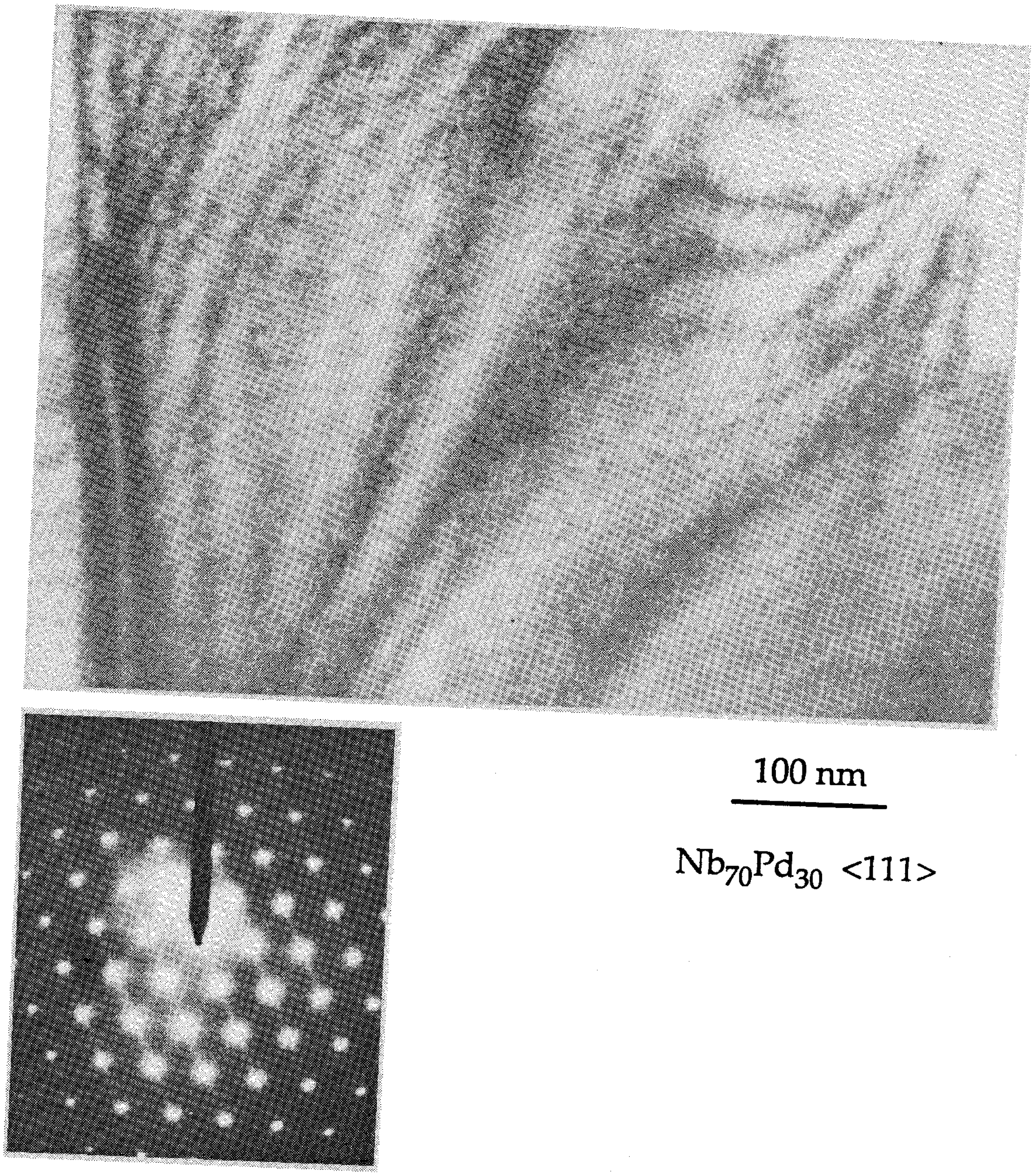

Figure 4.16(c): Bright-field TEM image and corresponding diffraction pattern of $Nb_{70}Pd_{30}$ taken down the $\langle 111 \rangle$ zone axis. Note the lack of a cross-hatched "tweed" microstructure as seen along the $\langle 100 \rangle$ and $\langle 110 \rangle$ zone axes. Lines of diffuse scattering can still be detected in the diffraction pattern, however.

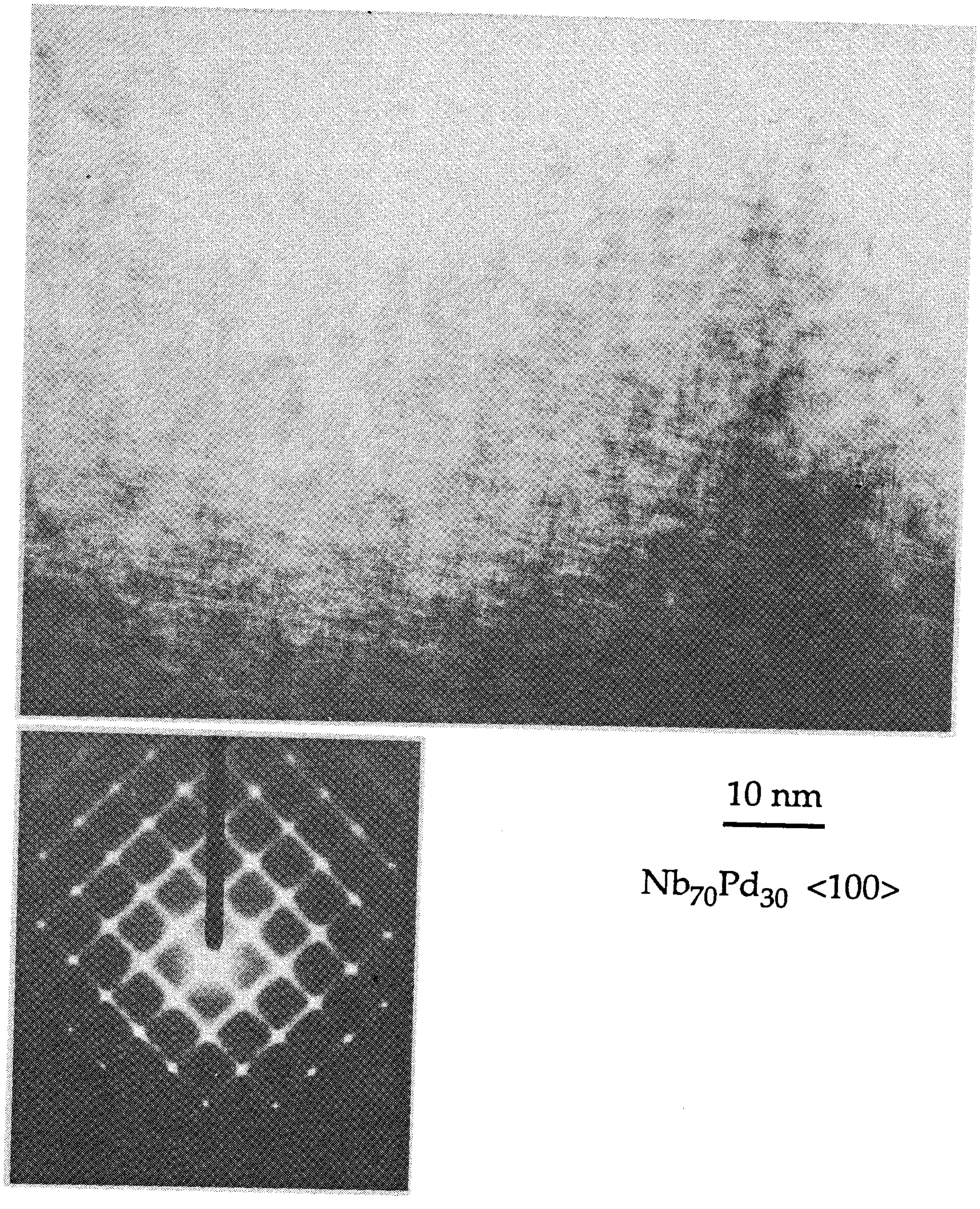

Figure 4.17: High-resolution and diffraction images of Nb$_{70}$Pd$_{30}$ taken down the $\langle 100 \rangle$ zone axis. The fine scale ($\lesssim 1\,\mathrm{nm}$) of the "tweed" microstructure is clearly visible.

placements occur only along $\langle 111 \rangle$ is the bcc $\rightarrow \omega$ phase transition [65, 66], which has been attributed to softening of a shear modulus; furthermore, the tendency to form the ω phase is often signaled by a buildup of diffuse intensity along $\{111\}$ planes in reciprocal space, which is consistent with the results of our TEM investigation [65]. The increase in $\langle u^2 \rangle_{\mathrm{stat}}$ at low temperature may reflect a buildup of ω-phase-like local distortions; $\langle u^2 \rangle_{\mathrm{stat}}$ would be expected to increase as a secondary effect of the softening of the lattice force constants associated with the elastic instability [67]. We will discuss this observed microstructure again in relation to a $\langle 111 \rangle$-direction instability recently observed during irradiation-induced amorphization of the intermetallic compound $\mathrm{Cu_4Ti_3}$ [68] (section 5.2.6).

4.5 Discussion

4.5.1 Calculating the atomic MSD

Is the rapid increase in Nb–Pd static disorder with Pd concentration an indication of growing instability in the bcc lattice structure? In order to answer this question, we must determine what portion of the static disorder is expected from packing together atoms of two different sizes and what portion can only be attributed to instability-induced disorder. The two most common ways of calculating the expected static disorder are based on bond-length fluctuations in a linear chain [69, 70, 71] and displacements in an isotropic continuum [72, 73, 74]. The static atomic MSD in a linear chain of overall composition $\mathrm{A}_{1-x}\mathrm{B}_x$ can be determined directly from the variance and average of the bond length b: $\langle u^2 \rangle_{\mathrm{stat}} = \langle b^2 \rangle - \langle b \rangle^2$ [69]. The authors of Ref. [69] calculate

$$\langle u^2 \rangle_{\mathrm{stat}} = \frac{1}{4} x(1-x)\left(b_{\mathrm{A}} - b_{\mathrm{B}}\right)^2 = x(1-x)\left(r_{\mathrm{A}} - r_{\mathrm{B}}\right)^2, \tag{4.22}$$

where r_{A} and r_{B} are the radii of the A and B atoms, respectively. According to the authors of Refs. [70, 71], generalization to three dimensions introduces only a symmetry-dependent constant C multiplying the rightmost expression in Eq. (4.22):

$$\langle u^2 \rangle_{\text{stat}} = Cx(1-x)\,(r_{\text{A}} - r_{\text{B}})^2\,. \tag{4.23}$$

They advocate the use of $C \approx 4$ for the alkali-metal alloys that they studied, but they provide no theoretical justification for this choice.

Huang [72] was the first to develop a more sophisticated model for static disorder by regarding a (dilute) solution as an elastic, isotropic continuum with distortion fields centered on the solute atom sites. The displacement of any atom in the lattice is given by the superposition of displacements arising from all of the distortion centers. The only displacement field $\mathbf{u}(\mathbf{r}{-}\mathbf{r}_0)$ centered at $\mathbf{r}_0$ that is consistent with the assumption of an elastic, isotropic medium has the inverse-square functional form [72, 73]:

$$\mathbf{u}(\mathbf{r}{-}\mathbf{r}_0) = \frac{c(\mathbf{r}{-}\mathbf{r}_0)}{|\mathbf{r}{-}\mathbf{r}_0|^3}, \tag{4.24}$$

where c is a constant. Using Eq. (4.24), Krivoglaz [74] calculated the static MSD expression for a cubic lattice of composition A_{1-x}B_x: to first order,

$$\langle u^2 \rangle_{\text{stat}} = c_1 \frac{27}{4\pi^2} x(1-x) \left(\frac{1+\sigma}{1-\sigma}\right)^2 \left(\frac{\partial a}{\partial x}\right)^2, \tag{4.25}$$

where σ is the Poisson ratio, a is the lattice parameter and $c_1 = 0.0932$ for bcc lattices.

We compute the static MSD in $\text{Nb}_{100-x}\text{Pd}_x$ alloys using Eqs. (4.23) and (4.25) and compare the calculated values to the measured values (Fig. 4.18). In Eq. (4.23) we use the apparent Pd radius in the Nb-rich solution estimated by extrapolating to pure Pd a linear fit to the compositional lattice parameter data of Fig. 4.6; also, we use $C = 4$, as suggested by Voronel *et al.* [70]. Likewise, for Eq. (4.25) we determine the value of $(\partial a/\partial x)$ from a linear fit to Fig. 4.6 and use a value of 0.3 for σ. As is evident in Fig. 4.18, the observed static MSD's are *much* larger than

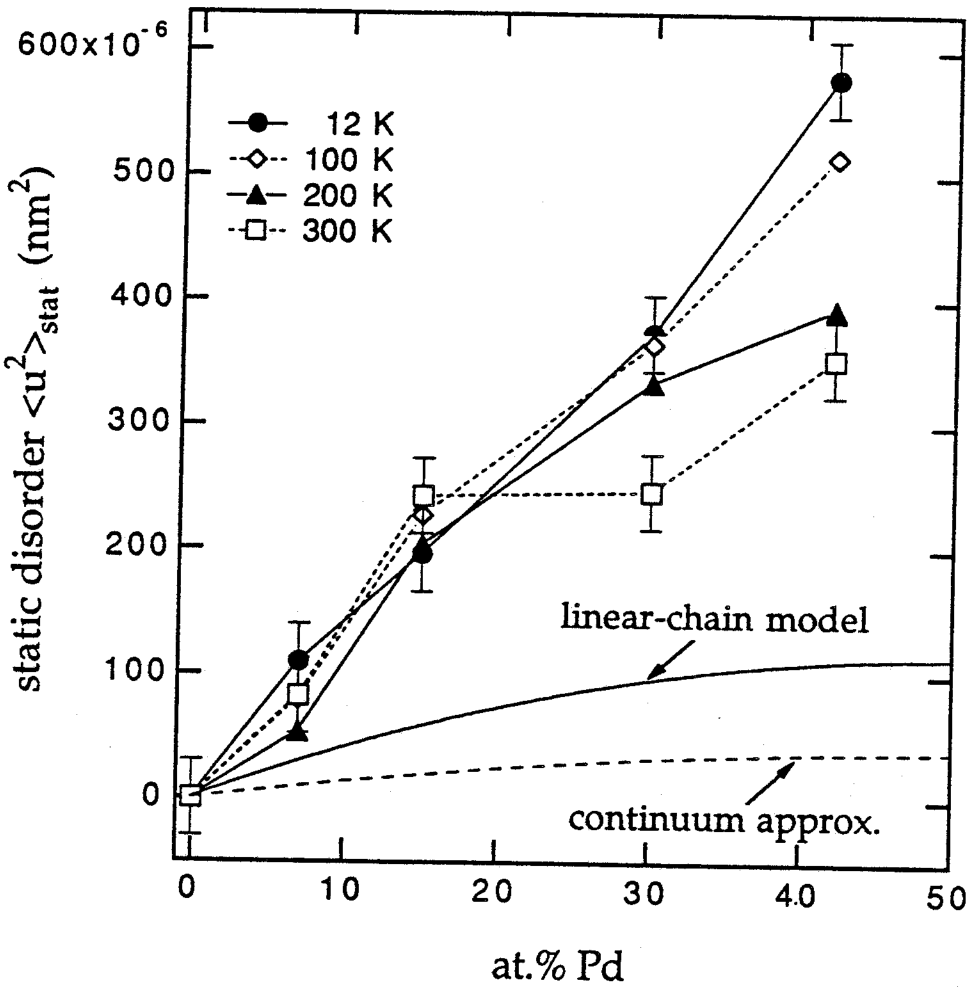

Figure 4.18: Measured and calculated static MSD's in Nb–Pd alloys plotted against Pd concentration. Neither the generalized linear-chain model [Eq. (4.23)] nor the more sophisticated continuum model [Eq. (4.25)] come close to predicting the magnitude of the observed $\langle u^2 \rangle_{\text{stat}}$.

the results of either calculation. It is true that the 200 K and 300 K data can be fit fairly well with an equation parabolic in x, as both theoretical expressions predict, but the calculated magnitudes are far too small. (The *linear* dependence of the observed static MSD's at 12 K and 100 K may result from the elastic instability discussed in the previous section.)

4.5.2 Failure of static MSD calculations

While fair agreement has been achieved between calculated and measured static MSD's in mixed alkali halide crystals [75], there are few measurements involving metals [73, 76, 77, 78, 79, 80] from which to assess the general reliability of the two models discussed above. The inability of the two models to account for the measured $\langle u^2 \rangle_{\text{stat}}$ in $\text{Nb}_{100-x}\text{Pd}_x$ for $x \geq 7$ must reflect a breakdown in one (or more) of the assumptions made in deriving the models, the most important assumptions being (i) no short-range ordering or clustering and (ii) isotropic displacement fields around point defects. Considering the first assumption, the presence of short-range ordering would actually *reduce* the static MSD because the atoms would tend to "pack" better [81]; clustering, on the other hand, would increase it. We did not observe any deviation in the average lattice parameter that would indicate the presence of clustering in the Nb–Pd alloys, except possibly at 42 at.% Pd, and the failure of the theoretical models to account for the static MSD began at 7 at.% Pd, where we don't expect clustering to occur. Hence, the anomalously high observed values of $\langle u^2 \rangle_{\text{stat}}$ probably do not originate from short-range clustering effects.

The second assumption—that the displacement field around a "point defect" is isotropic—is not so easy to justify. In fact, experimental evidence and theoretical models conclude that the displacement field about a defect in a crystalline lattice has a complex structure that depends on both distance and orientation with respect to the defect [82]. Thus, Eq. (4.24) is probably too simple to describe adequately the vector displacement at a point in the lattice caused by too big and too small atoms located at other points. Hence, the continuum model fails. The generalized linear chain model also relies on the assumption of isotropic displacement fields: if $\mathbf{u}(\mathbf{r}-\mathbf{r}_0)$ has a complex dependence on the distance and angle between $\mathbf{r}$ and $\mathbf{r}_0$, then it will not suffice to calculate $\langle u^2\rangle_{\mathrm{stat}}$ from an isotropic parameter like the difference in atomic radii.

Recall from section 4.3.2 that the temperature factor U_{iso} is equal to the total MSD (static plus dynamic) if the atomic displacements are either small or have a Gaussian distribution. In light of the probable violation of assumption (ii), it seems likely that at high Pd concentrations, the displacements in the Nb–Pd alloys are neither small nor distributed according to a Gaussian. Krivoglaz [74] has assessed the potential deviation of U_{iso} from $\langle u^2\rangle$ in such cases. He finds that in interstitial solutions the difference can be substantial, but in homogeneous substitutional solutions, like Nb–Pd, the relative difference is generally less than one percent. Therefore, we can continue to consider the refined temperature parameter to be an accurate estimate of the true total MSD of the atoms in the crystalline lattice.

4.5.3 Relationship to Lindemann melting criterion

The Lindemann melting criterion [section 1.3.1, Eq. (1.1)] dictates that melting will occur when the atomic root-mean-square displacement (RMSD) reaches a critical fraction of the interatomic spacing in the crystal [83]. Since the Lindemann criterion has been investigated primarily in elemental solids, little attention has been paid to the influence of static contributions to the MSD on the melting temperature. Rabinovich and colleagues [70, 71, 84] have recently demonstrated that the Lindemann criterion holds for alloys if the *total* MSD, rather than only the *dynamic* MSD, is used to predict the melting point. That is, the static MSD plays an equivalent role to the dynamic MSD in influencing the melting temperature of alloys.

This fact suggests that the degree of instability of the crystalline phase may be related to the fraction $\langle u^2\rangle^{1/2}/\langle u^2\rangle^{1/2}_{\max}$, where $\langle u^2\rangle^{1/2}_{\max}$ is the RMSD at the melting point as predicted by the Lindemann criterion. For bcc crystals, the atomic RMSD is approximately 15 % of the nearest-neighbor spacing at the melting point [85]. In pure Nb this represents a maximum RMSD of 0.043 nm, which decreases to 0.042 nm at 42 at.% Pd due to shrinkage of the unit cell. The difference between this maximum RMSD and the measured static RMSD's at the same Pd concentration indicates the additional amount of RMSD that must be imparted to the atoms of the crystal in order to cause polymorphous melting. In Fig. 4.19(a) we see that the 300 K static RMSD rises to approximately 43 % of the melting RMSD and at 12 K it reaches 58 %. By way of comparison, in Fig. 4.19(b) I have plotted the RMSD's measured by Seidel *et al.* [86] in Mn-implanted Al as a function of Mn concentration. The critical Lindemann fraction for fcc structures like Al is 12 % [85], resulting in a maximum RMSD of about 0.034 nm. Seidel *et al.* observed amorphization to occur suddenly at about 6 at.% Mn, at which point the RMSD is 67 % of the maximum at melting. This amount of static disorder may correspond to an instability of the crystalline phase with respect to amorphization. If we were to assume that the 67 % criterion holds for Nb–Pd, then we would predict by extrapolating the 12 K and 300 K RMSD data points in Fig. 4.19(a) to higher Pd concentrations that the bcc phase would become unstable with respect to amorphization at 60–65 at.% Pd.

Furthermore, substituting the expression for the dynamic MSD $\langle u^2\rangle_{\mathrm{dyn}}$ given by Eq. (4.20) into the Lindemann melting criterion for $\mathrm{Nb}_{100-x}\mathrm{Pd}_x$,

$$\langle u^2(x)\rangle_{\mathrm{stat}} + \langle u^2(x)\rangle_{\mathrm{dyn}} = \langle u^2\rangle_{\max} \approx (0.042\,\mathrm{nm})^2, \tag{4.26}$$

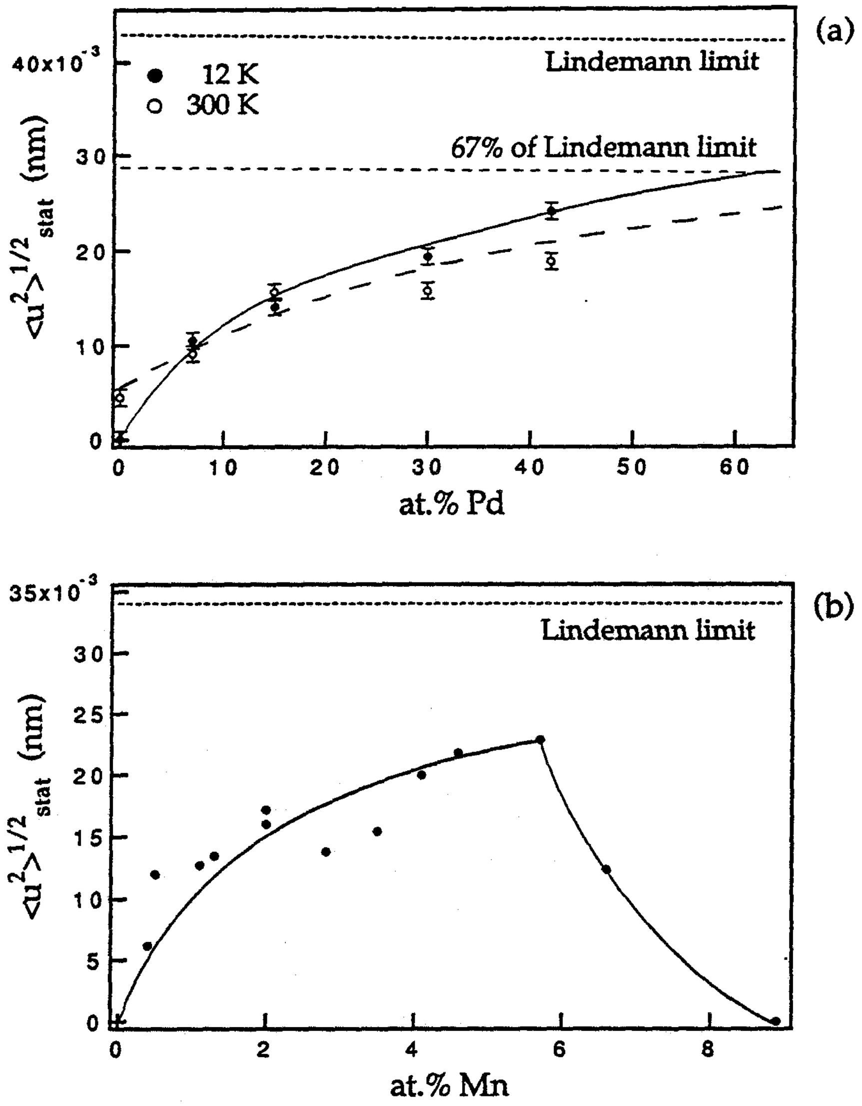

Figure 4.19: Static rms displacements in (a) Nb–Pd alloys plotted against Pd concentration (T = 12 K and 300 K) and in (b) Al–Mn alloys plotted against Mn concentration (data taken from Ref. [86]). Regions of the Al–Mn alloy begin to amorphize when $\langle u^2 \rangle_{\mathrm{stat}}{}^{1/2}$ reaches a maximum of ~67 % of the Lindemann limit for melting. The Nb–Pd alloys reach ~58 % of the Lindemann limit at 42 at.% Pd. At a Pd concentration of 60–65 at.% the $\langle u^2 \rangle_{\mathrm{stat}}{}^{1/2}$ of Nb–Pd would reach the fraction of the Lindemann limit at which the Al–Mn alloys began to amorphize.

yields an expression for the polymorphous melting temperature T_0 in terms of the measured static MSD and the Debye temperature θ_D at x:

$$T_0 \approx \frac{Mk_B\theta_D^2(x)}{9\hbar^2}\left[\langle u^2\rangle_{\max} - \langle u^2(x)\rangle_{\text{stat}}\right], \qquad T_0 > \theta_D, \tag{4.27}$$

where we have expanded the Debye function [Eq. (4.21)] $\Phi(y)$ for $y < 1$ [60]: $\Phi(y) + \frac{1}{4}y = 1 + \frac{1}{36}y^2 - \frac{1}{3600}y^4 + \cdots$. Given the measured Debye temperatures as a function of x in Fig. 4.13 and the static MSD's of Fig. 4.18, we use Eq. (4.27) to calculate the melting temperature $T_0(x)$ as a function of Pd concentration and superpose this on the Nb side of the Nb–Pd phase diagram (Fig. 4.20). The success of this approach in approximating the known T_0 line for Nb–Pd above the eutectic temperature suggests that a reliable way to extrapolate the T_0 line to lower temperatures (i.e., higher Pd concentrations) is to extrapolate the measured $\theta_D(x)$ and $\langle u^2(x)\rangle_{\text{stat}}$ curves to higher x and substitute into Eq. (4.27). Doing so enables us to map out the T_0 line until it approaches the Debye temperature (Fig. 4.20). Since the T_0 line must be vertical at the ideal glass transition temperature, which is located at about 40–60 % of the eutectic temperature [88], we can estimate the critical composition c^* of Fecht and Johnson's polymorphous phase diagram to be 65–70 at.% Pd in the Nb–Pd system. Note how close this prediction is to the instability concentration of 60–65 at.% Pd estimated from the "$\frac{2}{3}\langle u^2\rangle_{\max}$" criterion proposed above!

4.5.4 Conclusions

We have found several pieces of evidence suggesting that highly supersaturated bcc crystals of $\text{Nb}_{100-x}\text{Pd}_x$ have an underlying stability limit of $x \approx 65$. The unusually large static disorder and inhomogeneous strain at large x suggest that the atoms are not "packed" very well into the average lattice. The falling Debye temperature implies that the shear modulus of the crystalline phase decreases

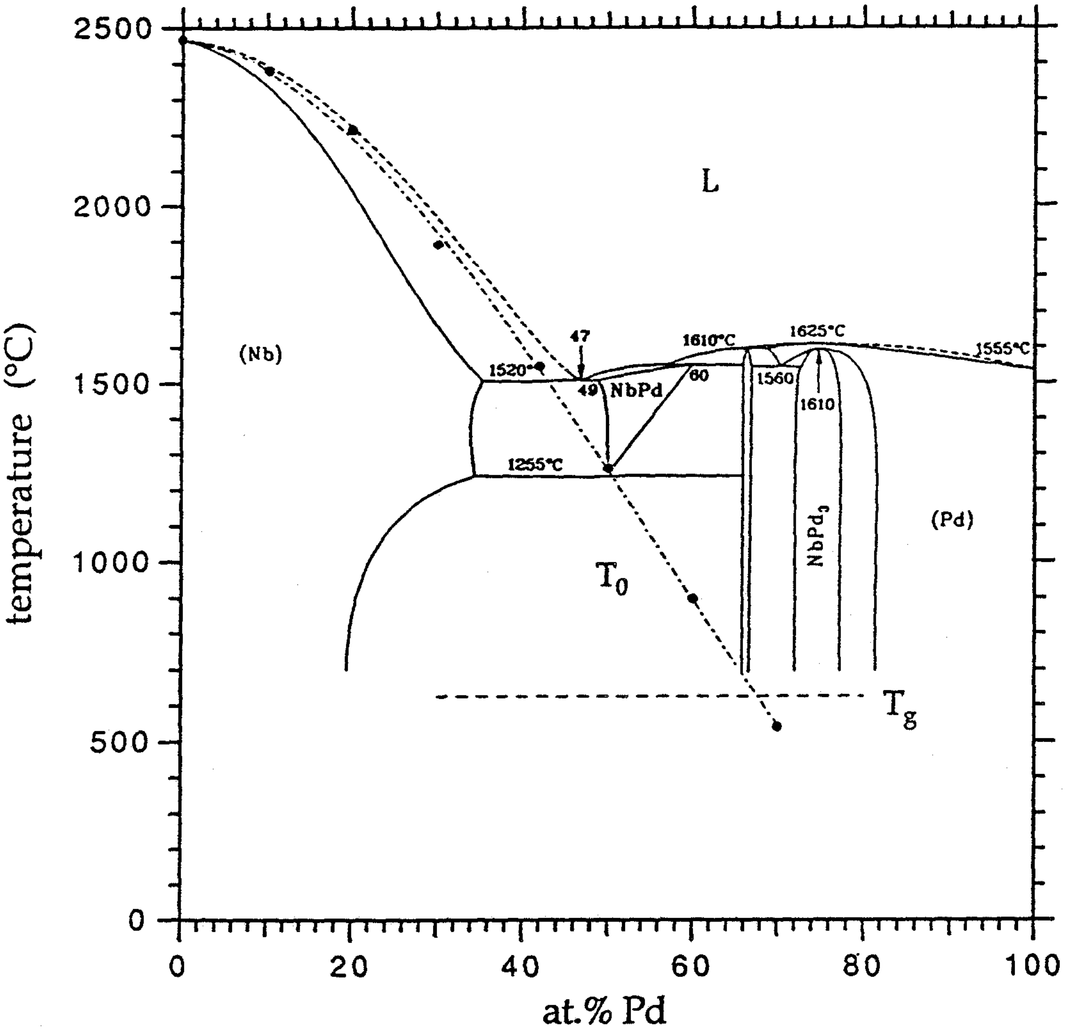

Figure 4.20: Calculated T_0 line superposed on the Nb side of the Nb–Pd phase diagram. The T_0 line was calculated using Eq. (4.27) and measured and extrapolated values for the terms therein. A value for $\langle u^2\rangle_{\max}$ of $(0.0392\,\mathrm{nm})^2$ was chosen to give the correct melting point for pure Nb. The slope of the T_0 line is expected to become infinite at the glass transition temperature of ~600 °C, which would entail a critical composition c^* of about 65–70 at.% Pd. Equilibrium phase diagram taken from Ref. [87].

with increasing Pd content. Finally, the unusual structure seen in the TEM micrographs of the most highly supersaturated sample may be a precursor of the elastic instability entailed by the falling Debye temperature. A generalization of the Lindemann criterion to alloys enables us to calculate the polymorphous phase diagram for Nb–Pd, which predicts a maximum solubility of 65–70 at.% Pd in the bcc crystalline phase. Such a composition cannot be reached by splat quenching because of interference from the fcc crystalline phase field at 50 at.% Pd, but another synthetic technique like implantation may enable samples to be prepared at higher concentrations near this ultimate limit, because the bcc phase would not need to be nucleated and grown from a more disordered phase, as with splat quenching.

References

[1] C. E. Krill III and W. L. Johnson, in *Kinetics of Phase Transformations,* edited by Michael O. Thompson, Michael J. Aziz and G. Brian Stephenson (Mater. Res. Soc. Symp. Proc. **205**, Pittsburgh, PA, 1992), pp. 313–318.

[2] C. E. Krill III, J. Li, C. Ettl, K. Samwer, W. B. Yelon and W. L. Johnson, to be presented at the Eighth International Conference on Liquid and Amorphous Metals, Vienna, 31 August–4 September 1992.

[3] T. B. Massalski, in *Physical Metallurgy,* 3rd ed., edited by R. W. Cahn and P. Haasen (Elsevier, Amsterdam, 1983), Part 1, pp. 158–160.

[4] B. C. Giessen, N. J. Grant, D. P. Parker, R. C. Manuszewski and R. M. Waterstrat, *Metall. Trans. A* **11A**, 709 (1980).

[5] M. S. Chandrasekharaiah, *Bull. Alloy Phase Diagrams* **9**, 449 (1988).

[6] David Turnbull, *Metall. Trans. A* **12A**, 695 (1981).

[7] Larry Jones, Staff Scientist, Materials Preparation Center at Ames Laboratory, Iowa State University, Ames, Iowa 50011, (515) 294-5236 (private communication).

[8] R. W. Cahn, in *Physical Metallurgy,* 3rd ed., edited by R. W. Cahn and P. Haasen (Elsevier, Amsterdam, 1983), Part 2, pp. 1785–1788.

[9] H. Jones, *Rapid Solidification of Metals and Alloys,* (The Institution of Metallurgists, London, 1982).

[10] *CRC Handbook of Chemistry and Physics,* 68th ed., edited by Robert C. Weast, Melvin J. Astle and William H. Beyer (CRC Press, Boca Raton, FL, 1987), p. D-185.

[11] Valery F. Sears, in *Neutron Scattering,* Part A, edited by Kurt Sköld and David L. Price, Methods of Experimental Physics, Vol. 23 (Academic, New York, 1986), Appendix.

[12] Neil W. Ashcroft and N. David Mermin, *Solid State Physics,* (Saunders College, Philadelphia, 1976), Chap. 25.

[13] Y. S. Touloukian, R. K. Kirby, R. E. Taylor, P. D. Desai, in *Thermal Expansion: Metallic Elements and Alloys,* edited by Y. S. Touloukian, Thermophysial Properties of Matter, Vol. 12 (IFI/Plenum, New York, 1975), p. 236.

[14] Y. S. Touloukian, R. K. Kirby, R. E. Taylor, P. D. Desai, in *Thermal Expansion: Metallic Elements and Alloys,* edited by Y. S. Touloukian, Thermophysial Properties of Matter, Vol. 12 (IFI/Plenum, New York, 1975), p. 248.

[15] Address: Institut für Werkstoffphysik, Universität des Saarlandes, D-6600 Saarbrücken, Germany.

[16] Charles Kittel, *Introduction to Solid State Physics,* 6th ed. (Wiley, New York, 1986), p. 139.

[17] Charles Kittel, *Introduction to Solid State Physics,* 6th ed. (Wiley, New York, 1986), p. 108.

[18] Address: Institut für Physik, Universität Augsburg, Memmingerstraße 6, D-8900 Augsburg, Germany.

[19] Richard A. Swalin, *Thermodynamics of Solids,* 2nd ed. (Wiley, New York, 1972), p. 31.

[20] R. Bachmann, F. J. DiSalvo, Jr., T. H. Geballe, R. L. Greene, R. E. Howard, C. N. King, H. C. Kirsch, K. N. Lee, R. E. Schwall, H.-U. Thomas and R. B. Zubeck, *Rev. Sci. Inst.* **43**, 205 (1972).

[21] R. L. Fagaly and R. G. Bohn, *Rev. Sci. Inst.* **48**, 1502 (1977).

[22] Desmond H. Kay, *Techniques for Electron Microscopy,* 2nd ed. (F. A. Davis Co., Philadelphia, 1965).

[23] P. J. Goodhew, *Thin Foil Preparation for Electron Microscopy,* edited by Audrey M. Glauert, Practical Methods in Electron Microscopy, Vol. 11 (Elsevier, Amsterdam, 1985).

[24] *CRC Handbook of Metal Etchants,* edited by Perrin Walker and William H. Tarn (CRC Press, Boca Raton, FL, 1991), pp. 879–884.

[25] *CRC Handbook of Metal Etchants,* edited by Perrin Walker and William H. Tarn (CRC Press, Boca Raton, FL, 1991), pp. 896–899.

[26] S. R. Elliott, *Physics of Amorphous Materials,* 2nd ed. (Longman Scientific & Technical, Essex, England, 1990), p. 87.

[27] B. E. Warren, *X-ray Diffraction,* (Dover, New York, 1990), Chap. 14.

[28] John M. Cowley, *Diffraction Physics,* 2nd ed. (North-Holland, New York, 1981), Chap. 8.

[29] B. D. Cullity, *Elements of X-ray Diffraction,* 2nd ed. (Addison-Wesley, Menlo Park, CA, 1978), Chap. 8.

[30] P. J. Brown, in *Neutron Scattering,* edited by G. Kostorz, Treatise on Materials Science and Technology, Vol. 15 (Academic, New York, 1979), pp. 81–84.

[31] John M. Cowley, *Diffraction Physics,* 2nd ed. (North-Holland, New York, 1981), pp. 128–129.

[32] A. K. Cheetham and J. C. Taylor, *J. Solid State Chem.* **21**, 253 (1977).

[33] H. M. Rietveld, *Acta Cryst.* **22**, 151 (1967).

[34] H. M. Rietveld, *J. Appl. Cryst.* **2**, 65 (1969).

[35] Allen C. Larson and Robert B. Von Dreele, *GSAS: General Structure Analysis System,* instruction manual for computer code **GSAS** (Los Alamos National Laboratory, Los Alamos, NM, 1990), pp. 110–113.

[36] G. Kostorz and S. W. Lovesey, in *Neutron Scattering,* edited by G. Kostorz, Treatise on Materials Science and Technology, Vol. 15 (Academic, New York, 1979), p. 25.

[37] Allen C. Larson and Robert B. Von Dreele, *GSAS: General Structure Analysis System,* instruction manual for computer code *GSAS* (Los Alamos National Laboratory, Los Alamos, NM, 1990), pp. 105–106.

[38] Allen C. Larson and Robert B. Von Dreele, computer code *GSAS: General Structure Analysis System* (Los Alamos National Laboratory, Los Alamos, NM, 1990).

[39] Th.H. de Keijser, J. I. Langford, E. J. Mittemeijer and A. B. P. Vogels, *J. Appl. Cryst.* **15**, 308 (1982).

[40] C. J. Howard, *J. Appl. Cryst.* **15**, 615 (1982).

[41] P. Thompson, D. E. Cox and J. B. Hastings, *J. Appl. Cryst.* **20**, 79 (1987).

[42] B. E. Warren, *X-ray Diffraction,* (Dover, New York, 1990), pp. 35–38.

[43] Stephen W. Lovesey, *Theory of Neutron Scattering from Condensed Matter,* (Oxford University Press, Oxford, 1984), pp. 107–114.

[44] M. Blackman, *Acta Cryst.* **9**, 734 (1956).

[45] A. W. Hewat, *J. Phys. C* **5**, 1309 (1972).

[46] B. E. Warren, *X-ray Diffraction,* (Dover, New York, 1990), pp.191–192.

[47] G. Kostorz and S. W. Lovesey, in *Neutron Scattering,* edited by G. Kostorz, Treatise on Materials Science and Technology, Vol. 15 (Academic, New York, 1979), p. 12.

[48] P. J. Brown, in *Neutron Scattering,* edited by G. Kostorz, Treatise on Materials Science and Technology, Vol. 15 (Academic, New York, 1979), pp. 90.

[49] Philip R. Bevington, *Data Reduction and Error Analysis for the Physical Sciences,* (McGraw-Hill, New York, 1969), pp. 242–245.

[50] H. J. Fecht and W. L. Johnson, *Nature (London)* **334**, 50 (1988).

[51] L. Vegard, *Z. Phys.* **5**, 17 (1921).

[52] L. Vegard, *Z. Cryst.* **67**, 239 (1928).

[53] W. B. Pearson, *The Crystal Chemistry and Physics of Metals and Alloys,* (Wiley, New York, 1972), pp. 174–179.

[54] L. D. Landau and E. M. Lifshitz, *Statistical Physics,* 3rd ed. (Pergamon, New York, 1980), Part 1, pp. 201–203.

[55] Neil W. Ashcroft and N. David Mermin, *Solid State Physics,* (Saunders College, Philadelphia, 1976), pp. 492–494.

[56] Richard A. Swalin, *Thermodynamics of Solids,* 2nd ed. (Wiley, New York, 1972), pp. 63–65.

[57] Harold P. Klug and Leroy E. Alexander, *X-ray Diffraction Procedures for Polycrystalline and Amorphous Materials,* 2nd ed. (Wiley, New York, 1974), pp. 660–665.

[58] Charles Kittel, *Introduction to Solid State Physics,* 6th ed. (Wiley, New York, 1986), p. 110.

[59] Boris W. Batterman and David R. Chipman, *Phys. Rev.* **127**, 690 (1962).

[60] B. E. Warren, *X-ray Diffraction,* (Dover, New York, 1990), pp.190–191.

[61] E. W. Collings, J. C. Ho and R. I. Jaffee, *Phys. Rev. B* **5**, 4435 (1972).

[62] J. M. Ziman, *Principles of the Theory of Solids,* 2nd ed. (Cambridge, New York, 1972), p. 64.

[63] Mikhail A. Krivoglaz, *Theory of X-Ray and Thermal-Neutron Scattering by Real Crystals,* (Plenum, New York, 1969), p. 223.

[64] John M. Cowley, *Diffraction Physics,* 2nd ed. (North-Holland, New York, 1981), pp. 254–261.

[65] S. L. Sass, *J. Less-Common Met.* **28**, 157 (1972).

[66] R. Currat and R. Pynn, in *Neutron Scattering,* edited by G. Kostorz, Treatise on Materials Science and Technology, Vol. 15 (Academic, New York, 1979), pp. 179–185.

[67] Stephen W. Lovesey, *Theory of Neutron Scattering from Condensed Matter,* (Oxford University Press, Oxford, 1984), pp. 129–133.

[68] D. E. Luzzi, *J. Mater. Res.* **6**, 2059 (1991).

[69] P. D. Dernier, W. Weber and L. D. Longinotti, *Phys. Rev. B* **14**, 3635 (1976).

[70] A. Voronel, S. Rabinovich, A. Kisliuk, V. Steinberg and T. Sverbilova, *Phys. Rev. Lett.* **60**, 2402 (1988).

[71] S. Rabinovich, A. Voronel and L. Peretzman, *J. Phys. C* **21**, 5943 (1988).

[72] K. Huang, *Proc. R. Soc. London, Ser. A* **190**, 102 (1947).

[73] Bernard Borie, *Acta Cryst.* **10**, 89 (1957).

[74] Mikhail A. Krivoglaz, *Theory of X-Ray and Thermal-Neutron Scattering by Real Crystals,* (Plenum, New York, 1969), p. 234.

[75] D. B. Sirdeshmukh and K. Srinivas, *J. Mater. Sci.* **21**, 4117 (1986).

[76] F. H. Herbstein, B. S. Borie, Jr. and B. L. Averbach, *Acta Cryst.* **9**, 466 (1956).

[77] C. G. Shirley and R. M. Fisher, *Philos. Mag. A* **39**, 91 (1979).

[78] S. K. Mohanlal and D. Pathinettam Padiyan, *Crys. Latt. Defects Amorph. Mater.* **14**, 23 (1987).

[79] S. K. Mohanlal and D. Pathinettam Padiyan, *Radiat. Eff. Defects Solids* **110**, 385 (1989).

[80] J. Baram and L. Zevin, *Scrita Metall. Mater.* **24**, 1605 (1990).

[81] Alan G. Fox and Robert M. Fisher, *Philos. Mag. A* **53**, 815 (1986).

[82] John M. Cowley, *Diffraction Physics,* 2nd ed. (North-Holland, New York, 1981), p. 378.

[83] F. A. Lindemann, *Z. Phys.* **11**, 609 (1910).

[84] S. Rabinovich, D. Berrebi and A. Voronel, *J. Phys.-Condens. Matter* **1**, 6881 (1989).

[85] Seung-Am Cho, *J. Phys. F* **12**, 1069 (1982).

[86] A. Seidel, S. Massing, B. Strehlau and G. Linker, *Phys. Rev. B* **38**, 2273 (1988).

[87] *Binary Alloy Phase Diagrams,* edited by Thaddeus B. Massalski, Hiroaki Okamoto, P. R. Subramanian and Linda Kacprzak (ASM International, Materials Park, OH, 1990), Vol. 3, pp. 2751–2753.

[88] Livio Battezzati, *Philos. Mag. B* **61**, 511 (1990).

Chapter 5

Quantifying the stability of nonequilibrium solid solutions

To what extent do the results of the previous chapters increase our understanding of the fundamental nature of crystal-to-amorphous and crystal-to-liquid phase transitions? The increase in atomic mean-square displacement (MSD) and in associated structural anomalies as a function of the Pd concentration in Nb–Pd alloys supports the idea that a crystalline solution can be driven toward an instability-induced transition to an amorphous phase by a combination of supersaturation and thermal energy. But does this finding provide any insight into the fundamental question of how to *quantify* the degree of destabilization? In this final chapter of the thesis, I shall survey the various means of parametrizing the stability of the crystalline phase relative to a liquid or amorphous phase of the same composition, indicating those measures that are favored by our experimental results. Prior to embarking on such a discussion, however, we shall find it fruitful to revisit the notion of metastability encountered in Chapter 1 and implicitly assumed in the remainder of the thesis. It will become apparent that the supposed sharp boundary between a solid's metastable and unstable regimes is actually quite diffuse, resulting in competing—rather than mutually exclusive—decomposition processes in crystals driven near the boundary and, consequently, in structural inhomogeneities on several length scales. We shall propose that these topological fluctuations are a fundamental feature of highly nonequilibrium crystalline phases and necessitate the use of a *local,* rather than global, parameter for stability.

5.1 The polymorphous constraint and metastability

Recall that a phase transition is called *polymorphous* when it occurs without change in local chemical composition. Analogously, we say that a crystalline phase satisfies the *polymorphous constraint* if its chemical composition remains uniform throughout the sample: the overall composition can change (as during alloying), but the change must be homogeneously distributed throughout the crystal rather than concentrated in certain regions. We shall see that the *thermodynamic* definition of metastability that we developed in Chapter 1 assumes the applicability of the polymorphous constraint. The physical impossibility of actually imposing such a constraint on a real solid and the observed tendency of real crystals, such as $ErFe_2D_{3.2}$, to violate it in subtle ways suggest that we should develop definitions of metastability and of instability that do not rely explicitly on this constraint.

5.1.1 Thermodynamic definition of metastability

The definition of metastability developed in section 1.5.1 is a fundamentally thermodynamic definition because of its reliance on the shape of free energy curves rather than on any kinetic concepts of the lifetime of the metastable state. Recall from the previous discussion that stable, metastable and unstable regions are determined solely by properties of one or more free energy curves: the stable/metastable boundary is determined by the common-tangent construction used to define an equilibrium two-phase region, and the metastable/unstable boundary is determined by the point at which the curvature of the free energy changes sign

[Figs. 1.1(a) and 1.1(b)]. Decomposition of a metastable crystalline phase occurs by a nucleation and growth mechanism because a finite energy barrier must be overcome to create compositional fluctuations in the phase [1]. In contrast, there is *no* energy barrier for the buildup of such fluctuations in an unstable crystal, at least for long-wavelength fluctuations, for which interfacial energies are negligible [1, 2]; this kind of decomposition results in, for example, the "tweed" microstructure seen in spinodal decomposition [3].

Note that the polymorphous constraint is implicitly assumed in drawing a continuous free energy curve over a wide range of compositions. The curve gives the free energy of a *chemically uniform* sample with fixed symmetry (i.e., bcc, fcc, hcp); the very existence of the curve relies on the concept of the polymorphous constraint. There is a fundamental problem with diagrams of this sort, however, that is related to the conceptual difficulties of defining the properties of an absolutely unstable crystal, such as one having a higher entropy than the liquid of the same composition (section 1.5.2). Thermodynamic stability criteria tell us that global thermodynamic energy functions must be convex functions of their variables [1, 4, 5]. Not surprisingly, sophisticated free energy calculational techniques (such as cluster calculations) yield no concave regions in the unstable region of Fig. 1.1(a); instead, the more accurate they get (corresponding to the larger and larger clusters that they include), the closer they approximate a free energy curve that is flat in the equilibrium two-phase region, as predicted by the common-tangent construction. In other words, global free energy curves *cannot* look like the curve of Fig. 1.1(a). Such a curve with concave regions can be interpreted only as "coarse-grained free energy functional" [1]—i.e., as a *local* free energy. In order to calculate local free energy curves, one must obviously suppress the phase separation entailed by the flat free energy curve in the equilibrium two-phase region [1, 2], but such a step is equivalent to imposing the polymorphous constraint!

The thermodynamic definition of metastability predicts a sharp boundary between metastable and unstable regions and a concomitant qualitative difference in decomposition mechanisms in the two regions. Recent theoretical studies of this boundary, however, find no sudden change in dynamic behavior when passing from the metastable region to the unstable [1, 2]; rather, there occurs a gradual transition from nucleation and growth to spinodal (i.e., long-wavelength) decomposition. The physical reason for this is that the nucleation barrier drops as the composition moves away from the equilibrium coexistence line (that is, as the overall composition moves deeper into the metastable region) until it is of the order of $k_{\mathrm{B}}T$. As the nucleation barrier shrinks, the rate of decomposition by nucleation and growth increases. Simultaneously, the closer the system gets to the spinodal curve, the lower the energy cost becomes for long-wavelength compositional fluctuations. In the region near the thermodynamically defined boundary between metastable and unstable regions, both decomposition processes occur simultaneously, with the predominant process changing gradually from nucleation and growth to spinodal decomposition as the system moves across the spinodal curve [1].

5.1.2 Kinetic definition of metastability

These observations suggest that the thermodynamic definition of metastability is poorly equipped to distinguish metastable from unstable phases, which, after all, is a primary task in studying the dynamic behavior of destabilized phases. A rather more useful definition can be formulated using kinetic criteria [1, 2]. Metastable phases fabricated in computer simulations and in actual experiments demonstrate two characteristic time scales, the difference between them being a measure of metastability. The first time scale, labeled τ_1, is the time for an order parameter (see section 5.2) characteristic of the metastable phase to settle down to a more or less "steady" value. The second time scale, τ_2, is the time at which it becomes apparent that the metastable state is not truly an equilibrium state but is in fact slowly relaxing; evidence for relaxation would come from a noticeable change in the "steady-state value" of the order parameter whose relaxation time defined τ_1. Metastability is signaled by a significant difference (i.e., many orders of magnitude) in the time scales τ_1 and τ_2; that is, metastability corresponds to a highly nonlinear decay of the order parameter with time [1, 2].

Though subject to a certain degree of arbitrariness, such a kinetic definition of metastability provides a practical, useful way to distinguish between metastable and unstable phases. This definition, moreover, makes explicit the smooth transition between metastable and unstable phases, since increasing destabilization (i.e., movement of the system away from equilibrium) will correspond to τ_2 and τ_1 approaching each other. It also makes clear the task in fabricating crystalline samples with progressively less stability: they must relax to the desired state during τ_1 and have a metastable lifetime $\tau_2 - \tau_1$ long enough to permit the necessary thermodynamic, mechanical and structural measurements to be performed. Such measurements must determine the extent to which the sample satisfies the polymorphous constraint, and they must evaluate the stability of the resulting crystalline configuration. We discuss the former task in the next section (section 1.1.3) and the latter task later in the chapter (section 1.2).

5.1.3 The polymorphous constraint and length scales

Recall that the enthalpy change upon heating $ErFe_2D_{3.2}$ powder in a sealed differential scanning calorimetry cell had the *opposite* sign to what is expected of polymorphous melting and amorphization (section 3.5.2). We assigned the cause of this discrepancy to violation of the polymorphous constraint: instead of preserving the uniform chemical distribution of the crystalline deuteride, the amorphous phase formed with Er-rich and Fe-rich clusters. Apparently, the final state of the crystal-to-amorphous transition fell in the unstable region of the homogeneous amorphous phase (see Fig. 3.18), resulting in enthalpy release upon amorphous phase decomposition. Had the final state been a chemically uniform amorphous phase, on the other hand, the transition would have been endothermic, as expected.

A moment's reflection makes it clear that violations of the polymorphous constraint should be quite common, especially since a crystal driven into the metastable region wants to phase separate in order to lower its total free energy. Decomposition into two or more crystalline phases, however, is easily detectable with diffraction techniques. What is unsettling about the deuteride case is that the clustering occurred on a nearly atomic-level length scale (most likely in regions less than 2 nm in size, as suggested by the size of the crystallized ErD_2 regions), but it had an enormous influence on the thermodynamics of the transition: the exothermic enthalpy release had about the same order of magnitude as one would have expected of the heat of fusion at that temperature! Clustering on such a short length scale, especially in the amorphous phase, is very difficult to detect by the commonly available tools for structural characterization. But it is at short length scales that changes in chemical ordering will have their greatest impact, since bond energies are dominated by nearest-neighbor interactions. In other words, the violations of the polymorphous constraint that are the hardest to detect are the ones that have the most significant thermodynamic effect. Our experiments on $ErFe_2D_{3.2}$ underscore the importance of restricting the class of polymorphous phase transitions to those in which *topological* order changes but *chemical* order does not.

Chemical inhomogeneities occurring on longer length scales are also difficult to detect in an amorphous phase. Recent studies by Sales and colleagues at Oak Ridge obtained a quantitative measure of structural differences at length scales of 5 nm and beyond (!) between amorphous lead pyrophosphate formed by water-quenching and by ion irradiation [6, 7]. [They were able to measure aspects of structure over such a long-range in amorphous phases by utilizing a novel technique—high-performance liquid chromatography (HPLC)—that is sensitive to chains of PO_4 tetrahedra in the amorphous phases.] The clear differences that they found in the amorphous product phases of two different synthetic routes contradict previous findings of path independence of amorphous phase preparation schemes in comparisons of atomic radial distribution functions (RDF) [8, 9], but meaningful RDF information can be determined only out to about 2 nm. Fortunately, the same reasons that make thermodynamic measurements sensitive to changes in short-range chemical structure render them rather insensitive to long-range changes during ostensibly polymorphous transitions.

5.1.4 Can crystal-to-amorphous transitions be polymorphous?

With all of the possible ways that a system can violate the polymorphous constraint and with the associated difficulties in detecting those violations when they occur over very short or long length scales, it is fair to ask if *any* crystal-to-amorphous phase transitions occur polymorphously. There are, of course, examples of polymorphous transitions in real materials, such as allotropic and displacive transitions and the melting of elemental solids. I know of no proof as yet, however, that any crystal-to-amorphous transitions—with the probable exception of pressure-induced amorphization of certain nonmetals—meet this constraint. Good candidate transitions would be those that destabilize an already-formed crystalline state, such as hydrogenation, ball milling, irradiation or implantation. We saw evidence in Chapter 3 that violation of the polymorphous constraint is the actual driving force for hydrogen-induced amorphization, thus eliminating hydrogenation from consideration. Likewise, the energy storage accompanying decrease in chemical order is thought to be necessary for irradiation-induced amorphization of intermetallic compounds [10]. That leaves ball milling and implantation as remaining possibilities. Some recent studies employing each method do, indeed, suggest experimental realization of a polymorphous crystal-to-amorphous phase transition. Let us briefly consider each one.

Mechanical alloying of Zr–Al

Mechanical alloying of up to 15 at.% Al with Zr results in a single-phase $Zr_{100-x}Al_x$ solid solution having the terminal α-Zr structure (hcp) [11, 12, 13, 14, 15]. For $x \gtrsim 17$ a homogeneous amorphous phase results; the two-phase crystalline+amorphous region separating the single-phase regions is remarkably narrow ($\lesssim 2$ at.% wide) [12, 15]. Ma and Atzmon [12, 13, 14] have produced rather convincing evidence (enthalpy measurements and calculated free energy curves) that the crystal/amorphous compositional formation boundary occurs within a few atomic percent of the room-temperature crossing point of the free energy curves; that is, the crossover from crystalline to amorphous occurs at about the composition of the T_0 line corresponding to room temperature. Furthermore, their lattice parameter measurements as a function of Al concentration are consistent with there being no solute segregation in the single-phase crystalline alloy up to the two-phase boundary. If the T_0 line for the α-Zr phase becomes nearly vertical at low temperatures like room temperature, the maximum composition of hcp Zr–Al made by mechanical alloying may be close to the isentropic maximum composition c^*.

It is difficult to understand, however, why the amorphous phase does not nucleate heterogeneously at a lower Al concentration due to the high defect density (dislocations, stacking faults, grain boundaries, etc.) of ball-milled powders. Furthermore, the broadening of x-ray diffraction peaks caused by grain-size refinement and strain [16] in the ball-milled alloys makes it impossible to determine the lattice parameter with sufficient accuracy to rule out small amounts ($\lesssim 10\,\text{at.\%}$) of solute segregation. The amorphous phase has not been checked for short-range clustering of the type seen in amorphous deuterated $ErFe_2$, but x-ray diffraction scans reveal no anomalous structure indicative of clustering, as with the deuteride. Ongoing experiments are still searching for enhanced thermodynamic or mechanical properties of the metastable crystalline powders near the calculated T_0 boundary. Efforts to measure the average mean-square displacement (MSD) by powder diffraction [15] and the grain boundary structure and dimensionality [17] by small-angle x-ray or neutron scattering (SAXS or SANS) [18, 19] hold particular promise.

Implantation of B into Nb and Mo

As discussed several times already, Linker and colleagues found that the implantation of boron into liquid-nitrogen-cooled films of Nb or Mo resulted in interstitial incorporation of B atoms until a critical concentration of B was reached, at which point regions of the sample became amorphous [20, 21]. In both cases, the critical concentration for amorphization (5–7 at.% B) is reasonably close to the maximum possible supersaturation concentration c^* defined by the concentration at which the T_0 line becomes vertical [Figs. 5.1(a) and 5.1(b)]. Again, it is difficult to verify the extent to which the amorphization in this case is polymorphous, even though it seems to occur (at least locally) at the instability line of the polymorphous phase diagram. The implantation process introduces defects that should produce sites for heterogeneous nucleation of the amorphous phase, and—as with the amorphous Zr–Al alloys discussed above—the amorphous Nb–B and Mo–B

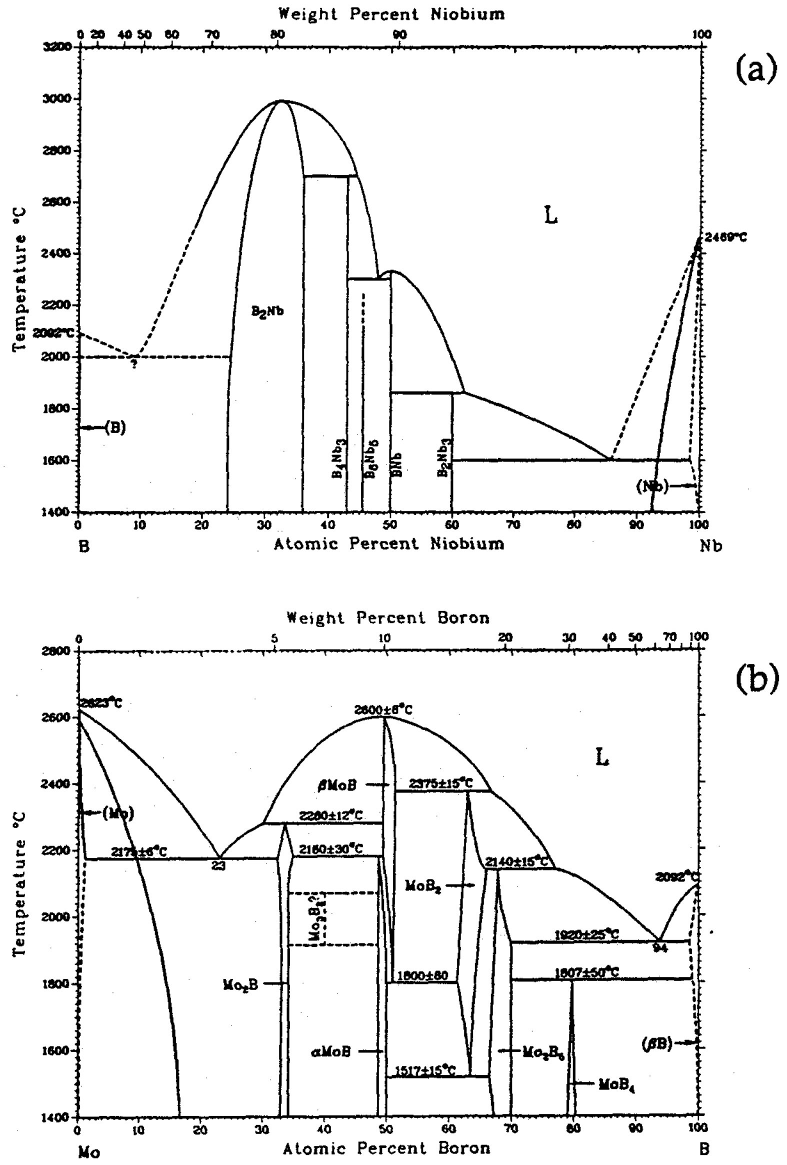

Figure 5.1: Phase diagrams of (a) B–Nb and (b) Mo–B taken from Refs. [22, 23]. We have sketched in reasonable T_0 lines for the Nb and Mo terminal solutions.

states were not checked for short-range clustering, which has been found in other metal-metalloid glasses [8].

5.2 Parameters for crystalline stability

We have seen in the previous sections that determining compliance with the polymorphous constraint during amorphization of a crystalline phase can be a daunting project. Now we turn to the associated task of quantifying the loss of stability as the crystalline phase is driven toward the amorphous state. A logical first step in attacking the latter problem would be to define crystalline stability in terms of an order parameter for the crystal-to-liquid or crystal-to-amorphous transition. An *order parameter* for a phase transition is an extensive variable that has a different value in the ordered and disordered phases on either side of the transition [1]. By convention it is chosen to be zero in the disordered phase and non-zero in the ordered phase. Depending on the nature of the phase transition, the appropriate order parameter can be a scalar, vector or tensor quantity [1]. For example, the order parameter for melting is the Fourier component of the atomic density at a reciprocal lattice vector $\mathbf{G}$. Just as with liquid phases, amorphous phases have $\rho_{\mathbf{G}} = 0$, as desired, so this is an appropriate order parameter for the crystal-to-amorphous phase transition, as well.

We now ask if it is possible to quantify the stability of the crystalline state in terms of this order parameter. As long as the crystal has long-range translational order, the Fourier component of the atomic density at reciprocal lattice vectors will be nearly constant; thus, such a quantity is relatively insensitive to the local structural changes that may accompany superheating and supersaturation. Alternatively, the fact that crystals can support shear forces and liquids cannot suggests using some kind of shear modulus as an order parameter for melting and amorphization. Amorphous phases can also support shear forces, however, so the shear modulus cannot be a proper order parameter for both phase transitions. How about the atomic mean-square displacement (MSD) that is fundamental to the Lindemann criterion for melting and, as we argued in the previous chapter, is a criterion for amorphization as well? In the liquid phase the MSD is clearly infinite, but in the amorphous phase it is certainly not infinite because the atoms are trapped within the shell formed by their nearest neighbors. If we were to define an order parameter by 1/MSD, for example, it would be finite in the solid and amorphous phases and zero in the liquid. Although it does not satisfy the criteria for being a proper order parameter for both melting and amorphization, it represents an improvement over the Fourier-component order parameter, for 1/MSD is observed to decrease as the stability of the crystalline phase decreases, be it due to heating or to supersaturation (Chapter 4).

The latter example suggests that it may be better to relax the definition of *order parameter* than either to search for a proper order parameter appropriate for both melting and amorphization or to deal with the complications of having *two* order parameters—one for each transition. In the spirit of the one-phase melting/amorphization instability theories discussed in Chapter 1, let us focus our attention on the crystalline phase alone and require only that the appropriate parameter vanish at the stability boundaries of the crystalline phase; in order to distinguish this new parameter from an order parameter as properly defined, we shall refer to it as a *stability parameter.* For example, the Lindemann criterion defines a maximum possible MSD for the crystalline phase: $\langle u^2 \rangle_{\mathrm{max}}$. Using this quantity we may define a stability parameter $\phi \equiv \langle u^2 \rangle_{\mathrm{max}} - \langle u^2 \rangle$ that would vanish at the stability limit of the crystalline phase against both melting and amorphization. This is not the only possible stability parameter, however: in Chapter 1 we discussed several lattice instability theories for melting and amorphization, each of which has an associated measurable quantity that can be cast in our stability parameter language. I shall conclude this thesis by comparing these various proposed parameters and attempting to identify which, if any, are most appropriate for describing crystal-to-amorphous phase transitions.

5.2.1 Atomic-level stress

As discussed in sections 1.4 and 2.2, the "atomic-level stress criterion" developed by Egami and Waseda [24] to account for the success of their empirical equation [Eq. (1.2)] for predicting glass formation ranges in binary alloys is predicated on an instability of the local topology of the crystalline phase [24]. The instability is caused by the buildup of hydrostatic stress in the lattice due to replacing A atoms with B atoms of a smaller or larger size [25]. Collapse occurs when a change in coordination number will relieve the (local) elastic energy arising from the size mismatch.

Egami and Aur [25] interpret this instability as a kinetic condition for glass formation: crystallization kinetics are slowed by the local instability of the crystal leading to "mistakes" in lattice plane registration during crystallization, resulting in the incorporation of many defects and drastically slowing the progress of crystallization in the undercooled melt. This interpretation highlights the fact that Eq. (1.2) was optimized to account for the boundary between crystallization and glass-formation during a rapid-quenching experiment from a disordered phase to an ordered phase, rather than being optimized to the stability boundary of the crystalline phase itself. In other words, the approximation $\lambda_{\mathrm{EW}} \approx 0.1$ for $x_{\max}|\Delta V|/V_{\mathrm{A}}$ is probably quite sensitive to cooling rate; its extrapolation to zero cooling rate would represent a more realistic stability limit for the supersaturated crystalline alloy. It should be noted, however, that empirical support for a value of 0.1 comes from vapor-quenching experiments by Liou and Chien [26], which demonstrated that Eq. (1.2) with $\lambda_{\mathrm{EW}} \approx 0.07$–$0.09$ does a good job of predicting the experimentally determined glass-formation ranges, even though the cooling rate of vapor-quenching is ~ 6 orders of magnitude faster than that of liquid quenching [27].

5.2.2 Volume expansion

The results of irradiation-induced amorphization have led to speculation that a critical amount of volume expansion, sometimes called *free volume*, triggers amorphization [10]. For instance, it was observed in irradiation experiments of 1 MeV Kr^+ ions directed at Zr_3Al that lattice expansion occurred without amorphization until a relative expansion of ~ 0.8 % was reached [28]; hydrogen-induced amorphization of Zr_3Al found no homogeneous amorphization until the lattice expansion reached the same value [29, 30]. This criterion has several drawbacks, however: It provides no explicit reason for loss of crystalline order at a particular volume expansion (a defect shared by the atomic-level stress criterion and the Lindemann criterion). There are also indications from computer simulation that the volume expansion is much more dependent on processing history than the atomic-level stress criterion is [31]. Furthermore, it is not clear how to measure volume expansion in substitutional alloys—as opposed to intermetallic compounds—for there is no well-defined *reference volume* of an "ideal" solid solution. Finally, we recall that some crystalline solids actually *shrink* upon amorphization when the transformation is induced by the application of pressure (section 1.1.6).

5.2.3 Crystal rigidity

The elastic moduli of the crystalline phase are direct measures of its mechanical stability. If one were to drop to zero or become very small (i.e., become soft), the crystalline lattice would become unstable with respect to the shape change associated with the soft modulus. For a cubic lattice there are three independent elastic moduli [10]: two shear constants, c_{44} and $C' = \frac{1}{2}(c_{11} - c_{12})$, and the bulk modulus, $B = \frac{1}{3}(c_{11} + 2c_{12})$, where the c_{ij}'s are the elastic stiffness constants [32]. In general, we do not expect the bulk modulus B to become small or vanish upon melting or amorphization because (i) the bulk moduli of metallic glasses are only a few percent less than those of corresponding crystalline phases [8], (ii) the bulk moduli of the crystalline phase of elemental solids extrapolate smoothly to the B of the liquid phase [33], and (iii) even systems with shear instabilities have normal B behavior (e.g., Mo–Re [34]). Thus, we expect any elastic instability to be reflected in the shear moduli (c_{44} and C') rather than in the bulk modulus.

There is evidence from irradiation experiments on intermetallic compounds that one of the shear moduli of the crystalline phase decreases as the radiation dose increases to the critical value for amorphization [10, 28]. In fact, if the normalized shear modulus C/C_0 is plotted as a function of the volume expansion of the lattice $\Delta V/V_0$, C/C_0 extrapolates to zero at about the volume expansion of the resulting amorphous phase! Tallon [33] has made a similar plot for the shear moduli of elemental cubic crystals versus the volume expansion that occurs upon heating up to and above the melting point. He finds that in each case one of the shear moduli extrapolates to zero at about the volume expansion of the resulting liquid phase.[1]

Thus, shear instability provides a mechanism for melting and amorphization triggered by volume expansion: at the critical volume expansion one of the shear moduli becomes small enough that the crystalline phase loses its rigidity and collapses to a disordered phase. While this makes it tempting to view volume expansion as the underlying cause of the shear instability, I feel that this view is mistaken, since the shear criterion is more generally applicable: it can explain, for

---

[1] This general relationship does not hold for materials having a *higher* density in the liquid phase than in the crystalline phase, of course. Examples of such exceptions include Si, Ge, Ga, Bi, Sb and H_2O [10, 35].

example, amorphization in solid solutions, which do not display significant volume expansion upon progressive destabilization [cf. behavior of lattice parameter upon supersaturation of Nb–Pd (Fig. 2.15)]. Also, one should not expect the shear modulus to depend fundamentally on lattice volume, since shearing of a unit cell affects its volume only to second order.

5.2.4 Hierarchy of instabilities

Tallon [35] recently proposed that the entropy instability of Fecht and Johnson [36] together with the volume and shear instabilities discussed above form a hierarchy of instability points for superheated elemental crystals. The *isentropic* instability—the temperature at which the crystal and liquid have the same entropy—is preceded by the *isochoric* point, which occurs when the crystal and liquid have the same volume. Empirical studies and computer simulation both identify the isochoric point as the temperature at which the entropy of the superheated crystal is equal to the entropy of the liquid less its communal entropy [35, 37]. Tallon assigns the *rigidity* instability to an even lower temperature at which the volume of the superheated crystal equals that of the liquid at the freezing point, and he points out that in Boyer's [38] thermoelastic instability theory of melting (section 1.3.2), the impending rigidity collapse causes a preemptive divergence of the crystalline phase's compressibility. Thus, starting from the equilibrium melting temperature, a superheated crystal would encounter instabilities in the following order [35]: elastic compressibility, elastic rigidity, isochoric instability and isentropic instability. In Tallon's opinion it would not be possible to access the isochoric and isentropic instabilities experimentally because the crystal would transform to a liquid upon losing rigidity.

Whether such a hierarchy applies to the crystal-to-amorphous transition remains open to question. Since the rigidity and isochoric instability points occur at nearly the same condition ($V_X \approx V_L$), Tallon's argument applied to amorphization implies that a highly destabilized crystalline alloy would have nearly the same volume as that of an amorphous phase at the same composition. Plots of the composition dependence of average atomic volume in the Fe–P and Zr-Rh alloy systems [Figs. 5.2(a) and 5.2(b)] seem to contradict this assertion: the extrapolated volume of the crystalline phase at the crystal/amorphous composition boundary is significantly smaller (2.7 % for Fe–P and 2.4 % for Zr–Rh) than that of the amorphous phase extrapolated to the same composition. If vanishing of the shear modulus is indeed linked to near equality of crystalline and amorphous volumes, then these volume dependences may indicate that the isentropic instability is more restrictive than the shear instability, at least in alloys.

5.2.5 Effective elastic modulus

The shear modulus could vanish *before* the volumes of the liquid and crystalline phases are approximately equal, of course. A general way to estimate the composition of rigidity collapse in crystalline alloys based only on the Debye temperature θ_D was proposed by Johnson [43] in the context of calculating an effective elastic modulus M_{eff}:

$$M_{\text{eff}} = \rho \left(\frac{k_B\theta_D}{\hbar q_D}\right)^2 = \left(\frac{a_1}{G^{3/2}} + \frac{a_2}{B^{3/2}}\right)^{-2/3}, \tag{5.1}$$

with Debye wavevector q_D, density ρ, isotropic shear modulus G, bulk modulus B and constants a_1 and a_2. We note that $M_{\text{eff}} \propto \theta_D^2$ and that if $G \to 0$, then $M_{\text{eff}} \sim G$ (we do not expect $B \to 0$ for reasons given in section 5.2.3). Thus, for $G \to 0$, $G \sim \theta_D^2$, a relation known to be generally true even when G is not small [44].

We now apply Eq. (5.1) to three binary systems for which the composition dependence of θ_D has been measured: Zr–Rh [45], Mo–Re [34, 46] and Nb–Pd. For the Zr–Rh system, the effective modulus (Fig. 5.3) falls rapidly as the Rh concen-

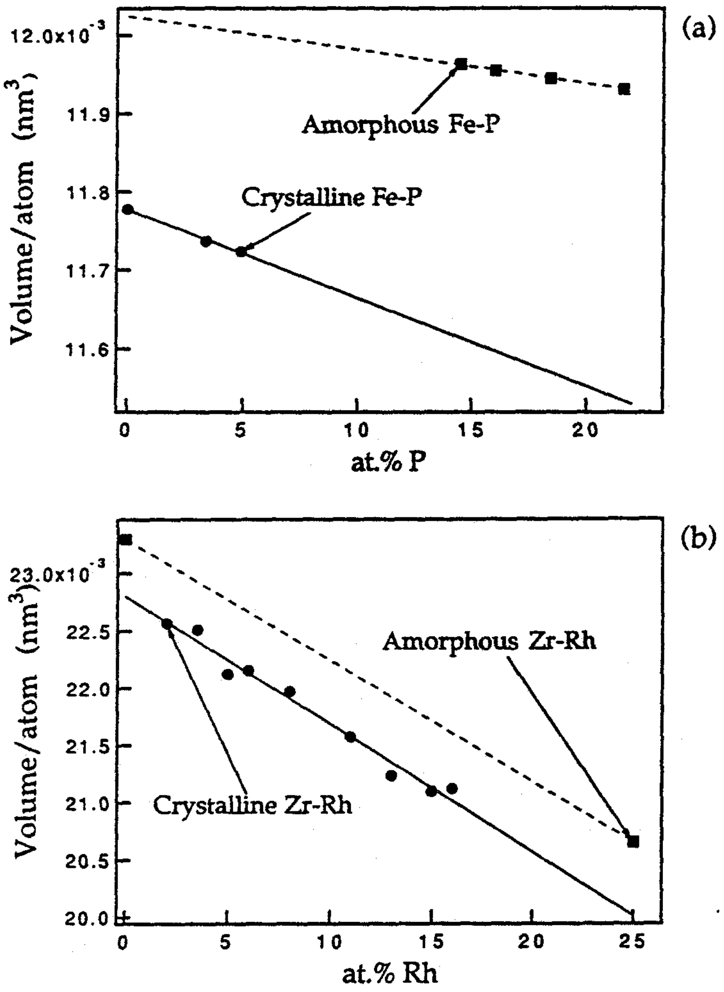

Figure 5.2: Atomic volume plotted against composition for (a) Fe–P and (b) Zr–Rh alloys. The difference between the atomic volume in crystalline and amorphous phases at all compositions suggests that the crystalline phase does not become unstable with respect to amorphization at an equal-volume condition. Data for Fe–P obtained from Refs. [39, 40]; data for Zr–Rh obtained from Refs. [41, 42, 54].

tration increases from zero to 9 at.%. An additional point can be extrapolated at ~ 15 at.% Rh using the superconducting transition temperature T_c measured for that alloy [54], its estimated electronic specific heat γ extrapolated from measurements at lower Rh concentrations [45] and the modified BCS-Morel relationship between T_c, γ and θ_D [55, 56]. Notice in Fig. 5.3 the significant difference between the effective modulus of the crystalline Zr–Rh alloys extrapolated to higher Rh content and both the effective moduli of the Zr–Rh intermetallic phases and of several Zr-based amorphous phases. M_{eff} of the crystalline phase at the crystalline/amorphous boundary found by melt spinning (~ 15 at.% Rh [54]) is lower than the extrapolated effective modulus of the amorphous phases or of the intermetallic compounds at the same boundary. Extending a curve through the effective moduli of the crystalline alloys to zero modulus (i.e., shear instability) finds a maximum Rh concentration of 20–25 at.%, which is nearly identical to the isentropic maximum concentration c^* that one would estimate from the Zr–Rh phase diagram (Fig. 5.4).

For the Mo–Re binary system both the compositional dependence of the Debye temperature and also that of the elastic moduli have been measured. Although the phase diagram of Mo–Re [58] indicates that the terminal Mo solution does not have a plunging T_0 line, it is possible to make amorphous films of Mo–Re by vapor quenching [59]. Compositional measurements of the elastic constants find a decrease in C' for increasing Re concentration but an *increase* in c_{44} and B [34]. The Debye temperature and, consequently, the effective modulus M_{eff} both decrease rapidly, with the effective modulus falling by nearly a third between pure Mo and $\text{Mo}_{60}\text{Re}_{40}$ (Fig. 5.5). The boundary between crystalline and amorphous phases for amorphous alloys with a crystallization temperature above room temperature falls at a composition (~ 50 at.% Re [59]) at which both C' and M_{eff} extrapolate to relatively small values, suggesting that the stability of the amorphous phase for

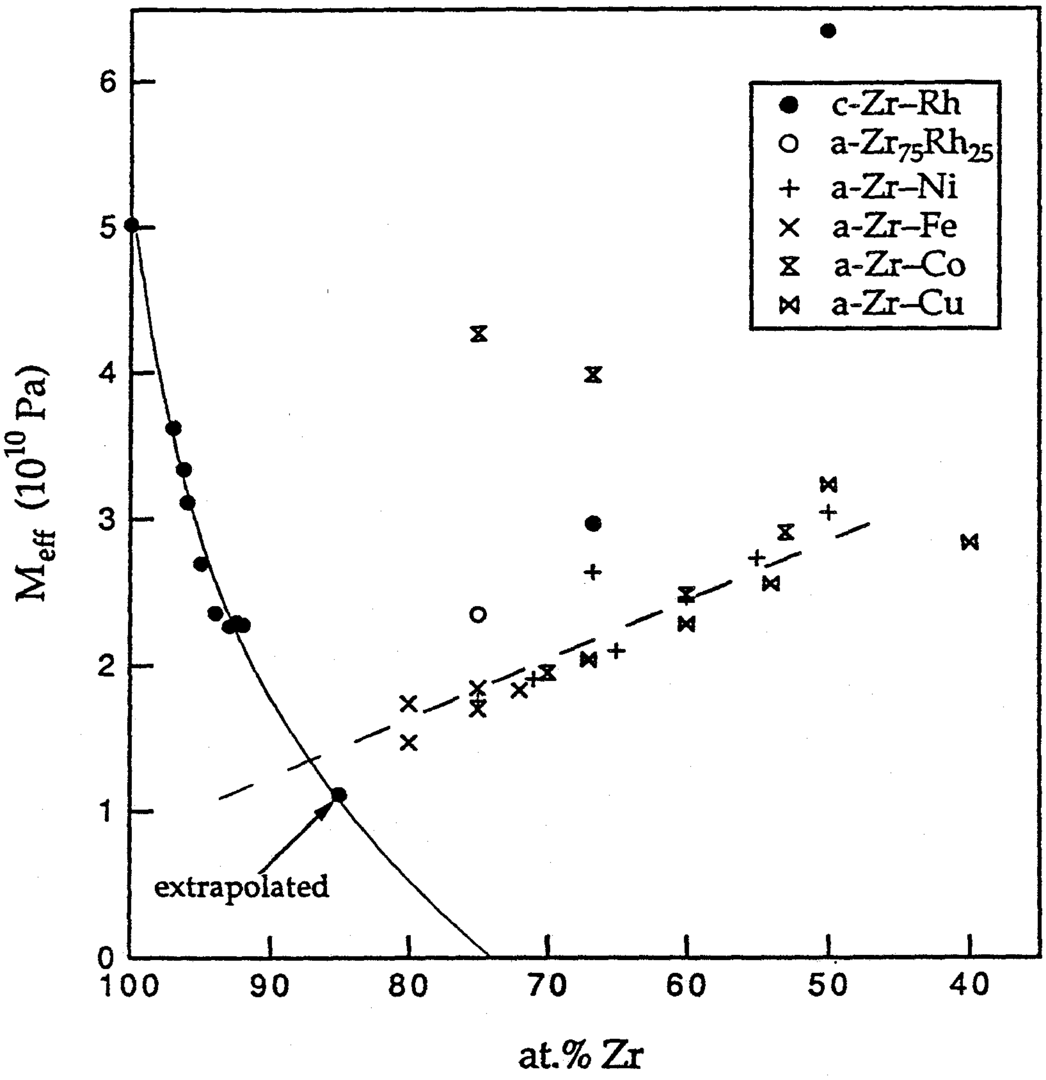

Figure 5.3: Effective modulus M_{eff} plotted against Zr concentration for crystalline Zr–Rh alloys, amorphous $Zr_{75}Rh_{25}$ and some Zr-based amorphous alloys. M_{eff} of the crystalline phases falls rapidly as the Rh concentration nears the experimentally observed crystalline maximum of 15 at.% [54]. Extrapolating M_{eff} to zero yields a maximum Rh solubility of 20–25 at.%. Data for calculating M_{eff} of amorphous Zr-based alloys obtained from Refs. [41, 47, 48, 49, 50, 51, 52, 53].

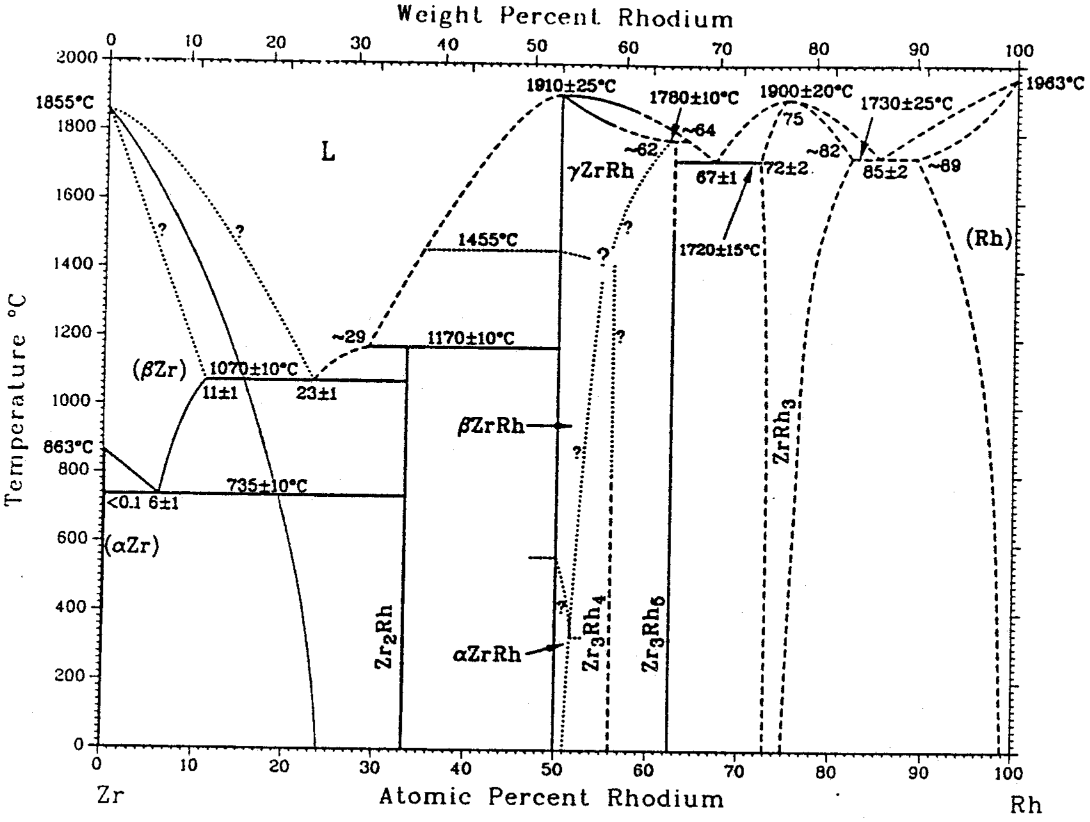

Figure 5.4: Phase diagram of Zr–Rh taken from Ref. [57]. We have sketched in a reasonable T_0 line for the β-Zr terminal solution; note that it becomes vertical at about the same Rh concentration as M_{eff} extrapolates to zero in Fig. 5.3.

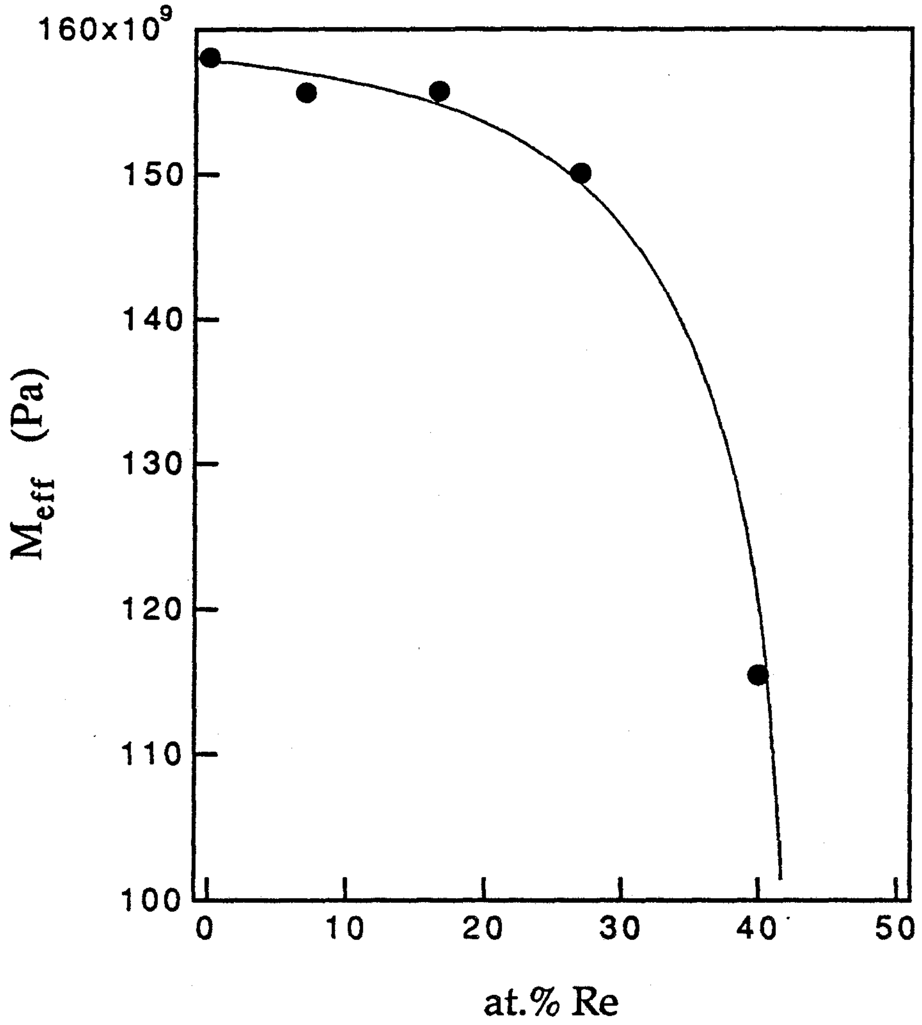

Figure 5.5: Effective modulus M_{eff} plotted against Re concentration for Mo–Re alloys. M_{eff} of the crystalline phases falls to a small value as the Re concentration approaches the composition ($\sim$ 50 at.% Re [59]) at which amorphous Mo–Re thin films are stable at room temperature.

Re concentrations above about 50 at.% is enhanced by the relative instability of the crystalline phase of the same composition. Incidentally, if the elastic constants had been measured on polycrystalline Mo–Re rather than on single crystals, only a directionally averaged shear modulus $G \approx \frac{1}{5}(2C' + 3c_{44})$ [60] could have been determined. In the Mo–Re case, such a G would actually *increase* until rather high Re concentrations, even though C' decreases monotonically [34] (Fig. 5.6)! From an experimental perspective, the Debye temperature θ_D can evidently be a more sensitive probe of crystalline stability than direct measurement of the elastic constants of a polycrystalline sample, which is usually the only form in which supersaturated solutions can be prepared.

Finally, using the measured compositional dependence of θ_D in Nb–Pd alloys (Fig. 4.13), we can compute the effective moduli of the bcc Nb-based alloys investigated in Chapter 4. Unlike the Zr–Rh case, M_eff for Nb–Pd (Fig. 5.7) does not fall rapidly to zero; rather, only at high ($\sim$ 30 at.% Pd) does it begin to drop quickly. Extrapolation to small M_eff is difficult because of the few data points in the region of large negative slope, but fitting a quadratic curve to the measured bcc-phase Debye temperatures of Fig. 4.13 allows somewhat reliable calculation of M_eff out to $\sim$ 70 at.% Pd. As is evident in Fig. 5.7, the extrapolated M_eff falls to less than one-third of its value in pure Nb by 70 at.% Pd, suggesting that a shear instability may be likely to occur near this composition.

5.2.6 Local topological collapse

In the preceding discussion of crystalline stability, we have focused almost exclusively on stability parameters characteristic of a whole sample, such as the Debye temperature, shear modulus, or average mean-square displacement. It is not necessary, however, for a crystalline solid to become unstable and collapse homogeneously—i.e., uniformly in every volume element of the whole. Rather, the

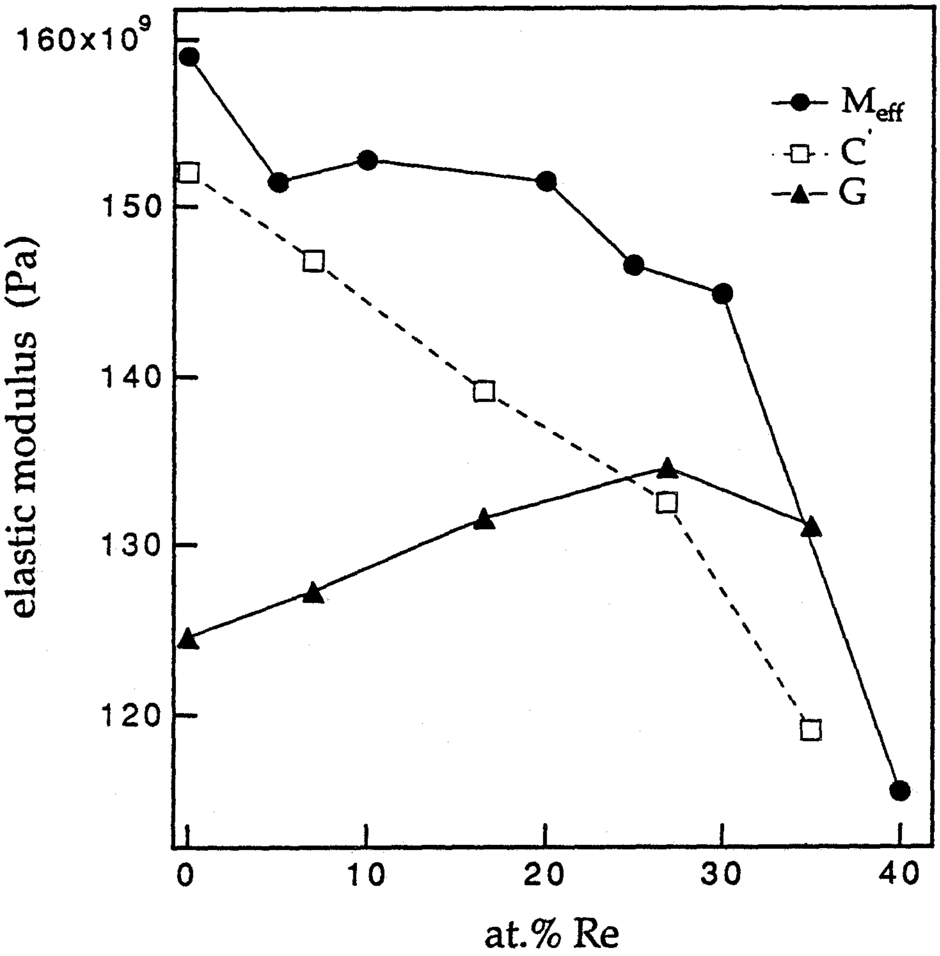

Figure 5.6: Plot of M_{eff}, the shear modulus C' and the directionally averaged shear modulus G against Re concentration for Mo–Re alloys. Note that M_{eff} and C' fall monotonically, but the averaging inherent in G causes it to rise until large Re concentrations are achieved. Data for C' and G taken from Ref. [34].

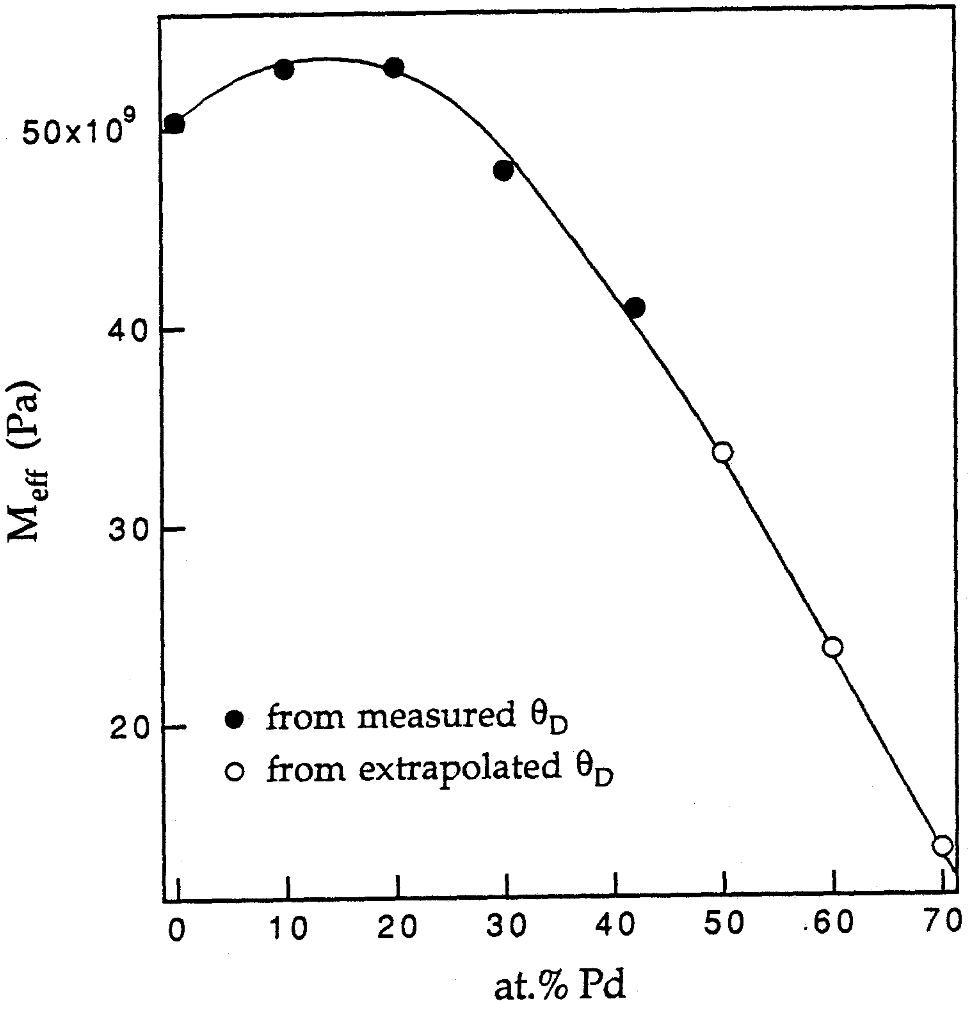

Figure 5.7: Effective modulus M_{eff} plotted against Pd concentration for Nb–Pd alloys. M_{eff} of the crystalline phase increases at first and then drops at higher Pd concentrations. Extrapolating M_{eff} to higher Pd concentration (open circles) by fitting a quadratic curve to the bcc data of Fig. 4.13 suggests that a shear instability could occur in Nb–Pd at 60–70 at.% Pd, by which point M_{eff} has dropped by about two thirds.

destabilization process could progress at different rates in different regions of the sample. Fluctuations in atomic-level stress, free volume, (local) shear modulus, (local) Debye temperature, etc., could lead to some regions of the sample melting or amorphizing before other regions do so. Such nonuniform nucleation of the disordered phase might be explained as simple heterogeneous nucleation at defects, but recent irradiation-induced amorphization studies [10, 61] call that explanation into question, at least in certain experimental circumstances. Let us consider some examples of experimental techniques that relate measurable quantities—diffuse scattering of electrons, mean-square atomic displacements, high-resolution transmission electron microscopy images—to local distortions in nonequilibrium crystalline phases.

Irradiation-induced amorphization of Cu_4Ti_3

Using high-energy electrons (2 MeV) in a transmission electron microscope (TEM), Luzzi [61] was able to observe irradiation-induced amorphization of Cu_4Ti_3 at a nearly atomic level. He found that the chemical order of the Cu_4Ti_3 decreased, but did not vanish completely, before amorphization began. Simultaneously, he witnessed the development of diffuse scattering upon looking down all zone axes of the unit cell except for the $\langle 771 \rangle$ direction (effectively, the $\langle 111 \rangle$ direction of the bcc subunit cell out of which the Cu_4Ti_3 unit cell is built). Such a finding indicates that displacements of atoms are occurring out of their equilibrium positions along the close-packed atomic chains of the bcc structure; the displacements occur preferentially in the $\langle 111 \rangle$ direction because this is the direction characteristic of atomic replacement collision sequences in irradiated bcc crystals [61].

In the TEM Luzzi was able to track the entire amorphization process of the sample from the completely crystalline initial state to the completely amorphous final state. He found that the amorphous phase first nucleated at isolated regions about 2 nm in size rather than nucleating uniformly throughout the sample. He accounted for this observation with a model of *local* buildup of topological disorder—predominantly along the ⟨111⟩ direction—that, upon exceeding a critical value, creates small regions of amorphous phase. Such local disorder cannot be attributed to fluctuations in the electron dose, since only minimal dose variations could occur over the small spatial extent of the islands. Neither can heterogeneous nucleation at defects account for the local amorphization, since no such defects could be observed in the crystalline phase either before or during irradiation. It appears, therefore, that the crystal prefers to relieve the ⟨111⟩ disordering by homogeneously amorphizing in small regions. It is not yet understood what governs the size or spacing of these amorphous zones.

Mean-square displacement as a *local* stability parameter

The implantation-induced amorphization experiments of Linker and colleagues [62] also support the idea of local amorphization. They observed that the mean-square displacement (MSD) of Al films grows approximately linearly with the concentration of implanted Mn until an amorphous phase is nucleated (see Fig. 4.19). At that point, the MSD of the remaining crystalline phase drops nearly to zero! The film apparently can relieve all of the built-up disorder caused by excess Mn in the crystalline Al matrix by forming regions of amorphous phase. Since the MSD parameter is measured as an average over the entire crystalline sample, it cannot distinguish between uniform and nonuniform distributions of topological disorder, but there is no obvious mechanism for the crystal to "dump" a homogeneous distribution of static displacements into the initial amorphous regions. Rather, it is more reasonable to assume that—as with irradiation-induced amorphization of Cu_4Ti_3—the *local* MSD varies significantly over distances of 1–5 nm in the crystalline phase as it is progressively supersaturated, implying a nonuniform distribution of local stresses, free volume, and defects that may be observable in an electron microscope.

Our high-resolution transmission electron microscopy images of nonequilibrium Nb–Pd solutions (section 4.4.7) support this interpretation: local distortions with wavelengths of $\lesssim 1\,\mathrm{nm}$ are observed looking down all but the $\langle 111 \rangle$ zone axis throughout the supersaturated crystals, implying—as with irradiation of Cu_4Ti_3—that distortions occur along the $\langle 111 \rangle$ direction. This is the direction of close-packed atomic chains in the bcc Nb–Pd crystals; it may indicate development of a pre-ω-phase instability, which would be expected to manifest itself in bcc crystals through distortions in the spacing of $\langle 111 \rangle$ lattice planes [63]. The temperature dependence of the static MSD of $Nb_{58}Pd_{42}$ (section 4.4.6) is consistent with the occurrence of an ω-phase instability at low temperature.

5.2.7 Conclusions

The significant anisotropy in local disorder seen by Luzzi in irradiated Cu_4Ti_3 and by us in supersaturated Nb–Pd point to the importance of a *local* parameter for crystalline stability. The MSD is typically measured as an average over a large region of the crystal, so it does not meet the criterion of locality, but its anomalous compositional dependence in Nb–Pd—inexplicable from elastic continuum theory—is likely a *measure* of the extent to which the static and dynamic structure of the crystal has become inhomogeneous. This local information can be complemented by Debye temperature measurements to provide an estimate for the softening of an effective modulus. Together, the two measurements provide an indication of the behavior of the *local* shear modulus, whose softening is the probable underlying cause of both melting and amorphization.

References

[1] Kurt Binder, *Rep. Prog. Phys.* **50**, 783 (1987).

[2] J. D. Gunton, M. San Miguel and Paramdeep S. Sahni, in *Phase Transitions and Critical Phenomena,* edited by C. Domb and J. L. Lebowitz (Academic, New York, 1983), Vol. 8, pp. 267–477.

[3] John W. Cahn, *Trans. Metall. Soc. AIME* **242**, 166 (1968).

[4] Herbert B. Callen, *Thermodynamics and an Introduction to Thermostatistics,* 2nd ed. (Wiley, New York, 1985), Chap. 8.

[5] David Chandler, *Introduction to Modern Statistical Mechanics,* (Oxford University Press, New York, 1987), Chap. 2.

[6] B. C. Sales, J. O. Ramey, L. A. Boatner and J. C. McCallum, *Phys. Rev. Lett.* **62**, 1138 (1989).

[7] B. C. Sales, *Bull. Am. Phys. Soc.* **37**, 632 (1992).

[8] W. L. Johnson, in *Metals Handbook,* 10th ed. (ASM International, Materials Park, OH, 1990), Vol. 2, pp. 804–821.

[9] Dokyol Lee, J. Cheng, M. Yuan, C. N. J. Wagner and A. J. Ardell, *J. Appl. Phys.* **64**, 4772 (1988).

[10] P. R. Okamoto and M. Meshii, in *Science of Advanced Materials,* edited by H. Wiedersich and M. Meshii (ASM International, Materials Park, OH, 1990), pp. 33–98.

[11] H. J. Fecht, G. Han, Z. Fu and W. L. Johnson, *J. Appl. Phys.* **67**, 1744 (1990).

[12] E. Ma and M. Atzmon, *Phys. Rev. Lett.* **67**, 1126 (1991).

[13] E. Ma and M. Atzmon, presented at the International Symposium on Mechanical Alloying, Kyoto, Japan, May 1991, submitted to Mater. Sci. Forum.

[14] E. Ma and M. Atzmon, presented at the Symposium on Solid-State Amorphization, TMS Fall Meeting, Cincinnati, OH, October 1991, submitted to the *J. Alloys Compounds.*

[15] Zezhong Fu (private communication).

[16] Harold P. Klug and Leroy E. Alexander, *X-ray Diffraction Procedures for Polycrystalline and Amorphous Materials,* 2nd ed. (Wiley, New York, 1974), Chap. 9.

[17] Rainer Birringer (private communicaton).

[18] A. Guinier, *X-Ray Diffraction in Crystals, Imperfect Crystals, and Amorphous Bodies,* (W. H. Freeman, San Francisco, 1963), Chap. 10.

[19] G. Kostorz, in *Neutron Scattering,* edited by G. Kostorz, Treatise on Materials Science and Technology, Vol. 15 (Academic, New York, 1979), pp. 227–289.

[20] G. Linker, *Nucl. Instrum. Methods Phys. Res., Sect. B* **B19/20**, 526 (1987).

[21] A. Seidel, G. Linker and O. Meyer, *J. Less-Common Met.* **145**, 89 (1988).

[22] *Binary Alloy Phase Diagrams,* edited by Thaddeus B. Massalski, Hiroaki Okamoto, P. R. Subramanian and Linda Kacprzak (ASM International, Materials Park, OH, 1990), Vol. 1, pp. 505–506.

[23] *Binary Alloy Phase Diagrams,* edited by Thaddeus B. Massalski, Hiroaki Okamoto, P. R. Subramanian and Linda Kacprzak (ASM International, Materials Park, OH, 1990), Vol. 1, pp. 502–503.

[24] T. Egami and Y. Waseda, *J. Non-Cryst. Solids* **64**, 113 (1984).

[25] T. Egami and S. Aur, *J. Non-Cryst. Solids* **89**, 60 (1987).

[26] S. H. Liou and C. L. Chien, *Phys. Rev. B* **35**, 2443 (1987).

[27] David Turnbull, *Metall. Trans. A* **12A**, 695 (1981).

[28] P. R. Okamoto, L. E. Rehn, J. Pearson, R. Bhadra and M. Grimsditch, *J. Less-Common Met.* **140**, 231 (1988).

[29] W. J. Meng, P. R. Okamoto, L. J. Thompson, B. J. Kestel and L. E. Rehn, *Appl. Phys. Lett.* **53**, 1820 (1988).

[30] W. J. Meng, J. Faber Jr., P. R. Okamoto, L. E. Rehn, B. J. Kestel and R. L. Hitterman, *J. Appl. Phys.* **67**, 1312 (1990).

[31] D. Kulp, T. Egami, D. E. Luzzi and V. Vitek, *Bull. Am. Phys. Soc.* **37**, 257 (1992).

[32] Charles Kittel, *Introduction to Solid State Physics,* 4th ed. (Wiley, New York, 1971), p. 139.

[33] Jeffrey L. Tallon, *Philos. Mag. A* **39**, 151 (1979).

[34] D. L. Davidson and F. R. Brotzen, *J. Appl. Phys.* **39**, 5768 (1968).

[35] J. L. Tallon, *Nature (London)* **342**, 658 (1989).

[36] H. J. Fecht and W. L. Johnson, *Nature (London)* **334**, 50 (1988).

[37] J. L. Tallon, *Phys. Rev. B* **29**, 4153 (1984).

[38] L. L. Boyer, *Phase Transitions* **5**, 1 (1985).

[39] H. Okamoto, *Bull. Alloy Phase Diagrams* **11**, 404 (1990).

[40] J. Logan, *Phys. Status Solidi A* **32**, 361 (1975).

[41] A. J. Drehman and W. L. Johnson, *Phys. Status Solidi A* **52**, 499 (1979).

[42] L. Battezzati and M. Baricco, *J. Less-Common Met.* **145**, 31 (1988).

[43] W. L. Johnson, *Prog. Mater. Sci.* **30**, 81 (1986).

[44] G. Grimvall and S. Sjodin, *Physica Scripta* **10**, 340 (1974).

[45] Gerald Dummer, *Z. Phys.* **186**, 249 (1965).

[46] F. H. Morin and J. P. Maita, *Phys. Rev.* **129**, 1115 (1963).

[47] R. Kuentzler and R. M. Waterstrat, *Solid State Commun.* **54**, 517 (1985).

[48] P. Garoche and W. L. Johnson, *Solid State Commun.* **39**, 403 (1981).

[49] D. G. Onn, L. Q. Wang and K. Fukamichi, *Solid State Commun.* **47**, 479 (1983).

[50] P. Garoche and J. Bigot, *Phys. Rev. B* **28**, 6886 (1983).

[51] R. Kuentzler, A. Amamou, R. Clad and P. Turek, *J. Phys. F* **17**, 459 (1987).

[52] S. K. Roy and A. K. Mondal, *J. Phys. F* **18**, 2649 (1988).

[53] Z. Altounian and J. O. Strom-Olsen, *Phys. Rev. B* **27**, 4149 (1983).

[54] Kazumasa Togano and Kyōji Tachikawa, *J. Appl. Phys.* **46**, 3609 (1975).

[55] P. Morel, *J. Phys. Chem. Solids* **10**, 277 (1959).

[56] E. W. Collings, J. C. Ho and R. I. Jaffee, *Phys. Rev. B* **5**, 4435 (1972).

[57] *Binary Alloy Phase Diagrams,* edited by Thaddeus B. Massalski, Hiroaki Okamoto, P. R. Subramanian and Linda Kacprzak (ASM International, Materials Park, OH, 1990), Vol. 3, pp. 3246–3250.

[58] *Binary Alloy Phase Diagrams,* edited by Thaddeus B. Massalski, Hiroaki Okamoto, P. R. Subramanian and Linda Kacprzak (ASM International, Materials Park, OH, 1990), Vol. 3, pp. 2647–2648.

[59] M. M. Collver and R. H. Hammond, *J. Appl. Phys.* **49**, 2420 (1978).

[60] R. Hill, *Proc. Phys. Soc. London, Sect. A* **65**, 349 (1952).

[61] D. E. Luzzi, *J. Mater. Res.* **6**, 2059 (1991).

[62] A. Seidel, S. Massing, B. Strehlau and G. Linker, *Phys. Rev. B* **38**, 2273 (1988).

[63] R. Currat and R. Pynn, in *Neutron Scattering,* edited by G. Kostorz, Treatise on Materials Science and Technology, Vol. 15 (Academic, New York, 1979), pp. 131–189.